Karlsruher Institut für Technologie

ETP-KA/2021-13

PERFORMANCE STUDIES ON 2S MODULE PROTOTYPES FOR THE PHASE-2 UPGRADE OF THE CMS OUTER TRACKER

Zur Erlangung des akademischen Grades eines

Doktors der Naturwissenschaften (Dr. rer. nat.)

von der KIT-Fakultät für Physik des
Karlsruher Instituts für Technologie (KIT)

angenommene

DISSERTATION

von

Alexander Droll, M. Sc.

aus Bühl

Tag der mündlichen Prüfung: 05.11.2021

Referent:	Prof. Dr. Thomas Müller	Institut für Experimentelle Teilchenphysik
Korreferent:	Prof. Dr. Ulrich Husemann	Institut für Experimentelle Teilchenphysik

Alexander Droll:
Performance Studies on 2S Module Prototypes for the Phase-2 Upgrade of the CMS Outer Tracker
November 2021

Contents

I Introduction and Basics 1

1 Introduction 3

2 The Compact Muon Solenoid Experiment at the Large Hadron Collider 5
2.1 The Large Hadron Collider at the CERN accelerator complex 5
2.2 The Compact Muon Solenoid Experiment 7

3 The High Luminosity LHC and the Phase-2 Upgrade of the CMS Outer Tracker 13
3.1 The High Luminosity Large Hadron Collider 13
3.2 The Phase-2 Upgrade of the CMS Outer Tracker 13

4 Particle Detection with Silicon Detectors 21
4.1 An Introduction to Semiconductor Physics 21
4.2 Interaction of Particles with Matter 28
4.3 Silicon Detectors 30
4.4 Radiation Damage in Silicon 33

II Experimental Setups and Methods 39

5 The CMS Binary Chip and the 2S Module Readout Chain 41
5.1 The CMS Binary Chip (CBC) 41
5.2 The 2S Module Readout Chain 48

6 2S Module Prototypes and Sensor Characterization 53
6.1 Sensor Material and Designs 53
6.2 Sensor Qualification and Test Stations 55
6.3 Neutron Irradiation Facility 61
6.4 The 2S Mini Module & Test Station 62
6.5 The DESY Beam Test 65

7 The High Rate Test Setup and Methods 79
7.1 The KArlsruhe High RAte TEst Setup 79
7.2 KARATE Run Analysis 83
7.3 CMSSW Simulation Based Pattern Generation 85

III Characterization of Strip Sensors and Module Prototypes 93

8 Sensor Preparation and Characterization 95
8.1 Irradiation and Annealing Procedures 95
8.2 Electrical Properties 96
8.3 Charge Collection and Annealing 100

9 Characterization of the 2S Mini Modules 103
9.1 Module Noise and Offset Calibration 103
9.2 Signal measurements 108

9.3 The Impact of Sensor Defects on the Module Performance 113
9.4 Conclusions 119

10 2S Mini Module Beam Test **121**
10.1 Cluster Efficiency and Irradiation 121
10.2 Spatial Resolution of the Sensors in the Mini Modules 128
10.3 The Stub Efficiency and Tests of the Stub Finding Logic 131
10.4 Sensor Alignment Reconstruction using Stub Bends and Particle Tracks 136
10.5 Conclusions for the Outer Tracker Material Decision 138

IV High Rate Studies of the 2S Module Readout Chain **139**

11 Commissioning and Characterization of the KARATE Setup **141**
11.1 Noise and Offset Trimming of the Injection Channels 141
11.2 Pulse Shape and Timing 141
11.3 Injector Channel Signal Calibration 143
11.4 CBC Readout Buffer Overflow Protection 144

12 Level-1 Data Bandwidth Studies **147**
12.1 Constant Trigger Frequency and Occupancy 147
12.2 CMSSW Based Stress Test of the Level-1 Data Path 151

13 CMSSW Simulation Based Analog Signal Injection **155**
13.1 Module Position and Discrete Signal Injection 155
13.2 Trigger Rate and Pileup 158
13.3 Threshold and Pileup 160

V Summary and Outlook **163**

14 Summary and Outlook **165**

VI Appendix **171**

A Additional Laboratory Test Plots **173**

B Additional Beam Test Plots **183**

C Additional Information on High Rate Measurements **191**

List of Figures **205**

List of Tables **209**

Bibliography **215**

Part I

Introduction and Basics

1

Introduction

The Large Hadron Collider (LHC) is currently the most powerful particle collider in the world. The discovery of the Higgs Boson during the first run of the LHC between 2010 and 2013 marks a highlight of particle physics research in the past decade. However, after more than a decade of operation no physics beyond the Standard Model has been observed at the LHC.

During the upcoming years the LHC will undergo a major upgrade to prepare for another 14 years of high-luminosity operation. By boosting the instantaneous luminosity of the LHC by a factor of five to seven the experiments will tenfold the recorded amount of data until 2040 and hence improve the sensitivity to rare undiscovered processes. During the high-luminosity operation the average number of particle interactions per bunch crossing (pileup) will increase from currently 30 to about 200. The higher pileup is accompanied by an intensified particle flux, which challenges the experiments. In addition, many components of the LHC and the experiments reach their initial design limits regarding radiation tolerance so that a replacement becomes mandatory. Thus, also the experiments have to be upgraded before the high luminosity operation begins.

One aspect of the upgrade is the complete replacement of the tracker of the Compact Muon Solenoid (CMS) experiment in 2026. The future Outer Tracker of the CMS experiment has to provide the following stronger requirements compared to the current one:

- increased granularity,
- contribution to the first trigger stage and
- improved radiation tolerance.

All these aspects are adressed by a new module layout. The so called p_T modules comprise two closely stacked silicon sensors to detect particles emerging from the collisions. By correlating hits in the two sensor layers the readout chips of the modules estimate the bend of the tracks in the magnetic field of the CMS detector and hence the transverse momentum p_T of the corresponding particles. A filter on tracks with low bend identifies particles with high-p_T already on module level. The selected hit information from high-p_T particles then contribute to the future track trigger system of CMS, which is an integral part of the first trigger level.

The future Outer Tracker will be equipped with two different flavors of p_T modules. The PS modules with one macro-pixel and one strip sensor will be installed in the innermost layers where a higher granularity is required. The outer layers will consist of 2S modules of which each comprises two strip sensors. To efficiently track the intensified particle flux, the strip length and pitch has been reduced compared to the old tracker. Furthermore, the signal detection switched from analog to binary operation to keep the required readout bandwidth at an acceptable level.

Regarding radiation tolerance the silicon sensors are the most critical components of the Outer Tracker modules. Damage by the harsh radiation degrades the performance of the sensors over time. During the past years extensive studies on different sensor materials and designs have been performed to assess their performance with respect to the future demands. These studies reduced the number of suitable and available sensor materials to two.

One main objective of the studies presented in this thesis is the identification of the sensor material best suitable to operate in combination with the CMS Binary Chip (CBC), the readout chip of the future 2S modules. For this purpose the two remaining sensor materials have been characterized in prototype 2S modules to determine the performance of the sensors in combination with the CBC. In total four prototype 2S modules with reduced size, called Mini Modules, have been built. The sensors of two Mini Modules have been irradiated with neutrons to two different fluences to mimic the radiation damage after years of operation in the High Luminosity LHC (HL-LHC). Chapter 6 introduces the Mini Module design, the test stations and measurement procedures. Before constructing the modules, the electrical properties of the sensors were determined and charge collection measurements have been carried out (chapter 8). After the construction of the modules, the influence of operation conditions (temperature, sensor bias voltage and leakage current), irradiation, annealing and sensor defects on the module noise and trimming performance have been quantified (chapter 9). Furthermore, the modules have been tested in a high energetic particle beam to determine the cluster detection efficiency, the tracking resolution and to validate the functionality of the p_T discrimination logic (chapter 10). Putting all measurement results into perspective of the expected operation conditions in the future Outer Tracker, one sensor material provides a slightly better performance. Sensors made from this material were ordered for the future Outer Tracker modules in 2019.

The other main objective is the investigation of the high rate stability and performance of the full 2S module readout electronics by using realistic data rates and patterns. A dedicated laboratory based setup, the KArlsruhe High RAte TEst (KARATE) setup, injects programmable hit patterns at the LHC's bunch crossing rate of 40 MHz into the analog front-end of the CBCs. In the scope of this thesis, the setup was extended to test the full 2S module readout chain. By comparing the injected patterns with the recorded hits efficiency studies on the readout chain have been performed. Chapter 7 introduces the KARATE setup and the methods to perform high rate tests on the 2S module readout chain.

Chapter 11 presents the commissioning of the KARATE setup, which includes the identification of the optimal timing between the pulse injection and sampling, pulse shape measurements and the calibration of the injection channels. In addition, the chapter elaborates the necessity of a Trigger Throttling System to veto triggers which would cause data losses by an overflow of the CBC's buffer at high trigger rates. A possible implementation of a trigger vetoing algorithm is presented and its functionality confirmed using the KARATE setup.

Chapter 12 summarizes the results of high rate bandwidth tests of the module readout electronics. In a first study the limitations of the single components have been quantified and compared with the expectations from the design parameters. A second study uses results from CMS Software (CMSSW) simulations of particle collisions and the detector response (Geant4) as input data to stress the readout chain in a more realistic way. Based on the simulation data injection patterns for the KARATE setup have been created to test the readout chain for different module positions in the tracker, pileup scenarios and trigger rates. By doing so the ultimate limitations of the 2S modules regarding trigger rate and pileup have been determined.

Finally, chapter 13 presents a study of analog-like signal injections at 40 MHz to inspect the behavior of the modules for realistic hit occupancies. The analog-like injection with KARATE is realized by a channel-wise pulse modulation following the expected signal amplitudes and channel occupancies from the CMSSW simulations.

2

The Compact Muon Solenoid Experiment at the Large Hadron Collider

The Large Hadron Collider (LHC) is currently the world's largest and most powerful particle accelerator. Operated by the European Organization for Nuclear Research (CERN) the LHC accelerates two counter-rotating beams of protons or heavy-ion nuclei to collide the particles at four interaction points [CER17]. Large experiments enclose the interaction points to detect and measure all collision products. The combination of all detector information allows the investigation of the physics processes taking place during the collisions. This chapter gives a short overview of the CERN accelerator complex and introduces the Compact Muon Solenoid (CMS) experiment and its subdetector systems.

2.1 The Large Hadron Collider at the CERN accelerator complex

To investigate the fundamental laws and particles of nature, physicists and engineers build ever more powerful particle colliders. The climax of this development was the launch of the LHC in 2010. It is located in a 26.7 km long circular tunnel 50 m to 175 m below the Franco-Swiss border close to Geneva. [CER17]

The main goal of the LHC is the delivery of proton collisions to study high energy particle physics phenomena and search for physics beyond the Standard Model (SM). Furthermore, the LHC can collide heavy-ion nuclei. These collisions generate extremely high dense Quantum Chromodynamics (QCD) matter states, which allow the investigation of the strong interaction. [Brü+04]

Two major parameters describe the performance of a collider: the center-of-mass energy $\sqrt{s}$ and its instantaneous luminosity $\mathcal{L}$. The LHC accelerates two bunched symmetrical beams of protons or heavy-ion nuclei up to an energy of 6.5 TeV or 2.56 TeV u^{-1}, respectively. Thus, it reaches a center of mass energy of 13 TeV for proton and 1150 TeV for lead collisions [CER17].

The interaction rate $\dot{N}$ of a certain process and its production cross section σ is correlated by the instantaneous luminosity $\mathcal{L}$

$$\dot{N} = \mathcal{L} \cdot \sigma. \tag{2.1}$$

For colliders, where the two beams strike under 180° with a Gaussian like beam profile, equation 2.2 approximates $\mathcal{L}$, with the number of bunches n, the number of particles in the two colliding bunches $N_{1,2}$, the orbital frequency f and the lateral extension of the beam profile $\sigma_{x,y}$. [HM18]

$$\mathcal{L} = \frac{n N_1 N_2 f}{\sigma_x \sigma_y} \tag{2.2}$$

The LHC design aims at the maximum instantaneous luminosity of $1 \times 10^{34}\,\mathrm{cm}^{-2}\,\mathrm{s}^{-1}$, which corresponds to an average pileup of about 25 interactions per bunch crossing. During the latest operation period in 2018 this value was pushed up to $2 \times 10^{34}\,\mathrm{cm}^{-2}\,\mathrm{s}^{-1}$ [CMS19b]. The reason for aiming for highest possible $\mathcal{L}$ is that also the generation rate of extremely rare events

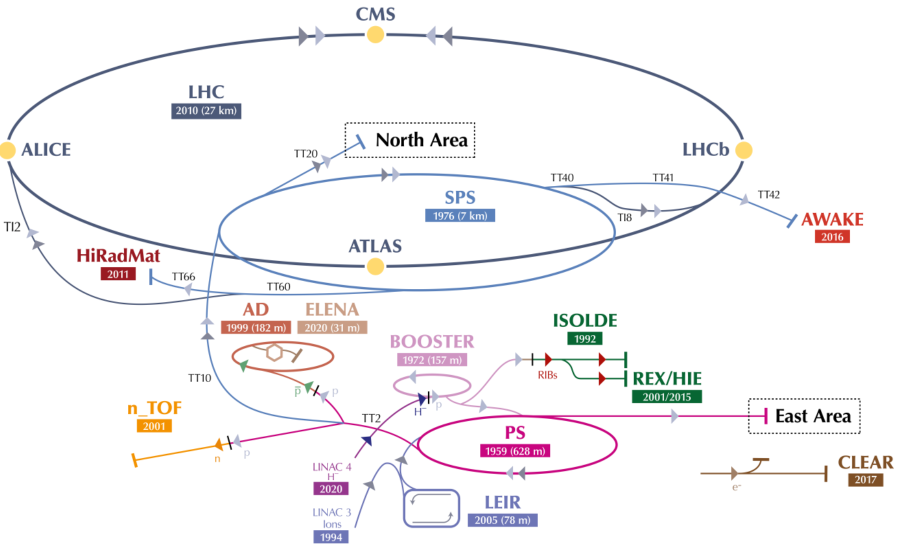

Figure 2.1: Schematic view of the CERN accelerator complex and the four major LHC experiments. Before being injected into the LHC, protons or heavy-ions pass several accelerator stages to gain energy. [Mob19]

enhances. Integrating equation 2.1 over time yields the total number of events of a certain process N_p

$$N_p = \int_0^T \mathcal{L}(t)\, \sigma_p \,\mathrm{d}t = \mathcal{L}_{\text{int}}\, \sigma_p. \tag{2.3}$$

This gives the integrated luminosity $\mathcal{L}_{\text{int}}$ as

$$\mathcal{L}_{\text{int}} = \int_0^T \mathcal{L}(t)\,\mathrm{d}t. \tag{2.4}$$

The integrated luminosity is an important quantity to describe the amount of data delivered by a collider. The longer it collides particles at high instantaneous luminosity, the higher is the integrated luminosity and the more events of a certain process are generated. Up to now the LHC delivered data equivalent to an integrated luminosity of about 190 fb^{-1} [CMS19b].

For the acceleration of the particles a series of different accelerator stages are necessary. Each stage increases further the particles' energy. In future (Run 3) the acceleration of protons will start with the linear accelerator, the LINAC 4. It will inject the protons into the Proton Synchrotron Booster (Booster) which passes them to the Proton Synchrotron (PS). After reaching an energy of 25 GeV the protons enter the Super Proton Synchrotron (SPS) which further increases the protons' energy up to 450 GeV. The SPS injects the protons into the LHC, the final stage of the CERN accelerator complex. Figure 2.1 shows all accelerators of the CERN accelerator complex.

During the acceleration process, the particles are packed into bunches. Each bunch contains up to 1.2×10^{11} particles. The LHC circulates and stores up to 2808 bunches per beam. Taking into account the circumference of the LHC, the distance between two consecutive bunches is about 7.5 m. In total, 1232 superconducting dipole magnets bend the beams on a circular trajectory. They are made of NbTi and operate at 1.9 K. Their maximum magnetic field strength of about 8.3 T limits the peak energy of the LHC. Besides the dipole magnets there are many magnets of higher order to focus and shape the beams. After acceleration the bunches collide at four interaction points at a bunch crossing rate of 40 MHz.

Four major and three smaller experiments are located around the interaction points. The experiments focus on different physics topics. Before describing the CMS experiment in detail in section 2.2 the other three large experiments at the LHC are outlined briefly:

- A Large Ion Collider Experiment (ALICE) targets the investigation of collisions of heavy-ion nuclei. The collisions form a quark gluon plasma, which is a state of extremely dense matter where quarks and gluons are in an unbound state. These studies allow a glimpse view of the conditions in the early universe. [ALI08]
- The A Toroidal LHC ApparatuS (ATLAS) experiment is a general purpose detector, with focus on the investigation of proton-proton collisions. Like the CMS experiment ATLAS explores a broad physics program. ATLAS published the discovery of the Higgs boson together with CMS in 2012 [ATL12; CMS12]. Furthermore, it performs precision measurement of the Standard Model and searches for new physics. [ATL08]
- The Large Hadron Collider beauty (LHCb) experiment focuses on the physics of b quarks and the investigation of CP violation. Compared to the other major experiments the LHCb detector has no cylindrical symmetry around the interaction point. The single-arm design in forward direction allows LHCb to precisely measure asymmetric boosted processes, like the paired production of b-mesons in forward direction. [LHC08]

2.2 The Compact Muon Solenoid Experiment

The Compact Muon Solenoid (CMS) experiment is a general purpose detector to investigate a broad range of physics phenomena. More than 5000 particle physicists, engineers, technicians and students working for over 220 institutes from 51 countries belong to the CMS collaboration [CMS19a].

In July 2012 the CMS and ATLAS collaborations announced the discovery of a Higgs like particle with a mass of 125 GeV [ATL12; CMS12]. The presence of Dark Matter and Dark Energy as well as the observed matter-antimatter asymmetry in the universe demonstrate the incompleteness of the SM. Thus, CMS searches for new physics beyond the SM like Supersymmetry (SUSY), heavy vector bosons or extra dimensions. Furthermore, CMS surveys high density states in heavy-ion collisions for precision measurements of the strong interaction. [CMS08]

To fulfill its broad physics program CMS detects particles generated in the collisions and determines their energy and momentum. At its design luminosity the LHC delivers about 25 inelastic proton-proton interactions per bunch crossing resulting in more than 1000 secondary particles. To cope with the large particle flux and to perform the targeted physics program, the requirements for the detector are the following [CMS08]:

- an almost full geometric coverage;
- a very precise muon system for muon identification, momentum resolution, dimuon mass reconstruction ($\approx 1\,\%$ at $100\,\mathrm{GeV}$) and charge identification (for $p < 1\,\mathrm{TeV}$);
- a precise tracking and vertexing system for b and τ tagging and high momentum resolution for charged particles;
- a highly granular electromagnetic calorimeter (ECAL), having a wide geometric coverage, high energy resolution and diphoton/dielectron mass resolution of about $1\,\%$ at $100\,\mathrm{GeV}$. Furthermore, at high-luminosity the ECAL has to efficiently isolate electrons and photons;
- an hadron calorimeter (HCAL) with high granularity lateral segmentation and large hermetic spatial coverage for a good missing-transverse energy and dijet-mass resolution;

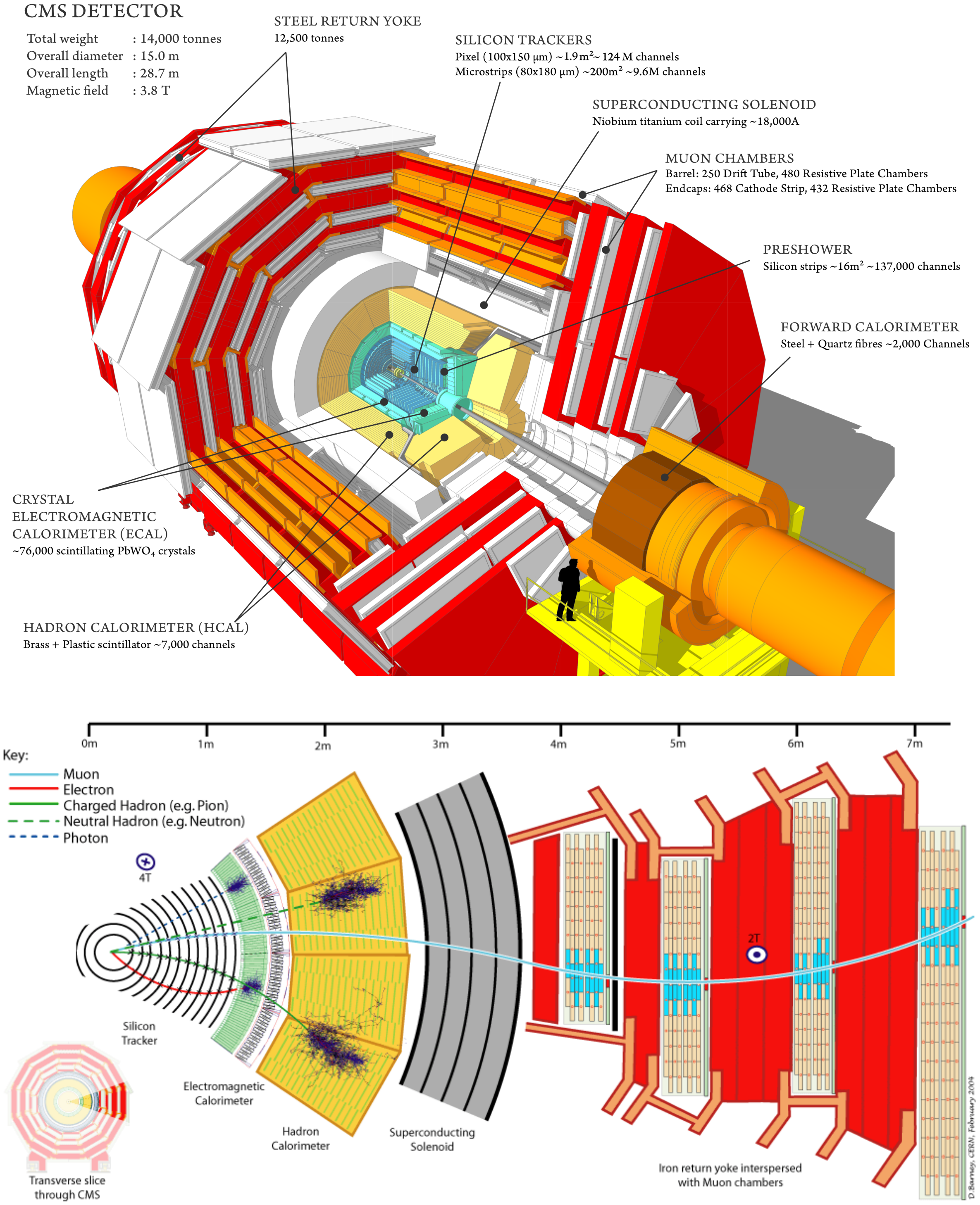

Figure 2.2: Schematic view of the CMS detector and its subdetector systems at the top (adapted from [Tay11]). The slice view (bottom) illustrates what kind of particle generate signals in which subdetector system [Dav16].

- and front-end electronics detecting signals at the collision rate of 40 MHz.

In total, the CMS experiment is about 21.6 m long with a diameter of about 14.6 m and weighs more than 14 000 t. Like most detectors at particle colliders, the CMS experiment features cylindrical symmetry around the central interaction point. CMS is composed of different specialized subdetectors. Each was optimized to tackle one or more of the requirements mentioned above. Figure 2.2 shows a schematic and a slice view of the CMS detector. The different detector systems from the outside to the inside are presented in the following.

Muon System

Muons are the only detectable particle type which is not stopped in the inner layers and the magnet of the CMS detector. Thus, the purpose of the outermost detector layer of CMS is the detection of muons. The efficient detection of and precise momentum determination for muons is important, since muons appear in the decay of many potentially undiscovered particles. The iron yoke of the solenoid magnet is equipped with three different types of gaseous detectors: drift tubes (DT), cathode strip chambers (CSC) and resistive plate chambers (RPC). The technology of choice depends on the required spatial resolution and response time as well as on the exposed particle rate predominating at different locations within CMS. [CMS97d]

Solenoid Magnet System

The measurement of the trajectories' curvature is essential for all momentum measurements of charged particles. In a magnetic field the Lorentz force deflects charged particles to helix-like trajectories, but for large momenta the curvature becomes very small. As a result the momentum resolution declines. Thus, a very strong magnetic field improves momentum measurements of high energetic particles [CMS19c]. The CMS experiment houses the most powerful solenoid magnet ever built. The magnet coil is made of superconducting niobium-titanium (NbTi), which operates at about 4 K [CMS19d]. A current of 18 500 A generates a magnetic field of up to 3.8 T in the coil's bore. To return the magnetic field an 12 000 t heavy iron yoke wraps the solenoid. [CMS97c]

Hadron Calorimeter

By absorbing hadrons like protons, neutrons, pions or kaons the hadron calorimeter (HCAL) measures the energy of these particles. In CMS the HCAL is a sandwich calorimeter composed of alternating layers of plastic scintillators and brass absorbers. The incident hadrons stop in the brass and create a shower of secondary particles. When a shower passes the plastic scintillator it generates light, which is detected by photodiodes. The HCAL is placed inside the solenoid magnet to prevent the absorption of hadrons in the magnet coil. Hence, the size of the magnet limits the dimensions of the HCAL. The minimal thickness in radial direction of the HCAL is about 5.15 nuclear interaction lengths λ. For this region additional layers of scintillators outside the solenoid act as a shower tail catcher. [CMS97b]

Electromagnetic Calorimeter

In contrast to the HCAL the electromagnetic calorimeter (ECAL) is a homogeneous calorimeter. More than 76 000 scintillating lead-tungstate ($PbWO_4$) crystals form the ECAL of the CMS experiment. This high density material ($\rho = 8.28\,\mathrm{g\,cm^{-3}}$) effectively absorbs electrons, positrons and photons with an radiation length of $X_0 = 0.89\,\mathrm{cm}$. For that reason, no further

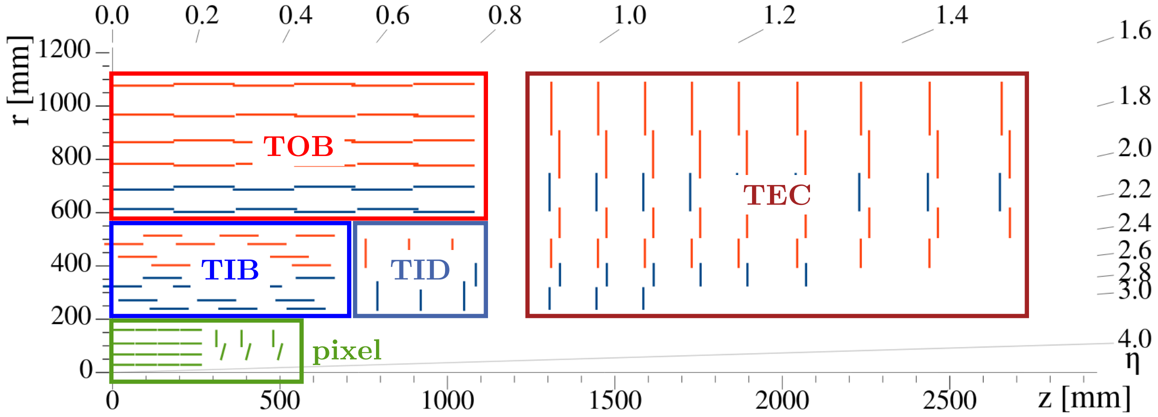

Figure 2.3: Schematic slice view of one quarter of the current CMS tracker (adapted from [CMS18]). Beginning from the interaction point, the innermost layers consist of pixel detectors. The outer region splits up into five sections: Tracker Inner Barrel (TIB), Tracker Inner Disks (TID), Tracker Outer Barrel (TOB) and Tracker EndCaps (TEC).

absorber material is necessary. At the end of each crystal avalanche diodes or vacuum phototriodes detect the scintillation light generated during the absorption process. [CMS97a]

Silicon Tracker

The central subdetector system of CMS is the silicon tracker. As it name suggests the tracker measures precisely the trajectory of charged particles. Therefore, more than 200 m^2 of silicon sensors, arranged in several layers, provide space points on the trajectory to reconstruct the particle tracks. Figure 2.3 shows the layout of the current tracker.

The requirements for the tracker are extremely high. It has to operate efficiently over years of exposure to a harsh particle flux from the hadron collisions. Furthermore, at LHC's design luminosity of $1 \times 10^{34}\,\mathrm{cm}^{-2}\,\mathrm{s}^{-1}$ in a single bunch crossing 20 to 30 inelastic interactions take place (pileup). The interactions result in about 1000 particles emerging from the interaction point. Thus, the tracker requires a high spatial resolution to isolate tracks of different particles and to identify primary and secondary vertices.

Beginning from the innermost tracker layer at a radius of $r = 4\,\mathrm{cm}$ the particle flux drops from about $1\,\mathrm{MHz/mm}^2$ to about $3\,\mathrm{kHz/mm}^2$ at the tracker's edge ($r = 115\,\mathrm{cm}$) [CMS08]. To keep the occupancy of the channels below 1 % the CMS tracker comprises two different detector types.

The innermost region consists of pixel detectors arranged in four cylindrical barrel layers and three endcap disks. The number of readout channels sums up to about 124 million distributed over an active area of about $2\,\mathrm{m}^2$ [Ada+21]. These detectors have a single point resolution of approximately 10 µm which is needed to correctly identify primary and secondary vertices [Dom07].

Costs and bandwidth limitations restrict the number of readout channels of the tracker. As a consequence, the outer region of the tracker is built up of strip detectors. To achieve the best possible performance, the tracker includes modules with different sensor geometries. Depending on its position within the tracker the strip lengths vary between 8 cm and 20 cm and the strip pitch between 80 µm and 205 µm [CMS08]. In total 15 000 modules cover an active area of 198 m^2 with about 10 million readout channels [CMS14].

The reconstructed tracks not only allow vertex identification but also provide information about the momentum and charge of the particles. In the magnetic field of the superconducting solenoid the Lorentz force deflects charged particles and bends their trajectories. The direction of the deflection reveals the charge sign of the particle. By measuring the radius R of the trajectory perpendicular to the proton beam the transverse momentum p_T of the particle in the magnetic field B is determined as [Lar19]

$$p_T \left[\frac{\mathrm{GeV}}{c} \right] = 0.3 B[\mathrm{T}] R[\mathrm{m}]. \tag{2.5}$$

With increasing transverse momentum the uncertainty on the reconstructed radius increases and thus the momentum resolution drops.

As explained before each detector system of the CMS experiment was designed and optimized to perform a specific measurement. The combination of the measurements in the different systems forms a unique signature for each particle type and allows the identification of the observed particles. The slice view in figure 2.2 illustrates the unique signature of different particle types. In CMS the particle flow algorithm reconstructs and identifies the particles emerging from the interaction point [CMS17a]

The magnetic field does not affect the uncharged *photon*. Thus, it emerges on a straight line from the interaction point. On its way out most high energetic photons penetrate the silicon tracker without interacting. However, the subsequent ECAL absorbs the photon. By the interaction the photon initiates a shower which in turn generates scintillation light. On the one hand, the shape of the shower identifies the initial particle as a photon and delivers its incident direction. On the other hand, the amount of light determines the energy of the photon. The ECAL also absorbs *electrons* and *positrons*. But since they are charged particles, they already interacted with the silicon tracker. The combined information from tracker and ECAL allows the distinction from photons.

The unique signature of *charged hadrons* (e.g. $\pi^{\pm}$) are trajectories from the tracker pointing to an energy deposition in the HCAL. *Neutral long living hadrons*, like the neutron, in turn behave similarly to the photon. They penetrate the silicon tracker undetected and also pass the ECAL without producing a signal. Finally, they deposit their entire energy in the HCAL by producing a shower. Again the shower shape determines the particle type and the incident direction. The shower intensity yields the particle energy.

The only detectable particle that penetrates the HCAL and the magnet system is the *muon*. Since it is charged it creates a signal in the tracker, and finally is identified by the matching track in the muon chambers.

However, there are also particles which are not detected by the detectors at all. The only known particles leaving CMS unrecognized are neutrinos. Nevertheless, they are reconstructed indirectly by the deficit of transverse energy. For hadron collider experiments the total transverse energy in the rest frame of the detector is zero. If there is missing transverse energy $\not{E}_T$ an undetected particle, like a neutrino, carried away the energy. To ensure the observation of all detectable particles, the detector has to be built in such a way that it encloses the interaction point as hermetically as possible.

The amount of data acquired by the subdetectors per event adds up to about 1 MB. Multiplying the event size with the bunch crossing rate of 40 MHz the data output of CMS scales up to $40\,\mathrm{TB\,s^{-1}}$ [CMS08]. To read out, store and process that much data is not possible with the existing computer farm at CMS. Fortunately, it is not necessary to read out all events. Only a small fraction of them contain information relevant for physics analysis. The trigger system of

CMS decides whether an event is read out and processed or rejected. It consist of two decision stages.

The first stage, the so called Level-1 Trigger (L1), is a hardware based system. It consists of commercially available Field Programmable Gate Arrays (FPGAs) and custom made Application Specific Integrated Circuits (ASICs). By using information of the muon system and the calorimeters it decides within 3.4 µs whether it triggers a readout of all subdetectors or not. Already this first stage reduces the event rate about a factor of 4000 to 100 kHz. [CMS17b]

The second stage is the High Level Trigger (HLT) which is software based and runs on a large computing cluster. It makes use of the information from all subdetector systems to search for interesting events. Since the HLT is software based, it is more flexible concerning the trigger decision criteria. The criteria can be adjusted to certain physics objectives and are continuously optimized. The HLT finally reduces the event rate written to disk to a few 100 Hz. [CMS17b]

3

The High Luminosity LHC and the Phase-2 Upgrade of the CMS Outer Tracker

The two most important parameters to characterize the performance of particle colliders are the collision energy and the instantaneous luminosity. Since its commissioning in 2010 the LHC improved these parameters continually. As a result, LHC reached a collision energy of 13 TeV during Run 2. The plans for Run 3, which is the operation period starting in 2022, include the increase of the collision energy to the LHC's design value of 14 TeV. Furthermore, the accelerator physicists and engineers pushed the instantaneous luminosity to a level of 2.5 times the nominal design luminosity, so that they are stressing the operation limits of the experiments. [CER21b]

3.1 The High Luminosity Large Hadron Collider

With the end of Run 3 LHC will have delivered more than 300 fb^{-1} of collision data. For many physics studies like the search for unknown heavy particles or precision measurements of the Higgs coupling this is not sufficient. Thus, in 2013 CERN announced the High Luminosity LHC (HL-LHC) upgrade to fully exploit the capabilities of the LHC. The central aspect of the upgrade is to extend the operation time of LHC at least until 2040, and to increase its nominal instantaneous luminosity. During this high-luminosity operation period LHC will tenfold the data recorded up to now and reach an integrated luminosity of 3000 fb^{-1} [Apo+17]. Figure 3.1 shows the schedule for the High Luminosity Upgrade of the LHC.

To increase the instantaneous luminosity by a factor of 5 to 7.5 the accelerator will be upgraded during the Long Shutdown 3 (LS3) between 2025 and 2027. Not only the peak instantaneous luminosity is of important to record more data but also that it remains at a high level as long as possible. Thus, improved luminosity levelling techniques will deliver a more constant high instantaneous luminosity over one filling of the HL-LHC [MP14]. However, the boost of the instantaneous luminosity has the side effect that the number of simultaneous interactions per bunch crossing (pileup) increases to value of 140 to 200 on average. Thus, not only the accelerator but also all experiments have to undergo an extensive upgrade to deal with the challenges of high-luminosity operation.

3.2 The Phase-2 Upgrade of the CMS Outer Tracker

As mentioned in the previous section the extended operation time of the LHC and its upgrade to high-luminosity operation also affects the experiments. To ensure high performance of the CMS Outer Tracker for more than ten years of operation it will be replaced before the begin of the high-luminosity operation. On the one hand, the radiation damage accumulated over the past years affects the performance of the present CMS Outer Tracker. The silicon sensors and readout electronics reach their design radiation limits and will not withstand another decade of operation. On the other hand, the high-luminosity upgrade will tighten the operation

Figure 3.1: The High Luminosity LHC Upgrade schedule in November 2021. After passing two Long Shutdowns (LS1, LS2) and an Extended Year-End Technical Stop (EYETS) the LHC will enter Run 3 in 2022. Already during Run 2, the LHC doubled its nominal instantaneous luminosity. During the next operation period it is planned to increase the maximum center of mass energy to 14 TeV. During Long Shutdown 3 (LS3) the accelerator and experiments will undergo an extensive upgrade before entering the high-luminosity operation in 2027. [CER21b]

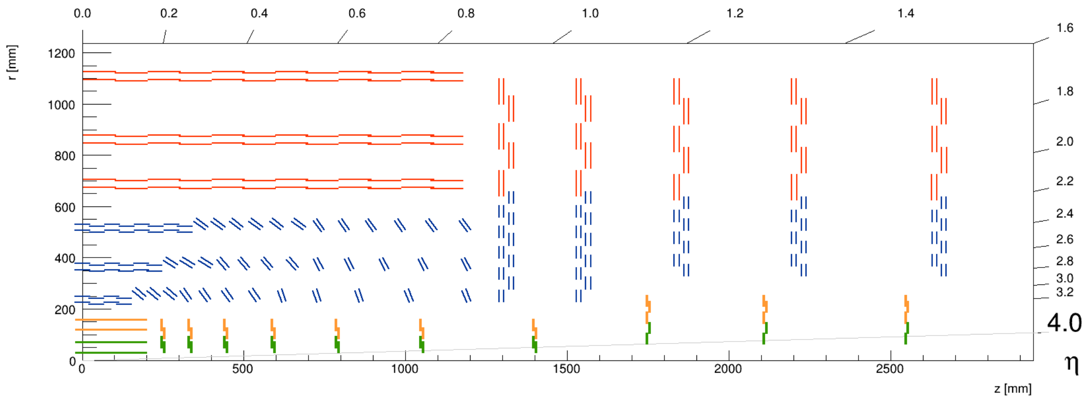

Figure 3.2: Schematic slice view through one quarter of the Phase-2 Tracker. Each colored line represents a sensor layer. The tracking acceptance of the Inner Tracker (green and orange lines) improves to $|\eta| < 4$ by adding additional endcap layers. The Outer Tracker consists of two flavors of p_T modules. Double blue lines symbolize the PS module and double red lines the 2S module flavor of the Outer Tracker modules. [CMS18]

requirements on the tracker fundamentally. Thus, one cannot just rebuild the existing tracker. To meet the new requirements the Outer Tracker community proposed a novel tracker concept in the Technical Design Report (TDR) [CMS18]. This section summarizes the Phase-2 Upgrade of the Outer Tracker.

High-luminosity operation involves a higher pileup and more intensive particle flux from the interaction point. This implies a much harsher radiation exposure of the tracker. The sensors and readout electronics have to be more radiation hard compared to the present tracker. In addition, the stronger particle flux involves an increase of the track density. To ensure efficient tracking and separation of the particle trajectories the occupancy of the readout channels has to stay below 3 % in the innermost layer of the Outer Tracker. Thus, the future Outer Tracker modules will use sensors with higher density of readout channels.

Furthermore, the intensified luminosity increases the single muon Level-1 Trigger (L1) rate, which will exceed 100 kHz. Even applying stricter selection criteria will not reduce the trigger rate sufficiently. However, a solution to improve the trigger performance is to provide tracking information to the L1 stage. [Hal11]

Thus, the contribution of the future Outer Tracker to the L1 stage is the most substantial innovation of the upgrade. The transfer of all hit information to the L1 decision logic would exceed the available bandwidth of the foreseen technology. Therefore, the new design of the Outer Tracker modules allows to select particles with transverse momentum (p_T) above a certain threshold. Then a hardware-based track finding logic performs a real-time tracking of these particles. The reconstruction of high-p_T tracks runs at 40 MHz bunch crossing rate and supports the L1 trigger decision. Section 3.2.3 explains the design and functionality of these novel Outer Tracker modules, called p_T modules.

3.2.1 The Phase-2 Tracker Layout

The layout of the tracker implements the track trigger concept. It still foresees the separation of Inner and Outer Tracker region. Thus, it will be still possible to remove the Inner Tracker for maintenance reasons, e.g. during year-end technical stops. Figure 3.2 shows a schematic slice view through one quarter of the Phase-2 Tracker.

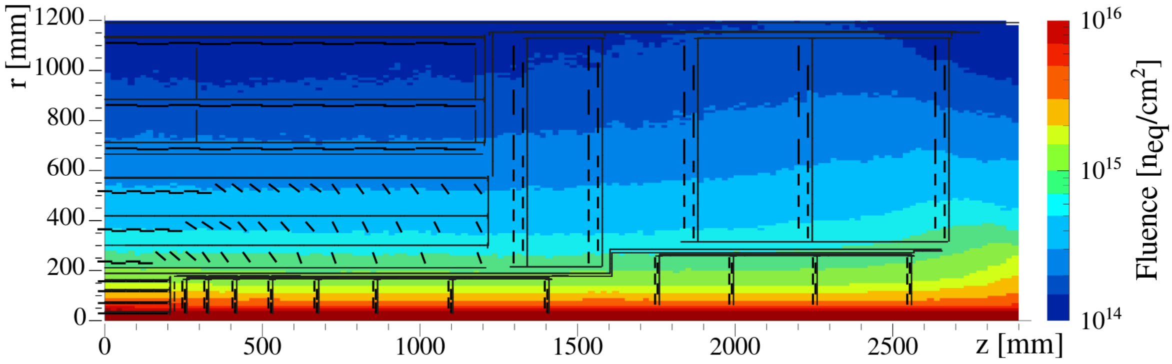

Figure 3.3: Radiation levels expected by FLUKA[2] simulations for $3000\,\mathrm{fb}^{-1}$ of data for one quarter of the Phase-2 Tracker. The innermost pixel layer accumulates an equivalent fluence of about $2 \times 10^{16}\,\mathrm{n_{eq}/cm^2}$. The PS and 2S modules are exposed to more moderate fluences of up to $1 \times 10^{15}\,\mathrm{n_{eq}/cm^2}$ and $3 \times 10^{14}\,\mathrm{n_{eq}/cm^2}$, respectively. [CMS18]

The most prominent modification in the layout are several additional disks in the very forward direction of the Inner Tracker. Hence, the tracking acceptance will increase from currently $|\eta|^1 < 2.4$ to $|\eta| < 4$. The Inner Tracker will consist of pixel detectors and will cover an active area of about $5\,\mathrm{m}^2$ with more than 3.8 billion readout channels. There will be two types of modules, either read out by two ASICs in the inner region or four readout ASICs in the outer region. The modules will be assembled in four layers in the barrel region and twelve endcap disks in the forward direction.

In contrast to the Inner Tracker, the acceptance of the Outer Tracker will remain unchanged. To provide tracking information for the Level-1 Trigger (L1) the layout of the Outer Tracker relies on two flavors of p_T modules (see section 3.2.3). More granular macro-pixel strip modules (PS modules) will compose the first three barrel layers and the inner rings of the endcaps. The macro-pixel approach improves the resolution in z direction to facilitate distinguishing between individual tracks. A tilt of some PS modules in the barrel region increases the detection efficiency for tracks of high-p_T particles. It takes account of the expected incident angles and ensures that both sensor layers of the modules are hit by the tracks. Besides that, the tilt also reduces the number of PS modules and thus the material in the tracking volume. For the outer three layers of the barrel and for radii $r > 700\,\mathrm{mm}$ in the endcaps the particle density is low enough to use strip sensors. There, strip-strip modules (2S modules) provide enough granularity for efficient operation (see also section 3.2.4). In total about 5600 PS modules and 7700 2S modules will form the Phase-2 Outer Tracker of the CMS experiment.

3.2.2 The Radiation Environment

The investigation of particle collisions at the LHC involves a harsh particle flux exposing all detector components of CMS. The accumulated radiation level scales linearly with the integrated luminosity. Thus, the future components have to cope with higher radiation levels compared to the current ones. Figure 3.3 shows the expected radiation levels for the Phase-2 Tracker.

---

[1] Pseudorapidity defined by $\eta = -\ln\left(\tan\left(\frac{\Theta}{2}\right)\right)$, where Θ is the angle between the particle trajectory and the z-axis, which is parallel to the beam axis

[2] **FLU**ktuierende **KA**skade [Bat+15]

Since the Inner Tracker is the part of the CMS detector closest to the interaction point it has to withstand the highest radiation levels of all systems. With increasing distance to the interaction point the radiation levels decrease. To collect $3000\,\mathrm{fb}^{-1}$ of data the innermost layer of the tracker is exposed to a fluence[3] of $\phi = 2 \times 10^{16}\,\mathrm{n_{eq}/cm^2}$.

In the Outer Tracker the radiation levels are more moderate but still challenging. The fluences vary from $1 \times 10^{15}\,\mathrm{n_{eq}/cm^2}$ for the PS modules down to $1 \times 10^{14}\,\mathrm{n_{eq}/cm^2}$ for the outermost layer of 2S modules. Thus, the CMS hardware group at Karlsruhe Institute of Technology (KIT) has evaluated different sensor materials and thicknesses for their application in the Outer Tracker. One part of this thesis investigates the behavior of silicon strip sensors of two different thicknesses in 2S module prototypes.

3.2.3 The p_T Trigger Module Concept

One of the main tasks of the future Outer Tracker is to provide tracking information to the first trigger stage of the CMS experiment. However, it is not possible to transmit all hit information to the L1 track finder, because of the limited bandwidth of the readout links. To reduce the amount of data the future tracker will only transmit hit information of particles with transverse momentum (p_T) above a certain threshold at 40 MHz to the trigger system.

The new p_T module concept realizes this task by combining hit information of two closely spaced silicon sensor layers. The spacing of the two sensor layers depends on the position of the module within the tracker. In the strong magnetic field of the CMS solenoid the Lorentz force deflects charged particles moving from the interaction point outwards. The higher the transverse momentum (p_T) is, the smaller is the curvature of the particle's trajectory. The logic on the modules correlates hits in both sensor layers to detect particles with high p_T.

Figure 3.4 illustrates the working principle of the correlation logic, called the stub finding logic. A common ASIC reads out both sensor layers. If the first layer, the seed layer, detects a hit the ASIC searches for another hit within a programmable window in the second layer, the correlation layer. Trajectories of particles with large p_T bend less and hit the correlation layer within the correlation window. The detection of a hit within this window then triggers the generation of a *stub* signal. This signal contains information about the position of the hit in the seed layer and its distance to the hit in correlation layer, which is called the bend of the stub.

The width of the correlation window has to be adapted for each module in such a way that only particles with $p_T > 2\,\mathrm{GeV/c}$ generate stubs. To find the correct window width also the position of the module within the tracker and the spacing of the sensor layers has to be taken into account. Not all modules are oriented perpendicular to the interaction point. Particles with large p_T strike the sensor layers of these modules with some inclination. An adjustable shift between the seed hit and the center of the correlation window corrects for this inclination.

Only particles with $p_T > 2\,\mathrm{GeV/c}$ are detected by the stub logic. Since only the stub information is sent to the L1 track finder the amount of data reduces by two orders of magnitude [PH10]. However, information of hits not accepted by the stub finding logic is not lost. A buffer in the readout ASIC stores all hit information for a certain time period. Only for a positive trigger decision the Data Acquisition (DAQ) system requests the readout of this information.

Figure 3.5 show both p_T module types. The sensors of the PS modules have an active area of $5 \times 10\,\mathrm{cm}^2$ with about 30 000 macro pixels or 2000 strips, respectively. With increasing distance to the interaction point the deflection of the particle trajectory increases and the particles strike the modules with larger inclination. To ensure efficient separation between particles

---

[3] Neutron equivalent per cm^2: particle flux normalized on the damage in silicon caused by neutrons with $E = 1\,\mathrm{MeV}$ [Mol99]

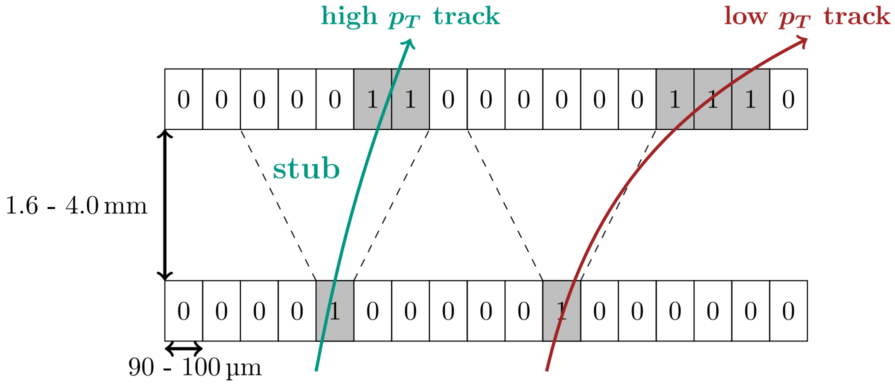

Figure 3.4: Working principle of the p_T module concept. Two closely separated silicon sensor layers detect charged particles. With increasing momentum the trajectory of a charged particles bends less in the magnetic field. Thus, for high enough transverse momenta the hits in the top sensor are most likely within a narrow correlation window above the hit in the lower sensor. For such hit doublets a *stub* signal is generated and sent to the Level-1 Trigger. Illustration following [CMS18].

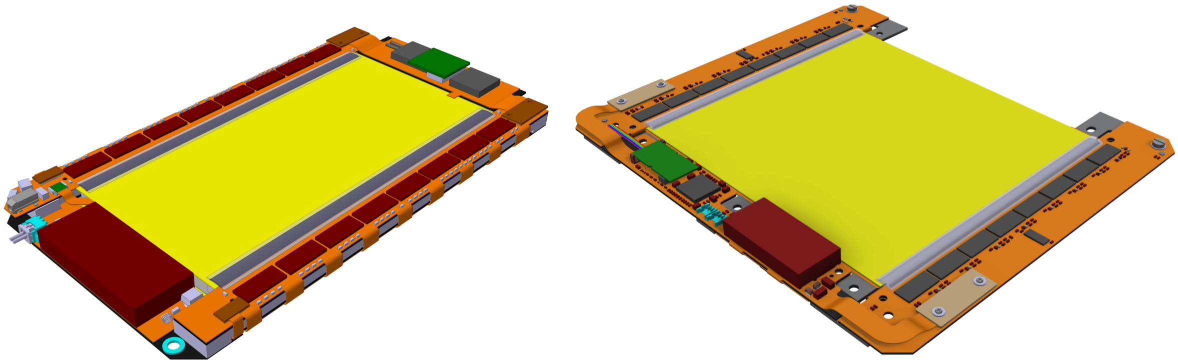

(a) PS module **(b)** 2S module

Figure 3.5: Drawings of the two different p_T module flavors. The more granular PS modules (a) comprise one macro-pixel and one strip-sensor and are used to equip the center region of the Outer Tracker. In turn the 2S modules (b) consist of two identical strip sensors and set up the outer region. [CMS18]

with low and high p_T the spacing of the sensor layers is larger for the innermost module layers. Thus, the PS modules comes with three different spacings: 4.0 mm, 2.6 mm and 1.6 mm.

This thesis focuses on the development and investigation of 2S module prototypes. Hence, section 3.2.4 gives a more detailed description of the 2S module design.

3.2.4 The 2S Module

The key components of the 2S module are two silicon strip sensors. Each sensor has an active area of about $10 \times 10\,\mathrm{cm}^2$. In total, 2032 strips of 5 cm length are arranged in two rows with a pitch[4] of 90 µm. The strips of the sensors have to be aligned in parallel to ensure a correct stub identification. Even a small rotation between the strips of more than 400 µrad causes a wrong determination of stub bends for some regions of the 2S module and the stub logic fails. Two bridges made of carbon-fiber reinforced aluminum (Al-CF) separate the sensors. The material was chosen for its low density, its similar coefficient of thermal expansion compared to silicon and its high thermal conductivity for cooling purposes. However, not only the sensors but all components of the 2S module are attached to the Al-CF bridges, as shown in figure 3.6.

Besides the sensors and bridges the 2S module comprises two front-end hybrids [Gad+18] and one service hybrid [Fel+18]. From both sides of the module the two front-end hybrids read out the signals from the strips. They are made of flexible material, allowing to fold the hybrids around a stiffener. By doing so, every second readout line is routed to the bottom sensor layer. Individual wire bonds connect each strip of the sensors to a readout line of an hybrid.

Eight CMS Binary Chips (CBCs) [Uch+18] are bump bonded to each front-end hybrid. One CBC reads out 254 strips, 127 from each sensor layer. The connected strips distribute to both sensor layers in an alternating way to facilitate the correlation logic. Furthermore, each front-end hybrid comprise one Concentrator Integrated Circuit (CIC) [Ber+19]. It collects the data from the CBCs. After compressing and serializing, it transmits the data to the service hybrid.

The service hybrid connects the module to the detector backend. It is responsible for monitoring, powering and communication of the module. The low power Gigabit Transceiver (lpGBT) [Mor18] receives zero-suppressed hit information from the two CICs. After serializing the data streams, the lpGBT transfers all data at 5.12 Gbit/s via the Versatile Link Plus Transceiver (VTRx+) [Tro+17] module to the data acquisition system of CMS. Furthermore, the lpGBT comprises a block to forward I2C commands for slow control of the module components and distributes the 320 MHz clock for the front-end chips.

The electrical power loss of cables scales with the square of the current I^2 and the inverse of the cable cross section A. To reduce the heat dissipation and the material budget in the tracker, the supply voltage for the modules is 11 V. This is far above the required 1.0 V and 1.25 V to operate the ASICs. Thus, the service hybrid also houses a DC-DC converter to provide the correct voltages for the front-end electronics. A more detailed description of the module readout chain and its components is given in chapter 5.

---

[4] distance between the strip implant centers of two adjacent strips

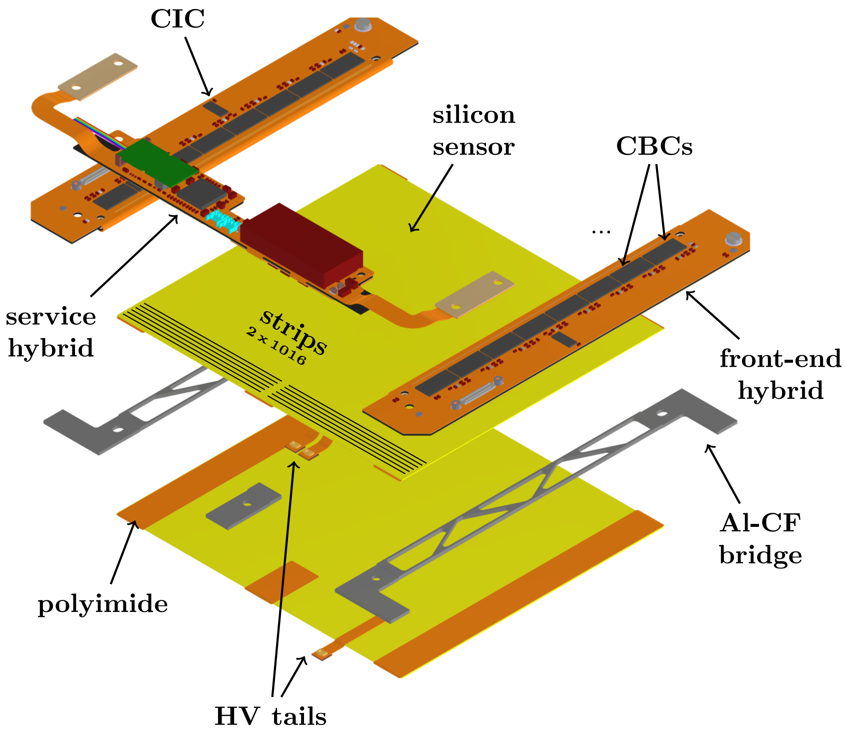

Figure 3.6: Exploded view of the 2S module. Two silicon strip sensors are arranged in parallel. Two Al-CF bridges separate the sensors and provide the mounting structure of all module components. Polyimide strips electrically isolate the bridges from the high voltage (HV) on the sensor backside. Two front-end hybrids, each equipped with eight readout chips (CBCs) detect the sensor signals. One service hybrid powers the module, monitors the module parameters and acts as data transmitter [CMS18].

4

Particle Detection with Silicon Detectors

The invention of the first semiconductor based transistor by Bardeen, Brattain and Shockley [BB48] in 1947 triggered the maybe most important technological development of the 20th century. The wide field of possible applications of semiconductors boosted innovation in this sector of industry and reduced prices over time. Today, silicon-based components are present in almost every electrical device like computers, mobile phones or solar panels.

In particle collider experiments like CMS the detectors have to cope with a very harsh radiation environment while detecting efficiently the emerging particles. Over the last decades silicon-based semiconductor detectors proved their reliability in particle tracking. This chapter introduces the theoretical concepts to understand the electrical behavior of semiconductors. Before explaining the working principle of silicon detectors and the influence of radiation damage on their performance, this chapter presents the interaction of particles with matter and their energy deposition in silicon.

4.1 An Introduction to Semiconductor Physics

To understand the working principle of silicon detectors a basic understanding of semiconductor physics is mandatory. This section introduces the theoretical concepts to understand the electrical properties of semiconductors. Furthermore, it explains techniques to manipulate the electrical behavior of semiconductors which are necessary for their application in high energy physics experiments.

4.1.1 The Energy Band Model

The energy band model is a concept from solid-state physics. By describing the energy states of electrons in the crystal lattice it explains macroscopic properties, like the electrical conductivity, of the solid. To determine the energy states of the electrons in a regular crystal lattice the Schrödinger equation is solved for a periodic potential. The resulting energy states form multiplets of very similar energy, this is why they are called energy bands. Gaps in which no energy levels for the electrons are present separate the different energy bands. [Dem16]

Since electrons are fermions, two electrons cannot occupy the same quantum-mechanical state. The probability to find an electron in a state with energy E depends on the temperature T and is given by the Fermi-Dirac distribution shown in equation 4.1. The chemical potential μ corresponds to the energy of the state with 50 % occupancy probability and k_B is the Boltzmann constant. [Hun17]

$$f(E) = \frac{1}{e^{(E-\mu)/k_\mathrm{B}T} + 1} \tag{4.1}$$

At $T = 0\,\mathrm{K}$ the chemical potential equals the Fermi energy E_F and the electrons occupy all energy states below E_F. For any temperature T above some electrons are thermally excited into higher energy states. The highest energetic band fully occupied by electrons at $T = 0\,\mathrm{K}$ is the *valence band* and the next higher energetic band is the *conduction band*. The width of

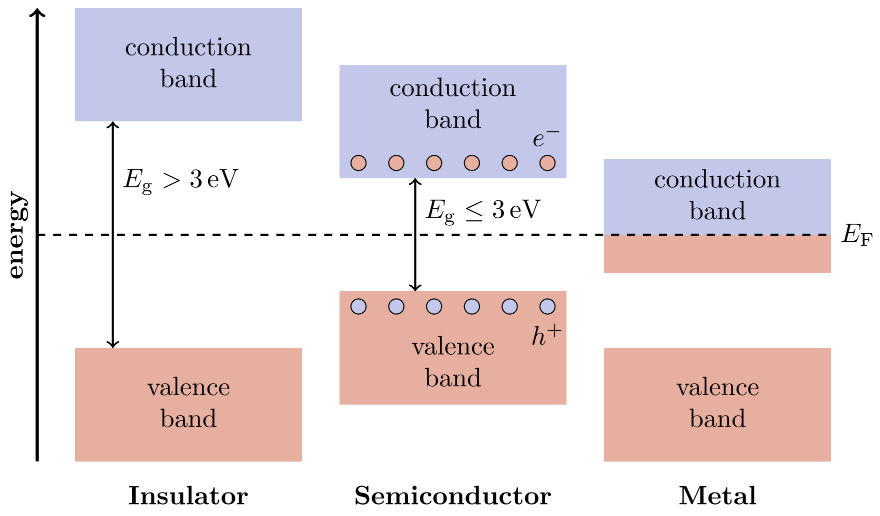

Figure 4.1: Schematic representation of the band structure to classify different materials. At $T = 0\,\mathrm{K}$ all electron energy levels up to the Fermi energy E_F are occupied. For insulators and semiconductors E_F is in the middle of the band gap between valence and conduction band. Insulators have a large band gap $> 3\,\mathrm{eV}$. At room temperature thermal excitations do not excite electrons into the conduction band. Thus, insulators are non-conductive. For semiconductors the band gap is much smaller ($\leq 3\,\mathrm{eV}$) and thermal excitation is possible. The conductivity strongly depends on the temperature. For metals E_F is within the conduction band, making them conductive even for very low temperatures. Illustration following [Dem16].

the band gap E_g between the valence and conduction band provides one possible classification of solids. [Dem16] Figure 4.1 illustrates this classification into insulators, semiconductors and conductors.

- For **metals** (conductors) the Fermi energy is located within the conduction band. Thus, even for very low temperatures a large number of electrons occupy electron levels in the conduction band. As a consequence metals have a high conductivity.
- **Insulators** have a large band gab $E_\mathrm{g} > 3\,\mathrm{eV}$. The probability to excite an electron into the conduction band is negligible at realistic temperatures. Thus, insulators are non-conductive [GM14].
- For $T = 0\,\mathrm{K}$ the conduction band of **semiconductors** is not occupied by electrons. Since the band gap $E_\mathrm{g} \leq 3\,\mathrm{eV}$ is much smaller compared to insulators, it needs less thermal energy to lift electrons from the valence into the conduction band. High enough temperatures excite electrons into the conduction band and increase the conductivity of the material. For this reason the conductivity strongly depends on the temperature. Besides the electrons in the conduction band the unoccupied energy levels (holes) in the valence band increase the conductivity.

The most commonly used semiconductor material for particle physics detectors is silicon. One reason is that it is widely used in industrial applications. Thus, the manufacturing processes are matured and provide high yield and quality at rather low costs. Regarding the application as particle detectors the number of intrinsic charge carriers has to be low to detect signals from particles.

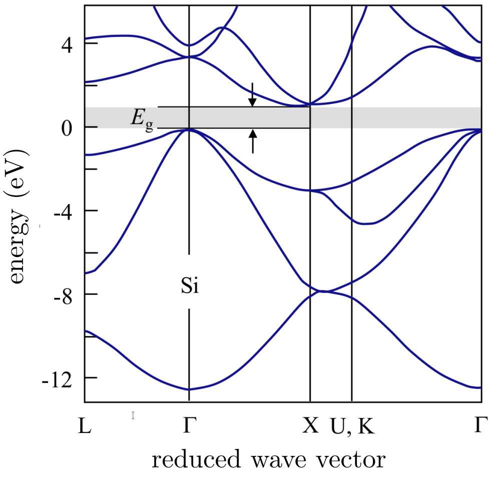

Figure 4.2: Band structure of the indirect semiconductor silicon. The maximum of the valence band and minimum of the conduction band are shifted in momentum space. Thus, silicon is an indirect semiconductor. The excitation with the band gap energy requires the interaction with an additional phonon and hence is very unlikely to happen. Thus, the mean excitation energy in silicon is 3.6 eV, which is more than two times larger than the band gap $E_g = 1.12\,\text{eV}$. [Hun17]

The band gap of silicon is $E_g = 1.12\,\text{eV}$. However this is not the mean energy necessary to excite an electron from the valence into the conduction band. Silicon is an indirect semiconductor, which means that the maximum of the valence band E_V and the minimum of the conduction band E_C are located at different positions in momentum space, as shown in figure 4.2. The excitation of an electron with the band gap energy requires an additional momentum transfer. The momentum of the massless photon is too small for an indirect transition with the band gap energy. Thus, to ensure momentum conservation, this transition involves the absorption or emission of an additional phonon. From the energetic point of view the indirect transition is favored. But since it is a three body process it is much more unlikely to take place than the direct, two body, transition. As a consequence the mean excitation energy to create an electron-hole pair in silicon is 3.6 eV. [GM14]

4.1.2 The Effect of Doping

Intrinsic semiconductors still have too many free charge carriers for the application as particle detectors. The number of free charge carriers in an typical silicon sensor with an area of $10\,\text{cm} \times 10\,\text{cm}$ and 300 µm thickness is in the order of $\mathcal{O}(10^{10})$. This number exceeds by far a typical charge deposition of about $22\,\text{ke}^-$ by charged particles passing a silicon sensor. [Har17] However, there is a technique called *doping* to modify the electrical properties of semiconductors in such a way that they become suitable for particle detection. The doping process implants foreign atoms into the crystal lattice of semiconductors. These impurities influence the electron level concentration in the band structure and hence the macrosopic electrical properties of the material. In the following the effect of doping is explained using silicon as an example.

Silicon is of the fourth main group of the periodic table and hence has four valence electrons. The valence electrons form covalent bonds with four neighboring silicon atoms to build up the crystal lattice. There are two types of dopings to distinguish. On the one hand, the doping with atoms of a higher main group adds additional unbound electrons to the crystal lattice. An example is phosphorous, which is of the fifth main group and has five valence electrons.

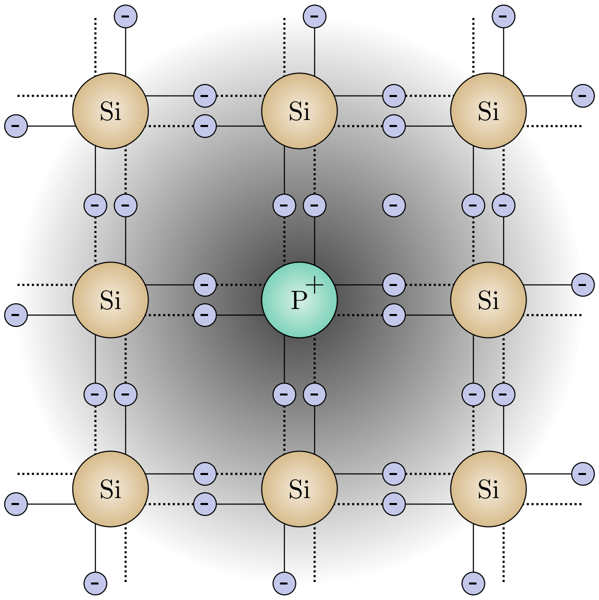

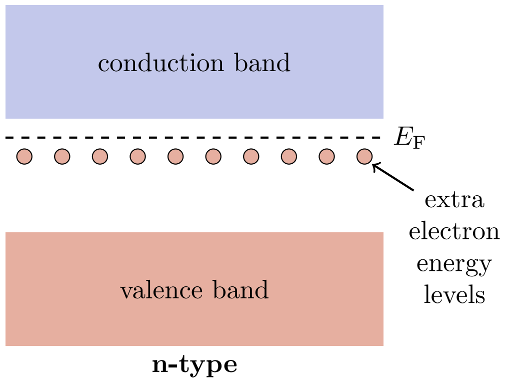

(a) Doping with phosphorous. Loosely bound electrons are brought into the crystal lattice. They create new occupied energy levels within the band gap close to the conduction band and increase the conductivity.

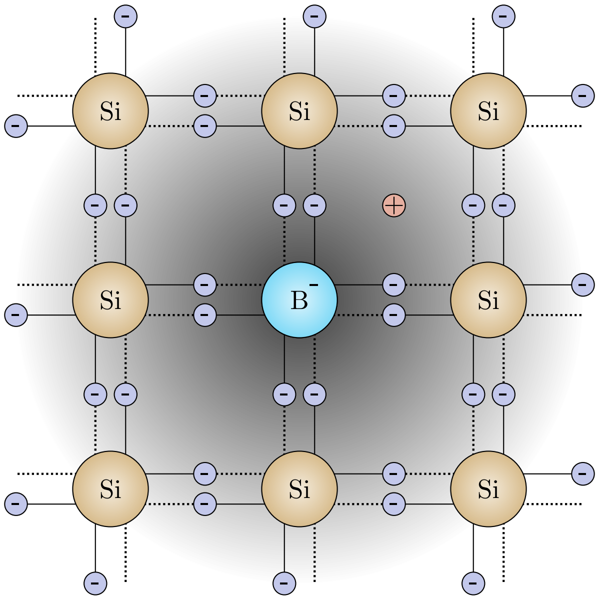

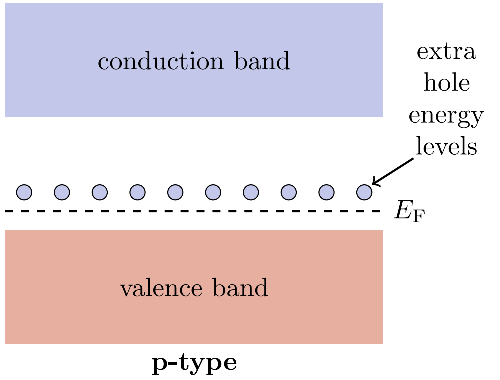

(b) Doping with boron. Electron vacancies are brought into the crystal lattice. They create new unoccupied energy levels within the band gap close to the valence band and increase the conductivity by hole conduction.

Figure 4.3: Illustration of the effect of n- and p-type doping on the silicon crystal lattice and band structure. Illustration following [Hun17].

These kind of dopants are also called donors or n-type dopants. Since there is no partner for the surplus electrons to form a covalent bond they are only loosely bound to the implanted atoms. In the band model, the additional electrons create new occupied electron energy levels within the band gap that are slightly below the conduction band. The energy necessary to excite these electrons into the conduction band is very low. This leads to an increase of the conductivity of the material. Figure 4.3a shows an illustration of the n-type doping and its effect on the crystal lattice and energy bands.

On the other hand, one can implant atoms of a lower main group with fewer valence electrons. An example is boron with three valence electrons. Boron atoms form covalent bonds to three neighboring silicon atoms. The missing electron can be filled by an electron of the surrounding silicon atoms; that is why this kind of implants are also called acceptors. By doing so the electron vacancy is moving through the substrate creating a positive charged quasi particle (hole). Regarding the band model, the electron vacancies create new unoccupied energy levels within the band gap that are slightly above the valence band. The energy necessary to excite electrons from the valence band in the new energy states again is very low. Excited electrons leave vacancies (holes) in the valence band, which increase the conductivity of the material. Figure 4.3b shows an illustration of the p-type doping and its effect on the crystal lattice and energy bands.

4.1.3 The pn-Junction

The doping process increases the number of free charge carriers in the material. However, one can use the electrical properties of doped semiconductors to generate substrates that are free from mobile charge carriers. By combining p- and n-doping in one piece of silicon a pn-junction is formed. The Fermi energy in p-/n-doped materials is slightly above/below the valence/conduction band. But the Fermi energy has to be constant within the substrate. To equalize the Fermi energy in the different doped regions charge carriers diffuse along the concentration gradient. In particular, holes diffuse from the p- into the n-type region and electrons from the n- into the p-type region, respectively. In the contact region the charge carriers recombine and leave the ionized doping atoms in the crystal lattice. As a result of the recombination process, an electric field forms between the differently doped regions. The field counteracts the diffusion process and grows until an equilibrium is reached. The contact region of p- and n-type silicon becomes free from mobile charge carriers. This is why it is also called the depletion or space-charge region. The electric field shifts the electrostatic potentials of the two regions by the builtin voltage V_0. In the picture of the band model, the bands deform by eV_0, where e is the elementary charge, to equalize the Fermi level. Figure 4.4 illustrates the pn-junction and the diffusion process.

The simplest silicon detector, a diode, consists of one pn-junction. The depletion region is essential to detect particles. An external voltage V_{ext} can extend the width of the depletion region until the whole substrate volume is depleted. The minimum voltage V_{dep} for which the full volume is depleted is an important design parameter for silicon detectors.

In the following a model to calculate the width of the depleted space-charge region and the depletion voltage is presented [Har17; Sau09]. In equilibrium, the Poisson equation describes the electrostatic potential $\Phi(x)$ of the pn-junction

$$\frac{\partial^2 \Phi}{\partial x^2} = \frac{1}{\epsilon_0 \epsilon_{\text{Si}}} \rho(x) \tag{4.2}$$

including the vacuum permittivity ϵ_0 and the relative permittivity of silicon ϵ_{Si}. The charge density $\rho(x)$ depends on the concentration of electrons $n(x)$ and holes $p(x)$, and the density of

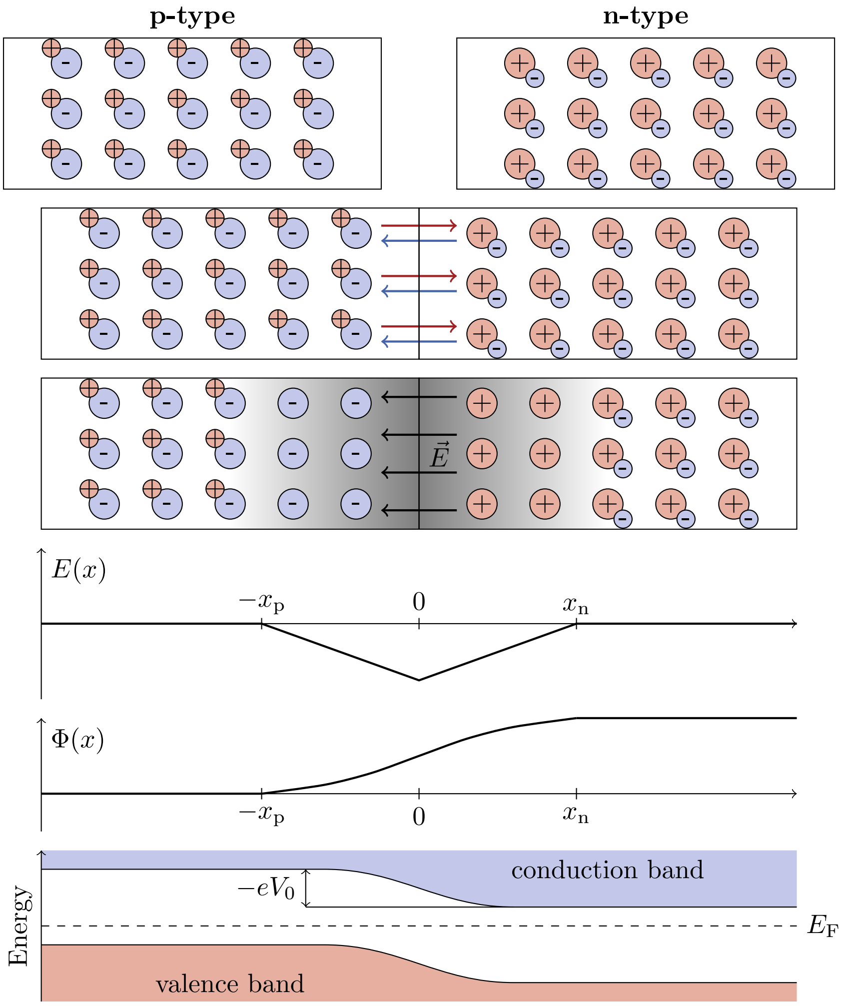

Figure 4.4: Illustration of the pn-junction. By contacting p- and n-type silicon the majority charge carriers begin to drift along their concentration gradient into the oppositely doped region. In the contact region the charge carriers recombine, which creates a space-charge region without mobile charge carriers. The ionized impurity atoms form an electric field counteracting the diffusion process until the processes balance in equilibrium. The space-charge region is non-conductive since no more mobile charge carriers are left over. Illustration following [Nür14].

acceptors N_A and donors N_D.

$$\rho(x) = -q\left[n(x) - p(x) + N_\mathrm{A} - N_\mathrm{D}\right] \tag{4.3}$$

In the space-charge region ($-x_\mathrm{p} \leq x \leq x_\mathrm{n}$) no free electrons and holes remain, so that $n(x)$ and $p(x)$ become zero. Assuming a discontinuous step of the doping concentration at the junction ($x = 0$) and a constant doping concentration for all other regions, $\rho(x)$ simplifies to

$$\rho(x) = \begin{cases} -qN_\mathrm{A} & \text{for } -x_\mathrm{p} \leq x \leq 0 \\ qN_\mathrm{D} & \text{for } 0 < x \leq x_\mathrm{n}. \end{cases} \tag{4.4}$$

Integrating equation 4.2 once reveals the electric field strength $E_{n/p}(x)$ for the n- and p-doped regions with linear dependence on x

$$\begin{aligned} E_\mathrm{p}(x) &= -\frac{qN_\mathrm{A}}{\epsilon_0\epsilon_\mathrm{Si}}(x + x_\mathrm{p}) \quad \text{for } -x_\mathrm{p} \leq x \leq 0 \\ E_\mathrm{n}(x) &= \frac{qN_\mathrm{D}}{\epsilon_0\epsilon_\mathrm{Si}}(x - x_\mathrm{n}) \quad \text{for } 0 < x \leq x_\mathrm{n}. \end{aligned} \tag{4.5}$$

A second integration yields the electrostatic potential Φ. Using the boundary conditions $\Phi(-x_\mathrm{p}) = 0$ and $\Phi(0^-) = \Phi(0^+)$, it simplifies to

$$\begin{aligned} \Phi_\mathrm{p}(x) &= \frac{qN_\mathrm{A}}{2\epsilon_0\epsilon_\mathrm{Si}}(x + x_\mathrm{p})^2 \quad \text{for } -x_\mathrm{p} \leq x \leq 0 \\ \Phi_\mathrm{n}(x) &= -\frac{qN_\mathrm{D}}{\epsilon_0\epsilon_\mathrm{Si}}\left(\frac{x^2}{2} - x_\mathrm{n}x\right) + \frac{qN_\mathrm{A}}{2\epsilon_0\epsilon_\mathrm{Si}}x_\mathrm{p}^2 \quad \text{for } 0 < x \leq x_\mathrm{n}. \end{aligned} \tag{4.6}$$

The difference of $\Phi(x)$ over the space-charge region is the *builtin* or *diffusion voltage* V_0

$$V_0 = \Phi_\mathrm{n}(x_\mathrm{n}) - \Phi_\mathrm{p}(-x_\mathrm{p}) = \Phi_\mathrm{n}(x_\mathrm{n}) = \frac{qN_\mathrm{D}}{2\epsilon_0\epsilon_\mathrm{Si}}x_\mathrm{n}^2 + \frac{qN_\mathrm{A}}{2\epsilon_0\epsilon_\mathrm{Si}}x_\mathrm{p}^2 \tag{4.7}$$

Before the diffusion sets in, the n- and p-type region are electrically neutral. By respecting charge conservation this leads to another boundary condition, which is

$$N_\mathrm{D}x_\mathrm{n} = N_\mathrm{A}x_\mathrm{p}. \tag{4.8}$$

Considering equations 4.7 and 4.8, the width w of the space-charge region is calculated with

$$w = x_\mathrm{p} + x_\mathrm{n} = \sqrt{\frac{2\epsilon_0\epsilon_\mathrm{Si}}{q}V_0\frac{N_\mathrm{D} + N_\mathrm{A}}{N_\mathrm{D}N_\mathrm{A}}} = \sqrt{\frac{2\epsilon_0\epsilon_\mathrm{Si}}{q}V_0\frac{1}{|N_\mathrm{eff}|}}. \tag{4.9}$$

Equation 4.9 also defines the effective doping concentration N_eff. For the silicon detectors investigated in this thesis, the concentrations of acceptors and donors differ by several orders of magnitude. Thus, the dopant with lower concentration mainly drives the width of the space-charge region. Furthermore, w takes up only a small fraction of the sensor volume. An external voltage V_ext applied to the pn-junction adds to the builtin voltage and hence changes w:

$$w = \sqrt{\frac{2\epsilon_0\epsilon_\mathrm{Si}}{q}(V_0 + V_\mathrm{ext})\frac{1}{|N_\mathrm{eff}|}}. \tag{4.10}$$

Depending on the polarity of V_ext the pn-junction behaves differently. In forward direction (negative V_ext) the external field counteracts the builtin voltage and decreases the space-charge region until the pn-junction becomes conductive. The more interesting operation mode for silicon detectors is reverse biasing. By applying a positive V_{ext}, the width of the space-charge region grows until it expands over the whole sensor. The external voltage V_{dep} for which a sensor of thickness d is fully depleted is

$$V_{\text{dep}} = \frac{q}{2\epsilon_0\epsilon_{\text{Si}}}|N_{\text{eff}}|d^2 \quad \text{with } V_{\text{dep}} \gg V_0. \tag{4.11}$$

The capacitance-bias voltage characteristic C(V) of a silicon detector identifies the depletion voltage of a sensor. The space-charge region electrically isolates two conductive regions from each other. This structure is similar to a parallel-plate capacitor filled with silicon as a dielectric. Its capacitance C is

$$C = \epsilon_0\epsilon_{\text{Si}}\frac{A}{w}. \tag{4.12}$$

A is the area of the pn-junction and w the separation between the conductive regions which is the width of the space-charge region. Taking into account equation 4.9, the capacitance normalized to the surface area is

$$\frac{C}{A} = \begin{cases} \sqrt{\frac{\epsilon_0\epsilon_{\text{Si}}|N_{\text{eff}}|}{2(V_0+V_{\text{ext}})}} & \text{for } V_{\text{ext}} \leq V_{\text{dep}} \\ \epsilon_0\epsilon_{\text{Si}}\frac{1}{d} = \text{const.} & \text{for } V_{\text{ext}} > V_{\text{dep}}. \end{cases} \tag{4.13}$$

Thus, the full depletion voltage of a sensor is the voltage for which the C(V) characteristics becomes constant. For $V_{\text{ext}} < V_{\text{dep}}$ the C(V) characteristic allows the measurement of the effective doping profile $|N_{\text{eff}}|$ by calculating [Spi05]

$$|N_{\text{eff}}| = \frac{2}{A^2\epsilon_0\epsilon_{\text{Si}}q\frac{\mathrm{d}(1/C^2)}{\mathrm{d}V_{\text{ext}}}}. \tag{4.14}$$

4.2 Interaction of Particles with Matter

The depleted space-charge region in silicon detectors allows the detection of small charge depositions. Thus, silicon detectors become suitable for the application in particle detection. Depending on the incident particle type, different physics processes contribute to the energy deposition in matter and the generation of charge carriers. This section describes the interaction of heavy charged particles, electrons and photons with matter.

4.2.1 Heavy Charged Particles

The main process contributing to the energy loss of heavy charged particles in matter is inelastic Coulomb scattering with shell electrons of the target material. As a result the shell electrons of the target material become ionized. In semiconductors the ionization process creates electron-hole pairs. The Bethe equation (equation 4.15) describes the average energy loss per unit length, also known as stopping power, of the incident particle [Par18].

$$-\left\langle \frac{\mathrm{d}E}{\mathrm{d}x} \right\rangle = 4\pi\, N_{\text{A}}\, r_e^2\, m_e\, c^2\, z^2\, \frac{Z}{A}\frac{1}{\beta^2}\left[\frac{1}{2}\ln\left(\frac{2m_e c^2\beta^2\gamma^2 T_{\max}}{I^2}\right) - \beta^2 - \frac{\delta(\beta\gamma)}{2}\right] \tag{4.15}$$

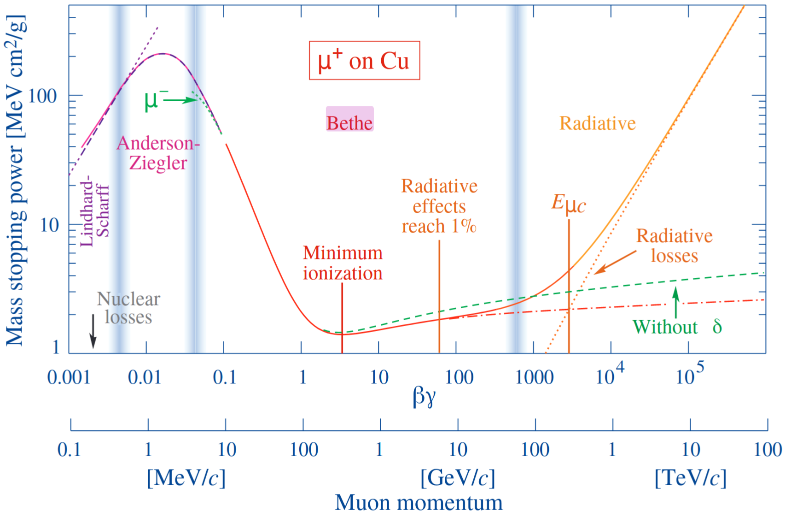

Figure 4.5: Stopping power of anti-muons in copper [Par18].

The stopping power depends on different constants, and properties of the incident particle and target material. In particular, it depends on:

N_{A}	Avogadro's number
r_e	classical electron radius
m_e	electron mass
c	speed of light
z	charge of the incident particle
Z	atomic charge of the target material
A	atomic mass of the target material
β	ratio of the velocity of the incident particle to the speed of light (v/c)
γ	Lorentz factor
$T_{\max}$	maximum kinetic energy transfer to an electron in a single collision
I	mean excitation energy.

The Bethe equation is only valid for $0.1 \lesssim \beta\gamma \lesssim 1000$ with an accuracy of a few percent. For particles at lower energy nuclear loses become dominant, and at higher energy radiative losses. Figure 4.5 shows the stopping power of anti-muons (μ^+) in copper for a wide range of $\beta\gamma$. For $\beta\gamma \approx 3 - 4$ the stopping power has a minimum. Particles with this energy are called minimal ionizing particles (MIPs). Particle detectors have to be sensitive to the detection of MIPs, to be sensitive on all energy scales.

4.2.2 Electrons and Positrons

The Bethe equation does not describe the stopping power of electrons and positrons, since incident and target particles are the same. For energies $E \lesssim 10\,\mathrm{MeV}$ elastic scattering processes (ionization, Bhabha and Møller scattering) dominate the energy loss. For higher energy bremsstrahlung in the electric field of the target nuclei prevails. However, in silicon ionization processes are dominant for the signal generation. The energy deposition in thin silicon layers is similar to the energy deposition by MIPs. [Par18]

In the scope of this thesis, a radioactive ^{90}Sr source is used to characterize silicon sensors. The emitted electrons deposit a similar amount of energy in a silicon sensor as a MIP (see figure A.10). Thus, the measurements with ^{90}Sr are a simple alternative to mimic the charge deposition of MIPs in the laboratory.

4.2.3 Photons

For photons there are three processes mainly contributing to the cross section in matter: the photoelectric effect, Compton scattering and electron-positron pair production. The total cross section depends on the photon energy and the target material. The photoelectric effect dominates the total cross section for photon energies $E < 1\,\mathrm{MeV}$. The absorption edges of the different atomic levels show up as discontinuities in the cross section. For a narrow energy range at $E \approx 1\,\mathrm{MeV}$, the partial cross section of the Compton effect exceeds the photoelectric effect. And at even higher energies $E > 1\,\mathrm{MeV}$ pair production in the nuclear electric field dominates the absorption. This process has a production threshold of $E = 1.022\,\mathrm{MeV}$ to create the rest masses of the electron and positron. [Par18]

4.3 Silicon Detectors

After introducing the pn-junction and understanding the interaction of particles with matter, all background information to understand the functionality of silicon detectors are available. This section explains the signal generation in thin silicon detectors. Furthermore, it presents causes for noise of silicon detectors. The section finishes with the basics of position sensitive silicon sensors.

4.3.1 Signal Generation

As mentioned before the most fundamental component of all silicon detectors is the pn-junction. By operating the pn-junction in reverse biasing mode the space-charge region expands on the whole volume of the silicon detector. Thus, the whole sensor volume becomes sensitive on small charge depositions. Charged particles mainly interact with the sensor material via ionization and generate free charge carriers. The mean energy to create an electron-hole pair in silicon is 3.6 eV. For charged particles passing a sensor the total signal deposition scales with the sensitive volume of the sensors.

For particle tracking thin silicon detectors are favourable to reduce scattering of the particles in the material. Highly energetic particles penetrate the thin layers almost unaffected and deposit only a small fraction of their energy in the material. However, the number of scatterings as well as the energy transmitted per scattering is subject to statistical fluctuations. The amount of energy and hence also of the charge deposited by a particle in the detector follows a Landau distribution. The Landau distribution has an asymmetric tail to high values. A physics process which causes the tail is the creation of secondary particles, like δ electrons, which again deposit energy in the sensor volume. One parameter that describes the Landau distribution is its most probable value (MPV). In terms of silicon detectors it expresses the most probable energy deposition in the detector. [Har17]

Figure 4.6 presents the energy loss of 500 MeV pions in silicon of several thicknesses. The Landau distribution and its MPV shifts to higher energy losses per unit length for thicker detectors. The reason for this behavior is that the probability to deposit a larger fraction of the kinetic energy increases with the sensor thickness.

4.3.2 The Shockley-Ramo Theorem and Weighting Field

Whenever a charged particle passes a silicon detector it generates electron-hole pairs along its track. Since the detector operates in reverse biasing mode an electric field fills the space-charge region. In the field the charge carriers immediately begin to drift along the field lines to the corresponding electrodes. By doing so, the electrons and holes separate before they can

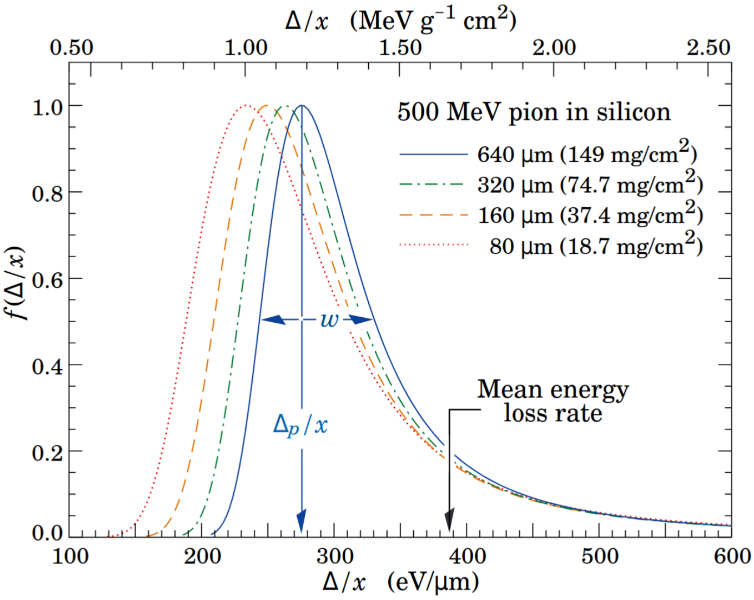

Figure 4.6: Energy deposition Δx of 500 MeV pions in silicon of various thicknesses normalized to unity on the most probable value. The deposited energy spectrum follows a Landau distribution, which has a tail to high values. The most probable energy deposition per unit length increases with the sensor thickness. [Par18]

recombine. The p-doped region (cathode) collects holes and the n-doped implants (anode) electrons.

The drift of the charge carriers generates a measurable current pulse in the electrodes. Integrating the current pulse over time yields the total charge which was ionized in the detector. The Shockley-Ramo Theorem [Sho38; Ram39] describes the signal generation in silicon detectors. It states that the induced current I in the electrode i is proportional to the charge q, the velocity of the charge carrier $\vec{v}$ and the weighting field $\vec{E}_{\mathrm{W}}$ [Spi05]:

$$I_{\mathrm{i}} = -q\,\vec{v} \cdot \vec{E}_{\mathrm{W}}. \tag{4.16}$$

Since electrons and holes have the opposite charge but also drift in opposite direction, the current induced by each has the same polarity.

The weighting field only depends on the geometry of the electrodes. To calculate the weighting field for a specific electrode the potential of the electrode is set to 1 and the potential of all others to 0 [HJ08]. However, the weighting field does *not* equal the electric field. The weighting field describes the coupling of moving charge to the electrode, whereas the electric field determines the velocity and direction ($\vec{v}$) of the charge. Only for the very simple case of a two electrode system (e.g. a diode) the electric and weighting field vectors are parallel. For more complex configurations, like for strip or pixel sensors, they strongly differ (see also [Har17]).

4.3.3 Noise of Silicon Detectors

Hartmann [Har17] presents different contributions to the noise of silicon detectors. The main factors driving the noise are the load capacitance C, the leakage current I_l and the parallel and series resistances R_P and R_L. The Equivalent Noise Charge ENC quantifies the noise by giving the number of contributing electrons. The ENC is the quadratic sum of its contributions:

$$ENC = \sqrt{ENC_C^2 + ENC_{I_l}^2 + ENC_{R_P}^2 + ENC_{R_L}^2}. \tag{4.17}$$

The most significant contribution is the load capacitance C. For a silicon strip sensor (see section 4.3.4) the strip capacitance, which is proportional to the strip length, mainly drives the load capacitance. It contributes linearly to ENC_C. The constants a and b depend on pre-amplifier specific parameters of the readout chip.

$$ENC_C = a + b \cdot C \tag{4.18}$$

Furthermore, in the space-charge region of silicon detectors thermal excitations continuously generate electron-hole pairs. These spontaneously generated charge carriers cause leakage current and compete with the signals generated by particles in the detector. The detector leakage current I_l and the peaking time of the readout electronics t_p determine the shot noise ENC_{I_l} contribution

$$ENC_{I_l} = \frac{e}{2}\sqrt{\frac{I_l \cdot t_p}{q_e}}. \tag{4.19}$$

The parallel thermal noise term depends on the bias resistance R_P and the temperature T

$$ENC_{R_P} = \frac{e}{q_e}\sqrt{\frac{k_\mathrm{B}T \cdot t_p}{2R_P}}. \tag{4.20}$$

The last term, the serial thermal noise, is also driven by temperature T and depends on the resistance in series R_S of the aluminum strip

$$ENC_{R_S} = C \cdot \frac{e}{q_e}\sqrt{\frac{k_\mathrm{B}T \cdot R_S}{6t_p}}. \tag{4.21}$$

Other constants included in the noise terms are the Boltzmann constant k_B, the Euler number e and the electron charge q_e.

4.3.4 Silicon Strip Sensors

The simplest silicon detector device is a diode, which consists of one pn-junction. This simple device can already detect charged particles. However, the position resolution scales with the size of the diode. By segmenting the pn-junction in many smaller junctions the position resolution improves. There are two common ways to subdivide the pn-junction. On the one hand, there is the segmentation in one dimension, which results in a strip sensor. On the other hand, segmenting the pn-junction in two dimensions, creates a pixel sensor. Since this thesis investigates strip sensors, this section focuses only on this kind of silicon sensors.

Figure 4.7 shows an illustration of the working principle of a silicon strip sensor. The base material of all silicon sensors is a slightly n- or p-doped silicon substrate. Since the silicon sensors of the future Outer Tracker of the CMS experiment will be made of a p-type bulk (n-in-p sensors) [CMS18], the following explanation focuses on this class of sensors. Highly doped n^{++} strip implants segment the sensor on its frontside. Each implant creates a pn-junction with the p-doped bulk material. A thin $\mathrm{SiO_2}$ layer on the surface protects the sensor from environmental impacts. In addition, it acts as an electric isolation layer between the implants and metal strips on top of them and guarantees a purely capacitive coupling. There are two ways to readout the sensor signals: a DC connection of the readout electronics and the implant; and AC coupling via the metal strips. The AC readout protects the readout electronics from the sensor leakage current.

An external voltage applied to the implant and backside is mandatory to deplete the sensor. The aluminum-coated backside is on negative potential and acts as cathode. A highly doped p^{++} backside guarantees a good ohmic contact to the metalized backplane. To apply positive

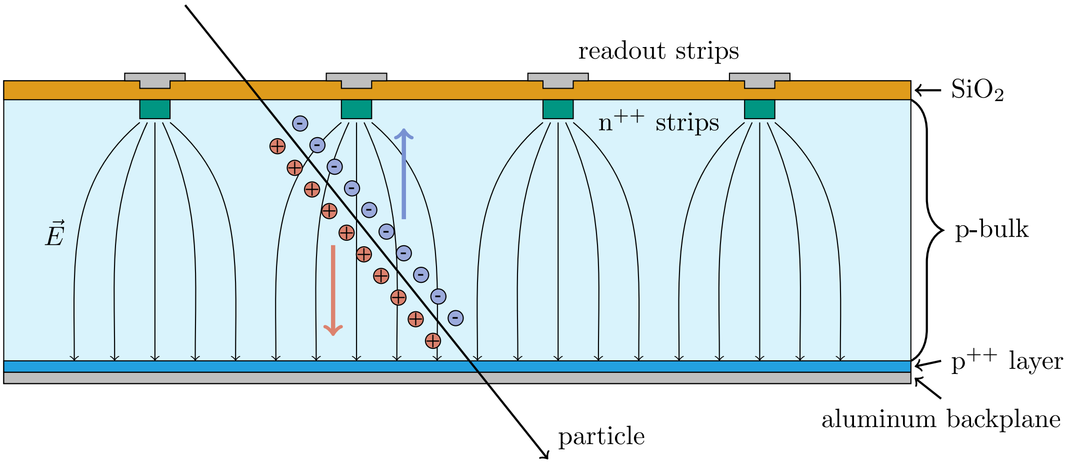

Figure 4.7: Illustration of the working principle of an n-in-p type silicon strip sensor. An external voltage between the n^{++} doped implants at the top and the aluminum-coated backside depletes the p doped sensor bulk. For a better ohmic connection the sensor back side is p^{++} doped. A particle passing the sensor generates electron-hole pairs. The electric field $\vec{E}$ separates the charges and guides them to the corresponding electrodes. Attached readout electronics detect the current signals, which are induced by the drifting charge carriers.

potential to the n^{++} implants additional structures in the periphery are necessary. Bias resistors connect the n^{++} implants with a surrounding bias ring to apply the positive potential.

By the potential difference an electric field forms in the bulk volume. The electric field separates charge carriers, e.g. generated by a particle traversing the sensor, and guides them to the corresponding electrodes.

4.4 Radiation Damage in Silicon

Operating the CMS Tracker at the LHC exposes the silicon sensors to a harsh flux of particles. Besides ionizing the shell electrons, passing particles can interact with atoms of the crystal lattice. These kind of interaction can create defects, which influence the sensor's electrical properties and performance. This section briefly introduces different classes of microscopic defects in the silicon bulk and surface oxide. Then it explains the macroscopic impact on the sensor and the effect of annealing.

4.4.1 Bulk Damage

Non-ionizing interactions of particles with the crystal lattice can produce different types of lattice damage. Figure 4.8 illustrates a selection of lattice defects. An energy transfer of more than 25 eV can knock out an atom from the crystal lattice. This so called primary knock-on atom (PKA) leaves a *vacancy* behind [Lin+80]. If it is trapped in a nearby interstitial position it creates a double defect named *Frenkel pair*. Apart from that, the PKA can travel further through the lattice. Along its path through the sensor it ionizes electron-hole pairs and interacts with more nuclei. As a result lattice defects accumulate in a very local region and create a *defect cluster*. Other defects are *impurities*, which are foreign atoms replacing atoms in the crystal lattice (*substitutional*) or get caught in an interstitial position. [Lut07]

The type of the incident particles has a major impact on the kind and density of the created defects. On the one hand, charged hadrons (e.g. protons) mainly interact via Coulomb

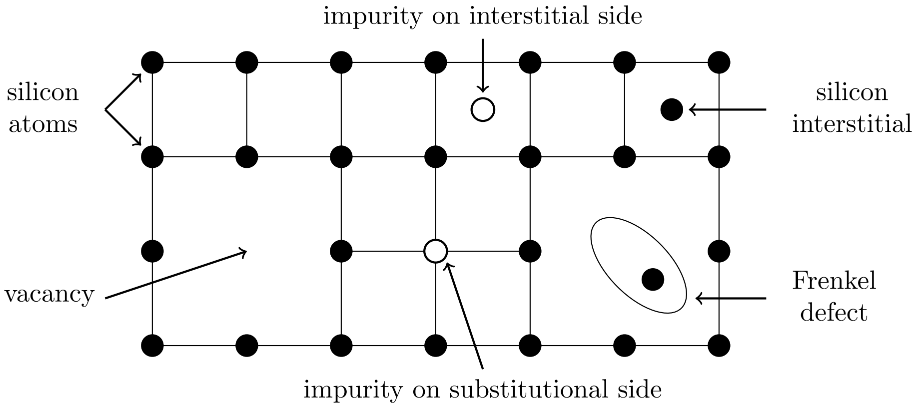

Figure 4.8: Illustration of bulk defects in the crystal lattice. Knocking out atoms from the lattice create *vacancies*. The atoms can be trapped in a nearby interstitial and create a *Frenkel pair*. *Impurities* can substitute single lattice atoms or be trapped on an interstitial side. Illustration following [Lut07].

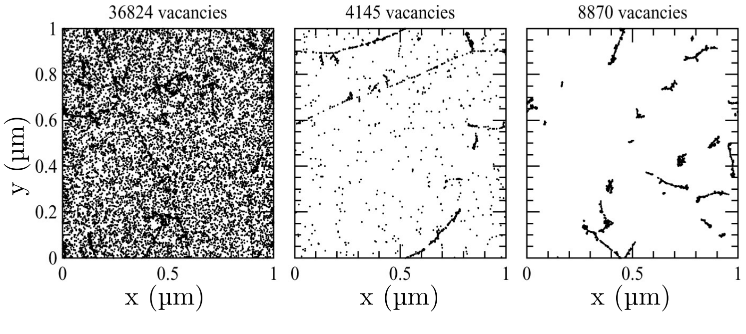

Figure 4.9: The initial distribution of simulated vacancies generated by 10 MeV protons (left), 24 GeV protons (middle) and 1 MeV neutrons (right) in 1 µm^3 silicon after the irradiation with a fluence of 1×10^{14} cm^{-2}. Depending on the particle type and energy, particles generate defect clusters or a more uniform spread of vacancies. [Huh02]

scattering and predominantly generate point like defects. On the other hand, neutral hadrons (e.g. neutrons) only interact via nucleus-nucleus scattering, which results in cluster defects. Figure 4.9 displays a simulation of vacancy generation in silicon for protons (10 MeV, 24 GeV) and neutrons (1 MeV). The number, density and distribution of vacancies not only depend on the particle type but also on its energy.

To make the degree of damage comparable for different particle types and energies, the particle fluence is scaled to the equivalent fluence Φ_{eq} by applying the non-ionizing energy loss (NIEL) hypothesis. The equivalent fluence Φ_{eq} describes the amount of damage created by neutrons of 1 MeV and has the unit $[\Phi_{\mathrm{eq}}] = \mathrm{n_{eq}/cm^2}$.

The NIEL is the energy a particle loses for displacing atoms from their original position in the lattice. The hypothesis states that the bulk damage scales linearly with the NIEL [Mol99]. In this thesis all particle fluences are normalized to the equivalent fluence.

4.4.2 Surface Damage

Besides creating defects in the bulk, ionizing particles damage the surface silicon dioxide, too. For silicon dioxide the damage of the crystal lattice can be neglected, but ionization becomes the main driver that affects the performance of the sensor.

On the one hand, the mobility of electrons and holes in silicon dioxide differ by several orders of magnitude ($\mu_e \approx 20\,\mathrm{cm^2\,V^{-1}\,s^{-1}}$, $\mu_h \approx 2\times10^{-5}\,\mathrm{cm^2\,V^{-1}\,s^{-1}}$) [Wun92]. Even though most of the ionized charge carriers recombine immediately some electrons begin to drift to the readout strips. Contrarily the immobile holes remain in the silicon dioxide and slowly move towards the interface between the silicon dioxide and the silicon bulk. Dangling (unbound) atomic bonds at the interface create new levels in the middle of the band-gap which trap the holes. The oxide layer is positively charged up by the trapped holes and attracts electrons from the bulk (e.g. from leakage current). Thus, the electrons accumulate at the interface and short-circuit the strip implants. Additional p^{++} implants between the strips (e.g. p-stops) prevent the shorts by their repulsive force on the accumulated electrons. [Har17]

4.4.3 Macroscopic effects

In the band model, lattice defects result in new energy levels within the band gap. The different types of levels are illustrated in figure 4.10. Depending on their position within the band gap, the defects modify different sensor parameters.

Leakage Current

Energy levels in the middle of the band gap, called deep levels, increase the overall leakage current of the sensor (figure 4.10(a)). Since the energy gap to the valence and conduction band is almost equal, deep levels serve as generation and recombination centers for electrons and holes. The probability for electron excitation from the valence band into the conduction band increases since the electrons can use the new levels as an interim state. With increasing fluence the number of deep levels and hence the leakage current rises. Studies by Moll [Mol99] showed a linear behavior of the leakage current increase ΔI per volume V with the exposed fluence Φ_{eq}. The correlation factor α is named the current related *damage rate*.

$$\frac{\Delta I}{V} = \alpha \Phi_{\mathrm{eq}} \tag{4.22}$$

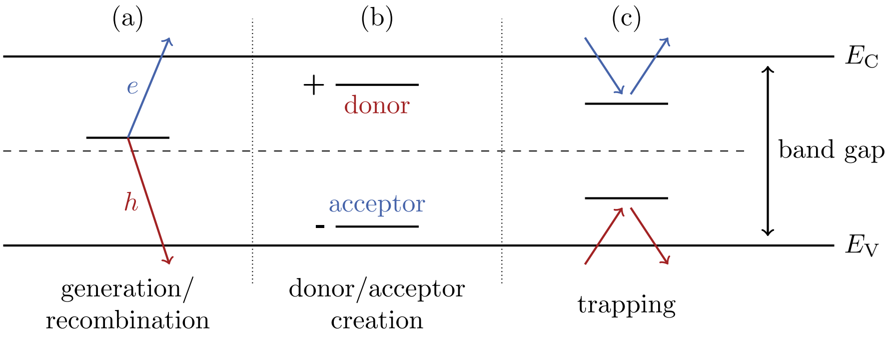

Figure 4.10: Energy levels created by lattice defects in the band gap. Levels close to the center of the band gap (a) serve as generation and recombination centers and increase the sensor leakage current. Levels close to the valence/conduction band (b) exhibit an acceptor/donor like behavior and change the effective doping and full depletion voltage, respectively. Intermediate levels (c) trap charge carriers. Since the trapping time is long compared to the sampling time of the readout electronics, these charge carriers do not contribute to the signal. Illustration following [Mol99].

The bulk leakage current of irradiated silicon sensors also strongly scales with the sensor temperature. Equation 4.23 describes the relation between leakage current I and temperature T [Chi13].

$$I(T) \propto T^2 \exp(-1.21\,\mathrm{eV}/2k_\mathrm{B}T) \tag{4.23}$$

k_B is the Boltzmann constant and the energy $E_\mathrm{eff} = 1.21\,\mathrm{eV}$ is called the effective bandgap.

Full Depletion Voltage

The energy levels close to the valence or conduction band, shallow levels, influence the full depletion voltage V_dep of the sensor (figure 4.10b). These levels show a similar behavior as those created by the doping atoms. Thus, the defects change the effective doping concentration N_eff. The exact ratio between acceptor and donor creation per fluence depends on many parameters like the incident particle type and energy and the sensor material (doping, impurities). In many cases the creation of acceptors is more effective than donor creation [Jun11]. In n-in-p type silicon sensors, the donor concentration of the p-doped bulk increases with fluence. As a result V_dep increases with fluence.

Charge Collection Efficiency

Additional energy levels at intermediate positions between the band gap center and the valence/ conduction band serve as traps for electrons or holes. Trapped charge carriers are immobile and thus do not longer contribute to the signal generation. Since the trapping time usually is much longer than the integration time of the readout electronics the recorded signal decreases. Besides that, a trapped charge can recombine with its counterpart during trapping. Both effects lower the overall detectable signal.

The charge collection efficiency is the collected charge (e.g. after irradiation) normalized to the charge signal of the same type of sensor before irradiation. After irradiation the charge collection efficiency of a sensor usually decreases.

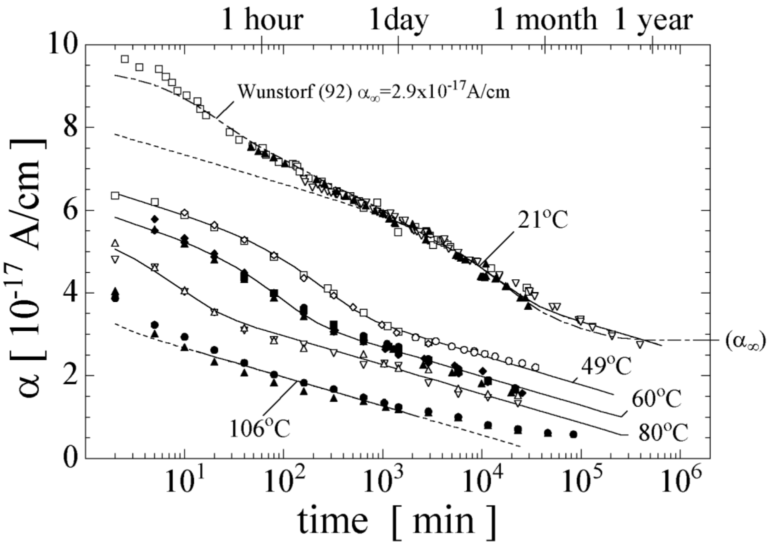

Figure 4.11: Annealing behavior of the damage rate α over time for different annealing temperatures [Mol99]. The current related damage rate α steadily decreases and saturates only for $T = 106\,°\mathrm{C}$ after several hundred hours of annealing.

Annealing

Sensor defects can evolve over time. For example displaced atoms may move through the crystal lattice and interact with other defects or impurities. By doing so the defects transform into more stable states. This behavior is called annealing. The mobility of the defects depends on the temperature. It almost vanishes for $T < 0\,°\mathrm{C}$ and accelerates by heating the sensor. In the Hamburg model, Moll parameterized the influence of annealing on the leakage current I_{leak} and on the effective doping concentration [Mol99].

A beneficial effect of annealing is the reduction of the damage rate α, as shown in figure 4.11. Thus, the leakage current decreases with annealing time. The Hamburg model states that a certain damage rate α corresponds to a particular equivalent annealing time at room temperature (21 °C). Thus, the translation into the equivalent annealing time at room temperature allows the comparison of annealing at different temperatures and of varying duration. [Mol99]

Furthermore, the annealing affects the effective doping concentration N_{eff}. Three different contributions add to the parameterization of N_{eff} by Moll [Mol99]. Besides a stable increase of N_{eff} there is a short time scale beneficial reduction and a long time non-stable increase. Figure 4.12 displays the interplay of the three contributions for annealing at 60 °C. A consequence of the change of N_{eff} is a fast reduction of the depletion voltage, which is followed by a steady increase after some weeks of annealing time at room temperature.

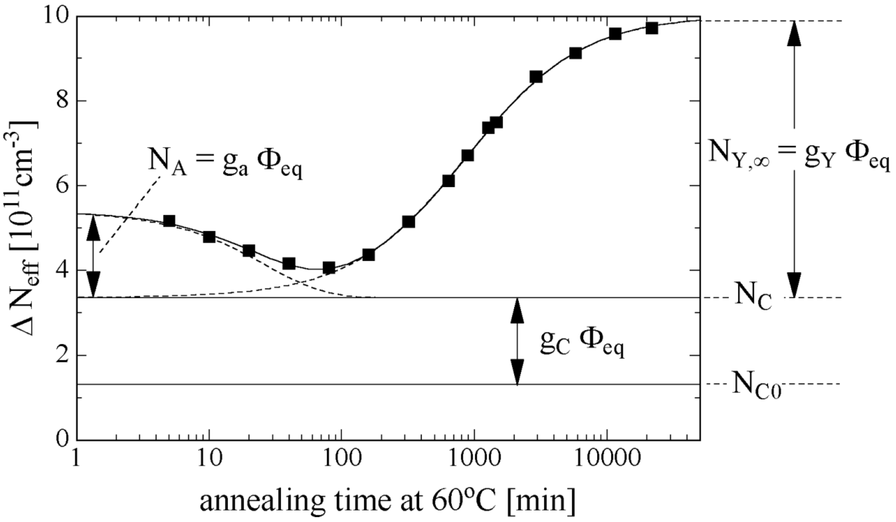

Figure 4.12: Three terms contribute to the parameterization of the annealing of the effective doping change ΔN_{eff}: a constant term, a beneficial short time scale reduction and a long time scale increase. [Mol99]

Part II

Experimental Setups and Methods

5

The CMS Binary Chip and the 2S Module Readout Chain

The Phase-2 Upgrade of the CMS Outer Tracker implements a novel concept to identify particles with large transverse momentum already on module level. To fulfill this task a new ASIC, the CMS Binary Chip (CBC), was developed by Imperial College London for particle detection and stub identification. This chapter introduces the CBC in detail, also presenting standard measurements and calibrations to determine performance parameters of the chip. However, the CBC is only the first stage in a chain of readout ASICs to transmit the information about charge deposits in the sensor to the CMS tracker data acquisition system. Thus, the second part of the chapter introduces all following components contributing to the 2S module readout chain, their specific tasks and details about their working principle. The chapter introduces the basic information to understand the studies carried out in the scope of this thesis.

5.1 The CMS Binary Chip (CBC)

The CMS Binary Chip (CBC) is the readout chip of the 2S modules. In total 16 CBCs on two front-end hybrids read out the 4064 strips of a full 2S module. One CBC samples the signals from 254 strips, 127 from the upper and 127 from the lower sensor. Since its architecture is based on binary readout, it only detects whether a strip was hit and does not record information about the magnitude of the detected charge signal. This section sums up the working principle of the CBC as presented in [Pry19].

The chip operates at two different clock domains. On the one hand, the data transfer and fast control runs at 320 MHz. On the other hand, the hit detection and the stub logic operates at 40 MHz, which is the bunch crossing rate of the LHC. The CBC recovers the 40 MHz clock from the fast control command signals. A programmable delay locked loop (DLL) adjusts the

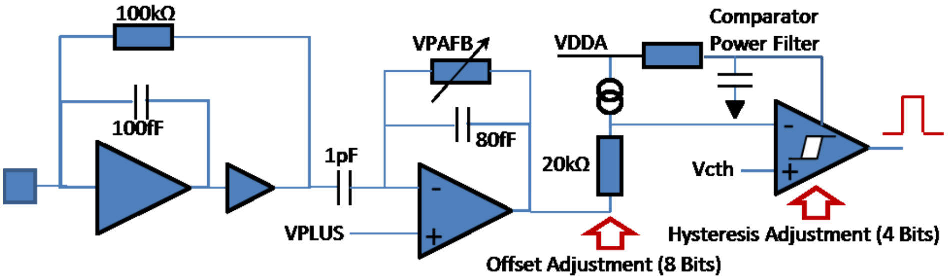

Figure 5.1: Analog front-end of the CBC. Two amplifier stages intensify and shape the charge pulse from the strip before it enters the comparator for digitization. VDDA is the supply voltage of the analogue supply rail, VPLUS is the post-amplifier reference voltage and VPAFB is the control voltage for the feedback loop of the post-amplifier. [Pry19]

phase of the 40 MHz clock in nanosecond steps. During the operation in the CMS detector the DLL aligns the 40 MHz clock phase relative to the bunch crossings of the LHC. By doing so, the DLL compensates time of flight effects of the particles for different module positions in the tracker.

The CBC emits data via six scalable low-voltage signalling (SLVS) output lines operating at 320 MHz. Five of the six SLVS links transmit the stub information for every bunch crossing of the LHC. The available bandwidth is sufficient to transmit up to three stubs per bunch crossing interval (25 ns). Each stub contains information about its position on the seed layer and the bend value encoded using a programmable lookup table. If the CBC detects more than three stubs in one bunch crossing, it only transmits the three stubs with the lowest position address.

The remaining SLVS output line transfers the triggered level-1 data. The data comprise the full hit vector of all 254 readout channels. Since there is no zero suppression implemented, it requires 38 bunch crossing intervals to send one full level-1 event. This corresponds to a trigger frequency of about 1.05 MHz.

Two interfaces control the CBC. One SLVS line transmits fast control commands (e.g. trigger signals, test pulse triggers or resets). In addition a 1 MHz I^2C slow control interface is used to read and write the chip registers.

5.1.1 The Analog Front-end and Digitization

Figure 5.1 shows a sketch of the analog front-end of one channel of the CBC. For the chip versions CBC3 and higher the design foresees to read out AC coupled n-in-p type silicon strip sensors. For each channel the strip pulses enter the analog front-end via a wire bond. Then a two staged amplifier shapes and amplifies the charge signal from the sensor. The first stage is a fixed gain charge sensitive *pre-amplifier*, which integrates the charge onto a capacitor. The second stage is an adjustable gain *post-amplifier*.

The design of the analog front-end of the CBC targets a noise below $1000\,e^-$ for 5 cm long strips with about 10 pF external capacitance and a strip leakage current below 1 µA [CMS18].

After the signal amplification the *offset adjustment* adds an offset voltage to the pulse. The channel wise programmable offset value with eight bits precision is used to equalize the response behavior of the individual channels (see section 5.1.4).

Then the adjusted pulse enters a *comparator*, which detects signals exceeding a programmable threshold. The comparator threshold voltage Vcomp is a global parameter and the same for all channels of one CBC. A digital-to-analog converter (DAC) with 10 bits precision adjusts Vcomp between the analog supply rail VDDA and ground GND. It is calculated using the comparator DAC by

$$\mathrm{Vcomp} = \frac{\mathrm{VDDA} - \mathrm{GND}}{1024} \cdot \mathrm{DAC}. \tag{5.1}$$

In the comparator the digitization of the signals takes place. The programmable *hysteresis adjustment* of the comparator suppresses fluctuations by noise and hence stabilizes the binary output signal. Since n-in-p type silicon sensors collect electrons, the analog pulses have negative polarity. Thus, the comparator generates a digital 1 output as long as the pulse signal is *below* Vcomp. Afterwards, the CBC processes the digitized information to identify stubs and generates the output data streams. In the scope of this thesis the unit Vcth refers to the comparator DAC value. In the CBC a high comparator DAC value corresponds to a low threshold and vice versa.

5.1.2 Digital Processing and the Stub Finding Logic

The first processing step after the digitization in the comparator is *channel masking*. It suppresses high signals from the comparator output in masked channels, e.g. to prevent fake hits from noisy front-end channels. Then the *hit detect logic* processes the comparator output. In total four different sampling modes are available. By default the CBC runs in the *sampled mode*, for which the comparator output is sampled at a fixed phase with respect to the 40 MHz clock. All measurements presented in the scope of this thesis were performed using the sampled mode. The other operation modes *fixed pulse width*, *logical OR output* and *HIP suppressed output* are described in [Pry19]. However, for all sampling modes the minimum width of the output pulse is one bunch crossing interval. At this point the data path splits.

For the level-1 data, a 512 event deep static random-access memory (SRAM) *pipeline* stores the hit information of all channels. At 40 MHz 512 events correspond to a delay of 12.8 µs which is the maximum allowed trigger delay for the data acquisition system. As soon as the CBC receives a trigger signal, it passes the associated event from the pipeline to a 32 event deep SRAM *readout buffer* where it waits for serialization and transmission.

In parallel the stub finding logic processes the hit information in a second data path to identify particles with large transverse momentum p_T on module level. First all hits pass a *logical OR* gate (OR254), which sets a flag of the stub data output stream to 1 if at least one hit was recorded. Depending on its position within the tracker, the 2S modules face the interaction point with its upper or lower sensor. Thus, the seed layer must be exchangeable for the correct working of the stub finding logic. The next processing stage, the *channel swapping layer*, can swap odd and even numbered channels so that the top sensor becomes the seed layer. At this point the CBC also shares the hit information of the edge channels with its neighbors to detect stubs shared by neighboring CBCs. This feature prevents inefficient areas between the chips. The next stage gathers adjacent hits into *clusters* and applies a cut on the *cluster width*, which is the number of hits in a cluster. It rejects clusters larger than a programmable size, since they hint at low-p_T particles crossing the sensors with large inclination. The maximum programmable accepted cluster width are four strips. All clusters containing five or more strips are rejected before the stub finding logic.

In the last step the CBC matches clusters of the seed and correlation layer. For each cluster in the seed layer the CBC searches for a cluster center within a programmable window in the correlation layer. The width of the window is programmed in half strip steps symmetrically around the window center. The programmable values range between zero (only the center strip) up to ± 7.

Depending on its position within the tracker high-p_T particles will hit the modules with different inclination. A programmable *offset* (± 3 strips) between the seed cluster center and the center of the correlation window corrects for this geometrical effect.

If the CBC detects a cluster in the correlation window it generates a stub. Each stub comprises 12 bits of information. The cluster position in the seed layer is encoded in 8 bits with half strip resolution. The remaining 4 bits contain information about the stub bend, which is the offset between the center of the cluster in the seed and correlation layer. The stub bend is encoded using a programmable lookup table and provides up to half strip resolution. In the default configuration the stub bend is transmitted in full strip precision.

5.1.3 Noise and Pedestal Measurement

One important parameter to quantify the performance of a readout chip like the CBC is its noise. Noise shows up in every system and depends on many system properties. For efficient operation the signal to noise ratio has to be maximized. Thus, a profound understanding of the parameters affecting the noise is crucial.

Due to its binary nature, the CBC cannot measure the noise amplitudes by recording the magnitude of noise hits. For a binary chip the noise is measured by recording the noise hit occupancy for a scan over different threshold values. This scan yields the s-curve, which is

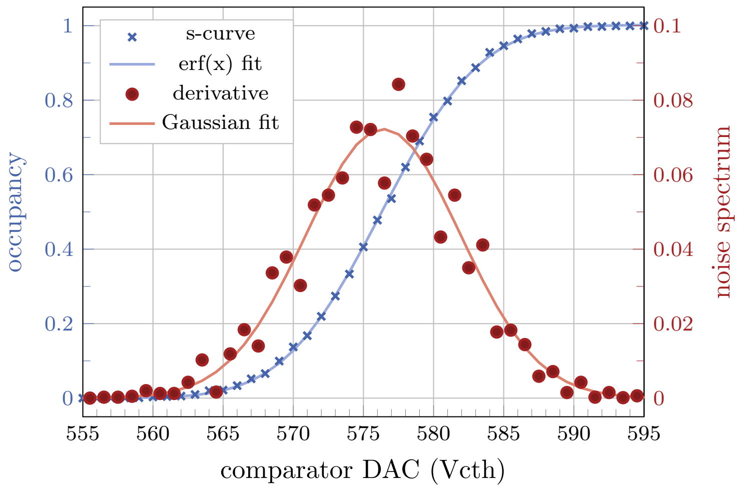

Figure 5.2: S-curve of one CBC channel. The error function describes the shape of the s-curve. Its derivative, a Gaussian distribution, is the noise signal spectrum. The mean of the derivative is the pedestal and the standard deviation the noise of the channel.

the integrated noise spectrum. Since the amplitudes of noise pulses are Gaussian-distributed, its integral, the error function, describes the shape of the s-curve. As mentioned before, low comparator DAC values correspond to a high threshold and vise versa. Thus, the s-curves of the CBC channels go from zero to one with increasing DAC value. From the s-curves two important parameters can be extracted: the width of the Gaussian distribution is the noise and the center is the pedestal. The pedestal is the comparator DAC value for which the channel occupancy becomes 50 %. Thus, the pedestal represents the analog front-end's baseline. The threshold in units of Vcth applied to the sensor signal is the difference between the recorded pedestal of the channel and the global comparator DAC value.

The CMS tracker community develops a common middleware framework to communicate with all future Phase-2 Inner and Outer Tracker modules and chips. The Phase-2 Acquisition and Control Framework (Ph2_ACF) includes a measurement routine to extract the noise and pedestal for each analog front-end. The algorithm differentiates the recorded s-curve, which yields the Gaussian-distributed noise amplitude spectrum. The standard deviation σ of the spectrum is the noise and its mean μ is the pedestal. Figure 5.2 shows an exemplary s-curve of one CBC channel and its derivative. The noise and pedestal of one chip is defined as the mean of the noise and pedestal of all of its channels. Figure 5.3 displays an exemplary pedestal and noise distribution of one CBC.

5.1.4 Channel trimming

For efficient particle detection it is mandatory that each channel shows equal response behavior. That means for a given charge signal the response of the comparator must be the same for all channels. Due to process variations the amplifier output varies from channel to channel. However, the comparator checks the strip signal against a threshold which is unique for all channels of one chip. Thus, an eight-bit programmable offset value on the amplifier output adjusts for the variations per channel. The equalization of the channels' response behavior is called trimming. There are different trimming strategies for chips like the CBC.

The trimming algorithm implemented in the Ph2_ACF equalizes the pedestals of all channels by performing the following steps. The first step is the identification of the optimal pedestal to trim for. The software measures the noise occupancy averaged over all channels while varying

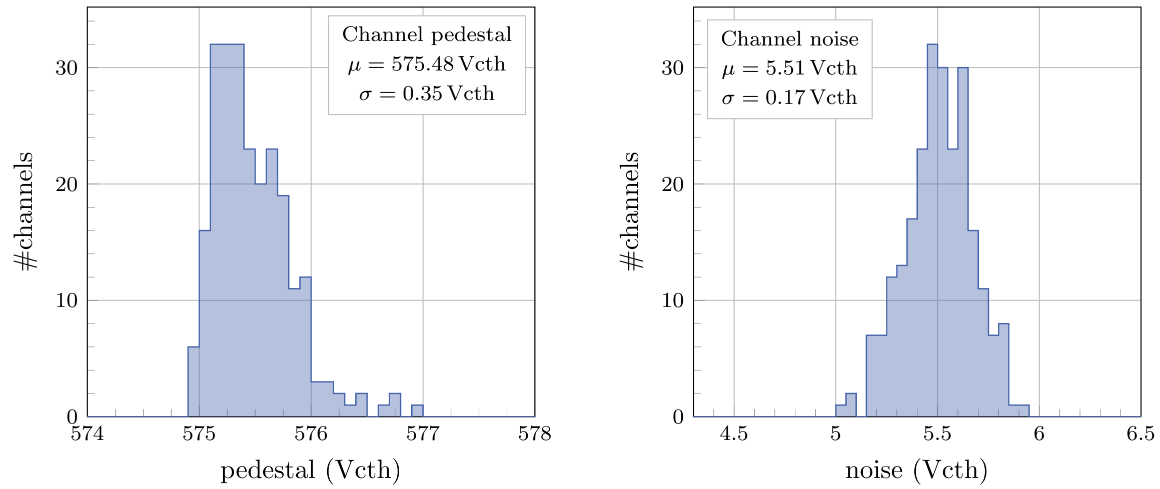

(a) Channel pedestals of one CBC

(b) Channel noises of one CBC

Figure 5.3: Noise and pedestal distribution of one CBC after trimming. Trimming equalizes the channels' response by adjusting their amplifier offsets. A narrow pedestal distribution represents a uniform channel responsiveness. A realistic threshold to operate the CBC is five times the noise above the pedestal.

the comparator DAC bit-wise from the highest to the lowest significant bit. For each step the software flips back the bit if the occupancy is above 56 %. The bit flipping has the effect that the noise occupancy approaches the 56 % level from lower noise occupancies. The resulting threshold after checking all bits is the ideal target pedestal for the trimming of one chip. Since this value varies from chip to chip, the target pedestal for one module is the average of the target pedestals of its chips. During the flipping procedure the offset of all channels is 128, which is the center of the programmable offset range. By doing so, the actual trimming has the largest possible trimming range in both directions.

The second step is the actual trimming of the channels. It makes use of a similar approach as the first step. Now the threshold is fixed to the target pedestal, which was identified in the first step. Then the software flips the offset of each channel bit-wise from the highest to the lowest significant bit. Again, the bit is flipped back if the occupancy of the channel exceeds 56 %. By doing so each channel offset converges so that its occupancy at the target threshold is as close as possible below 56 %. Figure 5.3a shows the pedestal distribution of one CBC after trimming. The algorithm reaches a very uniform pedestal distribution for all channels.

5.1.5 Hit Latency and Stub Latency Scans

The CBC emits two data streams, the triggered level-1 data and the continuous stub data stream. The firmware of the an FC7 readout board packs the two data streams into one common event format. Thus, each event consists of level-1 data and the associated stub information of the triggered event. When recording events with an external trigger the data streams have to be aligned with respect to the trigger signal.

The hit latency for the level-1 data is a programmable register of the CBC. It defines the distance of the current position in the 512 deep SRAM pipeline to the event associated with the trigger, that has to be read out. In this sense, the hit latency value is the time distance in units of 25 ns clock cycles between the arrival of the trigger signal and the recording of the data.

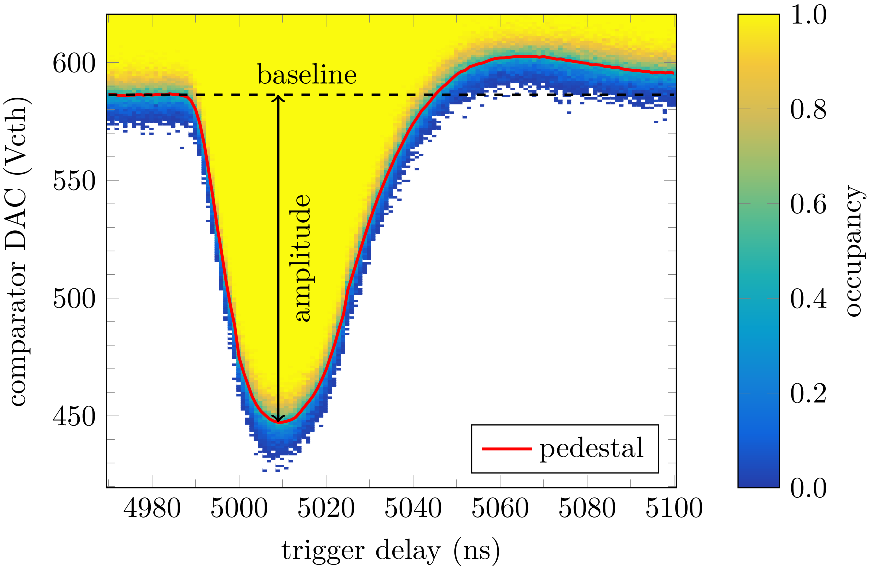

Figure 5.4: Test pulse recorded with one CBC channel by measuring the occupancy for a scan over threshold and time. The red line shows the pedestals associated with the s-curves. The injected signal is about 23 ke^- high. The amplitude of the pulse is the difference between the baseline (pedestal without injection) and the minimum pedestal of the time scan.

The alignment of the stub data stream is not a chip property. Since the CBC streams the stub data continuously, the firmware of the FC7 readout board has to align this data stream. To do so, it buffers the stub information. The stub latency is the delay in 25 ns clock cycles that matches the stub information with the arrival of the level-1 hit information.

The latencies depend on different properties of the setup, like cable lengths and processing time of the firmware. To measure the correct hit and stub latency one has to generate detectable signals in the same way as in the later measurement (e.g. hits and stubs generated by test pulses or by particles from a beam or a radioactive source). Then, the measurement routine scans the latency and records the number of hits/stubs for each step. The correct latency is the one for which the number of hits/stubs is maximal. This measurement has to be repeated and checked each time the setup or signal source changes to be sure that the timing is still correct.

The final 2S modules will operate synchronously with the particle collisions in the CMS detector. That means the 40 MHz chip clock operates at a fixed phase relative to the bunch crossings of the LHC. The individual phase of each module depends on the module's position within the tracker, due to different flight times of the particles from the interaction points. As described before, a chip internal DLL aligns the 40 MHz front-end phase in 1 ns steps with respect to the LHC clock.

5.1.6 Test Pulses and Threshold Calibration

The CBC features the injection of internal test pulses [Pry19]. The injection of well known pulses into the analog front-end is one way to determine the conversion factor of Vcth into an charge equivalent signal. A fast command from the FC7 board triggers the test pulse injection. Thus, for each individual clock cycle one can initiate a test pulse or not. The injection of the pulses takes place in eight groups of 31 or 32 channels, where a programmable register selects the group. A DAC with eight-bit precision adjusts the amplitude of the injected signal by

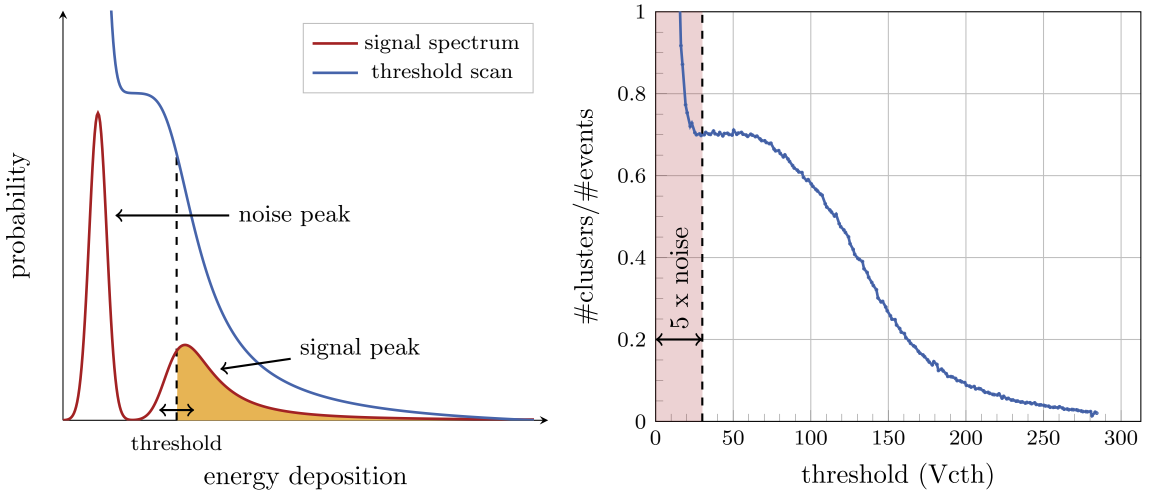

(a) Illustration of binary signal detection

(b) Example threshold scan

Figure 5.5: A binary chip detects all signals exceeding the threshold, resulting in the integrated spectrum (blue) for a threshold scan as illustrated in (a). The derivative yields the signal spectrum (red). An exemplary threshold scan of the cluster occupancy for a 290 µm thick silicon sensor is shown in (b). The signals were generated by electrons from a ^{90}Sr source. The scan is proportional to the integrated seed signal spectrum.

choosing the voltage to charge a 20 fF test capacitor. With 1.1 V DAC reference voltage the injection has a charge resolution of 0.086 fC. Because of process variations the tolerance on the capacitor's capacitance is 20 %.

Even though the CBC is a binary chip there is a way to measure the shape of the test pulse signal. The test pulse injections are at a fixed phase with respect to the 40 MHz clock of the CBC. Thus, one can record the pulse shape by performing a two dimensional scan of the hit occupancy over the threshold and the trigger time delay. The trigger time delay is configurable in steps of ns by combining the trigger latency and DLL settings. Figure 5.4 shows the result of an exemplary test pulse scan. For every trigger time delay an s-curve of the signal is recorded. Triggering the readout before the actual pulse injection (trigger delay < 4990 ns) yield the s-curve of the noise and the pedestal corresponds to the baseline. For later trigger the s-curve samples the pulse at the given time delay. Since every test pulse injection has the same amplitude the s-curve shifts to higher thresholds. The shift of the pedestal with respect to the baseline is the phase related amplitude of the signal. The maximum shift is the full amplitude of the pulse. The corresponding delay defines the optimal sampling time.

One method to determine the conversion factor of Vcth into an charge equivalent signal is to use such test pulses of known charge. The test pulse amplitude in units of Vcth correlates linearly with the injected charge. Thus, the slope of a linear fit of the injected charge over the reconstructed amplitude is the conversion factor.

5.1.7 ^{90}Sr Threshold Scan

One way to perform signal spectrum measurements of a ^{90}Sr source is to record threshold scans. As mentioned before, the CBC detects all signals exceeding its threshold. In other words, the CBC integrates over the signal spectrum above the applied threshold. This effect can be used to define observables to investigate the signal height distribution with a binary chip. The

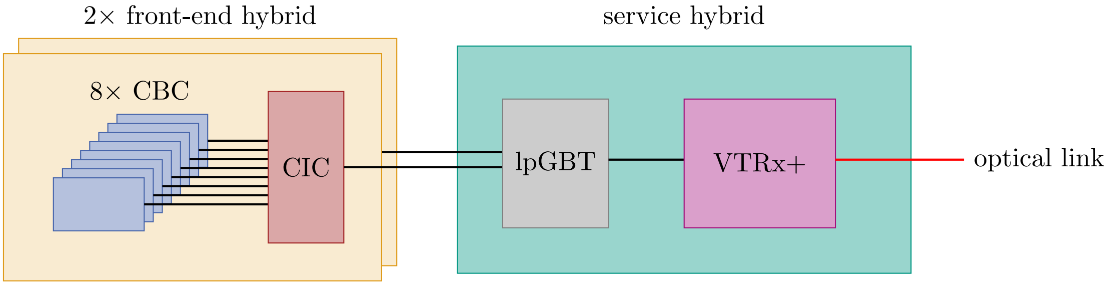

Figure 5.6: Sketch of the 2S module readout chain. One front-end hybrid comprises eight CBCs and one CIC. The CIC concentrates the data streams of the CBCs. Then, the lpGBT serializes the data streams from two front-end hybrids (two CICs) and distributes I^2C slow control commands to all chips. Finally, the VTRx+ sends the serialized data via an optical link to the CMS data acquisition system.

cluster occupancy o_{cl} is such an observable. It is defined as the number of detected clusters over the number of events:

$$o_{\mathrm{cl}} = \frac{\#\text{clusters}}{\#\text{events}} \tag{5.2}$$

The CBC detects all clusters for which the seed signal exceeds the threshold. The seed signal is the maximum strip signal in one cluster. Thus, the cluster occupancy is proportional to the integral of the seed signal distribution ρ_{s}. The integration interval is from the applied threshold τ to infinity.

$$o_{\mathrm{cl}}(\tau) \propto \int_{\tau}^{\infty} \rho_{\mathrm{s}}(E)\,\mathrm{d}E \tag{5.3}$$

The proportionality factor depends on different parameters, but mainly on the geometrical acceptance of the sensor under test with respect to the ^{90}Sr source. The derivative of o_{cl} yields the shape of the seed signal distribution.

Figure 5.5a illustrates a signal spectrum and the corresponding signal detection with a binary operating chip. Figure 5.5b in turn displays an exemplary threshold scan of the cluster occupancy. For the measurements, electrons from a ^{90}Sr source were focussed by a collimator on a 290 µm thick silicon sensor to generate signals. The threshold τ is defined as the difference between the pedestal p and the programmed comparator DAC value. For very low $\tau < 5\sigma$, where σ is the chip noise with attached sensor, noise starts to generate additional clusters and the cluster occupancy increases dramatically. For $5\sigma \leq \tau \lesssim 60\,\mathrm{Vcth}$ the cluster occupancy is almost constant, except for statistical fluctuations. Changing the threshold in this region does not change the number of clusters. Accordingly, the spectrum of the seed signals is zero for this region. Further increasing the threshold reduces the cluster occupancy, which means that the threshold cuts off the low energetic part of the seed signal spectrum. Finally, the cluster occupancy goes to zero when the threshold is higher than all injected cluster seed signals.

5.2 The 2S Module Readout Chain

To read out a full 2S module a chain of electronic components on the module is necessary. Each component fulfills a very specific task to transmit the hit information from the CBC to the CMS tracker data acquisition system. Figure 5.6 illustrates all components of the final 2S module readout chain. This section introduces the on-module components subsequently following the CBC in the data path.

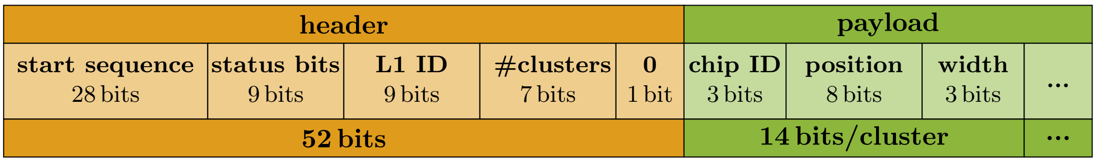

header					**payload**			
start sequence 28 bits	**status bits** 9 bits	**L1 ID** 9 bits	**#clusters** 7 bits	**0** 1 bit	**chip ID** 3 bits	**position** 8 bits	**width** 3 bits	**...**
52 bits					**14 bits/cluster**			**...**

Figure 5.7: CIC sparsified level-1 data output format. The level-1 event format starts with a 52 bits long header. The header also contains nine status bits, one for each CBC and one for the CIC. The CIC clusters the hits for compression. One cluster contains information about its position and width. Clusters with more than eight hits are splitted. Up to 31 clusters per CBC and 127 clusters per event can be encoded. Illustration following [Bra+16].

5.2.1 The Concentrator Integrated Circuit (CIC)

Besides eight CBCs one Concentrator Integrated Circuit (CIC) is placed on each front-end hybrid of the 2S modules. To reduce development effort and bundle capacities, the CIC was developed for the application in 2S and PS modules of the future Outer Tracker [Ber+19]. However, this section only focusses on the functionalities related to the 2S module readout. As its name suggests, the CIC collects and concentrates the data streams of eight CBCs. In total 48 SLVS lines at 320 MHz enter the CIC from the front-end chips, 40 of them transmit the stub data and eight the triggered level-1 information [Nod+19]. However, as a result of the data compression the number of outgoing data lines reduces to six SLVS lines running at 320 MHz. Depending on the data stream type the CIC performs different operations.

Stub Data:

The CBC emits stub data at 40 MHz bunch crossing rate via five SLVS lines. Up to three stubs per CBC can enter the CIC per clock cycle. However, it is not foreseen to provide the bandwidth to transmit up to 24 stubs per bunch crossing coming from the eight CBCs. The sorting and buffering algorithm of the CIC is a trade-off between minimizing the possible data loss and emitting the data synchronously.

The first step of the algorithm is to buffer the stub data for eight consecutive bunch crossings. Then it sorts the stubs by their bend code and transmits the information in an eight clock cycles lasting package. Five of the uplink data lines are reserved for the stub information. Taking into account the uplink bandwidth and stub size (12 bits) one CIC stub package transmits up to 16 stubs (20 without bend information). If the CIC receives more stubs within eight bunch crossing intervals, it rejects stubs beginning with the highest bend code. Besides the stub information the package also includes nine status bits (one for each CBC and one for the CIC).

Level-1 Data:

The CIC emits the level-1 data via one SLVS link. There are two different uplink data formats of the CIC to distinguish. The incoming level-1 data from the eight CBCs is not zero suppressed. On the one hand, the CIC can transmit the information as received from the CBCs and with an additional 28 bits long start sequence. In this operation mode the maximum trigger rate is limited by the bandwidth to about 140 kHz. However, for high occupancy operations like calibration and noise measurements this mode is necessary to prevent information losses.

On the other hand, the CIC can perform a sparsification on the CBC data. To compress the data, the CIC packs adjacent hits to clusters. Figure 5.7 displays the CIC output data format for the sparsified level-1 data [Bra+16]. It starts with a 52 bits long header, which is composed of a start sequence (28 bits), nine status bits, the nine bits long trigger counter (L1 ID), the number of clusters in the event (seven bits) and ends with one zero bit. The header is followed by the event payload which encodes each cluster in 14 bits. Each encoding includes information about the chip which detected the cluster (three bits), the position of the first hit (eight bits) and the cluster width. The maximum encodeable cluster width are eight strips. Clusters that contain more strips are split. Per triggered event the sparsification logic can cope with up to 31 cluster from one CBC. If there are more clusters in the data frame of one CBC the CIC drops clusters with the lowest position value. Furthermore, the output data format only allows up to 127 clusters per event from all eight CBCs. Again, if there are more clusters the CIC begins to drop the clusters with the lowest position value.

In the end the number of bits N necessary to encode one level-1 event scales linearly with the number of clusters n_{cl}:

$$N = 52\,\mathrm{bits} + n_{\mathrm{cl}} \cdot 14\,\mathrm{bits/cluster}. \tag{5.4}$$

The event encoding includes 52 bits for the header and additional 14 bits for every cluster. Independent of the operation mode, a 16 events deep final output FIFO buffers the output data frames of the CIC. A serializer block then transmits the level-1 data via one SLVS data line at 320 MHz.

Two *external interfaces* control the CIC. On the one hand, there is the I^{2}C slow control interface to read and write the chip registers. On the other hand, there are two dedicated SLVS links. On one link the CIC receives the 320 MHz clock. The other link is reserved for fast commands, like the trigger signal, fast reset, orbit reset or the test pulse trigger. The eight bit long commands are serialized at 320 MHz. From the fast commands, the CIC also recovers the 40 MHz reference clock.

5.2.2 The Low Power Gigabit Transceiver and the Versatile Link Plus Transceiver

The low power Gigabit Transceiver (lpGBT) is developed in an HL-LHC wide project and will be installed in many detector systems. It provides up and down links for multiple detector front-ends. Regarding the 2S module the lpGBT is located on the service hybrid. It serializes the data streams from two CICs, one for each front-end hybrid. Besides the uplink (up to $10.24\,\mathrm{Gbit\,s^{-1}}$) it receives a down-link ($2.56\,\mathrm{Gbit\,s^{-1}}$) including all commands and the clock signals to control and operate the 2S module.

Besides fast SLVS connection to communicate with the CICs, the lpGBTs comprise two generic I^{2}C masters to configure the ASICs on the modules. In addition, it includes a multiplexed DAC and analog-to-digital converter (ADC), on chip temperature monitoring, a programmable analog I/O port and current sources to drive external temperature sensors. For more information about the lpGBT see [Mor18] and [Des19].

Like the lpGBT the Versatile Link Plus Transceiver (VTRx+) front-end module is developed in an HL-LHC wide project. The VTRx+ provides the optical link between the electronics on the module and the CMS data acquisition system [Tro+17]. Its design foresees to operate in combination with the lpGBT. Thus, the optical up- and down-link have the same bandwidth as the lpGBT.

At the time the measurements presented in this thesis were performed, the lpGBT was still under development and not available. Thus, its predecessor, the Gigabit Transceiver (GBTx) was installed in the prototypes. The GBTx [MCW21] in combination with the Giga-Bit Transceiver - Slow Control Adapter (GBT-SCA) [Car+15] provide similar functionality as the lpGBT. The major difference is a slightly lower bandwidth of the uplinks, a higher power consumption and missing radiation tolerance of the GBTx. However, the bandwidth is fully sufficient for the data links in the 2S module. The optical link of the prototypes is a Versatile Link Transceiver module [Ama+09]. Even though it is not the final component, it provides the full bandwidth to transmit the data streams from the GBTx.

6

2S Module Prototypes and Sensor Characterization

One main focus of this thesis is to determine the performance of 2S module prototypes and to compare the results from prototypes employing two different sensor materials. The two materials investigated were last remaining candidates considered for the installation in the future Outer Tracker of the CMS experiment. This chapter introduces the 2S Mini Module design, the characterization methods and the measurements performed with the prototypes. Aside from using unirradiated sensors, modules were built with neutron irradiated sensors to mimic the expected radiation damage after years of operation in the CMS detector. The influence of operation parameters on the module noise and the effect of sensor defects have been investigated with a laboratory-based test setup. Furthermore, different methods to determine the conversion factor of the comparator threshold value Vcth into electrons have been evaluated. The measurements are completed by a beam test at Deutsches Elektronen-Synchrotron (DESY) to determine and compare the particle detection efficiency and resolution.

6.1 Sensor Material and Designs

In experiments at hadron colliders like CMS the silicon-based tracking sensors are exposed to an extremely harsh particle flux. Thus, the main focus of silicon sensor development is to improve the devices' radiation tolerance. To bundle expertise and facilitate the exchange of knowledge between different experiments, CERN founded the common research and development group, named RD50, in 2002. The aim of RD50 is the development of the next generation of silicon sensors for the HL-LHC [CER20]. Based on the results of the RD50 group the CMS Outer Tracker collaboration carried out a detailed sensor development study. Different materials and designs were evaluated to identify the most suitable sensor for the future Outer Tracker. The partner from industry producing the sensors on 6-inch wafers is Hamamatsu Photonics K.K. (HPK) [Ham]. The layout of the wafers includes different sensor designs and testing structures to investigate as many properties of the material as possible.

Many parameters impact on the performance of silicon sensors. The first choice to make is the sensor *base material*. Studies showed improved radiation tolerance of n-in-p sensors compared to the p-in-n sensors [Ada+17]. Thus, the n-in-p material became the baseline for the Phase-2 Outer Tracker sensors.

Another very important parameter is the sensor *thickness*. On the one hand, thin sensors reduce the material budget of the tracker and hence multiple scattering of particles. This improves the momentum resolution of the detector. Besides that the probability of photon pair production is reduced. Furthermore, the leakage current scales with the active thickness of the sensor and hence the heat dissipation by ohmic heating. Thus, the required cooling performance is lower for thinner sensors. On the other hand, the total signal generated by charged particles is reduced with the active thickness of the sensors [Har17].

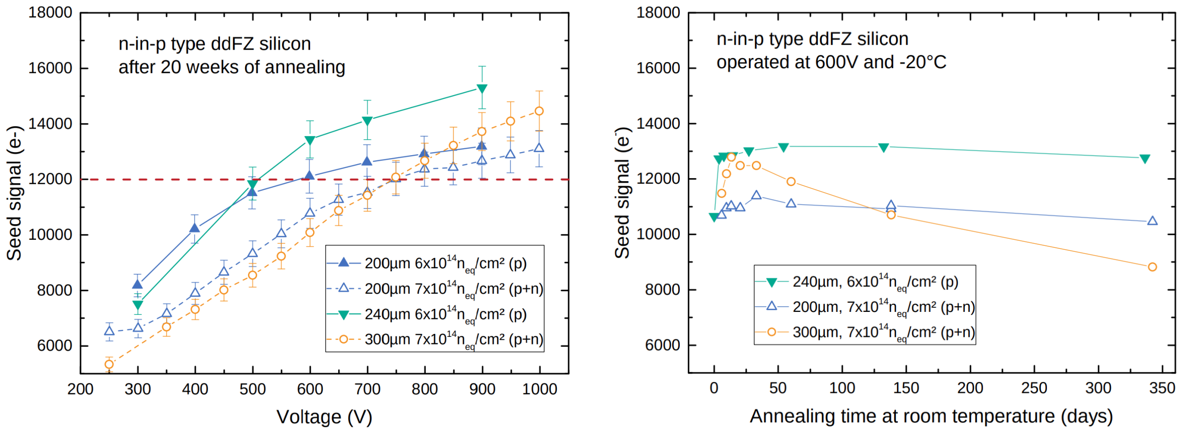

(a) Seed signal over bias voltage after irradiation.

(b) Seed signal over equivalent annealing time at 21 °C.

Figure 6.1: The influence of active thickness variations by deep diffusion on the seed signal for different sensor bias voltages (a) and annealing times (b) after irradiation. At 600 V sensors with an active thickness of less then 300 µm have a larger seed signal and are less sensitive to reverse annealing. [CMS18]

For the 2S modules the *seed signal* is a very important parameter to characterize the performance of a sensor. It is defined as the maximum signal detected by one channel in a cluster. To detect at least one hit of a cluster the seed signal has to exceed the threshold. Studies by the CMS Outer Tracker Sensor Group motivated that the most probable seed signal S_s of the sensor should be larger than twelve times the noise σ of the readout chip for efficient hit detection:

$$S_\mathrm{s} > 12\sigma. \tag{6.1}$$

Since the CBC is designed to have a noise of about 1000 e^- the expected minimum seed signal for the sensors of the 2S modules is 12 000 e^- [CMS18; Met20].

After irradiation the charge collection efficiency and hence the seed signal drops. Figure 6.1 shows the influence of irradiation and annealing on the seed signal for deep diffused sensors. The deep-diffusion technology enlarges the thickness of the heavily doped sensor backside implant. During the sensor processing heat drives the dopants further into the material and hence reduces the active thickness of the sensors. Sensors with larger active thickness suffers more from irradiation. For the target sensor operation voltage of 600 V the seed signal of 300 µm thick sensors is lower compared to thinner ones. The reason for this behavior is that after irradiation the thicker sensors are not fully depleted at 600 V. Besides that the electric field of thinner sensors is slightly higher at the same operation voltage. Thus, the drift velocity of the charge carriers is higher and the probability for trapping lower. Applying a bias voltage of 800 V or higher recovers the seed signal of the thicker sensors and they exhibit a better performance.

Another aspect to consider is the annealing behavior of the sensors. During operation in the CMS detector the sensor temperature will be about −20 °C, but during maintenance, possible down times or by intention the detector heats up to room temperature and annealing of radiation damage in the sensors sets in. Thicker sensors are more sensitive to reverse annealing, which reduces the seed signal for long annealing times. Considering all those aspects sensors with an active thickness of less then 300 µm show a better performance after irradiation and annealing.

However, the promising deep diffused material with 240 µm active thickness is not available any more. Thus, in a last remaining R&D iteration before the sensor procurement for the Phase-2 Outer Tracker upgrade two sensor materials with different thickness are investigated. The only vendor providing the required sensor materials and quality is HPK [Ham]. The sensors were produced on 6 inch wide and 320 µm thick wafers sliced from Float Zone [Pfa58] fabricated ingots. The active thickness of the sensors was reduced by two different procedures. On the one hand, shallow deep diffusion reduces the active region of the HPK standard material by approximately 30 µm to about 290 µm. In the scope of this thesis sensors of this type are titled FZ290. On the other hand, sensors were thinned physically to 240 µm with a thin backside implant. According to its thickness this material is titled thFZ240.

The *design* of the wafers includes a main sensor and additional test sensors and structures. All sensors investigated in this thesis are of the *baby* design. The baby sensor comprises 127 strips with a length of 48 mm. The pitch of the strips is 90 µm, which is the same as for the final 2S module sensors. These properties make the baby sensors perfectly suitable for building 2S module prototypes of reduced size. The 127 strips of one sensor exactly equip one layer of channels for the CBC readout. In addition, the strip length is almost the same as foreseen for the final 2S modules (50 mm).

6.2 Sensor Qualification and Test Stations

Before building prototype modules, all sensors have been electrically characterized to check whether they meet their specifications. The TDR of the Phase-2 Upgrade of the CMS tracker defines these specifications [CMS18]. Furthermore, charge collection measurements have been performed with irradiated and unirradiated baby sensors. The charge collection measurements are important to correctly interpret the beam test measurements. At the Institute of Experimental Particle Physics (ETP) at KIT dedicated setups are developed to perform these measurements. In this chapter the setups and measurement methods to characterize the investigated silicon sensors are introduced.

6.2.1 The Probe Station

Two custom made probe stations at ETP allow for the electrical characterization of sensors. For the measurement of the sensor properties different test pads on the sensors have to be contacted with needles. Figure 6.2 shows one of the two probe stations and a contacted baby sensor in the zoomed view.

A shielding box encloses the whole setup to suppress environmental influences on the measurements. It darkens the setup to prevent light-induced charge generation in the sensors. The sensor measurements take place on a movable vacuum chuck within the box. The vacuum guarantees a fixed position of the sensor on the chuck. Peltier elements coupled to a pre-cooled thermal bath stabilize the temperature of the vacuum chuck in the range between −20 °C and 60 °C. The shielding box is flushed with dry air to lower the humidity and prevent condensation. The needles for contacting the sensors are mounted on high precision needle holders. To perform the desired measurements a switching matrix can connect the needles with power supplies and different high precision measurement devices. A microscope with a camera within the box facilitates the positioning of the needles for the operator.

To bias a sensor the chuck and hence the sensor backplane is on negative high voltage potential. A bias needle on ground potential contacts the bias ring on the top side of the sensor. The bias needle holder is placed on a fixed table with respect to the chuck to guarantee contact even if the chuck is moving. The other needles contact pads of individual strips on the sensor surface. Figure 6.3 shows a sketch of a strip sensor and the different test pads on

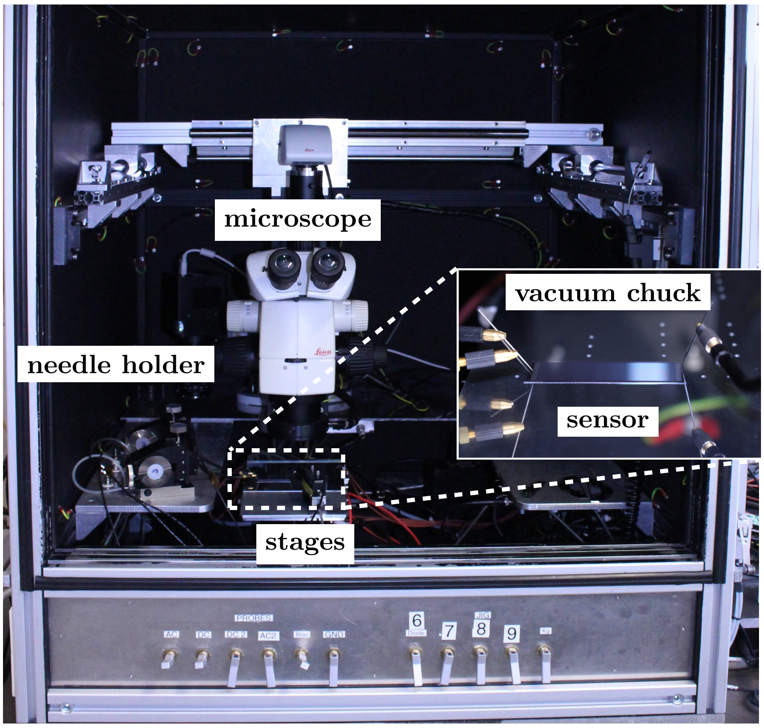

Figure 6.2: View into the Probe Station at the ETP. A temperature-stabilized vacuum chuck fixes the sensor under test and contacts its backside. Needles contact probing pads on the top sensor side to measure different electrical characteristics. To place the needles on the pads a microscope with a camera supports the operator. Stages move the chuck below the needles to perform automated scans. A housing encloses all components to shield from light and for protection purposes.

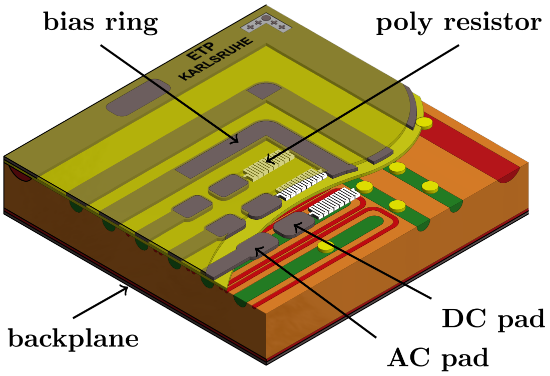

Figure 6.3: Illustration of contacting pads of a silicon strip sensor. To measure electrical properties of the sensors in the probe station different pads of the sensor are contacted [Har17].

its surface. An (x,y,z) stage moves the chuck below these needles to automate contacting and measurements of strip parameters. A Python-based software package developed at ETP controls the whole setup to perform the measurements.

I(V) and C(V) Characteristics

The most fundamental measurement to perform on a silicon sensor is to record its current-voltage I(V) and capacitance-voltage C(V) characteristics. Both measurements only require the bias needle to contact the bias ring. By applying negative high potential on the chuck the sensor is biased.

To record the I(V) characteristic the bias voltage is increased in steps and the corresponding current is measured. The measured current is the total leakage current of the sensor. For the operation in the CMS tracker the sensors have to operate stable for bias voltages up to 800 V. A strong increase of the current before reaching this limit indicates an early break down of the pn-junction inside the sensor. Figure 6.4a displays two typical I(V) characteristics of unirradiated baby sensors made of FZ290 and thFZ240 material. Even though the thFZ240 sensors are thinner they have a slightly higher leakage current. This is caused by defects on the backplane which were created by the thinning process. However, both sensors show a very low leakage current and are within the specifications.

The C(V) characteristics again is recorded by increasing the bias voltage stepwise. An LCR meter measures the capacitance for the different voltage steps at the frequency of 1 kHz. Figure 6.4b shows typical C(V) characteristics of unirradiated baby sensors. As described in section 4.1.3 the kink in the C(V) curve indicates the full depletion of the sensor. The thinner thFZ240 sensors get depleted at lower voltage (200 V) compared to the thicker FZ290 material (300 V).

Strip Measurements

Strip scans are fundamental for sensor quality control. The prototyping phase foresees the characterization of all sensors and the measurement of the electrical properties of all strips. Regarding the sensors for the prototypes examined in this thesis, six different strip measurements were conducted. The measurements can be classified into two groups, with respect to their contacting scheme.

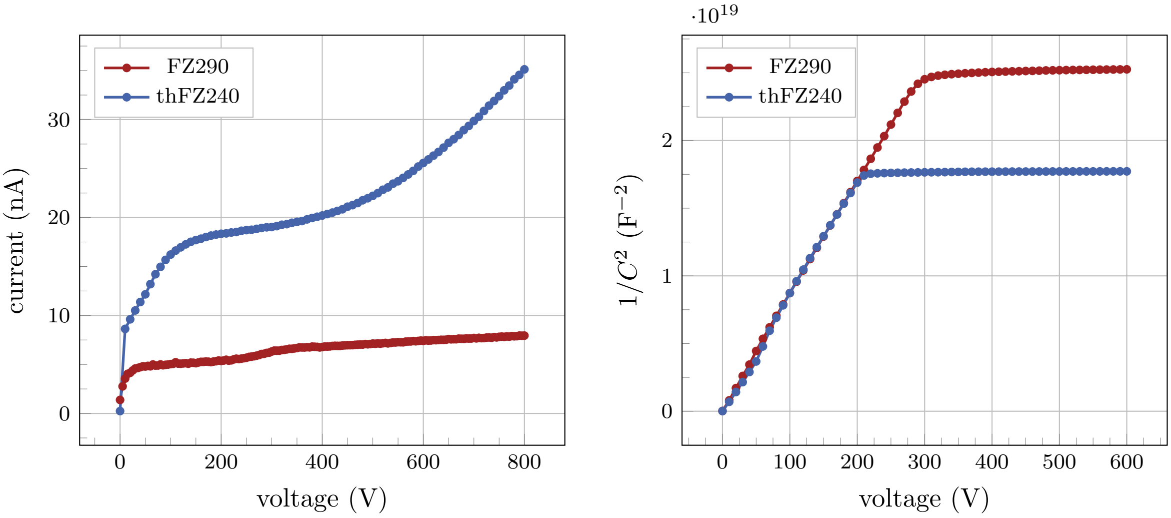

(a) I(V) **(b)** C(V)

Figure 6.4: Typical I(V) (a) and C(V) (b) characteristics of unirradiated baby sensors. Only sensors with high voltage stability (no breakdown before 800 V) were accepted for prototyping. The kink in the C(V) curve indicates the depletion voltage of the sensors, which is at about 200 V for the thFZ240 (blue) and 300 V for the FZ290 sensor (red), respectively.

By contacting the AC and DC pad of one strip four parameters are determined: the resistance of the poly resistor R_{poly}, the strip leakage current I_{leak}, the coupling capacitance C_{c} between the implant and the aluminum strip and the current through the SiO_2 isolation layer I_{diel}. Another configuration contacts the DC pads of neighboring strips to measure inter-strip parameters. By doing so the inter-strip resistance R_{int} and inter-strip capacitance C_{int} are quantified. Figure A.4 shows typical strip measurements for unirradiated baby sensors made of FZ290 and thFZ240 silicon.

The measurement of the electrical properties of individual strips discover possible strip defects before building the prototypes. One defect class are pinholes. A pinhole is a conductive connection through the SiO_2 isolation layer, that short-circuits the aluminum strip and the strip implant. A high I_{diel} current indicates the presence of a pinhole. A high strip leakage current or manufacturing faults can generate pinholes. A scratch on the top side of the sensor can short neighboring strips, which results in a low inter-strip resistance R_{int}. Section 9.3 investigates the influence of sensor defects on the performance of 2S module prototypes.

6.2.2 The ALiBaVa Setup

The ALiBaVa setup allows signal measurements on silicon strip sensors and to perform annealing studies. It is based on the ALiBaVa system as described in [Mar+07]. The heart of the system is the daughter board. It houses two Beetle chips, which were developed for the LHCb experiment [Löc02]. The Beetle chip comprises 128 analog readout channels to detect charge pulses from silicon strip sensors. Since the Beetle chip records the signal amplitudes it is suitable for signal studies. Besides the daughter board the ALiBaVa system consists of an FPGA based mother board. The mother board digitizes the analog signals from the Beetle chip into a ten-bit ADC value and handles external trigger signals.

The sensor under test is mounted on a custom made copper clad laminate Printed Circuit Board (PCB). The PCB comprises a biasing circuit for the strip sensor and a temperature

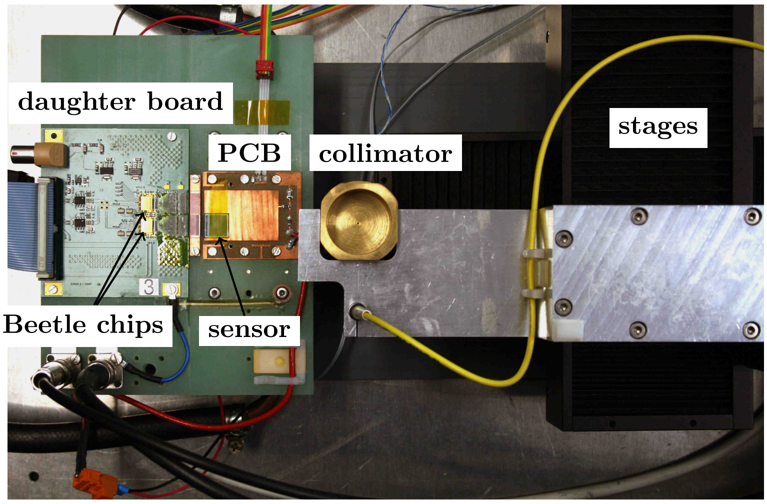

Figure 6.5: Picture of the ALiBaVa setup. The ALiBaVa daughter board is equipped with two Beetle chips. Each chip records analog signals of up to 128 strips. A custom made PCB comprises a biasing circuit for the sensor under test and a PT1000 temperature sensor for environmental control. All components are placed on a plastic board on a temperature controlled copper bridge. [Bra17]

sensor for environmental control. Both, the PCB and the daughter board are screwed on a Glass fiber Reinforced Plastic (GRP) carrier for fixation. The GRP board also comprises a copper inlay which is located below the sensor PCB. It thermally couples the sensor to a cooling bridge. A cooling system controls the temperature of the cooling bridge and hence the temperature of the sensor under test. Peltier elements couple the cooling bridge to a pre-cooled thermal bath. A controller adjusts the cooling/heating power of the Peltier elements to stabilize the temperature of the sensor at a programmable value. Typical operation temperatures for signal studies are between −20 °C and 20 °C. By heating the setup up to 80 °C irradiated sensors can be annealed.

For all measurements presented in the scope of this thesis a ^{90}Sr β^- source was used to generate signals in the sensor under test. A collimator with 0.8 mm aperture was used to focus the emitted electrons on the sensor. Three linear stages position the ^{90}Sr source above the sensor. A plastic scintillator, located below the sensor, detects electrons passing the sensor and triggers the readout of the system. A dry air flushed and lightproof aluminum box shields the setup components from environmental influences. The readout PC, the ALiBaVa motherboard and power supplies for the sensor, Peltier elements and scintillator are placed outside of the aluminum box. For more details concerning the setup see [Met16].

^{90}Sr Signal Measurement and Analysis

A detailed description of the signal measurement and underlying analysis is summarized by Metzler in [Met16]. This section shortly outlines the steps of the analysis.

The signal measurement is performed in four steps. In the first step, the noise measurement, the ALiBaVa system records 3000 randomly triggered events to determine the baseline and noise for each channel individually.

The second step is the gain calibration of the channels. By comparing the recorded DAC response to internal test pulses of known charge the individual gain for each channel is calculated. The response of the channels is equalized in the data analysis by using the gain corrections.

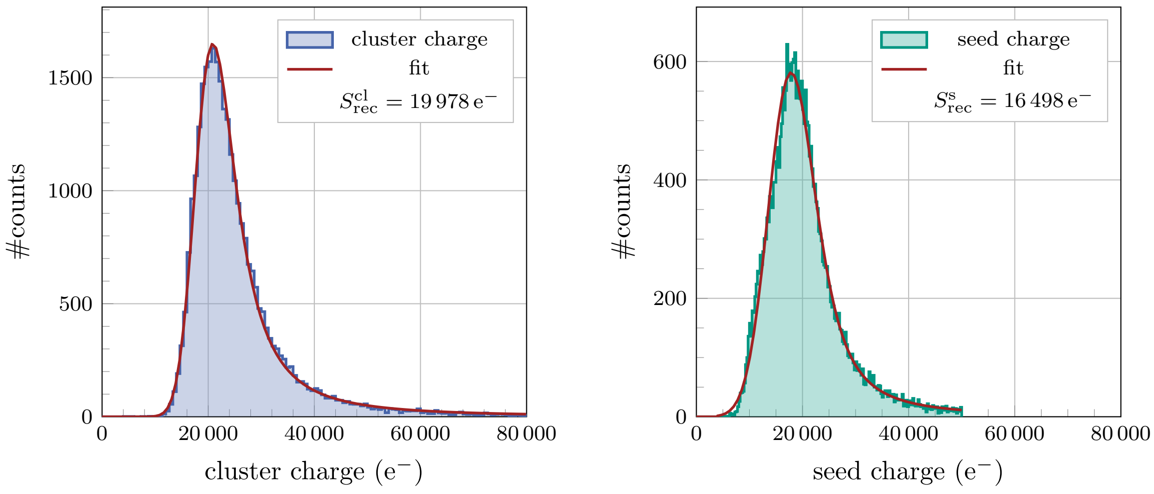

(a) Cluster signal distribution

(b) Seed signal distribution

Figure 6.6: ^{90}Sr cluster signal (a) and seed signal (b) distribution in a thFZ240 baby sensor at 20 °C and 400 V bias voltage. A convoluted Landau and Gaussian distribution fits the signal spectra.

The third step is the actual data acquisition using the ^{90}Sr source. A large number of events is recorded (e.g. 300 000), triggered by the plastic scintillator.

The fourth and last step is the signal analysis. Since the trigger signals do not arrive in phase with the clock of the Beetle chip the first step of the analysis is a timing cut on the trigger arrival time. The sampling time for triggers is 100 ns wide with a 1 ns time-to-digital converter (TDC) resolution. The analysis chooses the accepted TDC values individually for every run by the following conditions: For each TDC value the analysis calculates the mean cluster signal and identifies the maximum cluster signal of all TDC values. The final cut only accepts those TDC values exceeding 95 % of the maximum cluster signal. This guarantees that the following steps only accept events in which the signal amplitude was sampled in the pulse peak. For the remaining events the channel signals are corrected by the baseline from step one. Furthermore, a common mode noise correction is applied to compensate for event-to-event baseline fluctuations.

The next step of the analysis is the cluster identification. Metzler [Met16] describes the underlying algorithm in detail. The most important results from the analysis are the cluster and seed charge distribution and their most probable value (MPV) $S^{\mathrm{cl/s}}_{\mathrm{rec}}$. The cluster charge is the sum of the signals of all channels contributing to one cluster. The seed charge is the largest signal detected by one channel in the cluster. A fit of the seed and cluster signal distribution with a convoluted Landau and Gaussian function is used to determine in the most probable signal charge. Figure 6.6 shows the recorded cluster and seed signal distributions for a thFZ240 baby sensor.

Beetle Chip Signal Calibration

Even though the gain calibration equalizes the channels' response to a reference charge signal, a global calibration of the Beetle chip has to be performed. The uncertainty on the injected charge of the calibration run is 20 %. Thus, the uncertainty on the reconstructed signal is of the same order of magnitude.

A global calibration of the whole beetle chip reduces this uncertainty. To determine the global calibration factor of one Beetle chip the recorded cluster signal $S^{\mathrm{cl}}_{\mathrm{rec}}$ in a baby sensor made of the thFZ240 material is used. The active thickness of this sensor material is 240 µm. Nürnberg [Nür14] simulated the ALiBaVa setup using the Geant4 simulation tool for a 240 µm thick sensor. Figure A.10 displays the simulation results for the energy deposition of electrons from a ^{90}Sr source and 100 GeV muons (MIPs). The ionisation power of the lower energetic electrons is larger compared to MIPs. For a 240 µm thick sensor the expected MPV signal in the ALiBaVa setup is $S^{\mathrm{cl}}_{\mathrm{sim}} = 20\,689\,\mathrm{e}^-$ [Nür21]. The global calibration factor g_{B} for the Beetle chip is the ratio of the simulated $S^{\mathrm{cl}}_{\mathrm{sim}}$ and recorded $S^{\mathrm{cl}}_{\mathrm{rec}}$ signal

$$g_{\mathrm{B}} = \frac{S^{\mathrm{cl}}_{\mathrm{sim}}}{S^{\mathrm{cl}}_{\mathrm{rec}}}. \tag{6.2}$$

Figure 6.6a shows the recorded cluster signal distribution for a thFZ240 baby sensor. Based on these results, the global calibration factor is $g_{\mathrm{B}} = 1.036$. All following results of signal measurements with the ALiBaVa setup include a correction by this calibration factor. To compare the results for measurements from different sensors, irradiations and annealings, Metzler approximated the uncertainty on the MPV to be approximately $1000\,\mathrm{e}^-$ [Met16]. This equals a relative error of about 5 % for signal studies with an unirradiated thFZ240 sensors.

Binary Analysis

To compare the measurements of the ALiBaVa setup with the results from measurements with the CBC an analysis was implemented to mimic binary readout. After the timing cut, the baseline and the common mode correction a threshold is applied on the signal amplitudes to mimic the behavior of a binary chip. The signal in electrons for each channel is given by its ADC value multiplied with the corresponding channel gain and the global calibration factor g_{B}. If the signal exceeds the threshold the channel detects a hit. In the next step adjacent hits are gathered to clusters. The cluster occupancy, which is defined as the number of detected clusters over the number of triggered events, can be compared to the values obtained in the threshold scans performed using the CBC (see section 5.1.7).

Annealing with the ALiBaVa Setup

The temperature control unit of the ALiBaVa setup enables the automated execution of annealing steps. For one annealing step the setup heats up the sensor under test for a programmable time to a fixed temperature before cooling it down to −20 °C again. Typical annealing temperatures are 60 °C and 80 °C. The uncertainty on the gathered annealing time in the ALiBaVa setup is approximately ±2 % [Met16]. Since the annealing timer starts when the sensor reaches the targeted temperature, the greatest contribution to the uncertainty comes from the non-monitored heating and cooling intervals.

6.3 Neutron Irradiation Facility

The irradiation of the sensors for the 2S module prototypes was done with neutrons from the 250 kW TRIGA Mark II light-water reactor, which is part of the Reactor Infrastructure Center of the Jožef Stefan Institute (JSI) in Ljubljana, Slovenia. The targeted fluence for the sensors investigated in this thesis are $2.5 \times 10^{14}\,\mathrm{n_{eq}/cm^2}$ and $5.0 \times 10^{14}\,\mathrm{n_{eq}/cm^2}$. In the reactor the fluence is reached within a few minutes, with a precision of about 10 %. During the exposure the temperature of the sensors is about 40 °C. Afterwards they are stored for approximately half an hour at about 30 °C in the irradiation channel for the cool-down of activation products. [SŽT12] During the shipping from Ljubljana to KIT ice packs cool the

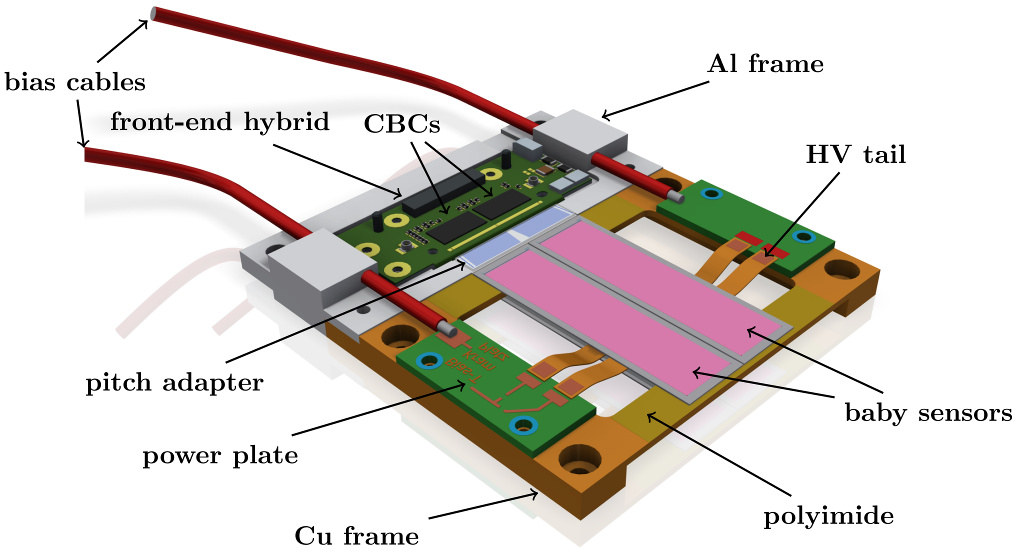

Figure 6.7: Rendering of the Mini Module CAD drawing. Two CBC3.0 read out four baby sensors with 127 strips each. The sensors are aligned in parallel in two layers with a spacing of 1.4 mm. The sensors of each stack are made of the same material. One double layer is made of FZ290 and one of thFZ240 sensors. Two power plates bias the two stacks separately.

sensors to prevent further non-monitored annealing. All annealing times stated in this thesis were determined starting after the arrival at KIT.

6.4 The 2S Mini Module & Test Station

Different working groups of the Outer Tracker collaboration take responsibility for the development of the fundamental components of the final 2S modules. The construction of prototype modules from these components and their validation are essential steps of the detector development process and quality assurance. The functionality of the components and their correct and efficient interplay can be tested in prototype modules using dedicated test setups. This section introduces the 2S Mini Module Design and the corresponding laboratory-based test station, which were developed in the scope of this thesis.

6.4.1 2S Mini Module Design

The 2S Mini Module is an intermediate prototype design to investigate the interplay between sensors and readout chips of 2S modules. It includes sensors with the final strip geometry and the CBC readout chip version 3.0, which is the first version including all required functionality. By arranging sensors in stacks the Mini Module mimics the structure of the final 2S module to validate the stub finding algorithm of the CBC. Figure 6.7 displays a CAD rendering of the Mini Module design and highlights its components.

The heart of the module is a *front-end hybrid* housing two CBCs. Furthermore, the module is equipped with four *baby sensors* arranged in two layers. The number of strips of one Mini Module adds up to 508. At the time of the Mini Module construction two different sensor materials remained in the sensor validation process, the thFZ240 and FZ290 material. To investigate the interplay of the CBC with different sensor materials, a Mini Module is built of two sensors of each material. Pairs of the sensors of the same material form a stack on top of each other with a spacing of 1.4 mm. Thus, one CBC reads out one stack of two baby sensors made from the same material.

Wire bonds on the top and bottom side connect the sensor AC pads with the analog front-end of the readout channels. The connection is established via custom made fan out *pitch adapters*. The analog readout pads on the front-end hybrid have a constant spacing. The pitch adapters compensate for the different spacing of the analog pads in between the chips and the gap in between of the sensors of one sensor layer.

Two *metal frames* support all components of the module. An aluminum frame fixes the front-end hybrid and the pitch adapters. In addition, it guides the high voltage cables away from the module and provides positioning holes for the installation of the module in the test setups.

To improve the cooling properties the sensor frame is made of copper. It supports the sensors and acts as a spacer for the sensor layers. The sensors are glued on the top and bottom side of the copper frame. A thin layer of *polyimide* electrically isolates the sensors from the copper frame. During the glueing process mechanical stops align the sensor stacks in parallel to enable tests of the stub finding logic of the CBC. However, this method does not provide the same alignment quality as required for the future 2S modules.

The sensors are biased via two *power plate* PCBs which are screwed on the copper frame. Each power plate houses a low-pass filter to reduce noise injections from the external high voltage source. Custom designed *HV tails* made of flexible PCB guide the high voltage potential from the power plates to the backside of the sensors. Dedicated ground bonds from the sensor frontside to the front-end hybrid ensure a common module ground of the high and low voltage circuits. Furthermore, they ensure the current backflow of the sensor leakage current to the power plates. A silicone elastomer encapsulates all bond connections to protect them from damage. To monitor the module and sensor temperature a *PT1000 temperature sensor* is glued on the copper frame.

In total four Mini Modules were assembled at the ETP. Two modules were built with unirradiated sensors. For the two others the sensors were irradiated with neutrons at the JSI in Ljubljana before the assembly. The sensors of one module were all irradiated by the same fluence. Furthermore, the sensors were annealed to two different equivalent annealing times at room temperature (13 d and 204 d). The short annealing time corresponds to a beneficial material state for which a minimum depletion voltage is expected. The long annealing time is a conservative estimation of the full annealing expected for 14 years of operation in the CMS experiment. Table 6.1 gives an overview about the Mini Modules constructed at ETP and the corresponding sensor irradiation and equivalent annealing times.

6.4.2 The 2S Mini Module Test Station

The 2S Mini Module Test Station allows the characterization and testing of the 2S Mini Modules under a controlled environment in the laboratory. Furthermore, it provides all devices necessary to operate a Mini Module. The station itself is enclosed by a dry air flushed aluminum box, which also shields the module from light.

To operate a Mini Module, additional hardware is necessary. The module is read out by an FC7 readout board which is equipped with a Xilinx Kintex 7 FPGA [Pes+15]. The FC7 runs a dedicated firmware to communicate with the readout chips and sends information via ethernet to a computer which in turn runs the Ph2_ACF middleware. The FC7 readout board is placed outside of the box to prevent light induced current generation in the sensors by the FC7 status light emitting diodes (LEDs). The Universal Interface Board Version 2 (UIBv2) [BBK18] provides the low voltage for the CBCs on the Mini Module. Furthermore, it connects the data

Table 6.1: Overview of the sensor configurations of the four Mini Modules built at ETP. The sensors of two modules were irradiated with neutrons at JSI and annealed to different equivalent annealing times at 21 °C.

Mini Module	**Sensor material**	**Fluence** $(1\times10^{14}\,\mathrm{n_{eq}/cm^2})$	**Eq. annealing** (days at 21 °C)
MiMo1	2×thFZ240	0.0	–
	2×FZ290	0.0	–
MiMo2	thFZ240	2.5	13
		2.5	204
	FZ290	2.5	13
		2.5	204
MiMo3	thFZ240	5.0	13
		5.0	204
	FZ290	5.0	13
		5.0	204
MiMo4	2×thFZ240	0.0	–
	2×FZ290	0.0	–

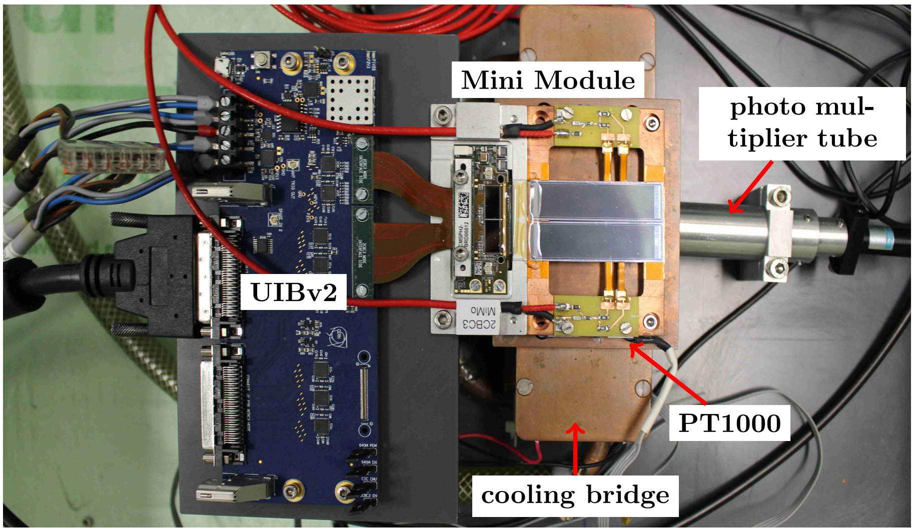

Figure 6.8: View into the Mini Module test station. A Mini Module is screwed on a cooling bridge. Peltier elements, which are coupled to a pre-cooled thermal bath, adjust the module temperature by cooling/heating the copper cooling bridge. A scintillator below provides a trigger for ^{90}Sr signal measurements. The UIBv2 board powers the CBCs and routes the data lines via a VHDCI cable to the FC7 readout board.

lines from the hybrid with the FC7 via one Very-High-Density Cable Interconnect (VHDCI) link. The UIBv2 and Mini Module are screwed together to prevent mechanical forces on the connectors.

To control the temperature of the module it is mounted on a copper cooling bridge. Peltier elements, which are coupled to a pre-cooled thermal bath, heat or cool the bridge to adjust the module temperature. A temperature control unit stabilizes the module temperature at a programmable value by adjusting the Peltier cooling/heating power. By doing so the module reaches sensor temperatures down to $-22\,°\mathrm{C}$.

The test station also provides the infrastructure for data taking with a radioactive ^{90}Sr source. A removable fixation positions the ^{90}Sr source above the sensors. Two collimators with different apertures (800 µm and 3000 µm) can be inserted in the fixation to focus the emitted electrons on the sensors. A scintillator below the module detects electrons penetrating the module and creates a trigger signal for the data acquisition.

In addition, two infrared LEDs with a wavelength of 950 nm are mounted at the lid of the aluminum box to uniformly illuminate the Mini Module's top side. The infrared light penetrates silicon and creates electron-hole pairs, which increase the sensor leakage current. Since the light is reflected at the sensor's aluminum back side only the upper sensor layer is illuminated. A constant current source controls the current flowing through the LEDs and hence the light intensity [Bra20].

Several low and high voltage power supplies provide the power for all components of the 2S Mini Module Test Station.

6.5 The DESY Beam Test

Laboratory systems are perfect to characterize the electrical properties of sensors or to perform signal measurements with radioactive sources. However, these laboratory based methods cannot quantify all performance parameters of the prototypes. In particular, the particle detection efficiency and spatial resolution cannot be measured. Prototype tests in high energetic particle beams provide a more realistic operation scenario. Additional detector planes with high spatial resolution form a beam telescope to individually track the passing particles. By using the particle tracks the prototypes' particle detection efficiency and spatial resolution can be measured. One test beam facility is located at Deutsches Elektronen-Synchrotron (DESY) in Hamburg, Germany. This chapter outlines the DESY test beam facility and presents the tools and procedures used to perform efficiency studies on the 2S Mini Module prototypes.

6.5.1 The DESY Test Beam Facility

The test beam facility located at DESY in Hamburg operates three beam lines as illustrated in figure 6.9. The DESY II accelerator provides electrons or positrons to generate the test beams. It accelerates one bunch of particles up to 7 GeV with 1.024 MHz revolution frequency. To generate the test beams the primary beam from DESY II hits a carbon fiber target in the middle of the beam pipe. The scattering process emits high energetic photons by bremsstrahlung, which leave the beam pipe in tangential direction. A subsequent metallic converter foil, transforms the high energetic photons into electron-positron pairs by pair production. Then, the pairs enter a spectrometer. The magnetic field of a dipole magnet fans out the beam and sorts the particles with respect to their energy and electric charge. A collimator cuts a small fraction of the fanned beam, which corresponds to a specific particle type and momentum. These particles are the beam that enters the test beam area. By tuning the magnet current the energy and particle type of the final test beam is chosen.

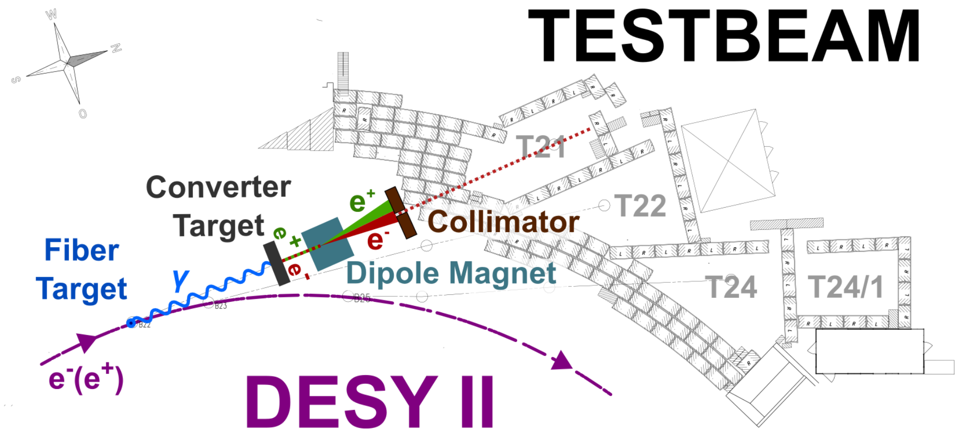

Figure 6.9: Illustration of the DESY test beam facility. The DESY II ring stores the primary beam for the three test beam areas. By bremsstrahlung at a carbon fiber target in the beam pipe highly energetic photons are generated. A metal converter foil transforms the photons into electron-positron pairs. The combination of an adjustable dipole magnet and a collimator chooses the particle type and energy for the final test beam. The provided beam energy is in the range of 1 GeV to 6 GeV. [Deu21b]

The selectable test beam energy is in the range of 1 GeV to 6 GeV. On the one hand, a high beam energy reduces the number of multiple scattering processes and thus increases the track resolution of the telescope. On the other hand, the particle rate decreases dramatically for the highest beam energies, so that the trigger rate reduces to $\mathcal{O}(10\,\mathrm{Hz})$ at 6 GeV. The chosen trade-off for the measurements presented in the scope of this thesis is to run at 5.6 GeV electron energy. For this energy a trigger rate of about 500 Hz to 700 Hz is achieved.

6.5.2 The DATURA Telescope

To perform efficiency and resolution studies on prototypes a precise tracking of the test beam particles is essential. The tracking for the measurements presented in this thesis was done with the DATURA[1] telescope at DESY [Jan+16]. The DATURA telescope consists of six monolithic MIMOSA pixel detector planes as illustrated in figure 6.10. Aluminum frames fix the MIMOSA detectors in two sets of three planes. With respect to their position along the beam direction, the two sets are also called the upstream and downstream arm of the telescope. The aluminum frames can slide over a fixation structure along the beam axis to adjust their relative distance. The device under test (DUT) is placed in the center between the two telescope arms. Motor stages move the DUT in x- and y-direction, and a rotary stage rotates it around the y-axis. To improve the tracking resolution the distances of the telescope arms $\Delta x_{u/d}$ to the DUT are reduced as far as possible. The minimum distance from the telescope arms to the DUT depends on the setup geometry and the rotation angle around the y-axis. For the measurements presented in this thesis, $\Delta x_u = 80\,\mathrm{mm}$ was chosen and had not to be changed during rotations, whereas Δx_d changed between 73 mm to 109 mm depending on the rotation angle of the DUT.

The MIMOSA detector has an active area of $10.6 \times 21.2\,\mathrm{mm}^2$ composed of 576×1152 pixel. The pixel pitch is 18.5 µm. Furthermore, the detectors are thinned to 50 µm, which reduces the material budget of the telescope and hence multiple scattering. The combination of small pixels and thin detectors result in a very good tracking resolution. The telescope without DUT reaches a track resolution of up to 3 µm [Jan+16].

---

[1] DESY Advanced Telescope Using Readout Acceleration

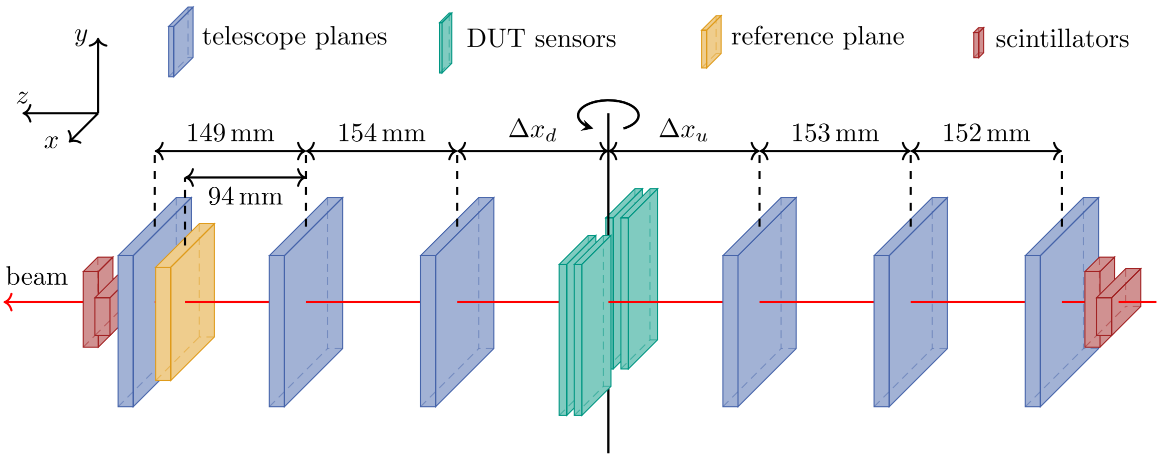

Figure 6.10: Sketch of the beam test setup geometry. The telescope (blue) consists of two arms with three planes each. An additional fast FE-I4 reference plane (orange) was installed in front of the last telescope plane in beam direction. Four scintillators (red) in coincidence trigger the readout. The DUT (green) sits on a rotary stage (y-axis) and movable xy-stage in the center of the two telescope arms. By sliding the telescope arms as close as possible to the DUT the distances $x_{d/u}$ are reduced to improve the tracking resolution.

The MIMOSA detectors have an integration time of $\mathcal{O}(100\,\mu s)$ for one readout sample. Thus, one readout sample of the telescope can contain more than one particle track. However, the shaper of the CBC has a very short integration time $\mathcal{O}(25\,ns)$ compared to the telescope. Thus, it will only see the tracks which triggered the readout. To identify the correct track an additional fast reference detector was placed in front of the last telescope plane in the downstream arm. For the beam test the FE-I4 chip was used as reference plane [Gar+11]. Since the FE-I4 has a comparable integration time as the CBC it will also see only the hits related to the particle track of interest. The track matching the hit on the reference plane corresponds to the particle which triggered the readout. The pixel size of the sensor attached to the FE-I4 chip is $50\,\mu m \times 250\,\mu m$. Taking into account the number of pixels (336×80) it covers an active area of $16.8 \times 20.0\,mm^2$.

6.5.3 The Trigger and Trigger Logic Unit

Four scintillators in coincidence generate the trigger signal to initiate the readout of the telescope, DUT and reference plane. The scintillators are arranged in pairs, two at the downstream and two at the upstream end of the telescope, see figure 6.10. The signal of the coincidence logic enters the Trigger Logic Unit (TLU), which is the central unit managing the trigger signals for all components of the DAQ system. Since the integration time of the different subsystems differs strongly a correct timing of the trigger signals is of importance. The TLU expects BUSY signals raised by the subsystems as long as their readout takes place. As long as at least one subsystem is BUSY no further triggers from the scintillators will be accepted. This ensures that every subsystem will record the same number of events. Besides this simple handshake the TLU distributes an incrementing trigger ID to the subsystems. By recording the TLU trigger ID and adding it to the event data stream of the subsystems a correct matching of the events is possible, even if events get lost. This trigger handshake protocol was used during data acquisition. [Cus09]

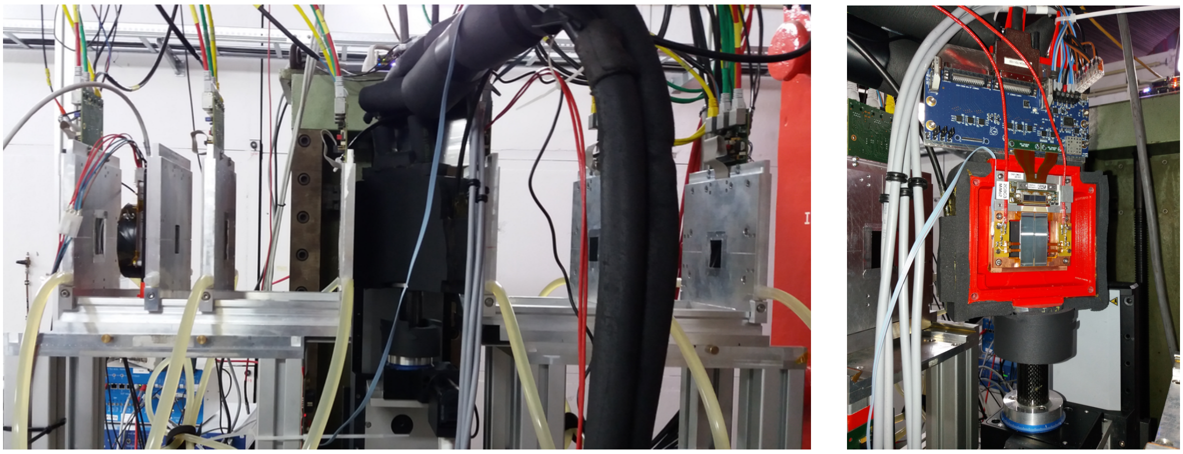

(a) The DATURA telescope, FE-I4 reference plane and the thermally isolated Mini Module cold box in the center. **(b)** Mini Module in the opened cold box.

Figure 6.11: Picture of the beam test setup at DESY. The DATURA telescope records tracks of particles (a) which allow efficiency and resolution studies of the Mini Module in its center (b). An additional FE-I4 reference plane identifies the correct track belonging to the trigger signal. The Mini Module can be cooled down to approximately $-20\,^{\circ}\mathrm{C}$ to perform measurements with irradiated modules. A 3D printed housing on a rotary stage protects and fixes the Mini Module during the measurement.

6.5.4 The Mini Module Beam Test Setup

For the beam test measurements with the Mini Modules dedicated mounting and cooling mechanics have been designed. All measurements were performed with the Mini Module in the center of the two telescope arms. The module was oriented in such a way that the hybrid is on the top and the strips of the sensors were aligned parallel to the vertical y-axis. Thus, the beam first hits the top and then the bottom sensors of the module. The mounting structure consists of a 3D-printed housing. To reduce multiple scattering the housing has beam windows on the front and backside. The windows were sealed with a thin polyimide foil. To operate modules with irradiated sensors, a copper cooling chuck was inserted into the housing. A chiller cools down a cooling liquid to $-23\,^{\circ}\mathrm{C}$ and pumps the liquid through the cooling chuck. The DUT is screwed on the cooling chuck to provide good thermal contact. By doing so the module was cooled down to approximately $-20\,^{\circ}\mathrm{C}$ to $-23\,^{\circ}\mathrm{C}$. To prevent condensation, the housing was flushed with nitrogen gas. Furthermore, a thermal insulation around the housing prevented the creation of ice on the surface. Like for the Mini Module test station, the readout and operation of the module in the beam test requires a UIBv2, the FC7 readout board and high and low voltage power supplies for the sensors and electronics. During the data acquisition environmental parameters, like the module temperature, sensor voltage and sensor current, were continuously monitored. Figure 6.11 shows pictures of the DATURA telescope with the cold box in its center and the opened cold box with a Mini Module.

6.5.5 The EUDAQ Analysis Framework

The EUDAQ framework is a general data acquisition software to orchestrate the data acquisition and record raw information from all telescope components and DUTs. The software project initially started as part of the EUDET project [EUD16b] and was later released in an independent open source project [EUD21]. For the Mini Module beam test EUDAQ v1.7 was used. The software runs different sub-processes which communicate via TCP/IP sockets. Each sub-process fulfills a specific task of the data acquisition. *Run Control* is the central process orchestrating all others. To simplify the handling for users, it comes with a graphical user interface (GUI). The GUI also displays live information about the current particle and trigger rate.

The subsystems connect to EUDAQ via individual *producers*. The producers register at the Run Control to receive commands (e.g. for initialization and starting the data acquisition). Furthermore, they stream the raw data produced by the subsystem to the *Data Collector*. As its name suggests, the Data Collector gathers all data streams from the subsystems and dumps it to a combined raw data file on disk.

For monitoring purposes there are two further processors. The *Log Collector* and *Online Monitor* provide information about the status of all subsystems, the beam and create live correlation plots of the hit positions to check the synchronicity of the data streams [EUD16a].

6.5.6 Definitions

This section defines some terminology which will be frequently used to describe the beam test measurement results.

- The **cluster efficiency** η_{cl} is defined as the ratio of the number of recorded clusters $n_{\mathrm{cl,rec}}$ in a certain sensor region over the number of expected clusters $n_{\mathrm{cl,exp}}$ by tracks hitting the same region.

  $$\eta_{\mathrm{cl}} = \frac{n_{\mathrm{cl,rec}}}{n_{\mathrm{cl,exp}}} \tag{6.3}$$

  The statistical uncertainty on the efficiency measurements is given by the uncertainty on the mean value of a counting experiment (binomial distribution) [Hen21]

  $$\sigma_\eta = \sqrt{\eta_{\mathrm{cl}}(1-\eta_{\mathrm{cl}})/n_{\mathrm{cl,exp}}}. \tag{6.4}$$

- The **stub efficiency** η_{s} is defined as the ratio of the number of recorded stubs $n_{\mathrm{s,rec}}$ in a certain sensor region over the number of expected stubs $n_{\mathrm{s,exp}}$ by tracks hitting the same region.

  $$\eta_{\mathrm{s}} = \frac{n_{\mathrm{s,rec}}}{n_{\mathrm{s,exp}}} \tag{6.5}$$

  The statistical uncertainty on the measurement can be estimated in the same way as for clusters in equation 6.4.

- The **residual** $\Delta x/\Delta y$ is the distance between the extrapolated track position $x_{\mathrm{track}}/y_{\mathrm{track}}$ in the local frame of the detector and the position $x_{\mathrm{rec}}/y_{\mathrm{rec}}$ recorded by the detector. For pixel detectors, like the telescope and reference plane, the residual is defined in two dimensions, since they provide two dimensional information. For strip detectors, like the DUTs, only the residual along the x-axis is of importance

  $$\Delta x = x_{\mathrm{track}} - x_{\mathrm{rec}}. \tag{6.6}$$

  The residual can be calculated for different observables, like the recorded cluster position x_{cl} or the recorded stub position x_{s}. In the scope of this thesis, the **resolution** of the DUT is the standard deviation of the residual distribution in x-direction (Δx). Since it includes the folding with the resolution of the telescope tracking and the limited resolution of the track reconstruction it is a worst-case scenario approximation of the DUT's intrinsic spatial resolution. Figure A.12 shows the result of the simulated telescope resolution with the Mini Module setup geometry for different DUT thicknesses and downstream distances x_d. The expected telescope resolution for the Mini Module setup is of the order of 4 µm to 5 µm. This is much better than the binary resolution of the DUT ($p/\sqrt{12} \approx 26\,\mu\mathrm{m}$) and hence can be neglected for the analysis.

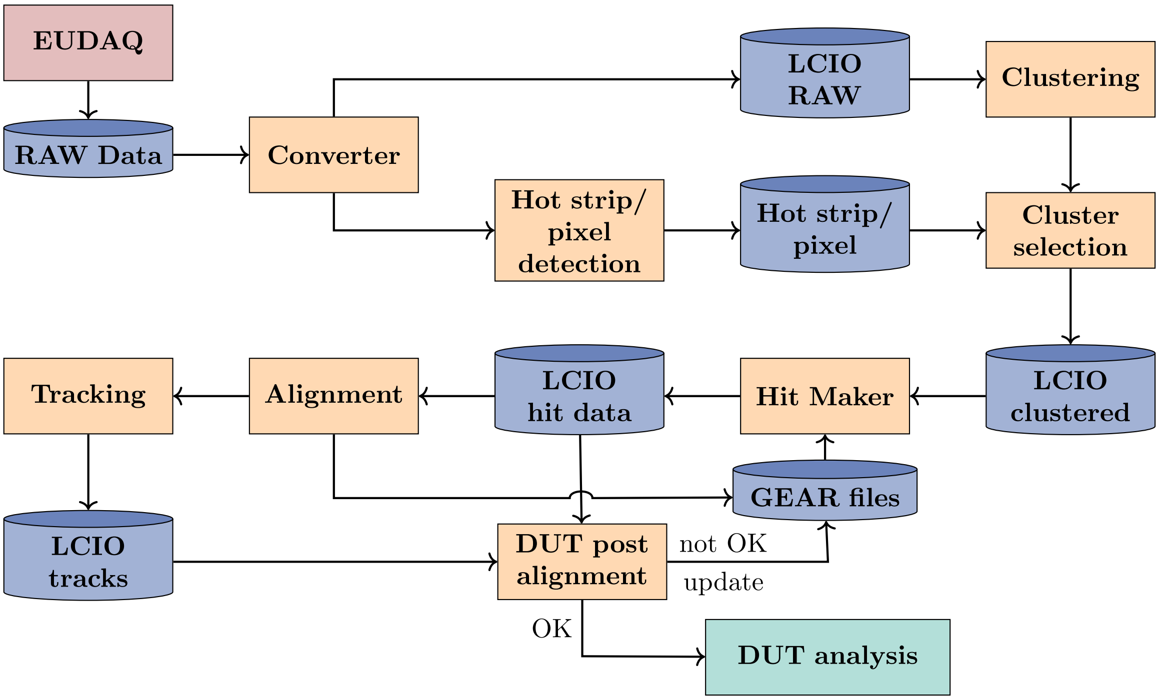

Figure 6.12: Analysis workflow for the beam test data. Blue cylinders represent stored database information, orange boxes processor steps performed by EUTelescope. First, the raw data is converted into a common LCIO data format, then hits are clustered and translated into 3D space points. After the alignment of the telescope and reference plane, a processor generates particle tracks. Using the tracks the DUTs are aligned. The final analysis step creates result histograms and profiles.

6.5.7 The EUTelescope Analysis Framework

To carry out the analysis of the raw data, the EUTelescope analysis framework was used [Deu21a]. EUTelescope is a modular software framework to reconstruct particle tracks in beam telescopes [Bis+20]. It provides different processors to perform chained tasks on the raw data sets. The workflow to analyse the data of the beam test with the Mini Modules is illustrated in figure 6.12. The following paragraphs briefly introduce the different steps of the analysis work flow. The DUT analysis will be described more in detail in sections 6.5.8 and 6.5.9.

Converter and hot strip/pixel detection

The *converter* translates the raw information, recorded by EUDAQ, into a common linear collider I/O (LCIO) data format. In the same data processing step the *hot strip/pixel detection* takes place. It detects pixel or strip cells having a hit occupancy[2] above a programmable threshold. The so detected pixels/strips are stored in the *hot pixel/strip* database for later masking of noisy channels in the analysis. For the DUTs the threshold hit occupancy to mask a strip was set to 1.5 %.

---

[2] defined as #hits/#trigger

Clustering and Cluster Selection

The charge generated by a particle passing a silicon pixel or strip detector can be shared by multiple sensor cells. This effect leads to clusters of hits in the region where the particle passed the sensor. The *clustering* step identifies groups of neighboring cells seeing a hit by the particle. Furthermore, it calculates the cluster center-of-gravity by using the weighted mean of the hit positions, where the weights are the recorded signal amplitudes. The combined hit information of several pixels of a cluster increases the spatial resolution compared to the binary resolution of the detector. In contrast to the telescope, the strips of the DUTs are read out by binary operating CBCs. For binary signal detection the amplitude of all hits is the same. Thus, the cluster center-of-gravity is the geometrical center of the cluster. The *cluster selection* rejects clusters containing hits from noisy channels to prevent fake hits disturbing the tracking.

Hit Maker

The *hit maker* creates 3D space points from the clusters' center-of-gravity in the global frame. To do so, Geometry API for Reconstruction (GEAR) xml files provide information about the detector geometries and relative positions. The relative positions of the sensors have been measured in the test beam area. Furthermore, the processor performs a rough pre-alignment of the setup.

Alignment

The 3D space points are the starting point for the *alignment* step. The precision of the position measurement is limited by mechanical and practical reasons and poor compared to the micrometre resolution of the setup. Thus, all setup components have to be aligned by software, too. The first step is the alignment of the telescope and the reference plane by using particle tracks from the recorded 3D space points. EUTelescope uses the Millepede II algorithm to perform the alignment [Blo07]. There are different processors to determine the particle tracks. The processor of choice strongly depends on the beam energy and material budget of the setup. Since the electron beam at DESY has a relative low energy (5.6 GeV) the alignment algorithm has to take into account multiple scattering at the detector planes and in the air. One approach to do this is the General Broken Lines (GBL) algorithm [Kle12]. The processor used for the Mini Module beam test is called *EUTelAlignGBL*. It performs a GBL-based track finding and generates the input parameters for the Millepede II algorithm. Millepede II returns correction values on the input geometry. In a last step, the processor updates the GEAR files with the correction. This alignment step is repeated several times to iteratively improve the alignment.

Tracking

After the alignment of the telescope and the reference plane the final *tracking* of the beam particles takes place. For this tracking the *EUTelTestFitter* is used. It takes into account multiple scattering of the electrons in the telescope layers, air and DUTs to improve the tracking resolution.

DUT post Alignment

The last step before the final analysis is the *DUT post alignment*. The glueing precision of the sensors is limited and hence one cannot expect a fixed relative orientation of the sensors with respect to each other within one module. Thus, the four sensors of the Mini Modules were treated as individual DUTs. In the following the term DUT stands for one sensor of the Mini

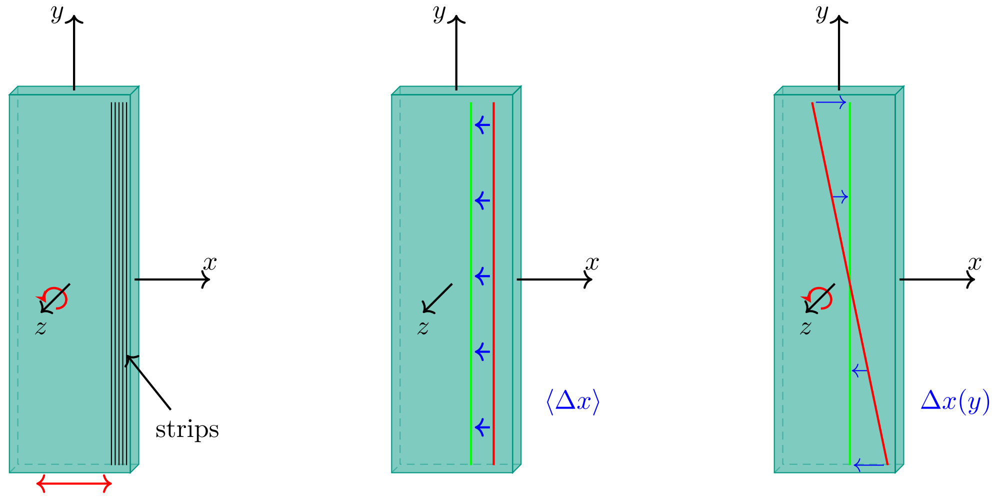

(a) Corrected degrees of freedom **(b)** Misalignment in x **(c)** Rotation around z

Figure 6.13: Sketch of the DUT post alignment. The alignment step of EUTelescope did not properly corrected the misalignment in x direction and the rotation around the z-axis. The post alignment corrects these degrees of freedom as displayed in (a). The misalignment in x is given by the mean residual $\langle\Delta x\rangle$ of the track position x_{track} and the recorded cluster position x_{cl} as visualized in (b). The rotation around the z-axis is the slope of the x residual over the y track position $\Delta x(y)$ as illustrated in (c).

Module. Unfortunately, the DUTs alignment of EUTelescope does not converge for all degrees of freedom. So an automated DUT post alignment was implemented. The post alignment of the DUT was done for each data run in an iterative way. For each iteration the residual distributions of the track and recorded cluster position were calculated and fitted. Depending on the residual axis different misalignments are tackled.

- **Misalignment in x**: correction by the mean of the x residual distribution $\langle\Delta x\rangle$,
- **Rotation around z**: correction by the slope of the mean x residual distribution over the track position in y direction $\langle\Delta x\rangle(y)$,

Figure 6.13 displays the corrected degrees of freedom and the method to determine the related misalignment. The particle beam hit the DUTs in the center region of the strips where the DUTs are not sensitive on the y position. Thus, the DUT alignment in y direction has not been corrected.

6.5.8 DUT Cluster Analysis

All steps introduced previously were necessary to prepare the beam test data for the final DUT cluster analysis. This analysis determines the performance parameters, like the cluster detection efficiency and resolution, of the DUTs. However, only tracks fulfilling several selection criteria contribute to this final analysis. The following list summarizes the criteria to accept a track:

- **Reference plane residual cut:** As mentioned before, the telescope has a long integration time compared to the CBC. Thus, it records the tracks of several particles for one triggered event. The reference plane identifies the particle track which triggered the

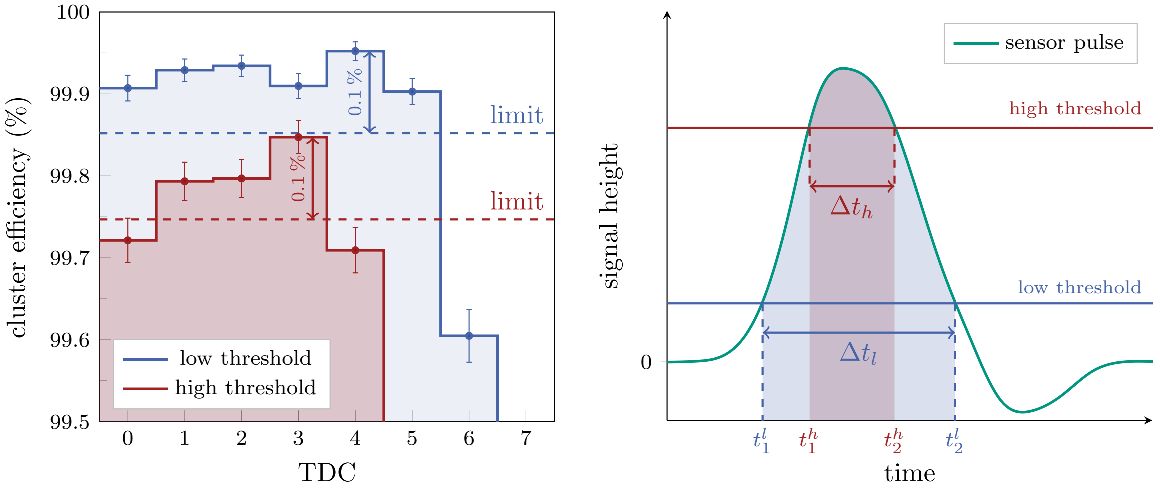

(a) TDC binned cluster efficiency and TDC cut limits (dashed lines) for a low and high threshold recorded with an unirradiated FZ290 sensor.

(b) Illustration of the time over threshold Δt dependence on the threshold. With increasing threshold the time over threshold decreases and correct timing becomes more important.

Figure 6.14: The beam and hence trigger at DESY are completely asynchronous with respect to the clock of the CBC. To correctly determine the particle detection efficiency the sensor pulse has to be sampled in the peak. Thus, only TDC values for which the efficiency is above 99.9 % of the maximum efficiency are accepted (a). The accepted time window is larger for small thresholds, because of a longer time over threshold, compared to high threshold operation (b).

readout. To be referenced, a track has to pass the reference plane within a given residual window around the recorded hit. Only tracks fulfilling this condition contribute to the analysis. The applied residual cuts for the reference plane in x- and y-direction are

$$\begin{aligned} |\Delta x_{\text{ref}}| &= |x_{\text{track}} - x_{\text{cl}}^{\text{ref}}| < 400\,\mu\text{m} \\ |\Delta y_{\text{ref}}| &= |y_{\text{track}} - y_{\text{cl}}^{\text{ref}}| < 200\,\mu\text{m}. \end{aligned} \tag{6.7}$$

- **TDC timing cut**: The data acquisition is not synchronized with the DESY particle beam. Thus, the trigger signals and also the pulse in the analog front-end of the CBC has an arbitrary phase with respect to the sampling time of the CBC. To ensure that the CBC samples the peak of the charge pulse an additional timing cut on the trigger arrival time has to be applied. This is done by using the TDC timing value, which splits the 25 ns clocking period into eight slices. Depending on the threshold and sensor bias voltage the accepted TDC values change. For every run the accepted TDC values were chosen individually by the following algorithm. First the cluster efficiency η_{cl} is evaluated for each individual TDC value and the maximum of all TDC values determined. All TDC values for which the cluster efficiency $\eta_{\text{cl}}(TDC)$ is equal or larger than 99.9 % of the maximum contribute to the analysis:

$$\eta(TDC) \geq 0.999 \cdot \max \eta(TDC). \tag{6.8}$$

By choosing 99.9 % the uncertainty of the TDC timing on the cluster efficiency is limited to 0.1 % which is of the same order as the statistical uncertainties of the measurement. Figure 6.14 illustrates the need for the timing cut (b) and shows the dependence of the cluster efficiency on the TDC value for a low and high threshold measurement (a).

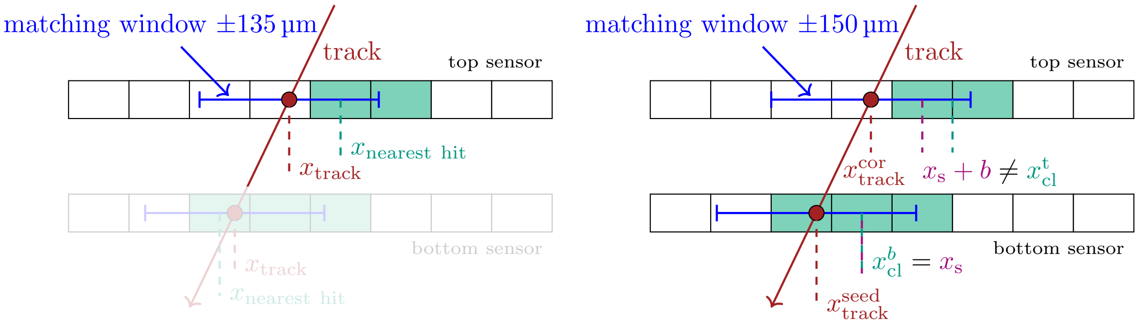

(a) Cluster matching **(b)** Stub matching

Figure 6.15: Illustration of the cluster (a) and stub matching procedure (b). For each individual DUT a track matches a cluster if its distance to the nearest hit of a cluster is less than 135 µm. A track matches a stub if its position on the seed layer $x_{\text{track}}^{\text{seed}}$ is closer than 135 µm to the stub position x_{s} and the position on the correlation layer $x_{\text{track}}^{\text{cor}}$ is closer than 135 µm to $x_{\text{s}} + b$ were b is the stub bend. Since b is in full strips, $x_{\text{s}} + b$ must not be the cluster position in the correlation layer x_{cl}^{t} but can be half strip off.

- **Spatial cuts:** The acceptance window of the telescope and reference plane covers an area larger than the sensitive area of the DUTs. Furthermore, the region in between the sensors of one layer in the Mini Module is insensitive for particle tracks. Thus, the spatial dimensions of the DUT has to be taken into account to select the tracks. Only tracks that pass the DUT within its active region are accepted for the analysis. The spatial cuts on the track in the local frame of the DUT[3] are:

$$\begin{gathered} -5.715\,\text{mm} < x_{\text{track}} < 5.715\,\text{mm} \\ -24\,\text{mm} < y_{\text{track}} < 24\,\text{mm}. \end{gathered} \tag{6.9}$$

  The cuts are given by the size of the active region of a baby sensor which is $11.43 \times 48\,\text{mm}^2$.

- **Strip masking:** There are two classes of strips that have to be masked for the analysis. On the one hand, hot strips have already been masked in the cluster selection step so that no hits from such strips enter the analysis. On the other hand, strips with an broken bond connection will not detect any hits from the sensor. All tracks pointing on such strips are rejected. In particular, the distance of the track position x_{track} to the center of the masked strips x_{strip} has to be at least half the strip pitch:

$$|x_{\text{strip}} - x_{\text{track}}| > 45\,\mu\text{m}. \tag{6.10}$$

Track-Cluster Matching

Figure 6.15a illustrates the track-cluster matching condition. A track is matched if the distance Δx of the extrapolated track position on the DUT x_{track} to the nearest hit of a recorded cluster $x_{\text{nearest hit}}$ is smaller than 135 µm:

$$|\Delta x| = |x_{\text{track}} - x_{\text{nearest hit}}| < 135\,\mu\text{m}. \tag{6.11}$$

The matching of the nearest hit and not of the cluster center is necessary to accept large asymmetric clusters generated by δ electrons. Depending on its release angle, the δ can generate

---

[3] the origin of the frame is located in the center of the sensor

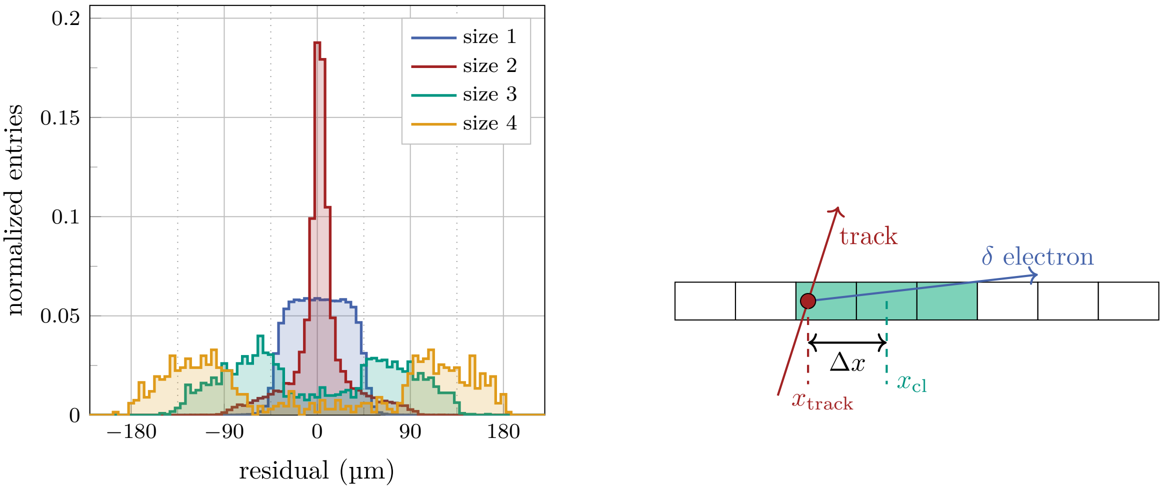

(a) Normalized residual distribution **(b)** Effect of δ electrons

Figure 6.16: Normalized residual distribution of clusters for different cluster sizes. The measurement was performed using an unirradiated FZ290 sensor and vertically inclined tracks (a). The majority of the clusters with size three and larger are dislocated from the track position and mainly generated by δ electrons. The residuals for such clusters accumulate in regions with a width of approximately 90 µm (pitch). The center of the accumulation region equals the expectation for radiated δ as illustrated in (b). E.g. for clusters of size three, $|\Delta x|$ accumulates in the range of 45 µm to 135 µm.

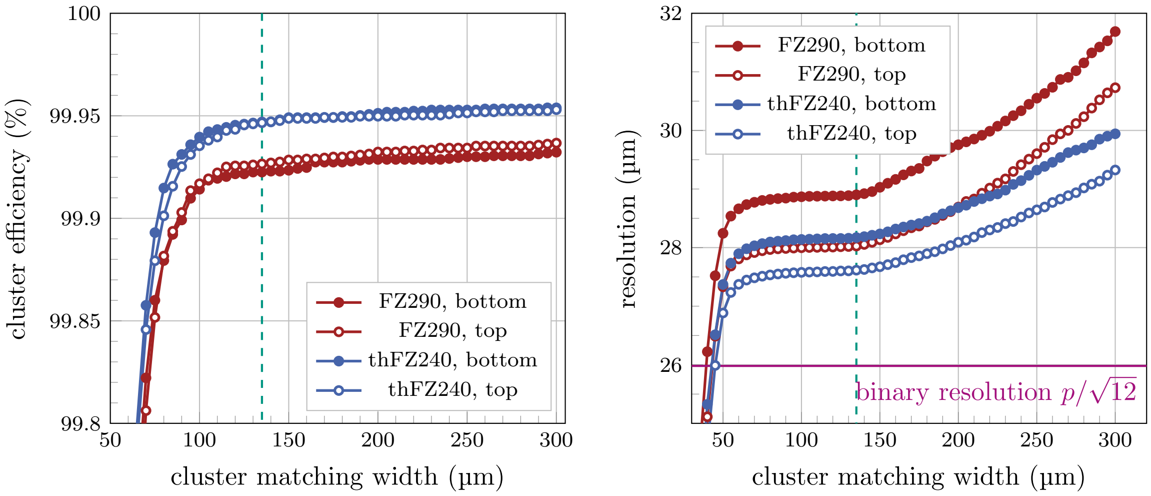

(a) Cluster efficiency **(b)** Resolution

Figure 6.17: Cluster efficiency (a) and resolution (b) for a scan over the cluster matching width. The measurement was performed with the unirradiated MiMo1 at 400 V bias voltage and a threshold of 33 Vcth for vertically inclined tracks. The chosen cluster matching width of 135 µm (dashed green line) is a trade-off between the cluster efficiency and resolution of the DUTs.

very large cluster asymmetric to the primary particle interaction point. For vertically inclined tracks the majority number of clusters with more than two strips are dislocated from the incident position as shown in figure 6.16.

The cluster matching width of 135 µm was chosen for several reasons. On the one hand, it is exactly one and a half times the strip pitch. That means the track is matched as long as it hits a strip next to a recorded cluster. On the other hand, figure 6.17 shows the DUT efficiency and resolution dependence on the cluster matching width. A value of 135 µm is a good trade-off between minimizing the resolution and maximizing the efficiency. The efficiency increases with the matching width, but saturates in the range from 120 µm to 150 µm. If the matching width is larger, the resolution decreases, since than cluster further away from the track begin to contribute the residual distribution.

6.5.9 Stub Analysis

The stub analysis follows a similar approach like the cluster analysis. One major difference is that a stub needs information from two sensor layers, or two DUTs. Thus, the stub performance parameters refer to a stack of sensors made of the same material. Furthermore, some of the selection criteria on the tracks have to be adopted slightly. The following list sums up the differences:

- **Reference plane residual cut**: This cut is not changed.
- **TDC timing cut**: For the stub analysis the same TDC values were accepted as for the cluster analysis to make the results of the same runs comparable.
- **Spatial cuts:** Since the hit information of two DUTs is necessary to generate a stub, the extrapolated track has to hit *both* DUTs within the acceptance window. The acceptance window in the local frame of each DUT remains the same.
- **Strip masking**: For the strip masking again both DUTs of a sensor stack have to be considered. Only these tracks are accepted which neither hit a masked strip in the seed nor in the correlation layer. Again the acceptance cut around the strip center is the same as for the cluster analysis. Furthermore, a number of additional strips had to be masked. The CBC3.0, which equips the Mini Modules, has a known bug in the stub finding logic. For five stub positions it creates corrupted stub information. The stub position depends on the cluster center in the lower sensor layer. Thus, tracks hitting one of the affected strips in the *seed sensor layer* were rejected for the analysis. The bug was fixed for the newer versions of the CBC.

Track-Stub Matching

In contrast to the cluster-track matching for the stubs one has to choose another approach. Figure 6.15b illustrates the implemented stub matching procedure. The stub finding algorithm in the CBC performs a clustering in both sensor layers. The stub position x_s corresponds to the cluster center in the seed layer and has half strip resolution. The bend b is the offset between the cluster centers of the seed and correlation layer. The configuration was such that stub bends returned in steps of full strips. Adding the bend value b to the seed position gives the position of the best estimation of the cluster center in the correlation layer $x_\mathrm{s} + b$. Due to the configured full strip stepping of the bend the reconstructed cluster position in the correlation layer can be half strip off the real cluster position (see figure 6.15b).

Since no information about the cluster width is known, the matching to the reconstructed particle tracks has to be performed on the stub position. Furthermore, not only the stub position but also the stub bend has to be taken into account. A track only matches a stub if the stub seed *and* the stub position in the correlation layer are within 150 µm around the corresponding track positions on the seed $x_{\text{track}}^{\text{seed}}$ and correlation sensor $x_{\text{track}}^{\text{cor}}$:

$$|\Delta x_{\text{seed}}| = |x_{\text{track}}^{\text{seed}} - x_{\text{s}}| < 150\,\mu\text{m} \quad \text{and} \quad |\Delta x_{\text{cor}}| = |x_{\text{track}}^{\text{cor}} - (x_{\text{s}} + b)| < 150\,\mu\text{m} \tag{6.12}$$

7

The High Rate Test Setup and Methods

The first part of this thesis focuses on the identification of the best suitable sensor material for the 2S modules. The second part investigates the 2S module readout chain in more detail. Common laboratory-based measurements (e.g. with ^{90}Sr sources) and beam tests do not stress the readout of the 2S module. The trigger rates for this kind of experimental setups are in the order of $\mathcal{O}(10\,\mathrm{kHz})$. This is far below the expected average trigger rate of 750 kHz during the high-luminosity operation of the LHC. In addition, the particle flux is much lower compared to the real operation in the future Outer Tracker. To test if the 2S module readout chain works correctly at high rates a test system that provides arbitrary trigger rates of up to 40 MHz and with full control over the hit injection is required.

This chapter introduces a laboratory-based high rate test setup to stress the limitations of the 2S module readout chain. Furthermore, it describes simulations of the CMS detector carried out using the CMS Software (CMSSW) package. Based on the results of the simulation the 2S module readout chain was tested with realistic input data.

7.1 The KArlsruhe High RAte TEst Setup

The initial KArlsruhe High RAte TEst (KARATE) setup was developed by Stefan Maier [Mai19] to test the CBC on its high-rate performance in the laboratory. The setup injects programmable hit patterns at 40 MHz into 48 front-end channels of the CBC. In the scope of this thesis the setup has been extended to test the full 2S module readout chain. The new focus of KARATE is the investigation of the interplay of the CBC, the CIC, the GBTx and the Versatile Link Transceiver (VTRx) using realistic hit occupancies and trigger rates.

7.1.1 The KARATE Hardware

The signal generation part of KARATE was not changed during the upgrade of the setup. Thus, its components and working principle is only outlined briefly. For more information see [Mai19].

Figure 7.1 illustrates the working principle of KARATE. The KARATE hardware is divided into two parts: the injector and the receiver part. The injector is responsible for the signal generation. An FC7 injector board initiates the pulse injection into 48 channels at 40 MHz bunch crossing rate. To separate the injector part galvanically from the receiver, 48 fast LEDs transform the electric pulses from the FC7 into light pulses. An external bias voltage pre-loads the LEDs to increase their rise time and light intensity. Plastic optical fibers guide the light pulses to the receiver part of KARATE. There an array of 48 photodiodes converts the light pulses back into electric pulses. The electric pulses are then injected into the analog front-ends of two CBCs.

There are two ways to vary the injected pulse height. On the one hand, the pre-load bias voltage adjusts the intensity of the LEDs. On the other hand, for each individual injection the pulse length can be adjusted. A longer pulse length results in a higher injection signal.

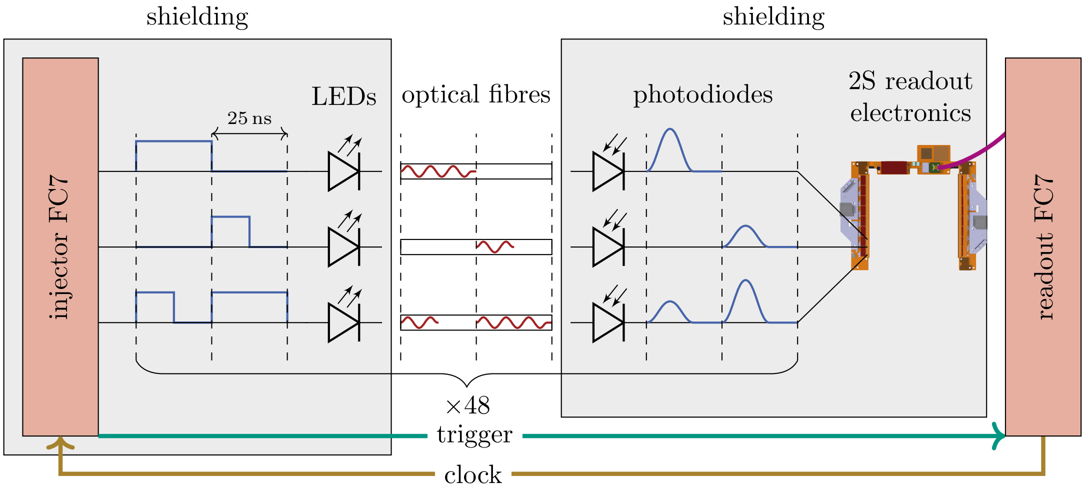

Figure 7.1: Sketch of the working principle of the KARATE setup. An FC7 injector board injects hit patterns with programmable pulse length at 40 MHz into 48 injection lines. Electrical isolation of the injector and analog front-ends on the receiver side guarantees the galvanic separation of the two parts. LEDs convert the signals into light pulses. Optical fibers guide the light pulses on photodiodes of the receiver, which convert the pulses back into electric signals. The signals couple into the analog front-end of 48 readout channels distributed over two CBCs. A common 40 MHz clock domain synchronizes the FC7 boards. The injector FC7 triggers the readout of the readout FC7. Illustration following [Mai19].

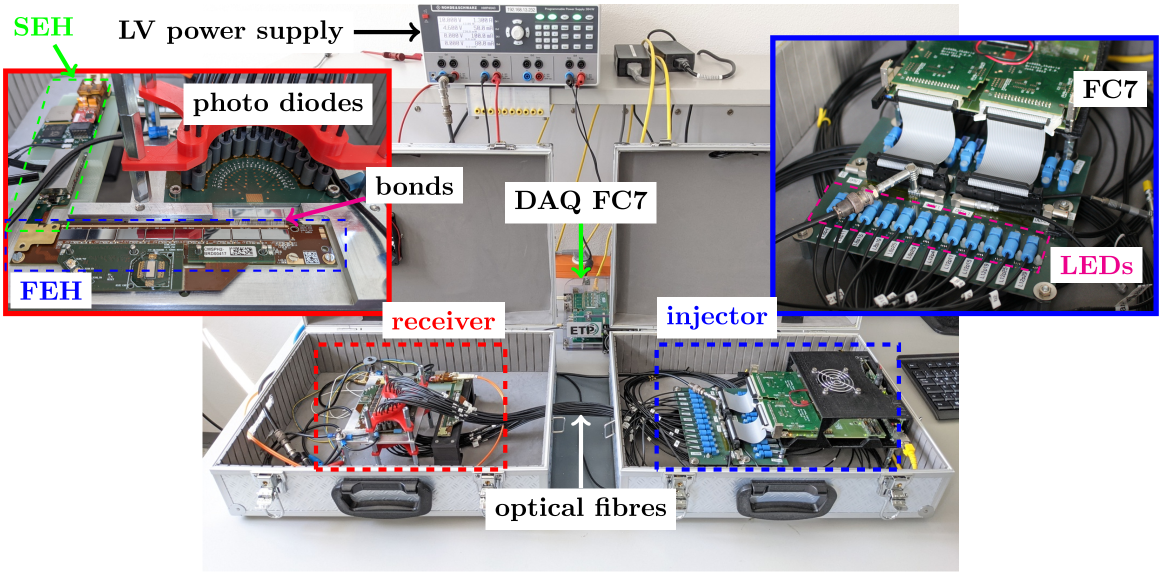

Figure 7.2: Picture of the KARATE setup. The injector consists of 48 LEDs. An FC7 board initiates LED pulses of a programmable length at 40 MHz. On the receiver side photodiodes convert the light pulses back into electrical signals. This guarantees a galvanic separation of the injector and receiver. Wire bonds connect the photodiodes with the front-end hybrid (FEH). The 2S module readout chain furthermore consists of a second FEH and a service hybrid (SEH). A second DAQ FC7 records the data from the readout chain via an optical connection. A low voltage (LV) power supply powers the readout system and provides the LED pre-load voltage.

The attached readout electronics comprise all components of the 2S module readout chain. The first stage are two front-end hybrids of which each comprises eight CBCs. The CBCs are of the final version 3.1. To each front-end hybrid an additional mezannine card with one CIC version 2.0 is attached. The CIC concentrates the data from the eight CBCs and distributes clock signals and fast commands. Both front-end hybrids are connected to one service hybrid version 3.1, which was developed in Aachen, Germany. This version of the service hybrid houses components to power and read out all parts of the 2S module. Two components are of importance for the readout. On the one hand, the GBTx, which serializes the two data streams from and to the CICs, and on the other hand, the VTRx, which transmits the serialized data stream via an optical fiber to the FC7 readout board. More information about the components of the 2S module readout chain were presented in chapter 5. Figure 7.2 displays a picture of the KARATE setup.

The 48 injection channels of KARATE instrument two CBCs of one front-end hybrid. In particular, the last 24 readout channels of the first CBC and the first 24 channels of the second CBC are connected to the receiver photodiodes. In the 2S modules the readout channels connect to the upper and lower sensor layer in an alternating manner. A fold-over of the hybrids enables the connection to the lower sensor. Thus, half of the injection channels connect to the pads on the top and half to the pads on the bottom side of the hybrid. By instrumenting two adjacent CBCs in their contact region also the functionality of the stub information sharing between them can be tested.

However, to stress the full readout chain both front-ends have to detect hits. To generate signals in the second front-end hybrid, the trimming offsets of a programmable number of channels are changed in such a way that the channels' baseline is raised above the threshold. By doing so, these channels will generate hits for every triggered event.

The readout FC7 injects its internal 40 MHz clock into the injector FC7. The common clock domain synchronizes the two boards. Futhermore, the injector FC7 is responsible for triggering. A dedicated trigger connection from the injector to the readout FC7 initiates the readout.

7.1.2 The Injector Firmware

The *injector firmware* is unchanged from Maier [Mai19]. The firmware stores up to 8×10^6 patterns in the internal DDR3 RAM of the FC7. Each pattern represents one clock cycle and comprise 256 bits. One trigger bit in the first word (32 bits) of the pattern initiates the emission of a trigger signal for the readout electronics. The following six words encode the pulse lengths in four bits for each of the 48 injection channels. The programmable pulse lengths vary between 0 ns to 46.875 ns in steps of 3.125 ns. The pattern finishes with an empty word.

There are two operation modes of the injector. In loop mode the injector loops through the pattern list continuously until it receives a stop command. This mode is mainly used for calibration purposes. The burst mode loops through the pattern list for a programmable number of iterations and then stops the injection. This mode is essential for the high-rate measurements conducted with the KARATE setup, since it guarantees synchronized data between injection and acquisition.

7.1.3 The Readout Firmware

The *readout firmware* is the standard 2S module readout firmware with some minor changes. One change is the extraction of the internal 40 MHz clock to synchronize the injector and readout FC7. The other change is the implementation of the orbit reset (BC0) emission by the FC7 readout board. The BC0 resets the level-1 trigger counters (L1ID) of the readout

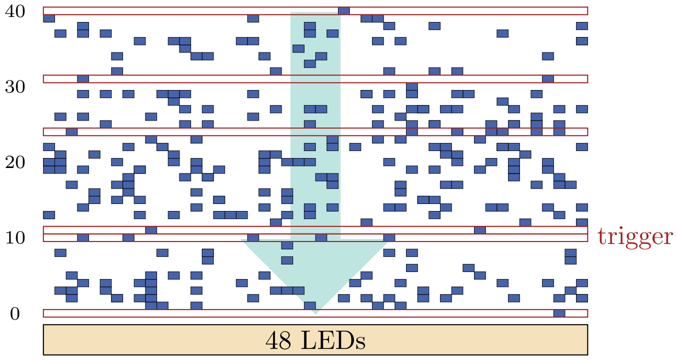

Figure 7.3: Sketch of the KARATE pattern injection. For each bunch crossing (row) the pattern defines which of the 48 injection LEDs emit a light pulse (blue rectangles) and whether the readout is triggered (red box) or not. The length of the light pulse is a 4 bit programmable value and adjusts the injected signal height on the receiver side.

chips. During the operation in the HL-LHC the BC0 will be emitted with the orbital frequency $f_O = 11.2455\,\text{kHz}$ in the orbit gap (every 3564 bunch crossings) [Tay02].

The firmware emits the BC0 fast command with a delay of m clock cycles after every n triggers. The values of m and n are configurable in the settings file, and were set to $m = 3$ and $n = 500$ for the measurements presented in this thesis. This change was necessary to properly operate the combination of CIC and CBCs. The CIC L1ID value of 511 is reserved for an error code. Thus, to ensure the correct operation of the CIC the value should never become 511. The BC0 emission every $n = 500$ trigger ensures the reset of the L1ID in time. The recovery of the CBC's L1ID after the BC0 requires one clock cycle. If a trigger rises during the recovery, the L1ID from the CBC will be one value off. Thus, the reception of a trigger signal in the same clock cycle or one after the BC0 corrupts the L1ID counting of the CBC. The shifted L1ID de-synchronizes the data stream, since the CIC matches the wrong CBC events with its own L1ID. The de-synchronization lasts until the readout receives another BC0 or fast reset. For this reason the delay m was implemented. For the high-rate measurements the pattern generation must guarantee that the injector does not send forbidden BC0 and trigger combinations.

7.1.4 The KARATE Software and Pattern Generation

The *KARATE software* was developed on top of the Ph2_ACF. It includes additional tool classes to steer the data acquisition, to program the injector board and to generate the injection pattern.

To generate an input pattern, the KARATE software generates the raw data pattern and stores it in the internal storage of the injector FC7. The pattern itself strongly depends on the measurement. For every clock cycle the pattern generator decides in which channels signals are injected, the length of the pulses and whether the readout is triggered or not. Figure 7.3 illustrates the pattern list injection of KARATE.

However, there are some checks which have to be performed on all patterns. On the one hand, the *BC0 trigger check*. As mentioned before, one cannot trigger the CBC in same or one clock cycle after a BC0 reset. Since the position of the BC0 reset in the pattern list can be calculated using m and n, the check prevents adding triggers for forbidden clock cycles. Furthermore, the injector runs i times through the pattern list. To prevent running into the BC0 issue over all iterations the number of triggers in the pattern list must be a multiple of

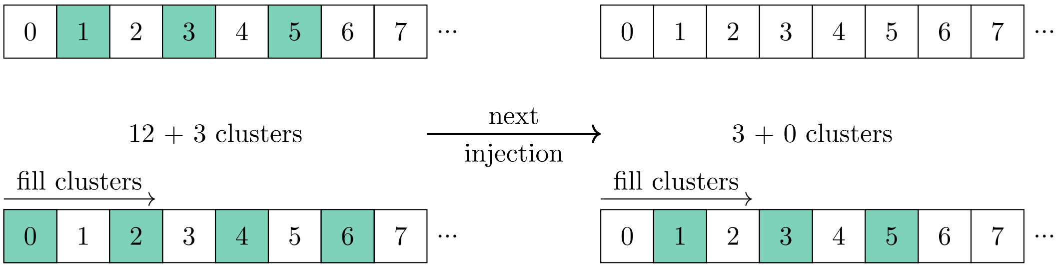

Figure 7.4: Pattern generation for the cluster injection. Green boxes represent channels with signal injection. For each clock cycle the algorithm receives the number of clusters n_{cl} to be injected. It creates clusters of width one with a gap of one channel. The filling starts in the lower layer, and continues after 12 clusters in the upper layer with one strip offset. The position of the first cluster in the layers alternates by one strip for every injection. The maximum number of clusters injectable by KARATE in one event is 24.

the BC0 separation $n = 500$. If there are more triggers in the pattern lists the check method cuts off the end of the list so that the condition is fulfilled.

Another check is the *CBC buffer overflow protection*. As the names suggests, it prevents the CBC's readout buffer from an overflow. In particular, for very high and non-constant trigger rates of the order of $\mathcal{O}(1\,\mathrm{MHz})$ the check is of importance. Section 11.4 describes the investigation of the CBC buffer overflows and the implementation of the buffer overflow protection algorithm more in detail.

A critical parameter regarding the data bandwidth of the 2S modules is the number of clusters in an event. Thus, the KARATE software includes a method to inject a given number of clusters per bunch crossing. Figure 7.4 illustrates the cluster pattern generation. For a given number of clusters n_{cl} in one injection pattern (event) the algorithm starts to fill the clusters from one side of the equipped channels, starting with the lower and then the upper layer. The start position of the filling for each layer alternates every injection by one strip to reduce the influence of possible crosstalk and afterglow of the signal pulses. However, the configuration of KARATE with its 48 injection channels limits the maximum number of clusters per event to 24. If a measurements requires more than 24 clusters, a static number of additional noise clusters are generated by changing the trimming offsets of non-equipped channels. This is also the procedure to generate clusters in the second front-end to fill the bandwidth. The filling and trigger strategy on top of this algorithm will be explained for each individual measurement.

7.2 KARATE Run Analysis

For every run the KARATE software stores the injected pattern and recorded events in a common ROOT data file. Thus, the analysis does not have to be performed on the fly but can be done offline using the data files. The most important feature for the signal injection with KARATE is the pattern list. The pattern list contains all information about the channel injections and the corresponding pulse lengths. Futhermore, it comprises the trigger decision. Thus, for each clock cycle the true information of the expected hits is known. The KARATE analysis compares the injection pattern (true data) with the recorded hits. By doing so it determines the detection efficiency and checks the correct functionality of the on-module electronics. Since the pattern list includes the injection patterns for every clock cycle, not only the triggered information are known but also the injected pattern for all non-triggered clock cycles. As a result the analysis can also search for correlations in the non triggered events.

The following list defines strategies and observables which will be frequently used to explain the results of the measurements with KARATE:

- **Error handling:** The KARATE setup focusses on stressing the 2S module readout chain. Thus, the measurements bring the components to or beyond their design limits. Stressing the limits will cause errors. If an event contains an error flag, the validity of its data is not guaranteed. Thus, all events including at least one error flag are treated as inefficient.
- **Fake, noise and latched hits:** Fake hits are all hits which were detected by the readout but not injected by KARATE. There are different causes for fake hits. One cause are latched hits by time-walk effects. If there was an injection in the same channel a bunch crossing before the trigger, the afterglow of the pulse can cause a hit in the triggered event. Those kind of fake hits are counted as latched hits. All other fake hits are noise hits. Noise hits do not correlate with a previous injection in the same channel. In general the number of fake hits N_f^h is the sum of the noise hits N_n^h and the latched hits N_l^h:

  $$N_\mathrm{f}^\mathrm{h} = N_\mathrm{n}^\mathrm{h} + N_\mathrm{l}^\mathrm{h}. \tag{7.1}$$

  Figure C.13 displays an example of the time correlation of fake hits with the previous and following injections into the same channel.
- **Missed and dipped hits:** Missed hits are all hits for which a signal was injected, but which were not detected by the readout. One effect of the signal injection is a slight undershoot of the baseline for about four clock cycles after a preceding injection. If there is another pulse injection during the undershoot, the shifted baseline lowers the full pulse amplitude, and hence reduces the detection probability for these kind of injections. All missed hits in the undershoot are dipped hits. This includes all missed hits up to four clock cycles after the last injection in the same channel.
- **Hit efficiency:** The hit efficiency η_h for one run with fixed configuration is defined as

  $$\eta_\mathrm{h} = \frac{N_\mathrm{inj}^\mathrm{h} - N_\mathrm{missed}^\mathrm{h}}{N_\mathrm{inj}^\mathrm{h}} = 1 - \frac{N_\mathrm{missed}^\mathrm{h}}{N_\mathrm{inj}^\mathrm{h}}, \tag{7.2}$$

  where $N_\mathrm{inj}^\mathrm{h}$ is the number of injected hits and $N_\mathrm{missed}^\mathrm{h}$ the number of missed hits in the run.
- **Cluster matching:** The KARATE run analysis create cluster from the injected and recorded hit pattern by combining adjacent hits to clusters. A recorded cluster matches an injected cluster if the seed strip of the injected was detected. The seed strip is the strip with the longest pulse length of the cluster.
- **Missed clusters** are all injected cluster which were not matched.
- **Cluster efficiency:** The cluster efficiency η_cl for a run with fixed configuration is

  $$\eta_\mathrm{cl} = \frac{N_\mathrm{inj}^\mathrm{cl} - N_\mathrm{missed}^\mathrm{cl}}{N_\mathrm{inj}^\mathrm{cl}} = 1 - \frac{N_\mathrm{missed}^\mathrm{cl}}{N_\mathrm{inj}^\mathrm{cl}}. \tag{7.3}$$

  It includes the number of injected clusters $N_\mathrm{inj}^\mathrm{cl}$ and the number of missed clusters $N_\mathrm{missed}^\mathrm{cl}$ in that run.

For many studies it is important to scan different operation parameters, like the trigger frequency or the number of clusters per event. The combination of many runs scanning one or more parameters is called a parameter scan.

7.3 CMSSW Simulation Based Pattern Generation

The CMS Software (CMSSW) framework is a software tool to simulate and analyse data of the CMS detector. One use case for CMSSW is the simulation of the complete CMS detector from the particle collisions to the analysed high level data. It includes Monte Carlo event generators to simulate the particle collisions and determines the interaction of the emerging particles with the detector components using Geant4 [Ago+03]. Then, it emulates the signal generation and subsequent electronics. The analysis part of CMSSW can either use simulated detector signals or real signals to perform a full event reconstruction. One class of high-rate measurements carried out in the scope of this thesis uses injection patterns based on CMSSW simulations. Since CMSSW includes the geometry of the CMS detector for the HL-LHC it delivers the best possible approximation for hit patterns from particle collisions. This section presents the CMSSW simulation and modifications to extract analog hit information in the sensors of the 2S modules of the future Outer Tracker. Furthermore, it explains the data processing to extract the KARATE injection patterns to stress the level-1 data stream. Finally, it describes the pattern generation to inject analog like sensor signals extracted from CMSSW simulations by using pulse length modulations of the KARATE injector.

7.3.1 CMSSW Version and Modifications

The simulations carried out in the scope of this thesis are based on the CMSSW version tag `CMSSW_11_2_0_pre11`. It includes the tracker geometry `D66`[1] with FZ290 sensors. For each CMSSW tag the CMS simulation group generates validation samples with simulated events of standard processes. All analysis and preparation steps are based on three centrally generated validation samples: Two samples with 10 000 minimum-bias events at average pileup 140 and 200 for the expected background activity from the particle collisions and one set of 10 000 $t\bar{t}$ events without pileup. The standard implementation of the 2S module readout in CMSSW includes binary data acquisition. Thus, it does not store the information about the height of the charge signals generated in the silicon sensors. To extract the analog charge signals of the silicon sensors the digitization process of CMSSW was modified. The modification includes the extraction of the simulated analog charge signals with the corresponding sensor IDs and strip rows and columns into a ROOT file for every single event of the simulation run. The data preparation for KARATE uses this information as a starting point.

7.3.2 Analysis and Data Processing of the Simulation Data

To simulate pileup CMSSW mixes minimum-bias events with signal events (e.g. $t\bar{t}$ events). In the simulation process of CMSSW the pileup mixing is performed after the digitization step. Thus, all events extracted by the modified digitizer only contain one minimum-bias or $t\bar{t}$ event without pileup. The first step of the data processing is the pileup mixing. For pileup n the analysis randomly superimposes n minimum-bias events and one $t\bar{t}$ event. By superimposing multiple events, it is possible that there are multiple charge deposition by different no-pileup events in the same sensor strip. Thus, the data processor aggregates multiple hits in the same

---

[1] https://github.com/cms-sw/cmssw/tree/CMSSW_11_2_0_pre11/Geometry/TrackerNumberingBuilder, TK-layout tag `OT800_IT615`

strip, by summing up multiple charge depositions. A clustering algorithm gathers adjacent hits of the same sensor column (1016 strips) to clusters.

The CMSSW simulations yield the charge depositions in the strips of the individual strip sensors. However, one 2S module comprises two sensors. To obtain module-level information the analysis combines the hit information of the two sensor layers which belong to the same module. Furthermore, the module readout is divided into two front-ends, each comprising one CIC and eight CBCs. One front-end reads out one strip column of each sensor (2×1016 strips on top of each other). Thus, the analysis groups the modules into two front-ends by combining hits from the same strip column to extract front-end related information.

To increase statistics the analysis makes use of the symmetries in the cylindrically shaped CMS Outer Tracker. In particular, the symmetries used in this analysis are the following:

- The **barrel** layers are symmetric for rotations around the beam axis (φ symmetry). Thus, sensors on the same barrel layer (radius r) and $|z|$ position along the beam axis see the same particle flux.

- The **endcap** disks are also symmetric for rotations around the beam axis. Sensors installed on the same disk and ring have a common $|z|$ and r symmetry.

By using these symmetries the 2S modules equip in total 61 different r and $|z|$ locations in the CMS experiment. Tables C.1 and C.2 list the different symmetric 2S module locations and the position encoding. Positions 0 to 24 belong to the modules in the endcaps and positions 25 to 60 belong to the modules in the barrel. Figure 13.2 displays a map of the tracker with the corresponding module positions.

This section presents different outcomes of the analysis of the CMSSW data. For reasons of clarity the plots only refer to two representative positions, one for the barrel and one for the endcaps. For the barrel, the plots refer to the modules at position 36. The modules of position 36 are installed on the innermost barrel layer (layer 4, $r \approx 687\,\mathrm{mm}$) and at the ladder positions 12 and 13, which are the ones with lowest $|z| \approx 47\,\mathrm{mm}$. For the endcaps, the plots refer to the modules at position 20. This position represents the modules of the innermost ring (ring 8 at $r \approx 665\,\mathrm{mm}$) on the outermost disk (disk 5 at $|z| \approx 2676\,\mathrm{mm}$). These 2S modules are exposed to the highest particle flux in the Outer Tracker.

Figure 7.5a displays an example of the simulated cluster charge distribution expected for the modules on position 20. A convoluted Landau-Gaussian function fits the cluster charge distribution for signals above $15\,\mathrm{ke}^-$. The MPV of the distribution is at $22\,886\,\mathrm{e}^-$.

Figure 7.5b compares the cluster width distribution of position 20 (endcap) with position 36 (barrel). The average cluster width in the barrel is slightly larger. Furthermore, the tail to large clusters is more pronounced for the barrel modules. The main reason for this effect is the deflection of the generated electron-hole pairs in the silicon by the Lorentz force in the magnetic field of the CMS detector [Boe+02]. In the barrel the charge carriers drift perpendicular to the magnetic field and hence are deflected. The deflections smear out the clusters and increase the average cluster size. In the endcaps the charge carriers drift in parallel with the magnetic field and hence are not deflected.

Regarding the level-1 data stream of the 2S modules each front-end has a bandwidth of $320\,\mathrm{Mbit\,s}^{-1}$. On each front-end hybrid one CIC sparsifies the event data by performing a hit clustering. The event size is dynamic and depends linearly on the number of clusters per front-end (see level-1 data format of the CIC in figure 5.7). Since the bandwidth is fixed the interplay of two parameters limits the readout: the trigger rate and the number of clusters per front-end and event.

However, the number of clusters emitted by the CIC $n_{\mathrm{cl}}^{\mathrm{cic}}$ can differ from the number of hit clusters in the front-end. The reason for this is the cluster encoding of the CIC, which

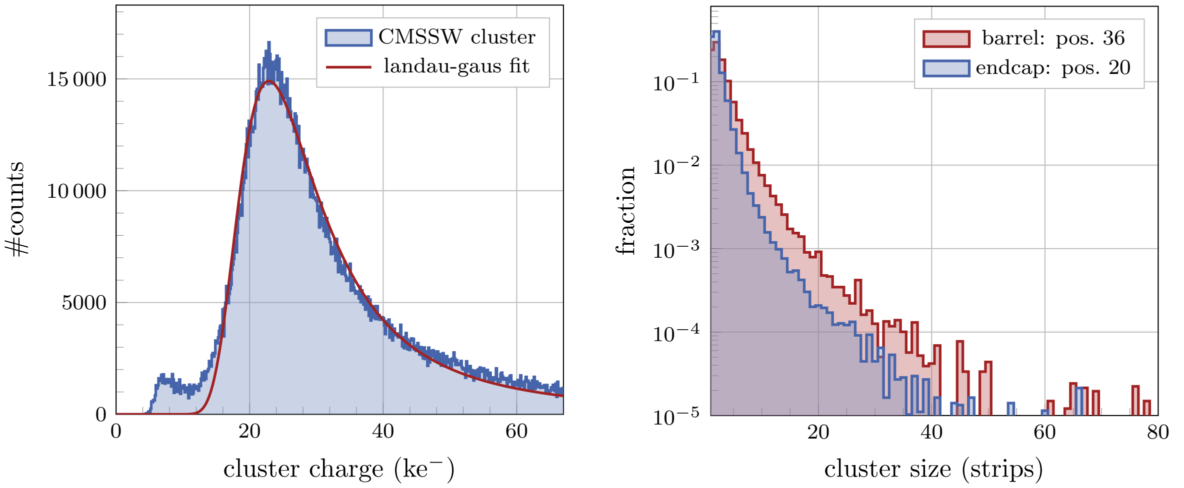

(a) Cluster charge for position 20 (endcap disk 5 ring 8)

(b) Cluster size for position 20 (endcap disk 5, ring 8) and position 36 endcap (layer 4, ladder pos. 12/13)

Figure 7.5: Example cluster charge (a) and cluster size distribution (b) based on CMSSW simulations. The MPV of the cluster charge is 22 886 e^{-}. The average cluster size in the barrel is slightly higher than for the endcaps. In the barrel the tail to large clusters is more pronounced.

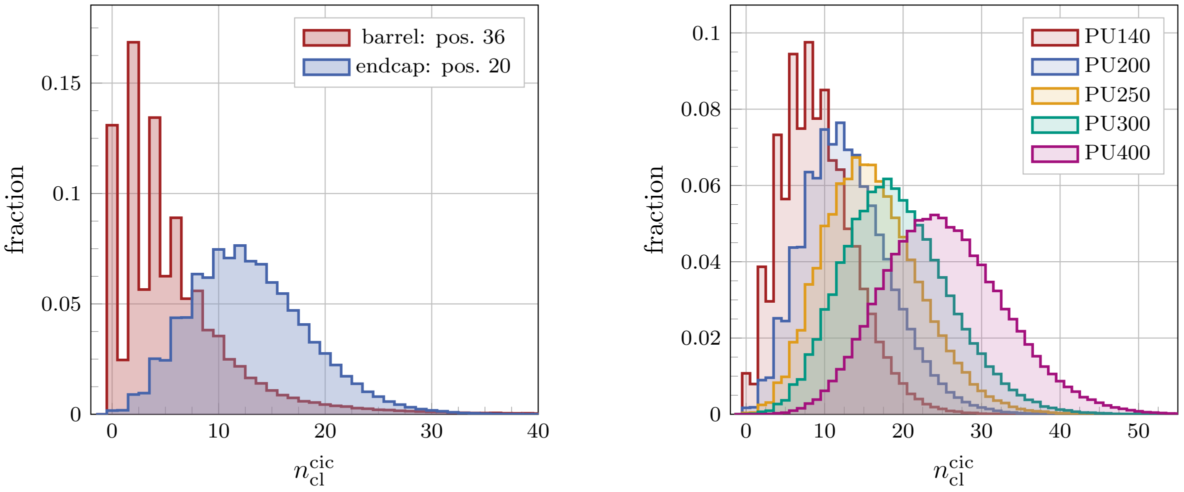

(a) Distribution of CIC clusters per front-end and event $n_{\mathrm{cl}}^{\mathrm{cic}}$ for position 20 and 36 at pileup 200

(b) Distribution of CIC clusters per front-end and event $n_{\mathrm{cl}}^{\mathrm{cic}}$ for position 20 and different pileup (PU) scenarios

Figure 7.6: CIC clusters per front-end and event distributions. (a) compares two reference positions 36 (barrel) and 20 (endcap) at pileup 200. The endcap sees a larger number of clusters since it is exposed to a higher particle flux. An even number of clusters is more likely due to the double-layer structure of the 2S modules. (b) displays the distributions in the endcap reference position for different pileup values. Higher pileup increase the number of clusters and reduces the excess for even numbers of clusters.

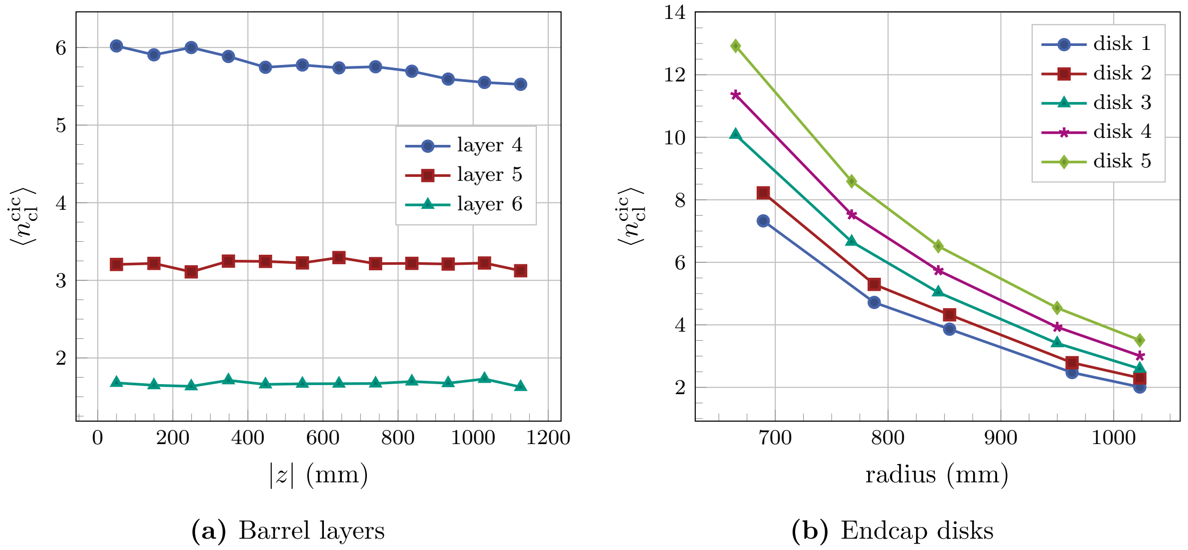

(a) Barrel layers

(b) Endcap disks

Figure 7.7: Average number of CIC clusters per front-end and event $\langle n_{\mathrm{cl}}^{\mathrm{cic}} \rangle$ for all 2S module positions. In the barrel (a) the number of clusters decreases with increasing radius (decreasing layer number) and there is only a small $|z|$ dependence of $\langle n_{\mathrm{cl}}^{\mathrm{cic}} \rangle$ for the innermost layer 4. In the endcaps (b) $\langle n_{\mathrm{cl}}^{\mathrm{cic}} \rangle$ increases with $|z|$ (disk number). The modules which see the highest number of particles equip the innermost ring of the outermost endcap disk (position 20).

limits the maximum encodeable cluster size to eight strips. If a hit cluster extends over more strips, the CIC splits the cluster every eight strips. As shown in figure 7.5b, the number of clusters larger eight or even larger 16 is not negligible. Thus, the splitting-induced increase of the number of clusters has to be taken into account for the level-1 bandwidth studies. In the following CIC clusters are all clusters emitted by the CIC and hence filling the bandwidth.

Figure 7.6a compares the distribution of the number of CIC clusters per front-end and event for the reference positions in the barrel and endcap. The modules in the endcaps see a far higher number of clusters. In addition, a particle passing a 2S module will most likely produce two clusters in the front-end, because of the double-layer structure of the modules. Thus, an even number of clusters per front-end is more likely than an odd number. Inclined tracks, overlapping clusters and particles passing the edge or the center region of the sensors can cause an odd number of clusters. This effect is more prominent for the endcap modules, since these modules see an overall higher particle flux.

Figure 7.6b shows the influence of pileup on the number of clusters per front-end and event for module position 20 in the endcap at the nominal pileup value of 200. With increasing pileup the expected number of clusters increase and becomes more Gaussian-like distributed. The excess of even numbered clusters vanishes more and more.

Figure 7.7 summarizes the average number of clusters per front-end and event $\langle n_{\mathrm{cl}}^{\mathrm{cic}} \rangle$ for all module positions in the barrel and endcap. The average number of clusters decreases with the radius (increasing layer number in the barrel). Furthermore, it is almost constant for the different $|z|$ positions of one layer in the barrel. Only for the innermost layer 4, the average number of clusters slightly decreases with $|z|$.

In the endcaps $\langle n_{\mathrm{cl}}^{\mathrm{cic}} \rangle$ increases with $|z|$ (disk number) and for lower radii. The endcap modules which see most clusters are installed in the innermost ring on the outermost disk (position 20).

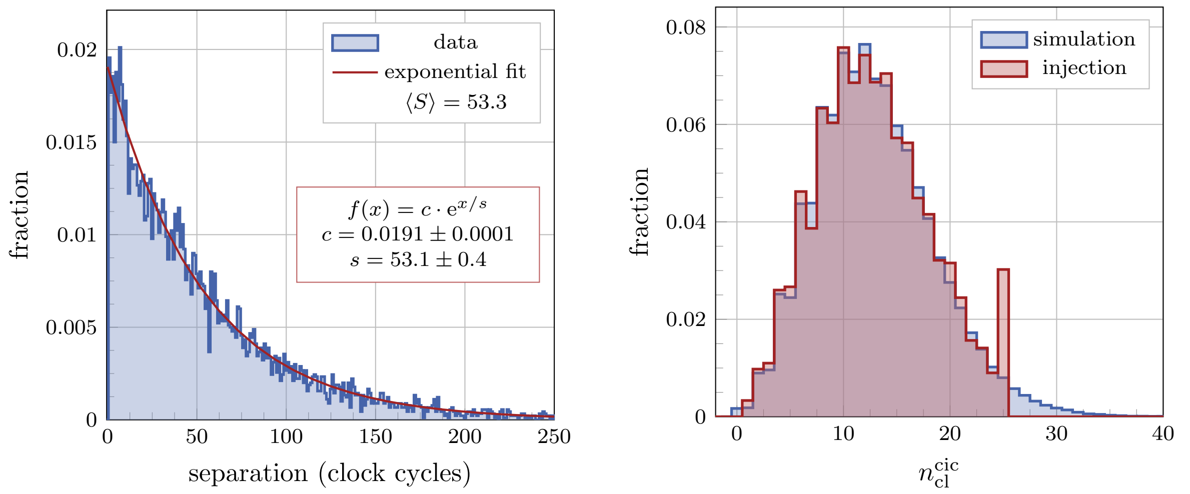

(a) Normalized injected trigger separation and exponential fit

(b) Normalized simulated and injected cluster distribution

Figure 7.8: For a fixed trigger probability the trigger separation (a) follows an exponential function, where the parameter s in the exponent is the average trigger separation. Simulated and injected cluster per front-end and event distribution (b). KARATE cannot inject more than 24 clusters at once. Clusters exceeding this value are latched in the next event. Additional noise channels add a constant number of clusters to each event (in this case one) to shift the range of possible cluster injections.

7.3.3 CMSSW Cluster Injection Pattern

The number of CIC clusters per front-end and event $n_{\mathrm{cl}}^{\mathrm{cic}}$ in combination with the available level-1 data bandwidth limit the maximum accepted trigger rate. The time to read out one event is

$$t = \frac{\text{event size}}{\text{bandwidth}} = \frac{52\,\text{bits} + n_{\mathrm{cl}}^{\mathrm{cic}} \cdot 14\,\text{bits/cluster}}{320\,\text{Mbit}\,\text{s}^{-1}}. \tag{7.4}$$

The maximum average number of CIC clusters per front-end and event is calculated by solving equation 7.4 for $n_{\mathrm{cl}}^{\mathrm{cic}}$ and using the expected average trigger rate $\langle f_T \rangle = t^{-1}$. For $\langle f_T \rangle = 750\,\text{kHz}$ the expected maximum average number of CIC clusters per front-end and event is 26.7.

However, in a realistic environment the number of clusters varies from event to event and strongly depends on the pileup. The distribution of CIC clusters per front-end and event describes the expected event-to-event fluctuations. Thus, they are the starting point for the CMSSW cluster injection pattern. The system mimics the expected data rates in the CMS detector by injecting a cluster pattern following the distributions. To prepare the pattern generation the cluster distributions were calculated for different pileup scenarios in the range between 0 and 400 and for the all module positions within the tracker.

The pattern generation itself comprises two steps. The first step is the trigger decision. For every injection pattern (or clock cycle) the pattern generator evaluates whether it is triggered or not. The probability for a physics process to occur is the same for every collision (clock cycle). Thus, also the trigger probability is fixed for each clock cycle[2]. The programmable parameter for the KARATE setup is the average trigger separation $\langle S \rangle$ in clock cycles. Then

---

[2] assuming a constant luminosity and no rules vetoing the trigger decision

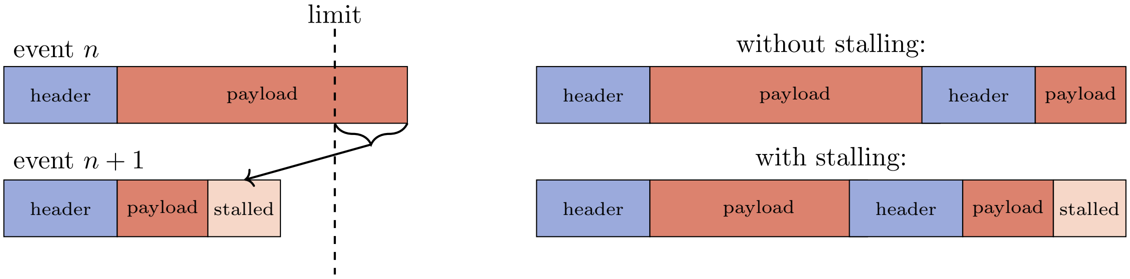

(a) Cluster stalling moves surplus clusters in the next event

(b) The effect of cluster stalling on the serialized data

Figure 7.9: Sketch of the effect of the cluster stalling. The maximum number of clusters that can be injected by KARATE in one event is 24. If more clusters have to be injected, the cluster stalling algorithm moves the surplus clusters in the next injected event (a). By doing so still the CIC has to transmit the same amount of data, but in a different order (b).

the trigger probability p is given by

$$p = \langle S \rangle^{-1}. \tag{7.5}$$

The average trigger rate is the collision rate divided by the average trigger separation:

$$\langle f_T \rangle = \frac{40\,\mathrm{MHz}}{\langle S \rangle}. \tag{7.6}$$

Figure 7.8a displays the normalized trigger separation of one run for $\langle S \rangle = 53$ ($\approx 755\,\mathrm{kHz}$). An exponential function is used to fit the histogram. The most probable trigger separation are two consecutive triggers.

The next step is the actual pattern generation. Regarding the level-1 data stream only the triggered events fill the bandwidth. Thus, KARATE only injects hit patterns in triggered events. Furthermore, the injection pulse length is fixed since no signal modulation is required for the bandwidth studies. For every triggered event the number of injection clusters has to be determined. This is done by generating a random number with respect to the simulated CIC clusters per front-end and event distributions for the given module position and pileup. As mentioned before, the KARATE setup can inject up to 24 clusters at once. However, the number of injected clusters can exceed 24 (see figure 7.6a). To reduce distortions of the injected cluster distribution two correction strategies have been implemented.

On the one hand, an additional static number of clusters adds to the injected distribution, by changing the trimming offsets. To still have the best possible dynamic range, the number of noise induced cluster n_{cl}^{n} is given by

$$n_{\mathrm{cl}}^{n} = \begin{cases} 0, & \text{for } \langle n_{\mathrm{cl}}^{\mathrm{cic}} \rangle \leq 12. \\ \lfloor \langle n_{\mathrm{cl}}^{\mathrm{cic}} \rangle - 12 \rceil, & \text{otherwise.} \end{cases} \tag{7.7}$$

If $\langle n_{\mathrm{cl}}^{\mathrm{cic}} \rangle$ is less or equal twelve there will be no noise induced clusters filling the bandwidth. This guarantees the possibility to inject zero clusters. Otherwise, the algorithm adds the rounded average number of clusters minus 12 additional noise-induced clusters. The number of injected clusters $n_{\mathrm{cl}}^{\mathrm{inj}}$ is then the calculated random number minus $n_{\mathrm{cl}}^{\mathrm{n}}$. The algorithm guarantees a symmetric injection window around $\langle n_{\mathrm{cl}}^{\mathrm{cic}} \rangle$.

However, this does not prevent $n_{\mathrm{cl}}^{\mathrm{inj}}$ to exceed 24. Since KARATE cannot inject more than 24 clusters at once, the surplus clusters are stalled in the next injection. This will increase the number of injected clusters in the next triggered event. By not simply rejecting the surplus clusters, all expected clusters still have to be transmitted by the level-1 data link and fill the bandwidth. Since the CIC serializes the events in the correct historical order, stalling clusters in the next event is the best approximation to fill the serialized data stream in a similar way as without stalling. Figure 7.9 illustrates the effect of the cluster stalling on the level-1 data stream. By the cluster stalling the data payload from the stalled clusters is delayed into the next event.

Having calculated the final number of clusters to inject in the bunch crossing, the cluster filling follows the algorithm as presented in section 7.1.4.

Figure 7.8b compares a simulated cluster distribution for pileup 200 and position 20 with an exemplary injected one. One additional noise channel prevents the occurence of zero clusters. Furthermore, the maximum number of injected clusters is limited by $n_{\mathrm{cl}}^{\mathrm{n}} + 24 = 25$.

7.3.4 CMSSW Analog Signal Injection Pattern

The pulse length variation of the KARATE injector allows a channel and bunch crossing wise modulation of the injected signal amplitude in the analog front-end of the CBC. The analog signal injection makes use of this functionality. It targets the injection of realistic hit and signal patterns in the injector channels. Therefore, the pulse length amplitudes modulate with respect to the sensor charge signals which were extracted from the CMSSW simulations. In a first step the pattern generator computes a set of 2×10^6 injection patterns for every pileup scenario and module position, which then are used for the injection in the system.

Starting point for the pattern generator algorithm are the superimposed CMSSW events (after pileup generation). These include information about the signal generation in each sensor strip. A full 2S module comprise 2×2032 strips, which are far more than the 48 injection channels of the KARATE setup. Thus, the algorithm slices the modules in packs of 2×24 strips, which are suitable for the injection with KARATE. By doing so the pattern generator extracts from every module in the superimposed event 84 injection patterns from one CMSSW event. Furthermore, it makes use of the tracker symmetries to increase the statistics.

Each pattern contains the signal information for the 48 injector channels. Before the injection the pattern generator shuffles the pattern list randomly. This ensures a mixing of the pattern belonging to the same superimposed CMSSW event. The final injected pulse length then calculates with calibration factors which have to be measured individually for every injector channel (see section 11.3). For every injection the trigger decision is evaluated individually in the same way as explained in the previous section. The trigger probability p is fixed and defined by the average trigger separation $\langle S \rangle$ by $p = \langle S \rangle^{-1}$. In contrast to the CMSSW cluster injection pattern, the analog pattern injection injects pulses every clock cycle and not only for the triggered events.

Regarding the analysis of analog patterns an additional fiducial volume cut for the cluster efficiency was implemented. Since the pattern generator slices the signals of a module in chunks of 2×24 strips, it also slices clusters shared by multiple chunks. These shared clusters will contribute to different injections. As a result, the seed of such a cluster can only be in one chunk. Since the cluster matching uses the seed matching as the efficiency criterion, this effect causes efficiency losses. Thus, only clusters which are fully contained in the 24 strips of one layer contribute to the efficiency analysis. In particular, the analysis rejects all clusters that include one of the edge channels of the injection window.

Part III

Characterization of Strip Sensors and Module Prototypes

8

Sensor Preparation and Characterization

The characterization of the electrical and the charge collection properties of the sensors for 2S modules is an essential step during prototyping. The measurements are crucial to fully understand the behavior of the sensors in the final prototype modules. Furthermore, the characterization of all sensors before building a module prevents from using broken sensors or those which do not fulfill the specifications on the sensor parameters. During the upcoming production of 2S modules the characterization of the sensor parameters is a powerful tool to monitor the vendor's production process quality. Thus, these measurements take a key role in the quality control process. This chapter presents all sensor preparation and characterization steps carried out before building the prototype modules.

8.1 Irradiation and Annealing Procedures

One part of this thesis covers the investigation of the joint operation of irradiated sensors with the CBC. Thus, two sets of baby sensors were irradiated to different fluences with reactor neutrons at JSI. The target fluences were chosen based on the results of FLUKA simulations for the Outer Tracker [CMS21]. Figure 8.1 shows the result of the FLUKA simulations for the sensors of the 2S modules. In particular, it displays the fraction of sensors exposed to the corresponding fluence or less for two different HL-LHC operation scenarios. In the standard scenario the HL-LHC will collect $3000\,\mathrm{fb}^{-1}$ data. There are also plans to extend the operation to $4000\,\mathrm{fb}^{-1}$ in an "ultimate" scenario.

To take both scenarios into account the fluences for the sensor sets were chosen as follows. One set of sensors (two FZ290, two thFZ240) were exposed to $2.5 \times 10^{14}\,\mathrm{n_{eq}/cm^2}$. After the standard operation time of the HL-LHC 69.8 % of the modules will be exposed to this fluence or less. The other set of baby sensors was irradiated to $5.0 \times 10^{14}\,\mathrm{n_{eq}/cm^2}$. This is more than the maximum fluence any 2S sensor will be exposed to in the $3000\,\mathrm{fb}^{-1}$ scenario. In the ultimate scenario only 1.2 % of the sensors will see a higher fluence.

During the operation in the CMS detector the sensors will operate at about $-20\,^{\circ}\mathrm{C}$ and thus not experience annealing; however during shutdown and technical stops it could be necessary to interrupt cooling and the sensors heat up to room temperature, e.g. for maintenance reasons or to apply intentional annealing. Even though annealing has a beneficial effect on the sensor leakage current it decreases the charge collection efficiency of the sensor for long annealing times (several weeks at room temperature). The reduced charge collection efficiency impacts the particle detection performance of the modules. In the worst case scenario for the HL-LHC, which includes two weeks of annealing at room temperature per year and operation until 2040, the annealing time accumulates up to about 200 d at $21\,^{\circ}\mathrm{C}$. Thus, one sensor of each fluence was annealed to 204 d equivalent annealing time to cover this worst case scenario. However, annealing can also be beneficial and increase the sensor signal. At about 13 d equivalent annealing time the sensor signal maximizes and hence this annealing time was chosen for the other sensor of the set.

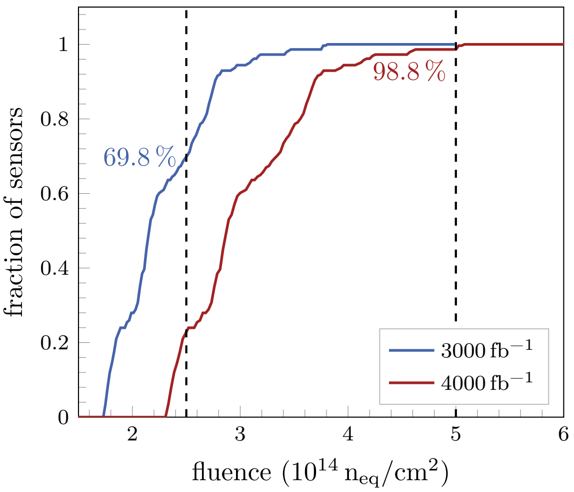

Figure 8.1: Fraction of the sensors of the 2S modules exposed to the corresponding fluence or less for two different HL-LHC operation scenarios. The two fluences for the module prototypes are marked by dashed lines. In the 3000 fb^{-1} scenario all sensors are exposed to less than $5.0 \times 10^{14}\,\mathrm{n_{eq}/cm^2}$ and 69.8 % to less then $2.5 \times 10^{14}\,\mathrm{n_{eq}/cm^2}$, respectively. In the ultimate scenario (4000 fb^{-1}) 98.8 % of the 2S sensors see less than $5.0 \times 10^{14}\,\mathrm{n_{eq}/cm^2}$. Data from [CMS21].

Table 8.1: Annealing procedure in the ALiBaVa setup. An annealing time of 199 d equivalent annealing at 21 °C is performed in six heating steps at 60 °C or 80 °C. About 104 h additional annealing at room temperature accumulate during the sensor characterization and module construction.

Step	ALiBaVa						Construction
Temperature (°C)	60	60	60	60	80	80	21
Duration (min)	20	20	40	76	15	29	6240
Acc. eq. annealing time (d at 21 °C)	3.8	6.9	13.3	27.1	77.9	199.4	203.7

The long term annealing was performed using the ALiBaVa setup. The full annealing time was split in six annealing steps plus additional 104 h for the module construction and sensor characterization. Table 8.1 summarizes the annealing steps and the corresponding equivalent annealing times. After each step signal measurements with a radioactive ^{90}Sr source were performed to monitor the influence of the annealing on the sensor signals. The short term annealing was performed in one 50 min step at 60 °C in a drying oven. Again 104 h at room temperature accumulated for the sensor characterization and prototype construction.

8.2 Electrical Properties

All sensors foreseen for the construction of prototypes have been extensively tested in advance. One aspect of the test is the characterization of the electrical properties of the sensors. For all sensors the I(V) and C(V) characteristics were recorded. Figure A.1 and figure A.2 show the results of those measurements before irradiation. All sensors of the same material show very similar I(V) characteristics and no early breakdowns. The leakage current of the thinned thFZ240 sensors is slightly higher compared to the thicker FZ290 sensors but with less than

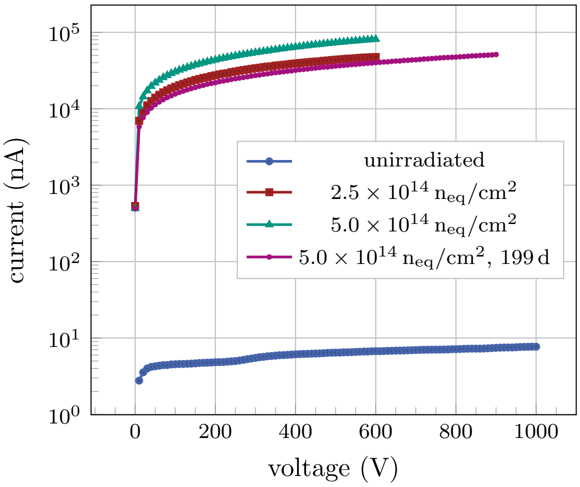

Figure 8.2: I(V) curves of FZ290 sensors before and after irradiation to $2.5 \times 10^{14}\,\mathrm{n_{eq}/cm^2}$ and $5.0 \times 10^{14}\,\mathrm{n_{eq}/cm^2}$. 199 d of equivalent annealing time at room temperature of the FZ290 with high fluence reduce the sensor leakage current.

30 nA at 600 V still at a very low level. The higher leakage current of the thFZ240 sensors is caused by the physical thinning process of the sensors, which generates surface defects that increase the leakage current. Four sensors were chosen for irradiation with neutrons. Again the I(V) behavior was recorded after the reception from the irradiation facility. Furthermore, the sensors were annealed to the targeted equivalent annealing times as described in section 8.1. Right before building the modules again I(V) and C(V) of all sensors were determined.

Figure 8.2 displays the I(V) curves of an exemplary FZ290 sensors before and after the irradiation with $2.5 \times 10^{14}\,\mathrm{n_{eq}/cm^2}$ and $5.0 \times 10^{14}\,\mathrm{n_{eq}/cm^2}$. In addition, it shows the I(V) of the sensor with higher fluence after annealing to 199 d at room temperature. The irradiation induced bulk damage increases the sensor leakage current by several orders of magnitude for typical sensor operation voltages. The annealing in turn has a beneficial effect on the sensor leakage current.

Different strip parameters have been measured before building the prototype modules. Figure 8.3 displays the measurement of I_{diel}, which is the current through the electrically isolating silicon dioxide passivation. A high I_{diel} indicates a missing electrically isolation between the implant and the aluminum strip on top and hence the existence of a pinhole. All sensors, independent of irradiation and annealing, show a very uniform behavior. Three pinholes have been identified by the measurements. The pinholes occured for three strips of irradiated sensors with long annealing. Before performing the strip scans these sensors have been bonded and annealed on the ALiBaVa setup to perform charge collection measurements (see section 8.3). After the measurements the bonds were removed. The physical stress during the (un)bonding process can promote the creation of pinholes. However, the investigation of sensors with pinholes (section 9.3) showed that pinholes do not affect the module performance.

Furthermore, the strip leakage current I_{leak} has been measured for all sensors. Figure 8.4 displays the strip leakage current for the irradiated sensors. The measurements have been performed at 350 V sensor bias and −20 °C. Both materials have a similar strip leakage current after irradiation. As expected from the I(V) measurements, also I_{leak} reduces with annealing. The maximum strip leakage current after $5 \times 10^{14}\,\mathrm{n_{eq}/cm^2}$ and 9 d equivalent annealing time is about 400 nA. Figure A.5 shows the strip leakage current of the unirradiated sensors. Before irradiation the leakage current is very low and of the order of about 0.1 nA. Only a few strips

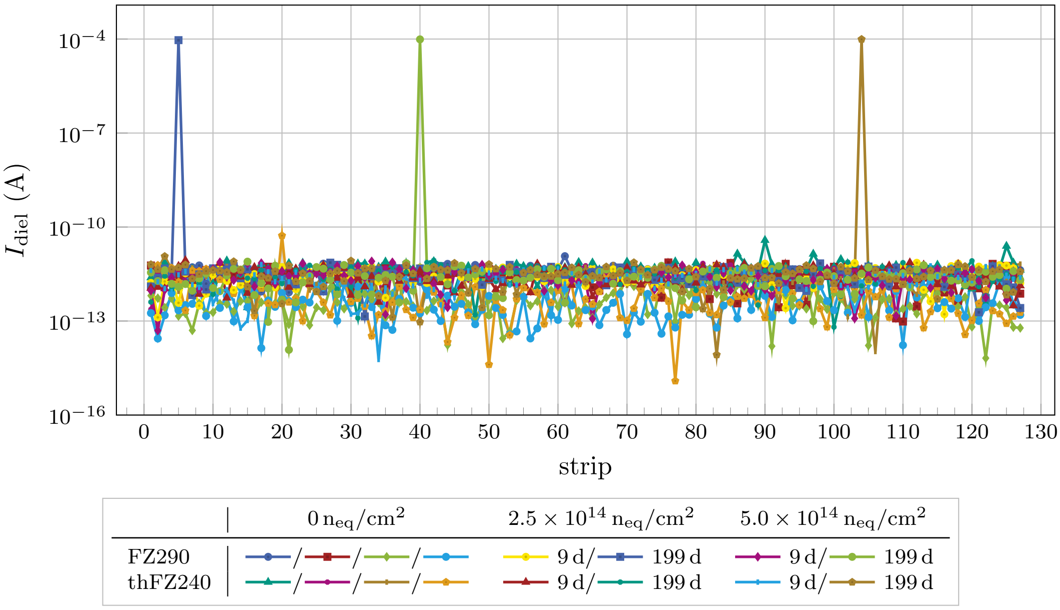

Figure 8.3: Strip scan of I_{diel} to identify pinholes for all sensors which were installed in Mini Modules. The sensor bias voltage was 350 V (300 V for the sensors with $5\times10^{14}\,\text{n}_{\text{eq}}/\text{cm}^2$) and the measurements conducted at 20 °C (−20 °C for irradiated sensors). Three pinholes (high I_{diel}) have been identified for irradiated sensors with long annealing.

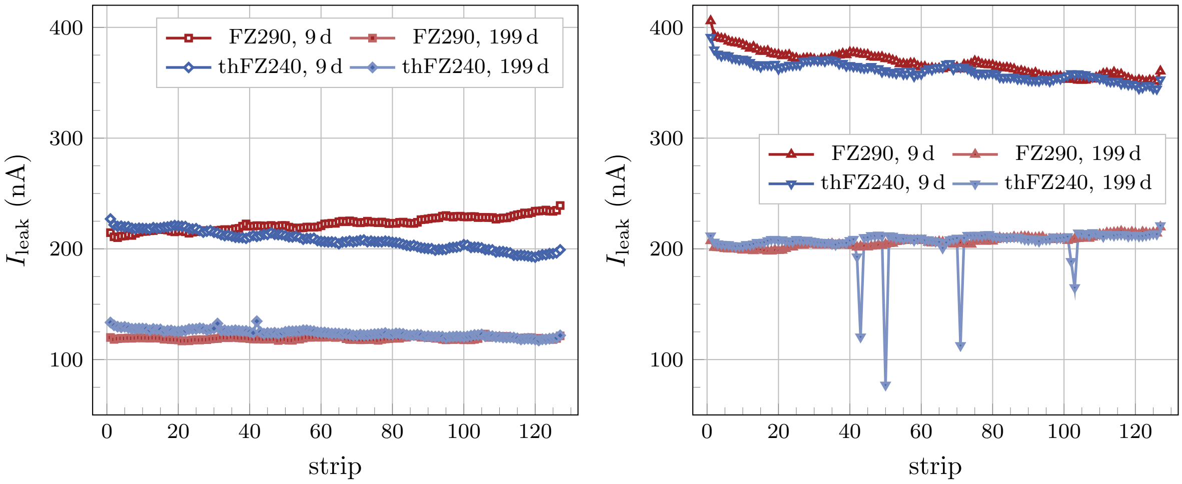

(a) $2.5\times10^{14}\,\text{n}_{\text{eq}}/\text{cm}^2$

(b) $5.0\times10^{14}\,\text{n}_{\text{eq}}/\text{cm}^2$

Figure 8.4: Strip leakage current I_{leak} of the irradiated sensors. Irradiation strongly increases the strip leakage current. An annealing time of 199 d equivalent time at 21 °C reduces the strip leakage current about a factor of two compared to the short annealing of 9 d. The strip leakage current after irradiation is almost the same for both sensor materials. The reduced I_{leak} for some strips is caused by a poor needle contact during the measurement.

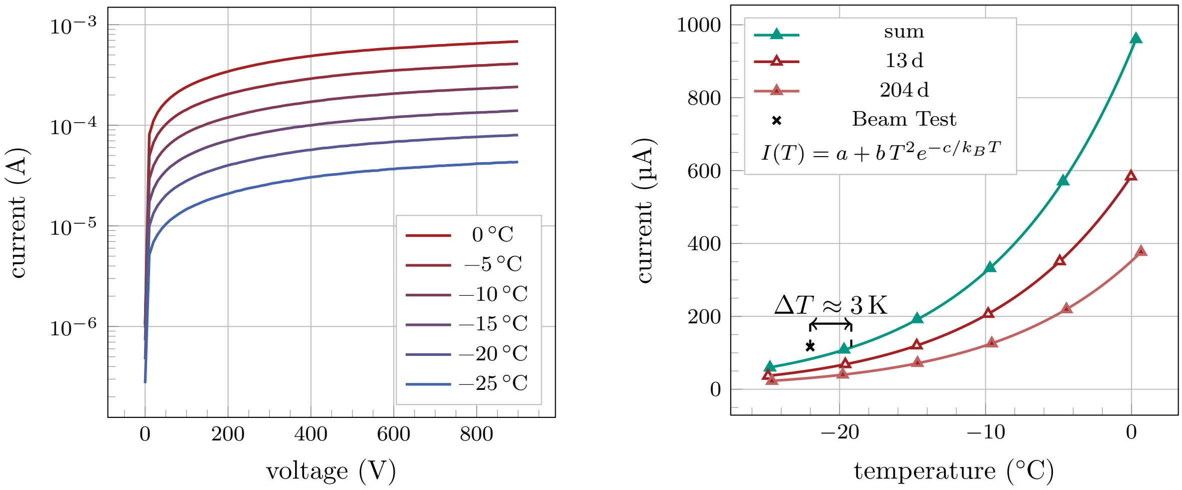

(a) I(V,T) for the FZ290 sensor with $5 \times 10^{14}\,\mathrm{n_{eq}/cm^2}$ and 13 d eq. annealing time. The leakage current strongly increases with temperature.

(b) Individual and summed I(T) with fit for the FZ290 sensors of MiMo3 at 600 V. The cross marks the module temperature and leakage current measured during the beam test.

Figure 8.5: Calibration I(V,T) measurements of one FZ290 sensor (a) and I(T) characteristics for the FZ290 sensors of MiMo3 (b). The recorded module temperature in the beam test was about 3 K below the calculated sensor temperature from the current measurement.

of two sensors have a slightly higher leakage current of about 0.5 nA, which could be caused by surface damage (scratches) due to the sensor handling. However, this strip leakage current increase is much lower compared to the irradiation induced increase.

Other strip parameters measured before constructing the modules are the coupling capacitance C_c (figure A.6) and the resistance of the poly resistor R_poly (figure A.7). Both parameters are not influenced by irradiation and annealing. The strips of the sensors show very uniform values. For the coupling capacitance measurement of one set of sensors the capacitance compensation failed which is responsible for the large offset for these sensors. The resistance of the poly resistors of all strips are in the order of 2 MΩ. However the irradiated sensors show a slightly higher resistance which is caused by the temperature dependent resistance of silicon. The irradiated samples have been cooled to −20 °C for the measurements whereas the unirradiated sensors were measured at 20 °C.

The leakage current of silicon sensors strongly depends on the sensor temperature, too. This effect can be used to determine the sensor temperature by measuring the leakage current (e.g. in module prototypes). In a first step the I(V) characteristics of all irradiated sensors were measured for known temperatures between −25 °C and 0 °C in steps of 5 K. Then for each operation voltage the I(T) characteristics is fitted by equation 4.23 with free proportional factor and bandgap energy. For a given operation voltage the I(T) fit can be used to calculate the sensor temperature from the measured leakage current.

Figure 8.5a shows the I(V) characteristics for the measured temperatures of one FZ290 sensor with a fluence of $5 \times 10^{14}\,\mathrm{n_{eq}/cm^2}$ and 13 d equivalent annealing at 21 °C. The sensor was later integrated in MiMo3. Figure 8.5b shows the individual and summed I(T) characteristics of the FZ290 sensors installed in MiMo3 at 600 V. Furthermore, the cross marks the corresponding current of the two sensors and the module temperature measured in the beam test setup. The actual sensor temperature extracted from the module current and I(T) curves is about 3 K

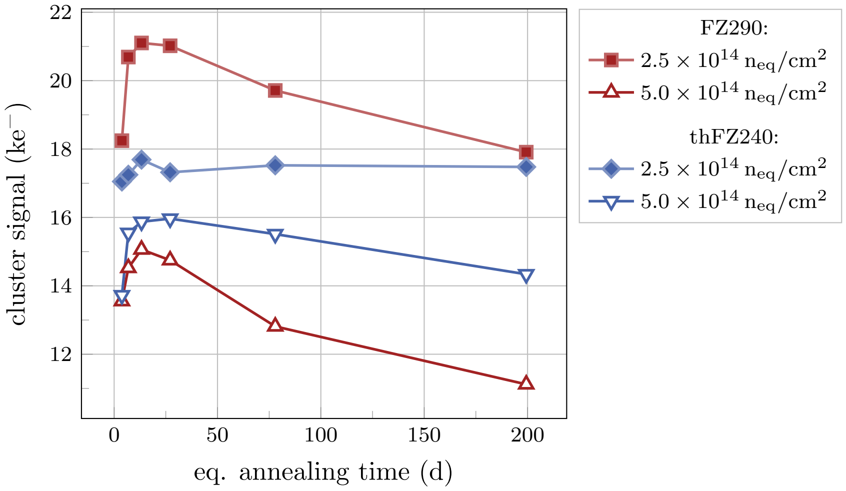

Figure 8.6: Cluster signal over equivalent annealing time at 21 °C and 600 V sensor bias for two different fluences. The FZ290 sensors are more sensitive to annealing. After 13 d at 21 °C the annealing is beneficial and the cluster signal reaches a maximum. For longer annealing times the signal decreases. The signal of the thFZ240 sensors suffers less from irradiation and annealing.

above the measured module temperature. This agrees with the expectation of the module design. The module temperature sensor is placed on the copper frame close to the cooling chuck. Thus, the expected temperature of the sensors is slightly above the module frame temperature.

In the scope of this thesis the given temperatures are the temperatures measured by the PT1000 sensor on the module frame. However, this measurement demonstrated that the actual temperature of the sensors is about 3 K above the frame temperature for measurements at about −20 °C.

8.3 Charge Collection and Annealing

To investigate the charge collection behavior of the two different materials one sensor of each material and fluence has been characterized in the ALiBaVa setup. Furthermore, the annealing procedure as described in section 8.1 has been performed using the setup. For each annealing step charge collection measurements of signals from a ^{90}Sr source have been carried out for sensor bias voltage ramps between 300 V and 900 V in steps of 100 V.

Figure 8.6 displays the annealing behavior of the cluster signal for the two materials at 600 V. As already observed by Metzler in [Met20] for sensors with shorter strip length the FZ290 material is more sensitive to annealing compared to the thFZ240 material. After a beneficial increase of the cluster signal with a maximum at about 13 d the cluster signal steadily decreases with further annealing. At the nominal fluence of $2.5 \times 10^{14}\,\mathrm{n_{eq}/cm^2}$ the cluster signal of the thFZ240 does not show a clear annealing dependence. This does not hold for the ultimate fluence of $5.0 \times 10^{14}\,\mathrm{n_{eq}/cm^2}$. For this fluence the thFZ240 shows a similar annealing behavior as the FZ290 material with a peak after 27 d equivalent annealing. The seed signal has a very similar behavior. The corresponding plot is shown in figure A.8.

For the nominal fluence the FZ290 sensor delivers a larger cluster signal for all investigated annealing steps. However, for the ultimate fluence the thFZ240 material provides a larger cluster signal. The dominance of the material with respect to the cluster signal even increases with annealing time.

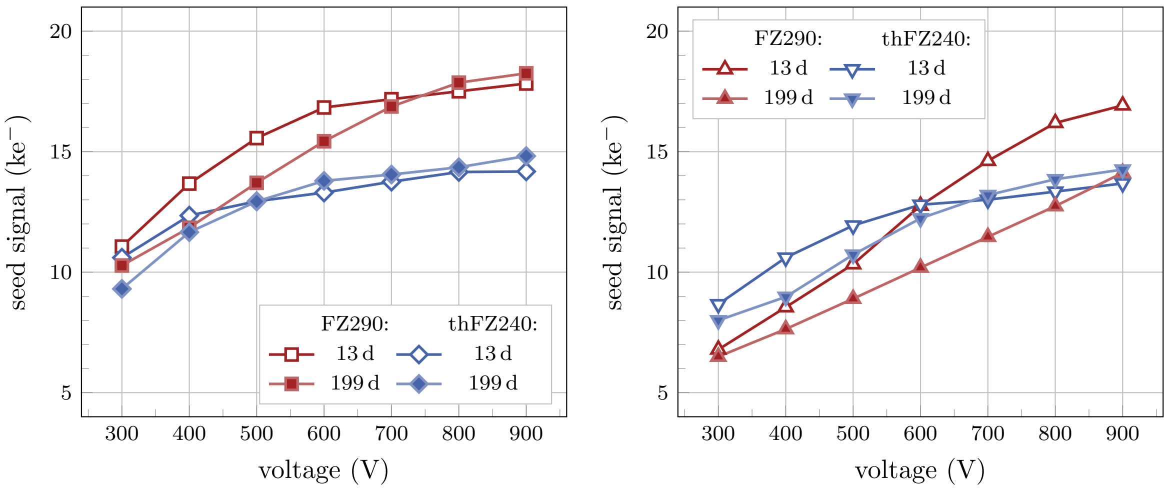

(a) $\Phi = 2.5 \times 10^{14}\,\mathrm{n_{eq}/cm^2}$ – MiMo2 **(b)** $\Phi = 5.0 \times 10^{14}\,\mathrm{n_{eq}/cm^2}$ – MiMo3

Figure 8.7: Seed signal over bias voltage for baby sensors at $2.5 \times 10^{14}\,\mathrm{n_{eq}/cm^2}$ (a) and $5.0 \times 10^{14}\,\mathrm{n_{eq}/cm^2}$ (b) with 13 d and 199 d equivalent annealing. At the lower fluence the FZ290 material yields a larger seed signal. For the ultimate scenario and long annealing the thFZ240 delivers a larger seed signal. By increasing the bias voltage to 900 V the seed signal of the long annealed FZ290 recovers to the same level as the thFZ240 sensors.

The CBC with binary signal detection only detects clusters of which at least one strip signal exceeds the threshold. By definition the seed signal is the largest strip signal in a cluster. Thus, the height of the seed signal significantly impacts the particle detection efficiency. Figure 8.7 shows the seed signal dependence on the sensor bias voltage for the two fluences. The shown equivalent annealing times (13 d and 199 d) correspond to the annealing of the sensors in the Mini Modules.

At $2.5 \times 10^{14}\,\mathrm{n_{eq}/cm^2}$ the FZ290 material delivers a larger seed signal. Furthermore, figure 8.7a demonstrates that an increase of the bias voltage to about 700 V compensates the reverse annealing effect of the seed signal.

At the ultimate fluence and nominal operation voltage (600 V) the seed signals of both materials are the same for 13 d annealing. After 200 d of annealing, the FZ290 sensor delivers about 2000 e$^-$ less seed signal at 600 V. However, by increasing the operation voltage to 900 V the seed signal of the long annealed FZ290 sensor recovers to the same level as the seed signal of the long annealed thFZ240 material.

In summary, the FZ290 material provides the same or larger seed signals for all scenarios except for the long annealing at ultimate fluence. However, an optional voltage increase to 900 V overcomes this drawback.

9

Characterization of the 2S Mini Modules

This chapter presents the results of the laboratory measurements on the 2S Mini Module prototypes. The first section describes the influence of operation parameters like bias voltage, temperature and sensor leakage current on the noise and trimming quality. Reducing the noise is crucial to improve the particle detection efficiency by improving the signal-to-noise ratio, whereas a uniform trimming of the channels is important to guarantee a similar response behavior on signals of the same magnitude. The results are discussed with regard to the expected operation parameters in the Outer Tracker.

The next section deals with signal measurements and the calculation of the gain factor to translate the threshold DAC value Vcth into a charge signal. This calibration is important to make the results, obtained with the CBC, comparable to other systems.

Sensor defects may occur during the production or the operation of the sensors in the Outer Tracker. However, the reliable operation of the modules must be guaranteed even under the presence of sensor defects. Thus, the chapter closes with a study of different kinds of sensor defects and their impact on the module performance. The study demonstrates that none of the investigated sensor defects causes a failure of the modules. Furthermore, it shows that pinhole-like defects will not affect the module performance even for high leakage current.

9.1 Module Noise and Offset Calibration

The noise level of semiconductor detectors depends on different factors. Section 4.3.3 introduces different sources of noise. This section investigates the influence of different operation parameters on the observed noise of the 2S Mini Modules.

9.1.1 Noise and Sensor Operation Voltage

The major contribution to the noise of the Mini Modules is caused by the load capacitance of the strips. The sensor capacitance strongly depends on the sensor bias voltage as shown in figure A.2. With increasing bias voltage the capacitance of a sensor decreases until it reaches full depletion. Thus, also the noise of the modules decreases with increasing bias voltage. Figure 9.1 shows the noise-bias voltage characteristics for the sensors of two Mini Modules at about $-20\,^{\circ}\mathrm{C}$. For each voltage step 50 s-curve measurements were recorded. The resulting noise for each individual strip is the average noise of the 50 measurements. The noise of one sensor is defined as the average noise of all its strips and the error bars display the standard deviation.

The noise of the unirradiated sensors of MiMo4 was measured at $-20\,^{\circ}\mathrm{C}$ for a voltage range between $0\,\mathrm{V}$ and $400\,\mathrm{V}$ (figure 9.1a). As expected the noise decreases with the sensor bias voltage and reaches a plateau at about $150\,\mathrm{V}$. In order to connect the sensor on the bottom side of the module, the hybrid is folded over a stiffener. Hence, the connection lines on the hybrid for the bottom sensor are longer and increase the load capacitance of the corresponding channels. As a consequence, the noise of the bottom sensor is slightly higher compared to the

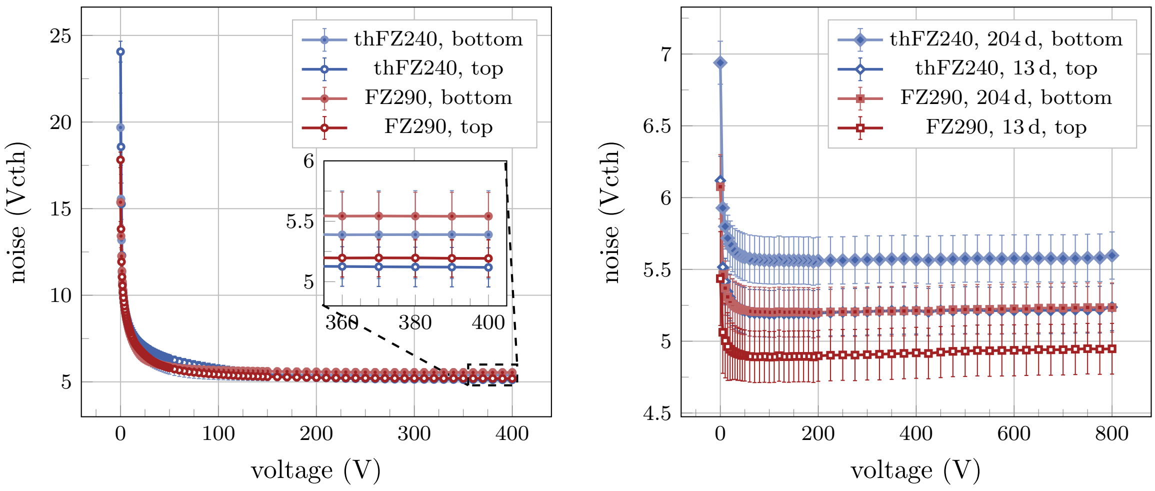

(a) MiMo4 at $T = -20\,°\mathrm{C}$

(b) MiMo2 at $T = -22\,°\mathrm{C}$

Figure 9.1: Noise dependence on the sensor operation voltage for MiMo4 and MiMo2 (sensors irradiated with $2.5 \times 10^{14}\,\mathrm{n_{eq}/cm^2}$). For high enough sensor voltage the noise saturates for both modules. The noise of the sensors on the bottom side of the module is slightly higher, caused by the additional load capacitance of the longer connection lines on the hybrid fold over.

top sensor, even though the same chip reads out both sensors. For MiMo4 the thFZ240 sensors have a slightly lower noise level compared to the FZ290 material. However, the difference is very small and within the measurement uncertainties. A possible reason is that the noise levels can vary due to chip-to-chip fluctuations.

Figure 9.1b displays the corresponding characteristics for MiMo2, which is equipped with irradiated sensors ($\Phi = 2.5 \times 10^{14}\,\mathrm{n_{eq}/cm^2}$). The noise for bias voltages less than 20 V is much lower compared to the unirradiated module. This indicates a reduced load capacitance for low bias voltages after irradiation. The C(V) characteristics of the sensors before and after irradiation confirm this assumption (see figure A.3). For sensor biasing voltages below 20 V the capacitance of irradiated sensors is lower compared to the unirradiated sensors.

At bias voltages of more than 100 V the noise for MiMo2 saturates at a constant level. For the same reasons as for MiMo4 the sensors from the module's bottom side show slightly higher noise level. In contrast to MiMo2 the sensors made from FZ290 material show less noise. Again the difference can be caused by chip-to-chip fluctuations.

For the operation in the Outer Tracker the nominal bias voltage is 600 V. In this voltage region the noise does not depend on the sensor voltage. Even a possible voltage boost to 800 V will not increase the noise.

9.1.2 Noise and Trimming vs. Module Temperature

Over the operation time in the CMS detector the sensors will suffer from radiation damage. One effect of radiation damage is the increase of the sensor leakage current. The heat dissipation of the sensors is proportional to the sensor leakage current. To cool away the heat and to prevent the sensors from undesired annealing the 2S modules have to be cooled during the operation in the Outer Tracker. A two-phase CO_2 cooling system removes the heat generated by the sensors and module electronics. Different parameters drive the final module temperature. The chips on the 2S module dissipate about 5.4 W. In addition, the sensors emit a thermal power of up to 0.5 W depending on the irradiation and annealing state [CMS18]. Thermal simulations for

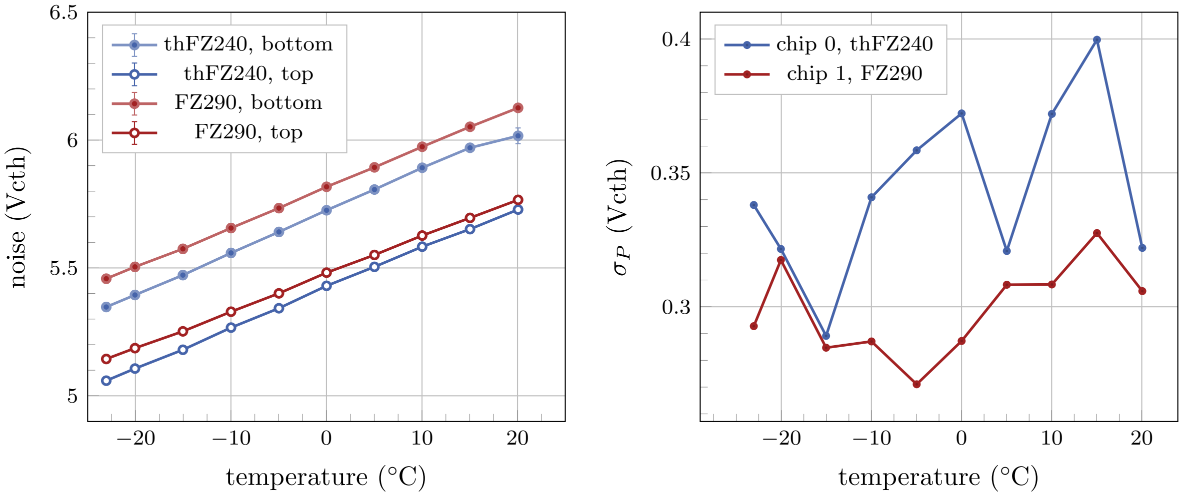

(a) Noise over module temperature for MiMo4 at 400 V sensor bias voltage.

(b) Standard deviation of pedestals σ_P over the temperature for the two CBCs of MiMo4 (400 V bias voltage).

Figure 9.2: Sensor noise (a) and the standard deviation of the channel pedestals σ_P (b) over the module temperature. The sensor noise depends linearly on the temperature and reduces with decreasing temperature. The trimming performance, quantified by σ_P, does not depend on the temperature and is an order of magnitude smaller than the sensor noise.

the 4000 fb^{-1} scenario showed that for a coolant temperature of more than −30 °C the cooling power is insufficient to cool away the dissipated heat of the modules. In such a scenario the sensors will start to heat up. The increasing sensor temperature in turn enhance the leakage current and even intensify the heat dissipation. Thus, the sensors continue to heat up and the modules run into a thermal runaway and finally destroy themselves. To prevent thermal runaways, the CO_2 cooling will operate at −33 °C or lower. For this coolant temperature the simulations show a stabilization of the sensor temperature at about −20 °C. [Rau20]

This section investigates the influence of the module temperature on the noise and trimming quality. A first scan recorded the noise of the sensors for different module temperatures between −25 °C and 20 °C. For each temperature step the channel offsets have been trimmed to a common pedestal. Then 50 s-curve measurements have been performed. The noise and pedestal for each strip is averaged over the 50 measurements. The noise of the sensor is the mean of the noise of all its strips. The uncertainty on the noise measurement is the standard deviation of the strip noises σ_N divided by the square root of the number of strips n_s.

Figure 9.2a displays the sensor noise over the module temperature for the unirradiated MiMo4 at 400 V sensor bias voltage. The noise of each sensor increases linearly with the module temperature. A linear fit describes the temperature dependence. Its slope reveals the relative noise increase per Kelvin. Table 9.1 summarizes the slopes for the individual sensors of MiMo4. The sensors on the bottom side of the module are slightly more sensitive to temperature fluctuations. Section 9.2.2 will show that the temperature dependence of the noise is not caused by a temperature dependent amplification of the CBC's analog front-end. Thus, the cooling of the modules has a beneficial effect on the module noise. For the operation in the Outer Tracker the expected hybrid temperature is −15 °C with the cooling running at −30 °C [Rau20]. For this temperature the estimated noise for the 2S modules is about 5.2 Vcth/5.6 Vcth for the top/bottom sensor layer.

Table 9.1: Results for the linear fit of the temperature noise characteristics of the sensor of MiMo4. The sensors were operated at 400 V.

chip	**sensor**	**slope** (Vcth K^{-1})
0	thFZ240, bottom	0.0165 ± 0.0004
	thFZ240, top	0.0158 ± 0.0003
1	FZ290, bottom	0.0157 ± 0.0004
	FZ290, top	0.0147 ± 0.0003

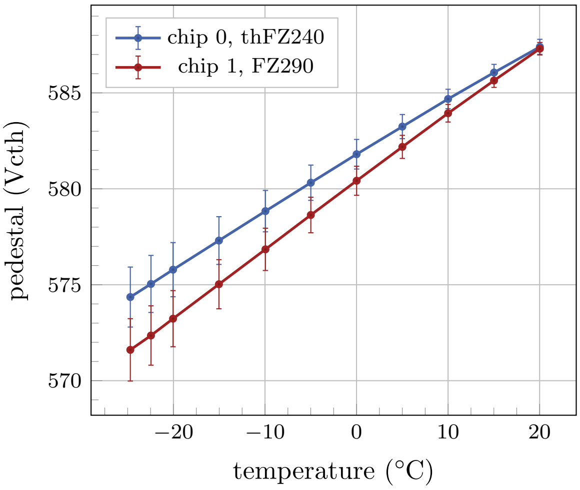

Figure 9.3: Temperature dependence of the pedestal for the CBCs of MiMo4 at 400 V sensor bias voltage. The chips were trimmed once at 20 °C and then the s-curves recorded for temperatures between 20 °C and −25 °C without repeating the trimming. The pedestal shows a linear dependence of the temperature. With increasing temperature difference ΔT from the trimming temperature the trimming quality (error bars) worsens.

Another important parameter for the operation of the modules is the trimming quality of the channels. Trimming adjusts the individual offsets of the channels to equalize their response behavior. A quantity to describe the trimming quality is the standard deviation σ_P of the channel pedestals of one chip. The lower the spread of the pedestals the better is the trimming. Figure 9.2b displays the temperature dependence of σ_P for the two chips of MiMo4 at 400 V sensor bias voltage. The trimming quality does not show a temperature dependence. Furthermore, σ_P is in the order of 0.4 Vcth which is more than one order of magnitude lower than the noise. Thus, random noise will influence the performance of the chip much stronger than the channel-to-channel fluctuations of the trimming quality.

Drifts of the module temperature without new trimming affects the operation of the 2S modules far more severely. Figure 9.3 demonstrates the effect of a temperature shift without trimming the channels. The y-axis displays the mean pedestal of all channels of one chip and the error bar is the standard deviation. For the measurement the chips were trimmed only once at 20 °C. For each temperature step again 50 s-curves were recorded to determine the noise and pedestal of the individual channels. The mean pedestal for each chip shows a linear dependence on the temperature. For chip 0 the slope is $m_0 = (0.293 \pm 0.002)\,\mathrm{Vcth\,K^{-1}}$, whereas for chip 1 it is $m_1 = (0.353 \pm 0.001)\,\mathrm{Vcth\,K^{-1}}$. Furthermore, the trimming quality σ_P worsens with increasing ΔT to the trimming temperature of the chips.

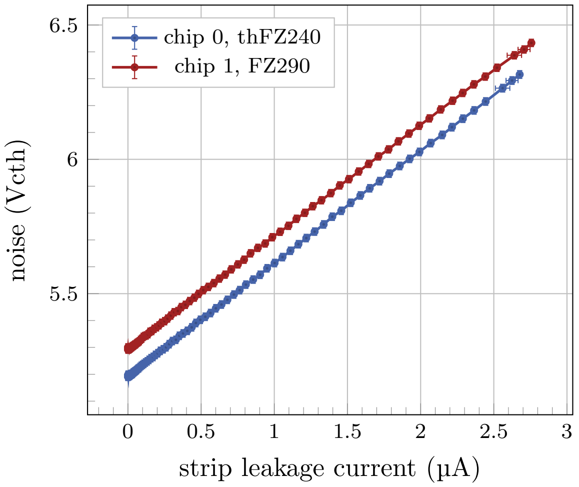

Figure 9.4: Noise leakage current characteristics for the two upper sensors of MiMo4. The sensor bias voltage was 400 V and the module temperature −20 °C. With increasing strip current the noise increases linearly.

This measurement demonstrates the importance of repeating the trimming as soon as the temperature of the system changes. Already a temperature drift of about 10 K will move the pedestals by several Vcth and worsen the trimming quality. Without re-trimming and adjustment of the threshold, temperature drifts can cause efficiency losses or an increase of noise hits. On the one hand, a drift to lower temperatures shifts the pedestals to lower Vcth values. Without adjusting the threshold value this would yield to a reduced threshold and increase the probability to detect noise hits. On the other hand, a drift to higher temperature has the contrary effect. This can lead to efficiency losses due to the higher effective threshold. During operation in the Outer Trakcer the heat dissipation of the chips will heat up the front-end hybrids almost 20 K above the coolant temperature [Rau20]. Thus, the trimming of the front-ends has to be performed not before the modules are in thermal equilibrium after switching on the electronics. In addition, the temperature has to be monitored carefully to guarantee a common response behavior on signals over time.

9.1.3 Noise and Sensor Leakage Current

As introduced in section 4.3.3, the sensor leakage current contributes to the noise of the sensor. During the operation in the Outer Tracker the sensors accumulate radiation damage, which increases the sensor leakage current. This will cause an increase of the noise over time. There are different methods to vary the leakage current of a sensor. One way is to change the temperature of an irradiated sensor. However, temperature changes strongly affect the noise of the CBC, which add to the leakage current-related noise changes.

To isolate current-related effects another approach was chosen. The Mini Module test station comprises tunable infrared LEDs to mimic the irradiation induced bulk leakage current. The infrared light is absorbed in the whole sensor volume and generates a light-induced photo current. The light intensity adjusts the photo current. Since the backplane of the sensors is aluminum coated it is non-transparent for infrared light. Thus, the light mainly generates photo current in the top sensor layer. To reduce uncertainties of the current measurement by contributions from the lower sensors only the top sensor layer was biased for the measurements.

Figure 9.4 shows the sensor noise over the strip leakage current. For the measurement MiMo4 was cooled down to −20 °C and the sensors were operated at 400 V with individual biasing.

Since only the top sensors were biased and illuminated the plot includes only the results for these sensors. By varying the LED current with a constant current source the light intensity was adjusted. For each measurement point 50 s-curves and leakage current measurements were conducted. The sensor noise was calculated in the same way as for the measurements in the previous sections. For a given light intensity the strip leakage current is the average sensor leakage current of the 50 measurements divided by 127, which is the number of strips per sensor. The uncertainty on the leakage current is the standard deviation divided by 127.

For the shown leakage current range the noise depends linearly on the strip leakage current. A linear fit reveals the proportionality constant for the two sensors/chips:

$$\begin{aligned} m_0 &= (0.420 \pm 0.002)\,\mathrm{Vcth}\,\mathrm{\mu A}^{-1} \\ m_1 &= (0.417 \pm 0.002)\,\mathrm{Vcth}\,\mathrm{\mu A}^{-1} \end{aligned} \tag{9.1}$$

Both results agree within the uncertainties. FLUKA simulation showed [CMS21] that in the ultimate scenario the strip leakage current will not increase to more than 1 µA for the most irradiated sensors. In this scenario, the noise increase caused by the higher leakage current is about 0.4 Vcth. Since this holds only for very small fraction of the 2S modules and the effect is small compared to the total sensor noise, the effect will hardly influence the tracker performance.

9.2 Signal measurements

Even though noise is an important parameter to describe the behavior of the module, it is essential to perform measurements with external signals. This section presents the results of calibration measurements to convert the comparator DAC unit Vcth into an charge equivalent signal using two different signal sources: chip internal test pulses and signals generated by electrons from a radioactive ^{90}Sr source.

9.2.1 Timing the Hit and Stub Latency

To detect and record external signals, a reference signal has to trigger the readout of the module. For every change of the signal source or of the setup the optimal timing between the trigger and the readout data stream has to be determined. On the CBC there are two data streams, one for triggered level-1 data and the continuously emitted stub data stream. For each of the data streams the timing has to be determined individually. Section 5.1.5 introduced the procedure to determine the optimal hit latency and stub latency.

Figure 9.5a shows an exemplary hit and stub latency scan for ^{90}Sr induced signals. In particular, it displays the number of recorded hits and stubs for the corresponding latency. For each latency steps the data for 1000 trigger (events) were recorded. The maxima of the curves correspond to the optimal latency to operate the module most efficiently. The number of stubs is lower compared to the number of hits, since the stub detection probability combines the hit detection probabilities of the two sensor layers.

In the case of an asynchronous external signal source, like ^{90}Sr, the particles pass the sensors at an arbitrary phase with respect to the clock of the system. The same holds for the trigger signal. The firmware adds a time stamp of the trigger arrival, which divides each clock cycle into eight TDC values or 3.125 ns steps, respectively. Regarding signal measurements, a correct timing is essential to detect the signals in their maximum. A signal sampling which is not in the pulse peak causes detection efficiency losses. Furthermore, the correct TDC timing depends on the threshold, because of time-walk effects. Thus, for each measurement the correct TDC timing has to be determined individually. The most efficient TDC value is the one which

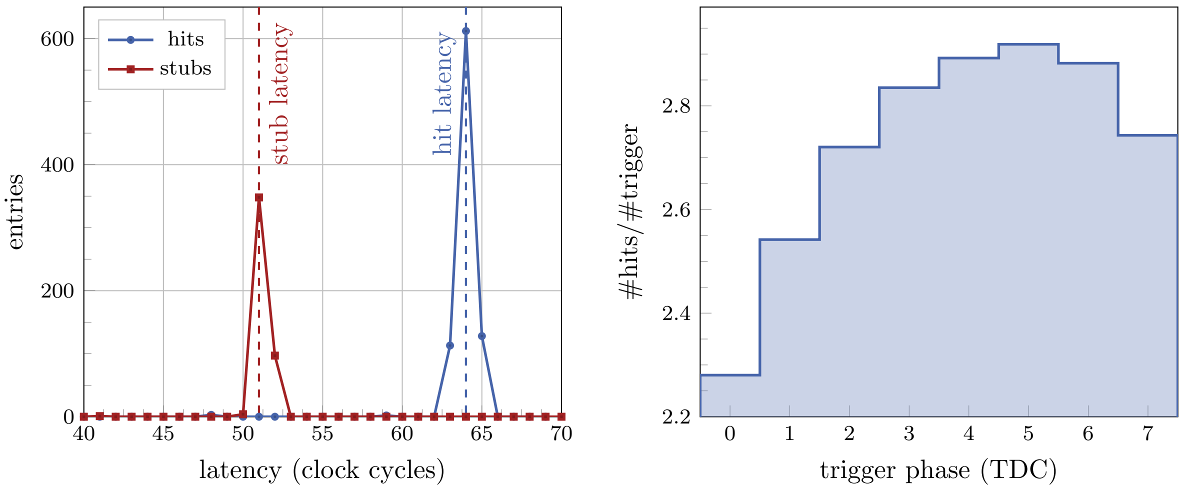

(a) Hit and stub latency scan

(b) #hits/#trigger over the trigger arrival phase

Figure 9.5: Hit und stub latency measurement (a) for signals of a ^{90}Sr source. The optimal latencies are 64 for the hit data stream and 51 for the stub data stream. A cut on the TDC value for which most hits per trigger are detected is essential for signal studies (b). The measurements were conducted with MiMo4 at 20 °C, 400 V bias voltage and 50 Vcth threshold.

maximizes the number of recorded hits normalized to the number of triggers. This procedure was performed for all measurements with ^{90}Sr as signal source. Figure 9.5b shows an exemplary TDC distribution of triggered ^{90}Sr events with a maximum at 5.

9.2.2 Temperature Dependence of the Signal Detection

Section 9.1.2 demonstrated that the sensor noise scales linearly with the module temperature. The measurement does not explain whether this is a real beneficial effect of the noise or if it is caused by a temperature dependence of the amplifiers in the analog front-end of the CBC. However, performing a threshold scan and recording the cluster occupancy for an external signal source, e.g. ^{90}Sr electrons, for different temperatures can check the temperature dependence of the amplifiers. If temperature affects the gain of the amplifiers the threshold scans would have a different shape for each temperature.

Figure 9.6 shows the cluster occupancy o_{cl} for threshold scans at different module temperatures between −20 °C and 20 °C. The plot displays the results for the upper FZ290 sensor of MiMo4 operated at 400 V. Electrons from a ^{90}Sr source were focussed on the sensor by an collimator with 0.8 mm aperture. For the different measurements only the temperature was changed and the geometry of the setup was unchanged. For each temperature step the channel trimming was repeated. The plot demonstrates that the signal spectrum does not change with temperature. Thus, the gain of the amplifiers of the analog front-ends are not temperature dependent. Furthermore, the effect of noise reduction by cooling is a real benefit for the signal to noise ratio and the modules in the Outer Tracker will profit from the cooling.

9.2.3 Threshold Calibration of the CBC

To compare the measurements using the CBC with other readout systems the calibration of the threshold DAC (Vcth) into an charge equivalent signal is necessary. The conversion factor from Vcth into a charge signal is called the gain g. This section presents the results of two

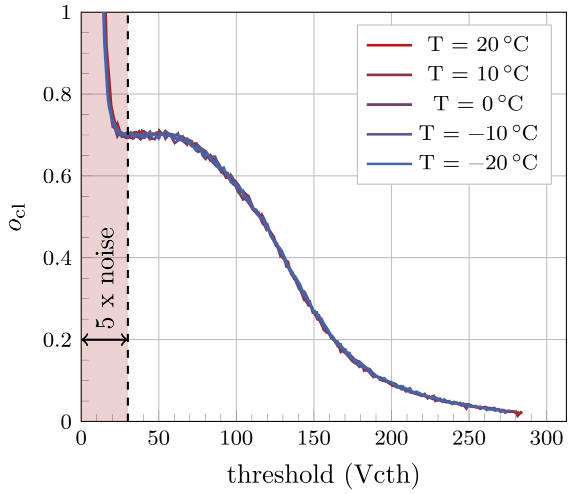

Figure 9.6: Threshold scan of the cluster occupancy o_{cl} for signals generated by ^{90}Sr electrons in the top FZ290 sensor of MiMo4. The scan was recorded for temperatures between −20 °C and 20 °C and with 400 V bias voltage. The threshold scans show no temperature dependence.

different calibration methods. The first method calibrates the gain factor with internal test pulses of the CBC. The second method calculates the gain by comparing the signal spectrum of a radioactive ^{90}Sr source with the results of a reference measurement. All measurements were conducted using the unirradiated MiMo4 at 400 V sensor bias voltage.

Calibration using Test Pulses

The calibration with test pulses makes use of the CBC's internal pulse generation. The charge of the pulse signal is known. Equation 9.2 shows the relation between the injected pulse charge S_{tp} and the programmed test pulse DAC S_{DAC} value [Pry19].

$$S_{\mathrm{tp}} = (255 - S_{\mathrm{DAC}}) \cdot 537\,\mathrm{e}^{-} \tag{9.2}$$

To determine the calibration gain factor the pulse shape for each channel and different test pulse charges between 0 ke^{-} and 50 ke^{-} were recorded as described in section 5.1.6. The pedestal in the pulse's peak depends linearly on the injected charge. Figure 9.7a displays the injected charge against the peak pedestal for one exemplary channel and the corresponding linear fit. Only data-points up to an injected charge of 45 ke^{-} contribute to the fit. For larger pulses the amplifiers of the CBC's analog front-end start to saturate.

Figure 9.7b shows the histogram of the channel gains for both CBCs of MiMo4. The mean gain $g_{\mathrm{tp},i}$ factor for the two chips i are

$$\begin{aligned} g_{\mathrm{tp},0} &= (151 \pm 2)\,\mathrm{e}^{-}\,\mathrm{Vcth}^{-1} \\ g_{\mathrm{tp},1} &= (150 \pm 2)\,\mathrm{e}^{-}\,\mathrm{Vcth}^{-1}. \end{aligned} \tag{9.3}$$

However, due to fabrication fluctuations the uncertainty on the charge injection is about 20 %. This systematic uncertainty drives also the accuracy of the gain factor so that the overall uncertainty is about $\sigma_{\mathrm{tp}} = 30\,\mathrm{e}^{-}\,\mathrm{Vcth}^{-1}$.

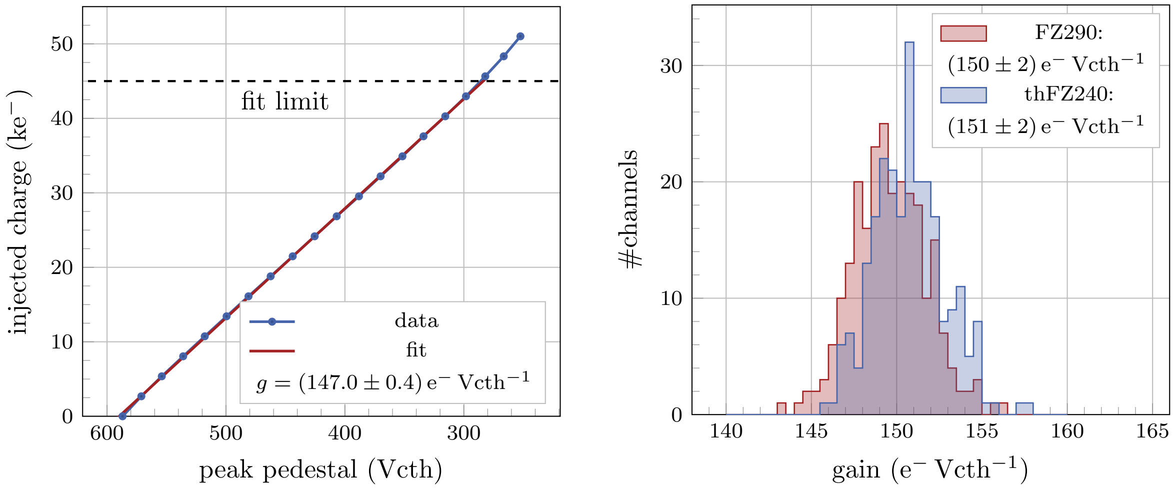

(a) Injected charge vs. measured pedestal for one channel

(b) Histogram of channel gains for MiMo4

Figure 9.7: Gain calculated from test pulses for both chips of MiMo4 at 400 V. Due to fabrication variations the uncertainty on the injected charge is 20 %.

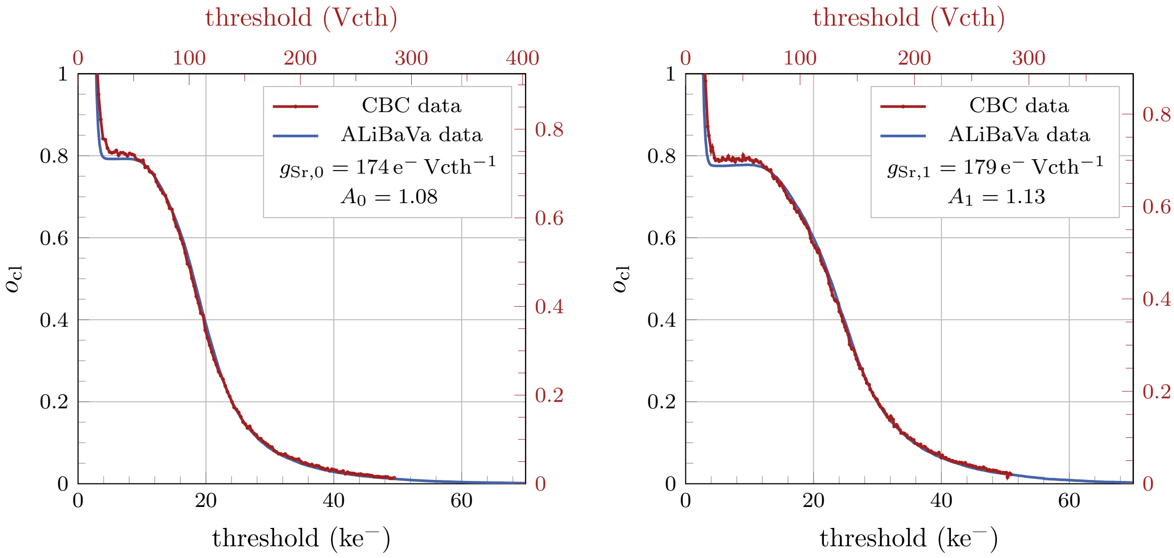

(a) thFZ240, chip 0

(b) FZ290, chip 1

Figure 9.8: Threshold scans of signals from a ^{90}Sr source in an unirradiated thFZ240 (a) and FZ290 (b) sensor recorded with MiMo4 (red) and the ALiBaVa setup (blue). The scaling factor $g_{\mathrm{Sr},i}$ between the two x-axes is the conversion factor from Vcth into an charge equivalent signal. The y-axis is also scaled to take the different geometries and acceptances of the setups into account.

Calibration using the ^{90}Sr Spectrum

This section presents a second method to determine the gain factor. The key idea of the method is to calibrate the CBC with a second, already calibrated, reference system. In particular, the ALiBaVa readout system is used to perform the reference measurement.

The common observable for both systems is the cluster occupancy o_{cl} for signals from electrons of a ^{90}Sr source. The threshold scan of o_{cl} reveals information about the signal spectrum as described in section 5.1.7. Since the Beetle chip of the ALiBaVa setup is an analog chip, the information were analysed in a binary way to obtain the threshold scan. This method was introduced in section 6.2.2.

The measurements in the ALiBaVa and Mini Module setup used the same collimator with an aperture of 0.8 mm to focus the electrons from the ^{90}Sr source on the sensors. The sensors were biased with 400 V and operated at 20 °C. The ALiBaVa readout board only comprises one sensor layer. Thus, only clusters in the top layer of the Mini Module contribute to the analysis. For the lower layer there would be additional uncertainties by scattering processes in the top sensor.

Figure 9.8 shows the threshold scans of the cluster occupancy for both systems and sensor materials. For the ALiBaVa measurement in total 300 000 events were recorded. By the definition of the binary analysis the ALiBaVa data decreases monotonously. For each Vcth step 100 000 events were recorded with the CBCs, from which about 12 000 remain after the TDC cut. Since the energy deposition of particles in matter fluctuates and for every threshold a new set of events have been recorded there are statistical fluctuations of o_{cl} for the CBC measurement.

The threshold for the ALiBaVa measurements is given in an charge equivalent signal (multiple of the electron charge) whereas the CBC threshold is in units of the comparator DAC (Vcth). The gain factor to convert Vcth into a charge signal is the scaling factor in x-direction to match the CBC scan to the ALiBaVa scan. However, the sensor acceptance for measurements with the different systems can vary. Masked strips or the geometric acceptance of the sensors and scintillator influence the acceptance. Thus, the saturation of o_{cl} for low thresholds differ and the y-axis has to be scaled as well.

The ALiBaVa threshold scan serves as a model to fit the CBC data. To determine the scaling factors the ALiBaVa points are linearly interpolated. The interpolation reveals in a continuous function $f(x)$ that describes the recorded cluster occupancy with the ALiBaVa setup. To fit the CBC data, additional free scaling factors are added to $f(x)$. Equation 9.4 shows the fit function with the corresponding scaling factor A in y-direction and g_{Sr} in x-direction to fit the ALiBaVa scan $o_{\mathrm{cl}}^{\mathrm{Ali}}(x)$ to the CBC data $o_{\mathrm{cl}}^{\mathrm{CBC}}(x)$.

$$o_{\mathrm{cl}}^{\mathrm{CBC}}(x, A, g_{\mathrm{Sr}}) = \frac{1}{A} \cdot o_{\mathrm{cl}}^{\mathrm{Ali}}(x/g_{\mathrm{Sr}})) \tag{9.4}$$

The scaling factor g_{Sr} is the gain to convert Vcth into an charge equivalent signals in number of e$^-$. Only CBC data points with thresholds larger than five times the noise contribute to the fit, since the noise of the two systems differ.

The result plots in figure 9.8 demonstrate the precise agreement of the measurements conducted with the two completely different systems for both sensor materials. The plots include the scaling factors in the different axis scalings. The fitted gain factors $g_{\mathrm{Sr},i}$ for the two chips i are

$$\begin{aligned} g_{\mathrm{Sr},0} &= 174\,\mathrm{e}^-\,\mathrm{Vcth}^{-1} \\ g_{\mathrm{Sr},1} &= 179\,\mathrm{e}^-\,\mathrm{Vcth}^{-1}. \end{aligned} \tag{9.5}$$

The uncertainty on the result is driven by the signal uncertainty of the ALiBaVa setup, which is of the order of 1000 e$^-$ or 5 % for a 20 ke$^-$ signal. The uncertainties on the fit parameters are about 2 %. Furthermore, the thickness of the sensors can vary. Measurements of the thickness of the thFZ240 showed a variation of about 1 % to 2 %. For the FZ290 sensors the uncertainty on the active thickness is even larger. Furthermore, there are systematic uncertainties of the measurement. Slightly differing positions of the ^{90}Sr source and particle incident angles, the acceptance of the scintillator trigger and the absorption and scattering in the second sensor of the Mini Module contribute to those uncertainties. Repeating the calibration measurements with a different collimator yield very similar results with a fluctuation of about 2 %. Thus, a conservative estimation of the uncertainty on the measurement is about 6 % or $\sigma_{\mathrm{Sr}} = 11\,\mathrm{e}^{-}\,\mathrm{Vcth}^{-1}$.

Conclusions

Both calibration measurements were conducted with the same module and the same environmental and operational conditions. The methods make use of uncorrelated approaches. Thus, to conclude a calibration factor of the CBC's comparator DAC both measurements are combined by using the weighted mean. Equation 9.6 displays the formula to calculate the gain g_i of one chip i, with the results from the test pulse and ^{90}Sr based calibration $g_{\mathrm{tp/Sr},i}$ [Leo94]

$$g_i = \frac{g_{\mathrm{tp},i} \cdot w_{\mathrm{tp},i} + g_{\mathrm{Sr},i} \cdot w_{\mathrm{Sr},i}}{w_{\mathrm{tp},i} + w_{\mathrm{Sr},i}}. \tag{9.6}$$

The weights $w_{\mathrm{tp/Sr},i}$ depend on the uncertainties $\sigma_{\mathrm{tp/Sr},i}$ of the measurement results of the two methods. They are calculated by

$$w_{\mathrm{tp/Sr},i} = \frac{1}{\sigma^2_{\mathrm{tp/Sr},i}}. \tag{9.7}$$

The combined uncertainty σ_{g_i} is given by

$$\frac{1}{\sigma^2_{g_i}} = \frac{1}{\sigma^2_{\mathrm{tp},i}} + \frac{1}{\sigma^2_{\mathrm{Sr},i}}. \tag{9.8}$$

Calculating the gains g_i for both chips i and the combined gain g, the result are

$$\begin{aligned} g_0 &= (171 \pm 10)\,\mathrm{e}^{-}\,\mathrm{Vcth}^{-1} \\ g_1 &= (176 \pm 10)\,\mathrm{e}^{-}\,\mathrm{Vcth}^{-1} \\ \Rightarrow g &= (173 \pm 7)\,\mathrm{e}^{-}\,\mathrm{Vcth}^{-1}. \end{aligned} \tag{9.9}$$

The combination of the two different methods and the information of both chips revealed the conversion factor g for the CBC. For all following consideration in this thesis $g = 173\,\mathrm{e}^{-}\,\mathrm{Vcth}^{-1}$ is used to express the comparator DAC units Vcth in an charge equivalent signal.

9.3 The Impact of Sensor Defects on the Module Performance

During the production of the 2S modules for the future Outer Tracker all sensors will be fully electrically characterized by the vendor. In addition, some of the measurements will be repeated by the sensor qualification centers on a random basis. Despite all quality control steps it is still possible that the modules contain sensors with defects. These can appear during transportation, sensor testing, module assembly or simply by handling the sensors. Furthermore, a small fraction of bad strips (e.g. strips with defects) have to be accepted from the vendor. This section investigates how different classes of sensor defects impact the performance of the modules. Besides that, methods are presented that help to identify the different classes of defects in modules.

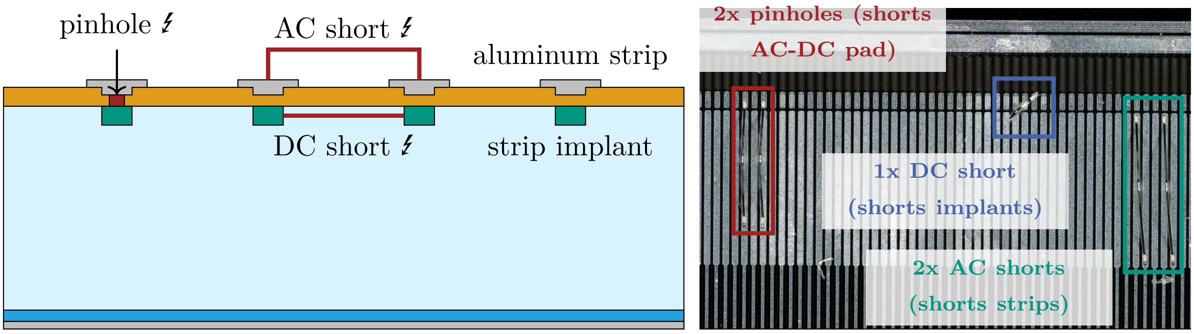

(a) Schematic illustration of sensor defects **(b)** Picture of generated defects

Figure 9.9: Illustration of sensor defects (a) and a picture of the wire bonds to artificially generate the defects (b). Wire bonds connect different sensor strip pads on MiMo2 and MiMo4 to generate pinholes, AC and DC shorts. For a pinhole the bond connects the AC and DC pad of one strip. A bond between the DC/AC pads of neighboring strips generates a DC/AC short.

9.3.1 Sensor Defects and their Creation

The occurence of sensor defects can have different reasons. The following list sums up the three different defect classes investigated in the scope of this thesis. Furthermore, the list presents possible causes for the defects and how they are artificially generated on the Mini Module prototypes.

- **Pinholes** are short circuits between the strip implant and the AC-coupled aluminum strip. They can occur during production and testing but also after years of operation in the tracker. High strip leakage current, in particular after irradiation, could lead to voltage drops between the aluminum strip and implant. Such voltage drops promote the creation of pinholes. Pinholes would make the readout become DC-like. As a consequence the CBC's analog front-end will not further be electrically isolated from the strip implant. Thus, leakage current from the sensor bulk drains into the analog front-end of the CBC via a pinhole. Unlike its predecessors, the third generation of the CBC provides no leakage current protection circuit [Pry19]. In that sense, it is crucial to investigate the CBC's behavior on pinholes. To artificially generate pinholes a wire bond short-circuits the AC and DC pad of a strip.

- **AC shorts** are shorts between adjacent aluminum strips. The handling of sensors during prototyping and sensor R&D showed that in most cases scratches on the sensor surface lead to this type of defect. The connection of the aluminum strips short-circuits the analog front-ends of the corresponding channels, which lead to a non-predictable behavior of the channels. A bond connection between the AC pads of neighboring strips creates an artificial AC short.

- **DC shorts** connect the implants of adjacent strips. Due to manufacturing faults the inter-strip isolation of strips can be insufficient, which leads to a conductive connection between neighboring implants. As a result, the capacitive load of the analog front-end increase due to the larger electrode area, resulting in enhanced noise. Fortunately, this kind of defects are very unlikely to occur. Again a bond connection emulates a DC short by connecting the DC pads of two adjacent strips.

Figure 9.9 illustrates the different sensor defect classes. Furthermore, it displays a picture of the bonds artificially generating the different defects. Not only single defects but also

Table 9.2: Three different classes of defects were artificially generated on the top sensors of MiMo4 and MiMo2. For all four sensors the same strip positions were chosen. Besides single defects also groups of defect clusters were investigated.

defect type	strips
pinhole	10, 21, 22, 33, 34, 35, 46, 48
AC short	116 – 117, 103 – 104 – 105, 88 – 89, 91 – 92
DC short	76 – 77

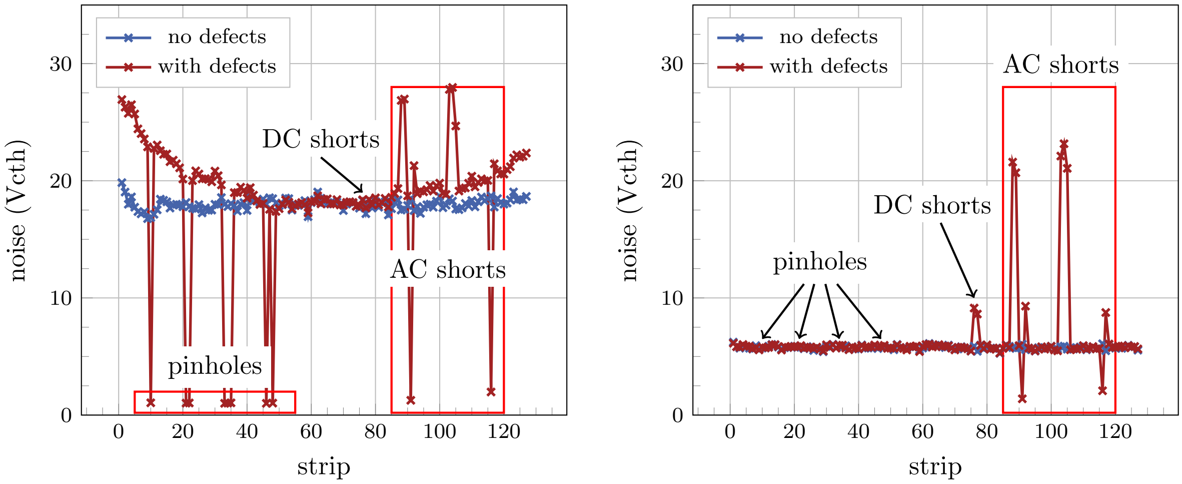

(a) 0 V

(b) 400 V

Figure 9.10: Strip noise with and without the defects of the top FZ290 sensor of MiMo4 for 0 V (a) and 400 V (b) at 20 °C. Without biasing (a) strips with pinholes exhibit very low noise (~ 1.5 Vcth). In the biased state (b) the noise of strips with pinholes is not affected. The noise of strips with DC shorts increased by about 50 %. Strips with AC shorts do not show a common behavior. Either the noise is very low, or high compared to non-affected strips. The noise of the surrounding strips without defects are not affected.

clusters of multiple strip defects were created, to investigate the influence of multiple defects on neighboring channels. The three defect classes have been created artificially on the unirradiated Mini Module MiMo4 and on the irradiated MiMo2 ($\phi = 2.5 \times 10^{14}\,\mathrm{n_{eq}/cm^2}$). Sensors made of both materials have been tested with the defects. Table 9.2 sums up the defects and for which strips they were generated.

9.3.2 Results

Different performance parameters of the sensors were investigated before and after adding the sensor defects. In particular, the strip noise and sensitivity to charge signals was recorded for different operation parameter (e.g. sensor voltage, temperature).

Figure 9.10 displays the strip noise for the top FZ290 sensor of MiMo4 (unirradiated) at 0 V and 400 V sensor bias voltage. The plot shows the measurement results before and after adding the sensor defects. Without biasing (figure 9.10a) the overall noise of the sensor is high. But for the *pinholes* the noise reduces to about 1.5 Vcth. This noise level is even lower as for unconnected strips and indicates a broken analog front-end of the channel. This effect vanishes

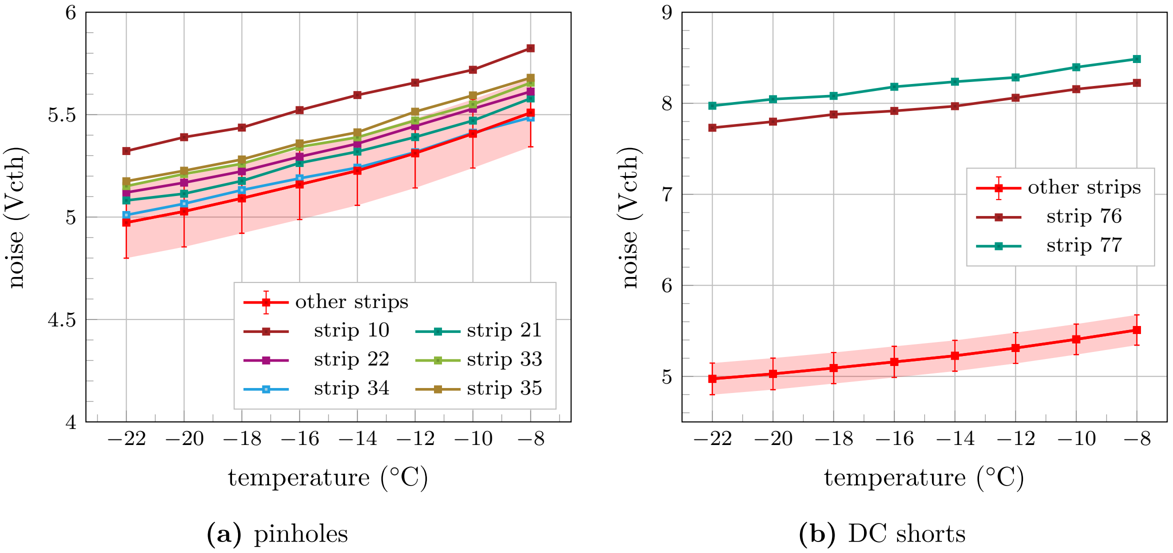

(a) pinholes

(b) DC shorts

Figure 9.11: Noise over temperature for the strips with pinholes (a) and DC shorts (b) compared with the average noise of the strips without defects. The measurements were performed with the top FZ290 sensor of MiMo2 at 600 V. For both defect classes the noise scales in the same manner as for the strips without defects. At about −10 °C the strip leakage current exceeds 1 µA, which is the maximum current expected after 4000 fb^{-1} [CMS21].

as soon as an external voltage is applied to the sensor. In biased operation, the noise of the strips with pinholes is the same as before adding the defects and comparable to strips without defect. A possible reason for the reduced noise can come from different potentials of the analog front-end and the strip implant. The potential difference then affects the baseline of the analog front-end. After irradiation this effect is gone (see figure A.11b).

For strips with *DC shorts* the noise increases by approximately 50 % to about 8 Vcth. This is caused by the additional load capacitance of the shorted implants. To reject noise hits from strips with DC shorts the threshold has to be increased. Depending on the irradiation state and hence the charge collection performance of the sensor it is not possible to increase the threshold without reducing the efficiency of all strips. Thus, in particular after irradiation strips with DC short will have to be masked to not generate noise hits.

The noise of strips with *AC shorts* do not show a common behavior. Either the strips show a very high or very low noise. The noise is independent of the sensor bias voltage. Since AC shorts connect the analog front-end of different channels the noise fluctuations can be a result of slightly different electric potentials of the analog front-ends. Channels with such a behavior have to be masked during the operation. Since these channels are already ruled out for the data acquisition from the noise point of view, in the following AC shorts will not be discussed more in detail.

To examine the influence of leakage current on the noise of strips with defects, the noise of the irradiated MiMo2 was measured at different temperatures between −24 °C and −8 °C. With increasing temperature the bulk leakage current increases. This was already observed and quantified in section 9.1. At about −10 °C the strip leakage current exceeds 1 µA, which is the maximum expected strip leakage current after 4000 fb^{-1} [CMS21]. However, strips with pinholes as well as with DC shorts show the same noise scaling with temperature as strips without defect. This is remarkable and not expected, since the analog front-ends of the CBC

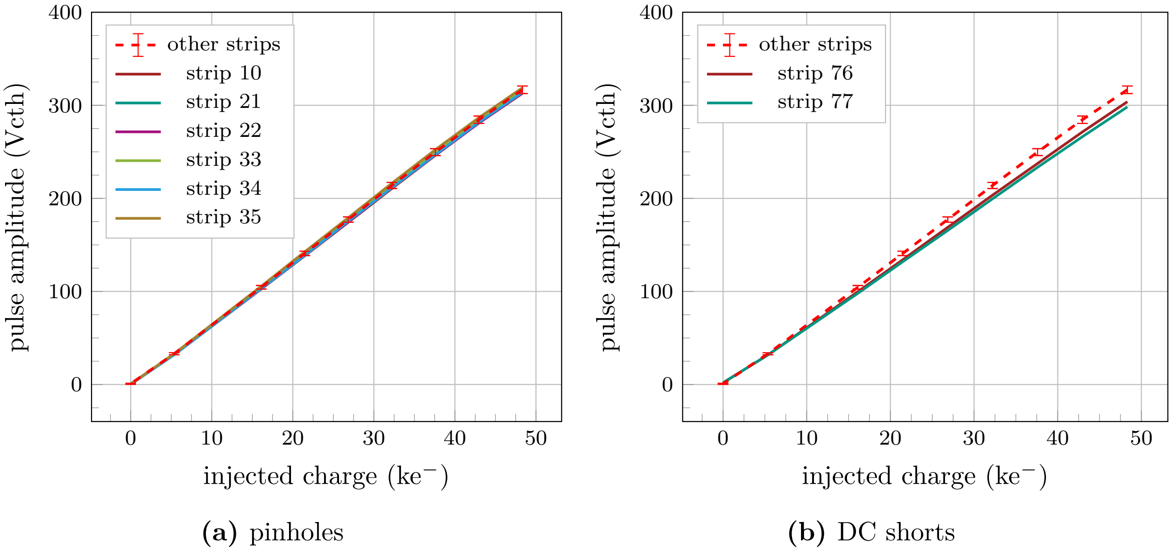

(a) pinholes **(b)** DC shorts

Figure 9.12: Measured pulse amplitude over the injected test pulse charge for strips with pinholes (a) and DC shorts (b). The plots show the results for the top FZ290 sensor of MiMo4 at 400 V and 20 °C. Channels connected to strips with pinholes see the same pulse amplitude as channels without defect. DC shorts lead to a small signal loss.

have no protection circuits against leakage current. The slightly increased noise of the strips with pinhole is a random effect, and was the same before adding the pinholes (see figure A.11).

Even though the noise is a very important quantity to describe the performance of the readout channels, it is important to see how they react on signals, too. Thus, the response of the channels on test pulses with different amplitudes was measured in the same way as for the test pulse calibration in section 9.2.3. Figure 9.12 compares the recorded pulse amplitude over the injected charge for strips with pinholes (a) and DC shorts (b) with the average response of the strips without defects. The measurements were performed with the FZ290 sensor of MiMo4 at 400 V bias voltage. The channels' response for strips with pinholes perfectly matches the expected behavior. Again no influence of the pinholes was detected. The channels connected to strips with DC shorts see less signal, as expected.

Finally, also the signals from a ^{90}Sr source were recorded, to inspect the response of the channels with defect to external signals generated in the sensors. Figure 9.13a displays the hit profile in the top FZ290 sensor of the unirradiated MiMo4. The events were recorded at $T = 20\,°\mathrm{C}$ and a threshold of $5000\,\mathrm{e}^-$. The number of hits, seen by strips with a pinhole, is comparable to the number of hits detected by strips in the vicinity of the defects. As expected from the noise and test pulse measurements, no excess or loss of hits is observed. However, the strips with DC short see a slightly increased number of hits, which comes from fake hits due to the higher noise for these strips. Furthermore, the hit profile demonstrates the malfunction of channels with AC shorts. On the one hand, the channels with very low noise do not see hits at all. On the other hand, noise hits dramatically increase the number of hits for channels with high noise.

After irradiation the Mini Module show the same behavior, as shown in figure 9.13b. The hit profile was recorded at $T = -10\,°\mathrm{C}$ with MiMo2 so that the strip leakage current was increased to about 1.2 µA.

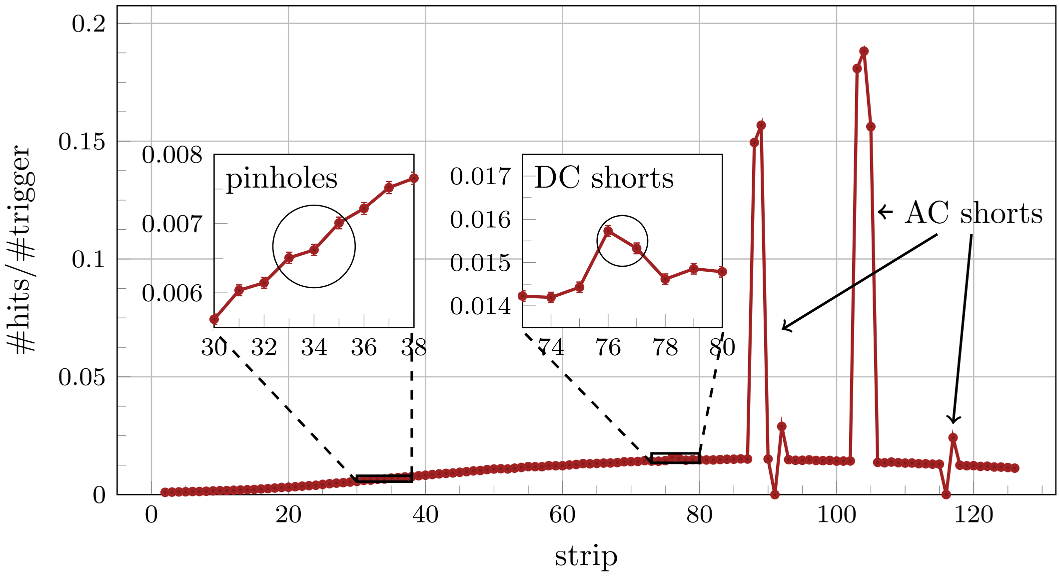

(a) MiMo4, $T = 20\,°\mathrm{C}$, threshold $5000\,\mathrm{e}^-$

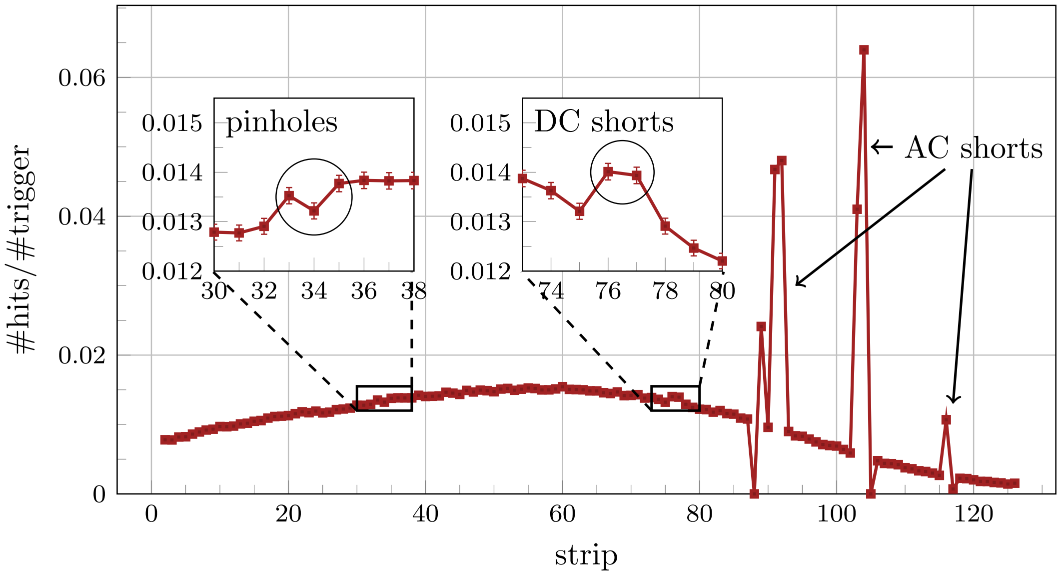

(b) MiMo2, $T = -10\,°\mathrm{C}$, $I_{\mathrm{strip}} \approx 1.2\,\mathrm{\mu A}$, threshold $5000\,\mathrm{e}^-$

Figure 9.13: Hit profiles in FZ290 sensor with defects, before (a) and after (b) irradiation. The number of hits in strips with pinholes is comparable to the surrounding, whereas strips with DC shorts see a slightly increased number of hits by noise. The operation of strips with AC shorts is not possible, either they see large excess of noise hits or no hits at all.

However, for all classes of defects neither an effect on the readout chip as a whole nor on the strips next to the defects was observed. Thus, for the operation in the CMS detector channels connected to strips with defects can be simply masked and do not have to be disconnected from the strips.

9.4 Conclusions

The Mini Modules built in the scope of this thesis were used for a wide range of laboratory measurements. Different module characteristics have been studied. Besides extensive studies of the modules' noise dependence on temperature, sensor voltage and sensor leakage current, the modules' behavior under the influence of sensor defects (pinholes, AC shorts and DC shorts) has been investigated. The measurements demonstrate the robustness of the CBC against pinholes even at high sensor leakage currents, as it is expected after years of operation in the CMS detector. Furthermore, the comparator DAC value Vcth of the CBC has been converted to an charge equivalent signal by using reference measurements of the ALiBaVa setup and internal test pulses. The resulting gain factor is $(173 \pm 7)\,\mathrm{e}^{-}\,\mathrm{Vcth}^{-1}$. Taking into account this gain factor the measurements demonstrated that the noise of the CBC is below the $1000\,\mathrm{e}^{-}$ design value for the expected operation conditions of the future Outer Tracker.

10

2S Mini Module Beam Test

Beam tests provide a perfect environment to determine the performance of detector prototypes. In the scope of this thesis three Mini Modules were characterized in a beam test at DESY in Hamburg. The main focus of the beam test was the comparison of the performance of the two sensor materials thFZ240 and FZ290 in combination with the readout chip of the 2S modules, the CBC. Besides an unirradiated Mini Module two modules with irradiated sensors were tested in the beam to study the influence of radiation damage and annealing on the module performance.

This chapter first compares the cluster efficiency of the different materials, fluences and annealing times for different thresholds. Furthermore, it evaluates the influence of the sensor bias voltage and particle track inclination angle on the efficiency. The excellent track resolution of the telescope allows the identification of inefficient regions on a substrip scale.

Besides the investigation of clusters the stacked sensor design of the Mini Modules allows the verification of the stub finding logic of the CBC. The second part of the chapter shows the stub detection efficiency and its dependence on the threshold, bias voltage and track inclination for the different materials, fluences and annealing times. The descriptions of the analysis, selection criteria and matching conditions were already given in section 6.5

10.1 Cluster Efficiency and Irradiation

One important parameter that determines the performance of the Mini Module is the cluster detection efficiency. For each of the four sensors of the modules the efficiency was determined individually as described in section 6.5. However, the efficiency depends not only on the material type but also on many other parameters, like irradiation fluence, annealing, sensor bias voltage and the detection threshold of the readout chip. This section evaluates the influence of these parameters on the cluster detection efficiency.

10.1.1 Threshold Scans

Since the CBC is a binary readout chip it only detects signals exceeding a programmable detection threshold. In general, a lower threshold results in a better cluster detection efficiency. However, lowering the threshold increases the probability to detect hits generated by noise, too. Thus, the optimal threshold of the CBC maximizes the cluster detection efficiency while restricting the noise occupancy to an acceptable level. For the operation in the CMS Outer Tracker, an acceptable trade-off is to have at least a cluster detection efficiency of 99.5 % with a noise hit occupancy below 10^{-4} [The20]. To evaluate whether such an operation point exists, threshold scans at nominal sensor voltage have been performed for all Mini Modules. The modules were positioned in such a way that the acceptance window of the telescope covered both sensor stacks of the module. Thus, the results for one threshold point have been measured for all sensors of a module during the same run. The electron beam passed the sensors in vertical direction from the top side at a beam energy of 5.6 GeV. One million events were

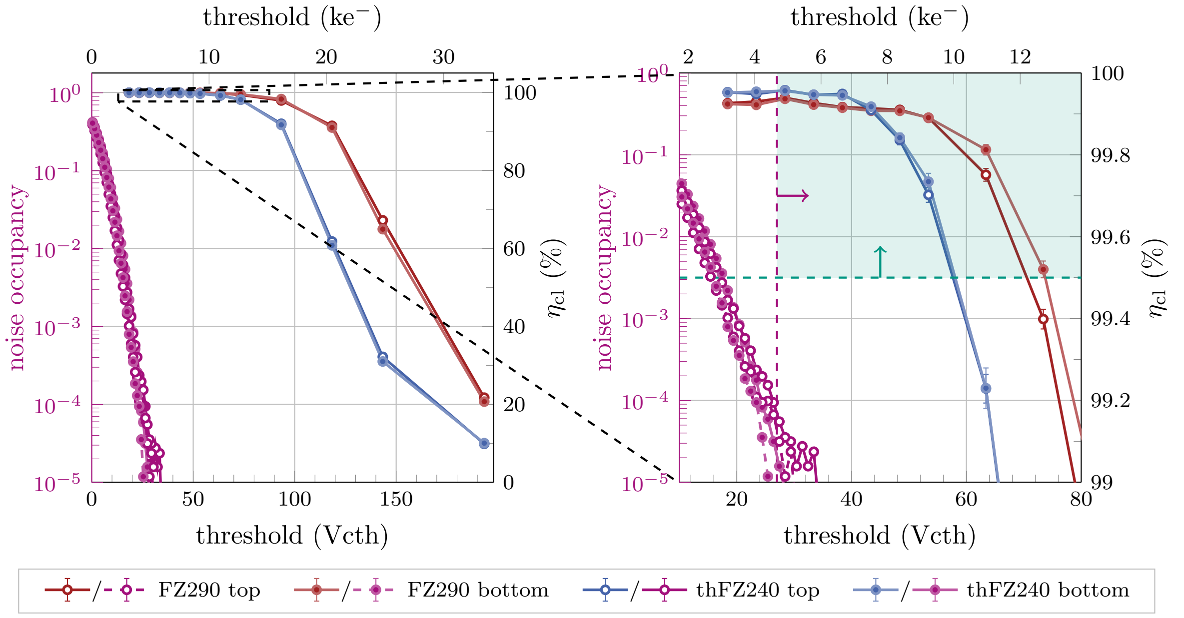

Figure 10.1: Cluster efficiency (red and blue, scale on the right) and noise occupancy (purple, scale on the left) over threshold for the unirradiated MiMo1 at 20 °C and 400 V bias voltage. The zoomed plot (right) demonstrates that both materials meet the requirements to operate efficiently in the future Outer Tracker (green region) and reach a cluster detection efficiency of more than 99.9 % with a noise occupancy below 1×10^{-5}. The thinner thFZ240 sensors (blue) starts to lose efficiency at lower thresholds compared to the thicker FZ290 sensors (red).

recorded for each run, resulting in approximately 250 k to 300 k referenced tracks for each sensor stack. The remaining tracks were passing the module in the gap between the two sensors.

Before performing a threshold scan the channel offsets were trimmed to equalize the strips' response behavior. This trimming was done once with biased sensors and in thermal equilibrium at the targeted operation temperature. Furthermore, for all modules threshold scans of the noise were recorded in the beam setup (without beam) to determine the background noise occupancy. Figures 10.1 to 10.3 display the outcome of the cluster efficiency threshold scans (red, blue) and noise measurements (purple). Dashed lines mark the acceptable noise and efficiency limits and the green region the accepted region for efficient operation. Every measurement point in the green region reflects an operation point fulfilling the specifications. This section discusses the results of the measurements more in detail.

The *unirradiated MiMo1* was operated at 20 °C. Since the thFZ240/FZ290 sensors are fully depleted at 200 V/300 V the sensors were biased at 400 V, which is well above the full depletion voltage. The results of the threshold scan shown in figure 10.1 demonstrate that both sensor materials meet the requirements for the operation in the Outer Tracker. Both reach a cluster detection efficiency of more than 99.9 % with a noise occupancy below 1×10^{-5}. Since the thicker FZ290 material delivers a larger seed signal compared to the thinner thFZ240 material it fulfills the condition for a wider threshold range. That was already expected from the charge collection measurements with the ALiBaVa setup (see also figure A.9). However, the thFZ240 sensors reach a slightly higher cluster efficiency. One reason could be the stronger electric field in the thinner thFZ240 sensors which generates a slightly sharper charge pulse in the analog front-end.

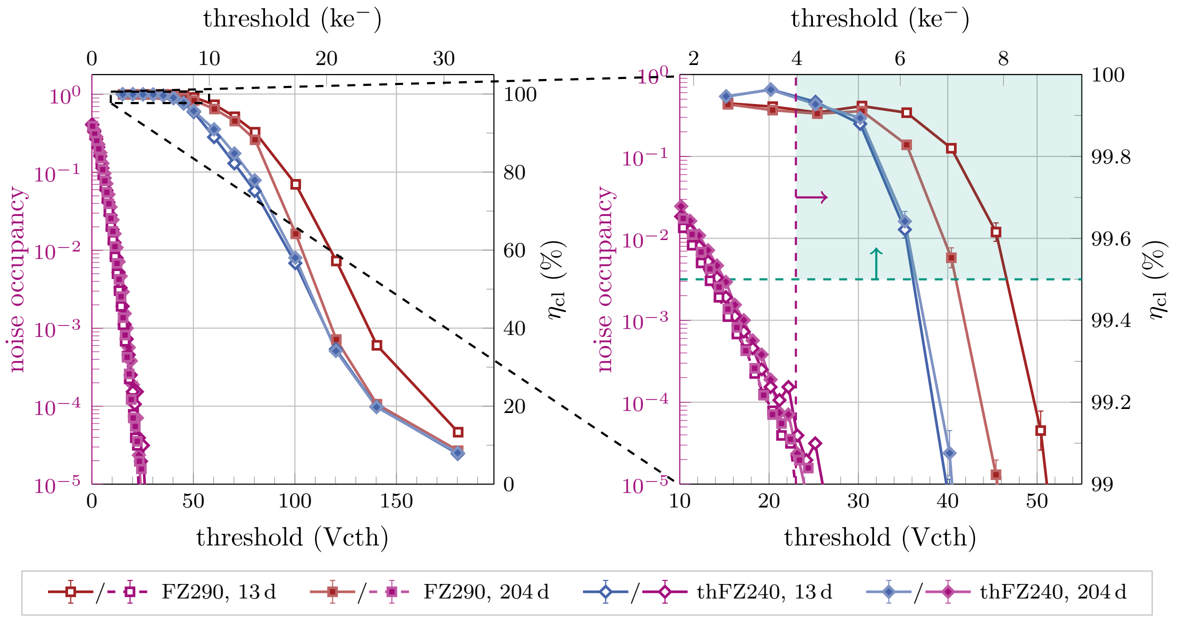

Figure 10.2: Cluster efficiency (red and blue, scale on the right) and noise occupancy (purple, scale on the left) over threshold for MiMo2 ($2.5 \times 10^{14}\,\mathrm{n_{eq}/cm^2}$) at −22 °C and 600 V bias voltage. The zoomed plot (right) demonstrates that the FZ290 sensors (red) exceed the required efficiency limit for a wider threshold range compared to the thFZ240 sensors (blue). Long annealing (204 d eq. at 21 °C) reduces the efficiency of the FZ290 sensors, whereas the thFZ240 sensors are not prone to annealing at this fluence. All sensors reach more than 99.9 % efficiency.

The sensors of *MiMo2* were irradiated with neutrons to fluences of $2.5 \times 10^{14}\,\mathrm{n_{eq}/cm^2}$, which corresponds to the maximum expected fluence for about 70 % of the 2S modules in the nominal $3000\,\mathrm{fb}^{-1}$ scenario. The top/bottom sensors of the stacks have been annealed to 13 d/204 d equivalent annealing at room temperature. For the measurements the module was cooled down to about −22 °C and the sensors biased with the nominal 600 V. Figure 10.2 shows the cluster efficiency and noise occupancy for the recorded threshold scan. Compared to the unirradiated sensors the cluster efficiency starts to drop at lower thresholds, since radiation damage reduces the charge collection efficiency of the sensors. Both FZ290 sensors deliver more signal than the thFZ240 sensors and hence stay above the required efficiency limit for a wider threshold range. Furthermore, the FZ290 material is more sensitive to annealing. While both thFZ240 sensors exhibit a very similar efficiency over threshold characteristics, the long annealing reduces the performance of the FZ290 material. This corresponds to the observations of the charge collection measurements with the ALiBaVa setup as shown in figure 8.7a. An increase of the sensor bias voltage can compensate the charge efficiency loss, as discussed later. However, all sensors irradiated to $2.5 \times 10^{14}\,\mathrm{n_{eq}/cm^2}$ reach more than 99.9 % efficiency and meet the specified efficiency and noise occupancy requirements.

In the ultimate $4000\,\mathrm{fb}^{-1}$ scenario a small number of 2S modules will be exposed to fluences of more than $5 \times 10^{14}\,\mathrm{n_{eq}/cm^2}$. Thus, the sensors of *MiMo3* were irradiated with neutrons to this fluence. Again the sensors of the two layers were annealed to 13 d and 204 d equivalent annealing time at room temperature. For the measurements the module was cooled down to approximately −22 °C and operated with nominal 600 V sensor bias. Figure 10.3 presents the results of the threshold scan. The cluster efficiency of all sensors starts to drop at much

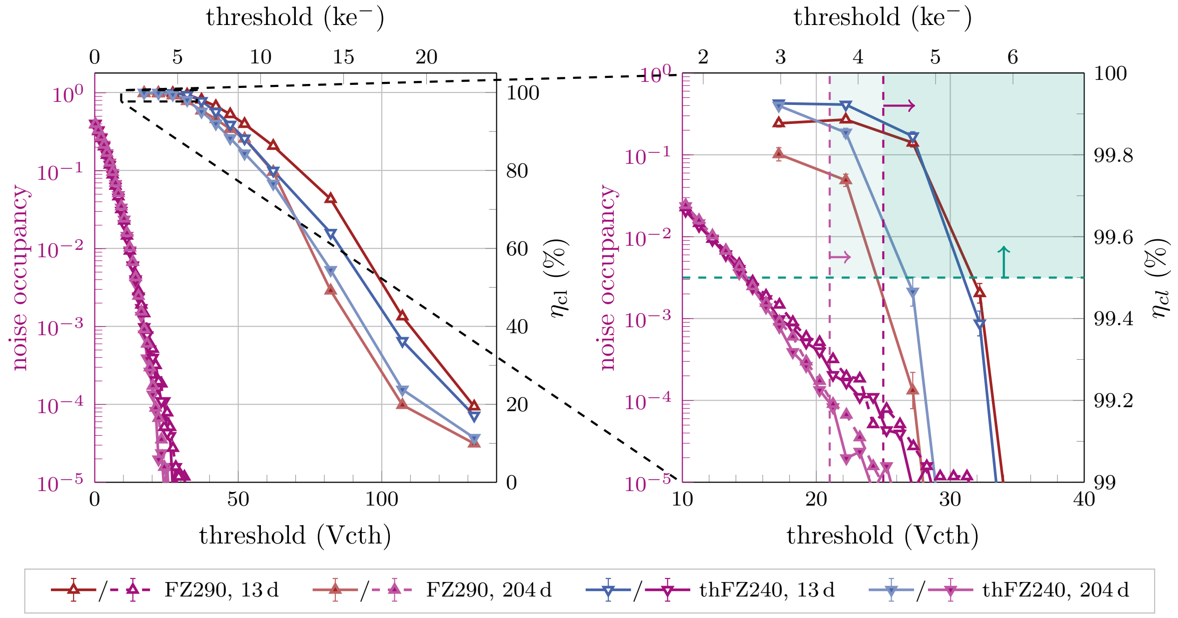

Figure 10.3: Cluster efficiency (red and blue, scale on the right) and noise occupancy (purple, scale on the left) over threshold for MiMo3 ($5 \times 10^{14}\,\mathrm{n_{eq}/cm^2}$) at −22 °C and 600 V sensor bias. The zoomed plot (right) demonstrates that the long annealing (204 d eq. time at 21 °C) reduces the cluster detection efficiency of both materials. In addition, the annealing has a beneficial effect on the noise occupancy so that the minimal threshold reduces about 700 e$^-$ (pale purple dashed line). All sensors fulfill the requirements for the operation in the 2S modules.

lower thresholds compared to the less irradiated sensors. Thus, all sensors strongly suffered from the strong radiation damage. Furthermore, the different annealing times influence both sensor materials in the same manner. For the shorter annealing of 13 d equivalent time at room temperature the cluster efficiency of both materials have a similar threshold dependence. Sensors of both materials can be operated at about 99.85 % efficiency with a noise occupancy below the specified upper limit.

The longer annealing of 204 d equivalent time at room temperature reduces the cluster detection efficiency of both materials. However, still for both materials a suitable threshold can be found that fulfills the operation requirements. The efficiency of the FZ290 sensors suffers stronger and lowers to about 99.75 %. Even after the long annealing the cluster efficiency of the thFZ40 sensor is about 99.85 %. Remarkable is the influence of the annealing on the sensor noise. The beneficial effect of the annealing on the sensor current reduces the sensor noise. By the noise reduction, the long annealed sensors fulfill the specifications on the noise occupancy even at a threshold about 700 e$^-$ lower compared to the sensors with short annealing (dashed and pale purple line). Only due to this noise reduction the long annealed FZ290 sensor meets the operation requirements. Again the results obtained in the beam test match the seed signal measurements with ALiBaVa setup as shown in figure 8.7b. Regarding the more conservative nominal threshold of 5000 e$^-$ (five times the noise) none of the sensors exceed 99.5 % cluster efficiency for the next higher thresholds investigated in this study. However, the extrapolation of the data points around 5000 e$^-$ threshold suggests that there could be a suitable operation point for the sensors with short annealing.

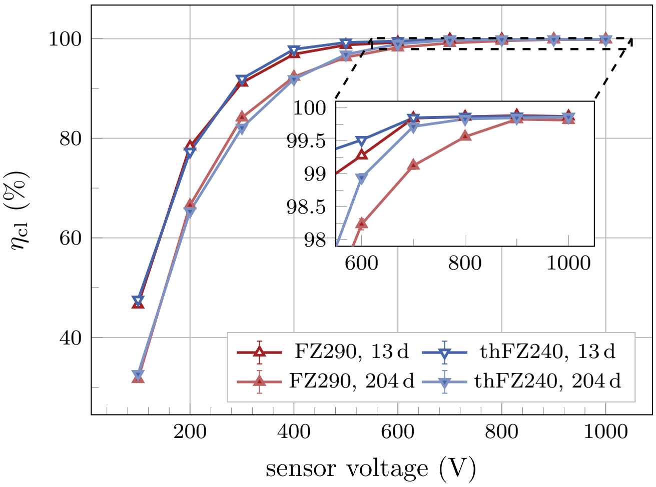

Figure 10.4: Cluster efficiency over the sensor bias voltage for MiMo3 ($5 \times 10^{14}\,\mathrm{n_{eq}/cm^2}$). The applied threshold for the sensors range between 5000 e^- and 5700 e^-. An increase of the bias voltage improves the cluster detection efficiency. The sensors with shorter annealing times and the long-annealed thFZ240 sensor reach an efficiency plateau of more than 99.8 % at about 700 V. The FZ290 sensor with 204 d eq. annealing time at 21 °C reaches the plateau at about 900 V.

In summary, already the threshold scans show that both sensor materials meet the requirements for the operation in the 2S modules of the future Outer Tracker of the CMS experiment. The irradiation with $5 \times 10^{14}\,\mathrm{n_{eq}/cm^2}$ neutrons will bring the sensors very close to requirement limits and annealing becomes crucial. If at some point the ultimate scenario of the HL-LHC becomes the baseline, the detector operation group will have to monitor carefully the annealing status of the tracker and its influence on the particle detection efficiency. Even though long annealing has a beneficial effect on the sensor leakage current and thermal behavior of the sensors, it will reduce the cluster efficiency. Fortunately, there are other operation parameters which improve the cluster detection efficiency, as discussed in the following.

10.1.2 Sensor Bias Voltage Scans

Not only the threshold of the CBC has an influence on the cluster detection efficiency but also the sensor bias voltage. The depletion voltage of sensors increases with irradiation and hence a high enough bias voltage is crucial for efficient operation. Furthermore, the higher sensor voltage increases the electric field in the sensor and hence attenuate charge trapping. Thus, the cluster detection efficiency of all sensors and modules was measured for different bias voltages.

Figure 10.4 shows the result of the bias voltage scan for MiMo3. Again the module was cooled down to approximately −22 °C. Unfortunately, the threshold value was not recorded correctly so that it had to be determined for the individual sensors by comparing the 600 V point with the threshold scan results. The thresholds for the DUTs are in the range of 5000 e^- to 5700 e^-. However, this does not influence the outcome of this measurement, since the threshold for each individual DUT was fixed over the scan. The outcome of this measurement is that an increase of the sensor bias voltage indeed improves the cluster efficiency. Again the sensors with longer annealing times are less efficient compared to sensors with shorter annealing times. At about 700 V both thFZ240 sensors and the FZ290 with short annealing (13 d eq. at 21 °C) reach the efficiency plateau at about 99.8 %. As already observed in the threshold scan, the FZ290 sensor is more prone to annealing and the longer annealed sensor reaches its maximum efficiency

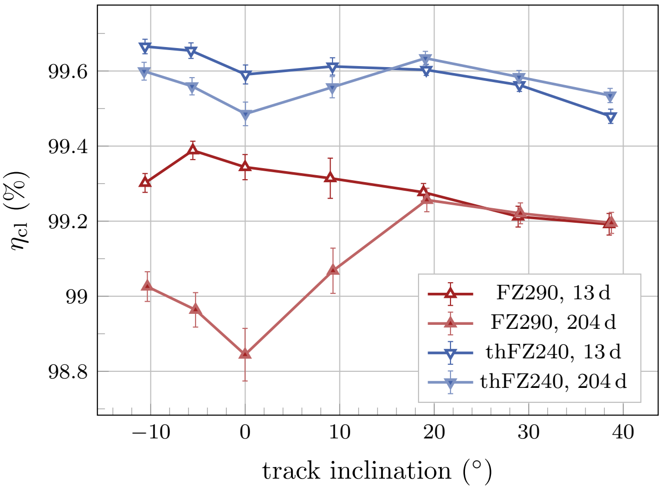

Figure 10.5: Cluster efficiency for different track inclinations between −10° to 40° for MiMo3. The bias voltage was 600 V, the threshold in the range of 4800 e^- to 5500 e^- and the module cooled down to −22 °C. The sensors lose some efficiency for larger track inclinations. The cluster efficiency of the long annealed sensors increase for angles up to 20° and then shows the same characteristics as the short annealed ones. The increase of the efficiency is more pronounced for the long annealed FZ290 sensor.

not before 900 V. However, this measurement demonstrates that the optional increase of the sensor bias voltage to at least 800 V improves the cluster detection efficiency. In the 4000 fb^{-1} scenario this opportunity is mandatory if intentional long annealing is necessary to reduce the sensor leakage current.

The corresponding plots for the unirradiated MiMo1 and for MiMo2 with $2.5 \times 10^{14}\,\mathrm{n_{eq}/cm^2}$ are shown in figures B.1 and B.2, respectively. The voltage scan for MiMo1 validates that a bias voltage of 400 V is sufficient to achieve the full cluster detection efficiency. Furthermore, the measurement with MiMo2 shows that 600 V nominal bias voltage is sufficient for the operation.

10.1.3 The Influence of Inclined Tracks on the Cluster Efficiency

All results showed in the previous sections were recorded with particles passing the sensors in perpendicular direction. However, in the Outer Tracker this will not always be the case. In the tracker geometry the sensors of the 2S modules do not exactly face the interaction point, but with some inclination. In addition, the magnet of CMS deflects charged particles so that they hit the 2S modules under different inclination angles. The inclination angle is defined as the angle between the sensor normal vector and the particle track. For inclined tracks the path lengths of the particles through the sensors increase, and hence also the energy they deposit. As a result, the cluster efficiency increases with the particle inclination. Only for very large inclination angles the mean path length of the particles below the readout strip will begin to decrease again for geometric reasons. Thus, the cluster efficiency starts to decrease again as well.

Figure 10.5 shows the cluster efficiency for various inclination angles measured with MiMo3. The sensors were biased with 600 V and the module cooled down to −22 °C. For the measurements the module was rotated in both directions around the y-axis, which is parallel to the strips. For the same reasons as before the threshold had to be determined by the threshold scan and is approximately 4800 e^- to 5500 e^-, but fixed for the individual sensors. For the

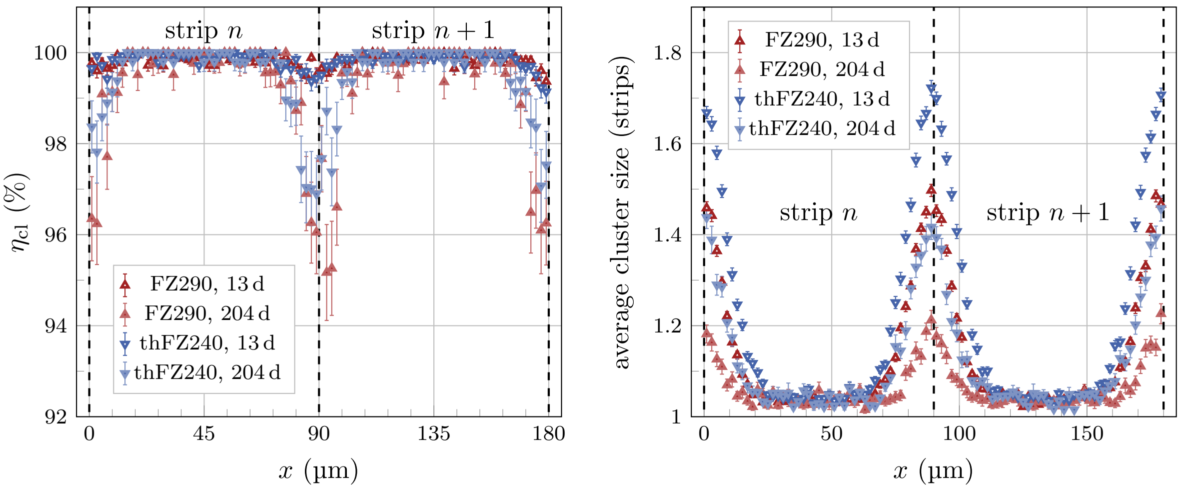

(a) Sub strip cluster efficiency **(b)** Averaged sub strip cluster size

Figure 10.6: Sub strip efficiency (a) and average cluster size (b) over the track position in two strip unit cells recorded with MiMo3 and vertically inclined tracks. The module temperature was −22 °C, the sensors biased with 600 V and the threshold at 4600 e^-. The efficiency of the sensors in the region between the strip implants reduces due to charge sharing. This effect is more pronounced for the longer annealed sensors. The effect of charge sharing manifests in the on average larger cluster size for tracks passing in between of the strips.

sensors with short annealing times (13 d eq. time at 21 °C) the cluster detection efficiency drops slightly with increasing angles. The effect is more pronounced for the thicker FZ290 sensors. A reason could be additional scattering in the thicker FZ290 sensors, that reduces the tracking performance of the telescope. Furthermore, the downstream distance of the telescope x_d was increased to measure large inclination angles for mechanical reasons. This also reduces the telescope resolution as shown in the simulation results in figure A.12b.

For the sensors with long annealing times (204 d eq. time at 21 °C) the cluster detection efficiency increases with the inclination angle until reaching a maximum for an inclination of about 20°. This effect is more pronounced for the FZ290 sensors and comes from the overall lower efficiency of the FZ290 sensors at this threshold and vertical inclination (see figure 10.3). For larger inclinations the cluster efficiency decreases again and follows the characteristics of the sensor with short annealing.

Figures B.3 and B.4 display the complementary measurements for MiMo1 and MiMo2. The sensors of both modules are fully efficient at the recorded threshold and thus no efficiency dependence on the inclination angle can be observed. The sensors reach more than 99.9 % efficiency for all tested particle track inclination angles.

The main result of this scan is that even in the ultimate 4000 fb^{-1} scenario the sensor with the lowest cluster efficiency (FZ290 and long annealing) profits strongly from the different track inclinations expected in the CMS Outer Tracker.

10.1.4 Sub Strip Efficiency

The high resolution of the telescope tracks not only allows the evaluation of the global DUT efficiency but also the scanning of the efficiency on sub strip scales. To increase the statistics the track position information is folded into two strip unit cells. By doing so inefficient regions over the unit cells become visible. The strip implants are at x positions 45 µm and 135 µm.

Figure 10.6 displays the cluster efficiency (a) and the average cluster size (b) of vertical tracks over the track position in two strip unit cells. The run was recorded using MiMo3 at $-22\,°\mathrm{C}$, $600\,\mathrm{V}$ bias voltage and $4600\,\mathrm{e}^-$ nominal threshold (five times the noise).

The only area for which the sensors lose efficiency is in the central region exactly between the strip implants. The adjacent strip implants share the charge, which was generated by particles passing this region. By this charge sharing effect the individual strip signal is only a fraction of the total ionized charge. Since the CBC detects only signals exceeding the threshold the probability to detect a hit is reduced in this region. The strength of this effect depends on the threshold and charge collection efficiency of the sensors. Since the threshold is the same for all sensors the charge collection efficiency drives the outcome of this measurement.

The sensors with short annealing times show only a very slight efficiency dip in the central region. This matches the observation of the threshold scan and ALiBaVa measurements, for which the sensors with short annealing times reach higher efficiencies and larger seed signals, respectively. The FZ290 sensor with 204 d equivalent annealing time at 21 °C shows the strongest dip. The efficiency in between the strip implants drops to approximately 94 %. This less efficient area is responsible for the poorer performance of the whole sensor (in particular at vertical inclination) as shown in figures 10.3 and 10.5.

The average cluster size over the track position in two strip unit cells demonstrates the effect of charge sharing. For particles passing the sensors in between of two strip implants the recorded average cluster size is increased. The cluster size of the sensors with short annealing times is larger compared to the long annealed sensors. Furthermore, the thFZ240 sensors show a larger cluster size compared to the FZ290 sensors of the same annealing state.

Figures B.5 and B.6 show the corresponding plots for the unirradiated MiMo1 and MiMo2 ($2.5\,\mathrm{n_{eq}/cm^2}$). At nominal threshold there are no efficiency losses in the central region between the strip implants; however, the average cluster size still demonstrates the effect of charge sharing. Furthermore, the measurements demonstrate that the charge sharing increases with irradiation, since the average cluster size in the central region increases. Possible reasons for this effect are the changing electric field with irradiation and the different bias voltages.

10.2 Spatial Resolution of the Sensors in the Mini Modules

Another very important parameter that drives the tracking performance is the spatial resolution of the DUT. The binary resolution of an ideal binary detector for vertically inclined track and one strip clusters is $p/\sqrt{12}$, with the strip pitch p. However, this is not the case for real detectors. The resolution of a real detector depends on several parameters. Charge sharing between neighboring strips improves the resolution. If a particle passes a sensor in the region in between strips charge sharing can cause hits in both strips. In this case the cluster center is in between the strips and a better estimation of the track position compared to the individual strip hits. The same effect improves the resolution for tracking of inclined tracks. If the particle passes the sensor under a non-zero inclination angle it promotes the generation of a cluster expanding over multiple strips. Again this effect improves the resolution.

For geometrical reasons a binary chip yields the best tracking resolution for an average cluster size of $n + 0.5$ strips ($n = 1, 2, \ldots$). In this case there are regions where n and $n + 1$ strips contribute to the cluster and the cluster center yields a better estimation of the track position. However, the measured average cluster size does not only depend on the track inclination angle but also on other operation parameters, like the threshold and bias voltage. Furthermore, the probability to create δ electrons and for scattering increases for larger inclination angles. Both effects also increase the cluster size.

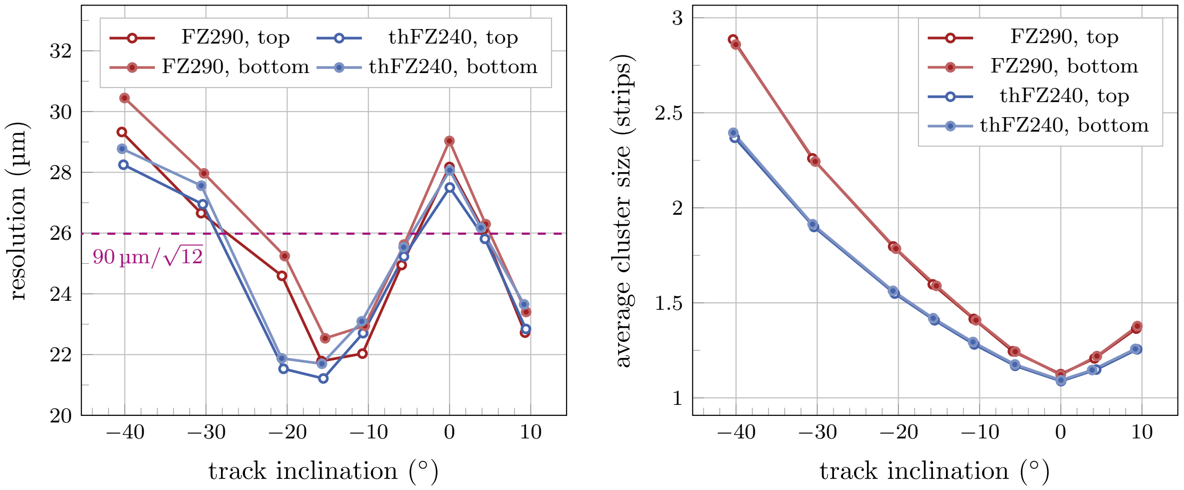

(a) Resolution over track inclination **(b)** Average cluster size over track inclination

Figure 10.7: Resolution (a) and average cluster size (b) over the particle track inclination angle for the unirradiated MiMo1. The sensors were biased with 400 V and the threshold was 4800 e⁻. All DUTs reach their best resolution for an average cluster size of 1.5 strips. The spatial resolution varies between 22 µm and 30 µm, depending on the inclination angle

A first order approximation of the DUT resolution is the standard deviation $\sigma_{\Delta x_{\mathrm{cl}}}$ of the track-cluster residual distribution, as described in section 6.5.6. However, this is a worst case approximation of the *real* DUT resolution, since the residual also contains the tracking resolution. But since the expected resolution of the telescope for the setup is in the range between 4 µm and 5 µm (see figure A.12), this has only a minor effect on the residual distribution.

Figure 10.7 shows the resolution and average cluster size of the *unirradiated MiMo1* for different particle inclination angles. The sensors were biased with 400 V and the threshold was approximately 4800 e⁻. The rotation angles of the DUTs were reconstructed individually for every DUT during the alignment process. Since the DUTs rotate within the beam the rotation angle equals the inclination angle of the particles.

The DUTs of different sensor material reach their best resolution for different rotation angles. For the thinner thFZ240 sensors the particles have to strike the sensors under a larger inclination angle to create the same average cluster size compared to the FZ290 sensors. However, sensors of both materials reach a resolution of 22 µm to 23 µm at the inclination angle were the average cluster size becomes 1.5 strips. This resolution is also far better than the binary resolution of one strip clusters, which is approximately 26 µm. The average cluster size over the unit cell for the different inclination angles and the two different materials is displayed in figure B.7.

For even larger clusters with an average size of 2.5 strips there is no minimum in the resolution measurable. This could have several reasons. At the rotation for which the cluster size becomes exactly 2.5 no measurements has been performed. Only for the thFZ240 sensors the 40° rotation is close to that point, and indeed the resolution worsens not as strong as for the FZ290 sensor for this rotation. Furthermore, the tracking resolution decreases for larger rotation angles. On the one hand, for mechanical reasons the telescope distance to the DUT was increased for the measurements of large angles. On the other hand, the track extrapolation onto the DUT reference plane, where the residual is defined, suffers from the rotation of the sensors. The uncertainty on the track has to be projected into the sensor frame.

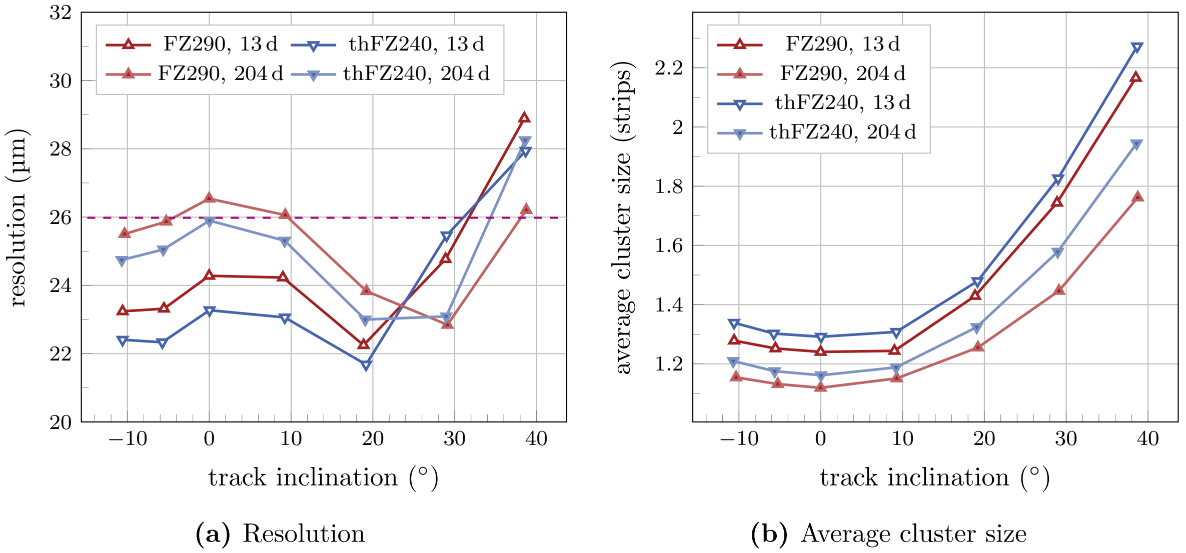

(a) Resolution **(b)** Average cluster size

Figure 10.8: Resolution (a) and cluster size (b) over the track inclination angle for MiMo3 ($5 \times 10^{14}\,\mathrm{n_{eq}/cm^2}$). The sensors were operated at 600 V and a threshold of about 4800 $\mathrm{e^-}$ to 5500 $\mathrm{e^-}$ was used. All DUTs have their optimum resolution for an average cluster size of 1.5 strips. The spatial resolution varies depending on the rotation angle between 22 µm and 29 µm. For vertically inclined tracks the irradiated sensors reach the binary resolution ($90\,\mu\mathrm{m}/\sqrt{12} = 26\,\mu\mathrm{m}$) or better.

The measurements with *MiMo3* ($5 \times 10^{14}\,\mathrm{n_{eq}/cm^2}$) exhibit a similar behavior. Figure 10.8 displays the outcome of the measurements. The sensor bias voltage was 600 V and the threshold of the individual DUT in the range of 4800 $\mathrm{e^-}$ to 5500 $\mathrm{e^-}$ for the same reasons as explained before. However, the threshold of each DUT was fixed during the scan. Again all sensors yield the best resolution for an average cluster size of 1.5 strips. The longer annealed sensors (204 d eq. time at 21 °C) reach the best resolution at about 30°. This is a far larger inclination angle compared to the short annealed sensors, which reach the optimum at 20°. The reason for this behavior is the reduced charge collection efficiency for the long annealing. To generate a larger cluster a sensor with less charge collection efficiency requires a larger particle inclination angle. The larger angle increase the average path length of the particle in the sensor and thus the deposited signal.

Remarkable is the better resolution for low inclination angles ($< 10°$) of the irradiated sensors compared to the measurements with MiMo1. The resolution of the unirradiated sensors mainly suffers from large displaced cluster from δ electrons (see figure 6.16). Since the charge collection efficiency decreases with irradiation the probability to detect such clusters reduces, too. Besides this effect the differing thresholds also influence the resolution measurement.

In summary, all sensors tested in the beam test yield a resolution of better than 30 µm. For inclined particle tracks the resolution improves down to approximately 22 µm, which is better than the binary resolution for single strip clusters. Radiation damage in the sensors does not spoil the resolution, but rather improves the resolution by suppressing the detection of displaced δ clusters for vertically inclined tracks. However, due to the binary nature of the readout no weighted cluster center can be determined, which limits the resolution for the particle detection compared to analog readout.

10.3 The Stub Efficiency and Tests of the Stub Finding Logic

One novelty of the future Outer Tracker is its contribution to the level-1 trigger stage of CMS. To reduce the amount of data passed to the level-1 trigger, the future modules will identify particles with large transverse momentum already on module level. In case of such a particle the modules generate a stub signal and emit the stub signals at 40 MHz bunch crossing rate. An FPGA based track trigger uses the stub information to perform a real time tracking of the high-p_T particles at bunch crossing rate. The track information of high-p_T particles is transmitted to the level-1 trigger to support and improve the trigger decision. Thus, the efficient stub finding is crucial for tracking and the correctness of the trigger decisions.

To investigate the performance and functionality of the stub finding logic a similar layered structure as in the 2S modules was chosen for the design of the Mini Modules. In the Mini Modules the two sensors of the same material form a stack on top of each other. Thus, the signals of the sensors of the same material contribute to the stub finding of one CBC. For time reasons only one stub logic setting has been investigated during the beam test. All results were obtained using the following stub logic options:

- The *cluster size cut* was set to three strips, so that only clusters with a maximum size of three strips were accepted by the stub finding logic. The cut holds for both sensor layers.
- All four *offsets* for the different regions of the CBCs were set to zero.
- The *correlation window* was set to 3.5 strips (7 half-strips).

The firmware of the FC7 readout board combines the data of the level-1 and stub data streams in one event. Thus, the following results were recorded for the same runs and tracks as already shown for the cluster efficiency and resolution analysis.

10.3.1 Threshold Scan

This section discusses the threshold dependency of the stub efficiency for vertically inclined tracks. As for the cluster efficiency, also the stub detection efficiency η_s strongly depends on the detection threshold. The simultaneous recording of the stub and cluster data allows the comparison of the two data streams. Thus, besides the stub efficiency, also the combined cluster efficiency η_comb of the sensor stack is shown. It can be calculated as

$$\eta_\mathrm{comb} = \eta_\mathrm{cl,3}^\mathrm{top} \cdot \eta_\mathrm{cl,3}^\mathrm{bottom}, \tag{10.1}$$

where $\eta_\mathrm{cl,3}^\mathrm{top/bottom}$ is the cluster efficiency for clusters containing three or fewer strips, in the top/bottom sensor layer. All clusters containing more strips were treated as inefficient, since the stub finding logic also rejects those clusters. The combined cluster efficiency gives an estimation of the expected stub finding performance of the module. Since the efficiencies of the individual sensor layers are not uncorrelated the stub efficiency does not exactly match the combined cluster efficiency.

Figure 10.9 displays the stub and combined cluster efficiency for the threshold scan of the unirradiated MiMo1. The sensor voltage was 400 V and the modules were operated at 20 °C. The maximum achievable stub efficiency is about 99.5 %, depending on the threshold and sensor material. However, this is far below the reached cluster efficiency. The reason for this behavior is the rejection of large clusters by the stub finding logic. In addition, this is also the reason for the better performance of the thFZ240 sensors. The thicker FZ290 sensors show a larger fraction of clusters containing four or more strips (see figure B.9). Another non-intuitive behavior is the rise of the stub detection efficiency in the low threshold domain.

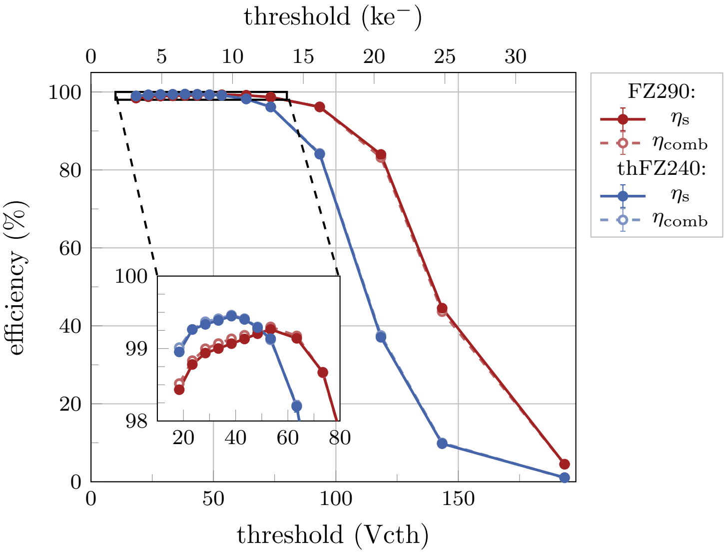

Figure 10.9: Stub efficiency and combined cluster efficiency (cluster size < 4) for a threshold scan with MiMo1 and vertically inclined tracks. The sensors were biased with 400 V at a module temperature of 20 °C. The sensors reach a stub efficiency up to 99.5 %, depending on the material and threshold. The cluster size cut of the stub logic limits the maximum stub efficiency. For very low thresholds the stub efficiency first improves due to the threshold related reduction of the cluster size. For even higher thresholds the cluster efficiency and hence stub efficiency drops.

The explanation again is the cluster size. One process generating large clusters is the release of δ electrons. On their way through the sensor the δ electrons ionize the material and generate displaced hits from the track position. For geometrical reasons the signals of the edge strips of the cluster are the lowest. With increasing threshold the probability to detect the signals of the edge strips decreases. As a consequence, the cluster size also decrease, and more clusters start to contribute to the stub finding. The cluster efficiency threshold scans of MiMo1 showed a wide range of thresholds for which the cluster efficiency does not decrease. The combination of the edge strip loss at full cluster efficiency improves the stub efficiency. However, for too large thresholds the cluster detection efficiency begins to suffer and the stub efficiency worsens. Since the charge signal of unirradiated sensors scales with the sensor thickness the threshold for which the efficiency drop sets in is higher for the FZ290 sensors compared to the thFZ240 sensors.

The corresponding measurement with MiMo2, with a sensor fluence of $2.5 \times 10^{14}\,\mathrm{n_{eq}/cm^2}$, follows the same behavior as for MiMo1. The bias voltage was 600 V and the module was operated at about −22 °C. Figure B.8 shows the result plot. Compared to MiMo1 the efficiency drops for lower thresholds, due to the radiation damage of the sensors. However, the sensor stacks still reach stub efficiencies of more than 99 % for a wide range of thresholds.

MiMo3, with a sensor fluence of $5 \times 10^{14}\,\mathrm{n_{eq}/cm^2}$, represents the ultimate $4000\,\mathrm{fb^{-1}}$ HL-LHC scenario. The result of the stub efficiency threshold scan is displayed in figure 10.10. All sensors were biased with the nominal 600 V and operated at about −22 °C. Even for this very harsh radiation scenario both sensor stacks yield about 99 % stub efficiency for a reasonable threshold (see also noise measurements in figure 10.3). In contrast to the threshold scans of the cluster efficiency, the stub efficiency of both materials show a very similar behavior. This is caused by the combination of the two sensor cluster efficiencies of one stack. Each stack includes sensors in different annealing states and thus different cluster detection efficiencies. The sensor with

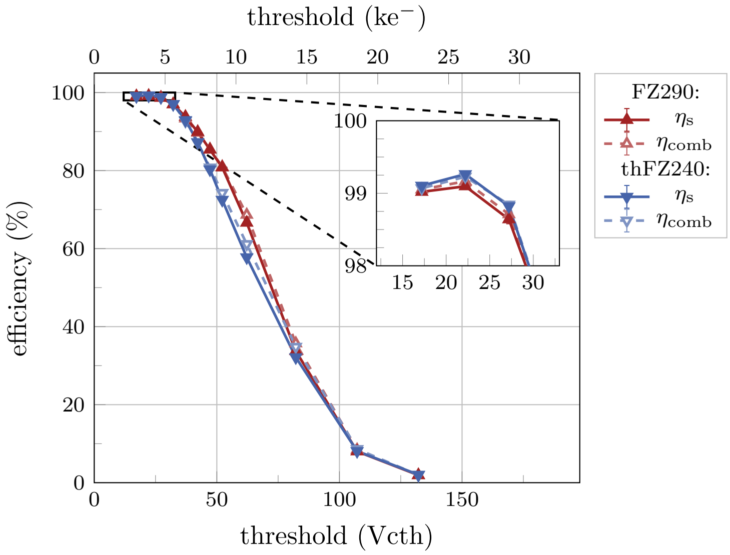

Figure 10.10: Stub efficiency and combined cluster efficiency (cluster size < 4) for a threshold scan with MiMo3 and vertically inclined tracks. The sensors were biased with 600 V at a module temperature of $-22\,°C$. Even after a fluence of $5 \times 10^{14}\,n_{eq}/cm^2$ the sensor stacks reach a stub efficiency of up to 99.2 %. In contrast to the cluster efficiency scan both materials have a very similar stub efficiency over threshold characteristics.

the lower cluster detection efficiency in the stack drives the stub efficiency. For both materials the sensors with long annealing (204 d eq. time at 21 °C) have a similar cluster efficiency over threshold characteristics. Thus, the dependency of the stub efficiency on the threshold shows a very similar behavior for both materials, too.

10.3.2 Sensor Bias Voltage Scan

As demonstrated in section 10.1.2, the sensor bias voltage has a strong influence on the cluster efficiency. Thus, it also influences the stub detection efficiency. Figure 10.11 displays the stub efficiency over the bias voltage for the unirradiated MiMo1 and for MiMo3 with a fluence of $5 \times 10^{14}\,n_{eq}/cm^2$. Again the plots show the combined cluster efficiency for clusters comprising three or fewer strips.

The measurements with *MiMo1* were conducted at 20 °C and with a threshold of 4800 e^-. Both materials reach a maximum stub efficiency of about 99.3 % to 99.4 %. Again the limiting factor for the maximum stub detection efficiency is the cluster size limitation of the stub logic. Thus, the thFZ240 sensor stack slightly outperforms the FZ290 sensor stack. Furthermore, the FZ290 sensor stack starts losing efficiency again when increasing the sensor voltage above 150 V. For this voltage the sensors reach a plateau with the maximum cluster detection efficiency (see figure B.1). Further increasing the voltage depletes a larger volume of the sensors and the probability to detect small signals, e.g. by δ electrons, increase. A closer look into the distribution of the different cluster sizes (see figure B.10) demonstrates that the fraction of clusters comprising more than three strips increases with the sensor voltage. Since the stub detection logic does not accept such clusters the stub efficiency decreases. However, the stub efficiency stabilizes at about 300 V. At this voltage the FZ290 sensors are fully depleted and the cluster size composition stabilizes, too.

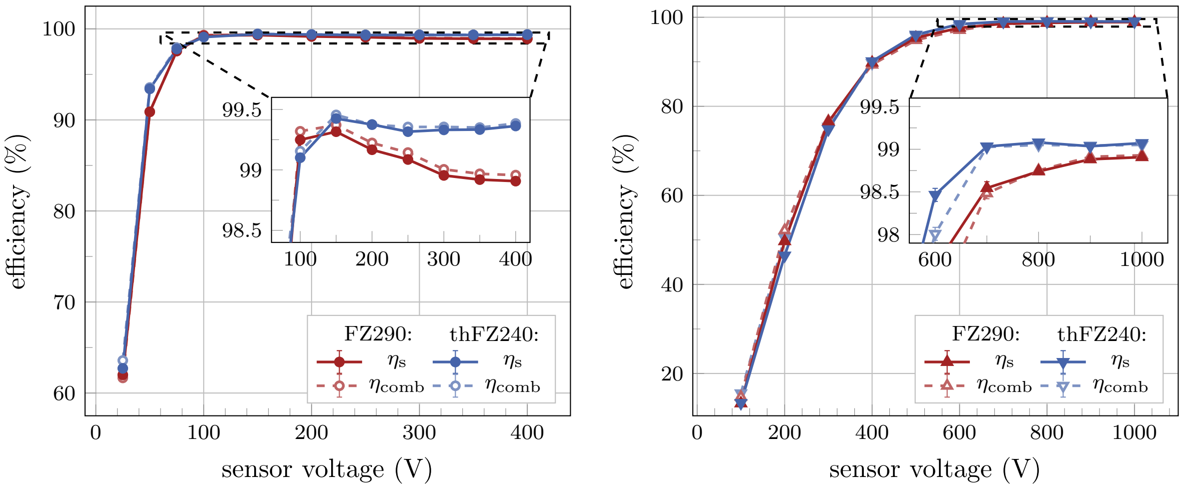

(a) MiMo1, 20 °C, 4800 e⁻ threshold **(b)** MiMo3, −22 °C, 5000 e⁻ to 5700 e⁻ threshold

Figure 10.11: Stub efficiency and combined cluster efficiency over the bias voltage for the unirradiated MiMo1 (a) and MiMo3 (b) with sensors at $5 \times 10^{14}\,\mathrm{n_{eq}/cm^2}$. Increasing the sensor voltage improves the stub detection efficiency. For the unirradiated FZ290 material the stub efficiency begins to decrease at about 150 V and stabilizes when reaching the depletion voltage at 300 V. All sensors reach a stub efficiency of about 99 %.

MiMo3 represents the ultimate HL-LHC operation scenario. Since the thresholds for the individual sensors vary between 5000 e⁻ and 5700 e⁻ an absolute comparison of the stub efficiency for the two materials is not possible. As for the threshold scan, the stub efficiency is driven by the sensor with the poorer efficiency. For both materials this is the sensor with long annealing time (see also cluster efficiency scan in figure 10.4). Like the cluster efficiency, the stub efficiency of the FZ290 sensor stack heavily profits from a voltage increase from 600 V (nominal) to at least 800 V. But also the stub efficiency of the thFZ240 sensor stack profits from a voltage boost to 700 V.

10.3.3 Inclined Particle Tracks and Stubs

The runs with inclined particle tracks allows the investigation of the functionality of the stub finding logic. From the configuration of the stub logic settings and the module geometry, the maximum inclination of the tracks to create stubs $\varphi_{\max}$ can be calculated as shown in equation 10.2. The equation includes the width of the correlation window c_w in strips, the strip pitch p, the sensor thickness d and the spacing between the sensor layers s.

$$\varphi_{\max} = \arctan\left(\frac{c_w \cdot p}{d+s}\right) \tag{10.2}$$

For the configured correlation width of 3.5 strips the maximum accepted inclination for the thFZ240 sensor stack in the Mini Module is 10.9° and for the FZ290 sensor stack 10.4°. However, the focus of the beam test was the comparison of the performance of the two sensor materials, and for time reasons only a small number of different rotation angles have been recorded.

Figure 10.12 displays the stub efficiency over the particle inclination angle for the unirradiated MiMo1 and MiMo3 with a sensor fluence of $5 \times 10^{14}\,\mathrm{n_{eq}/cm^2}$. As expected both modules exhibit a very similar dependency on the track inclination. At about 10° inclination the stub efficiency drops to 0 %, which matches the expectations from the geometrical considerations. However,

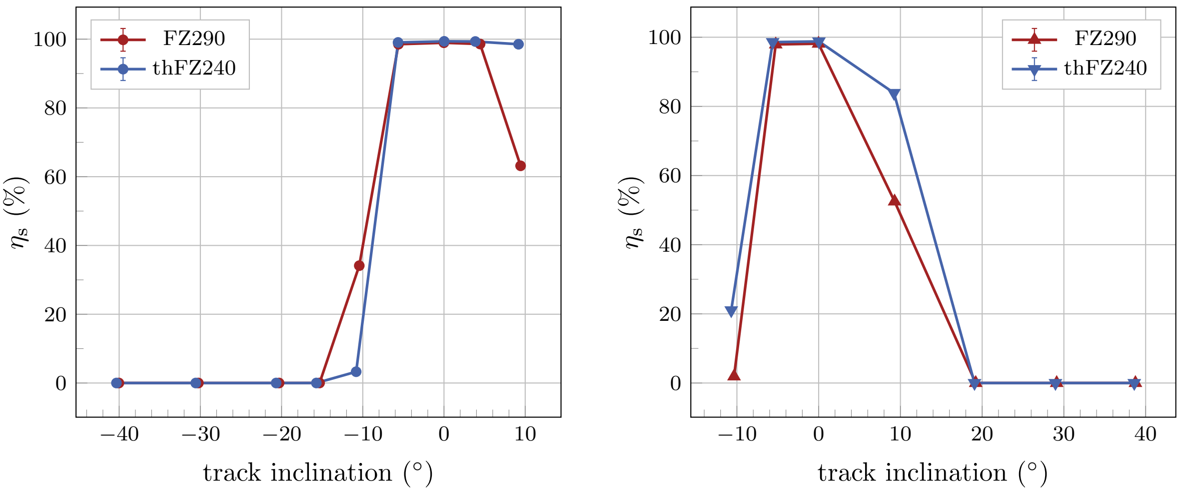

(a) MiMo1, 20 °C, 4800 e⁻ threshold, 400 V

(b) MiMo3, −22 °C, 4800 e⁻ to 5500 e⁻ threshold, 600 V

Figure 10.12: Stub efficiency over the track inclination for the unirradiated MiMo1 (a) and MiMo3 (b) with sensors irradiated to $5 \times 10^{14}\,\mathrm{n_{eq}/cm^2}$. The stub acceptance window was set to 3.5 strips and the offset to zero. As expected from the module geometry and stub settings, the stub efficiency drops at about ±10°.

the coarse angle scan does not allow the evaluation of the turn-on angle of the stub efficiency from the data. Dedicated beam tests on the final module geometry and sensors will investigate this topic more in detail.

A stub includes the information of the stub position and its bend, which is the displacement of the cluster centers in the two sensor layers. The average bend code $\langle b \rangle$ for a certain particle inclination φ and perfectly aligned sensors is

$$\langle b \rangle = \tan(\varphi) \cdot \frac{s+d}{p}, \tag{10.3}$$

where s is the sensor separation, d the sensor thickness and p the strip pitch. Figure 10.13 shows the measurement and expectation of the average bend code in strips for different module rotations in the beam recorded with MiMo1 and MiMo3. The uncertainty on the bend code is the standard deviation of the bend codes recorded for this track inclination. For all sensor stacks the measurements match the expectation within the measurement uncertainties. However, the recorded bend codes are slightly shifted to lower values. A possible reason is a non-perfect alignment of the two sensor layers. If the sensors of one stack are misaligned or rotated with respect to the other, the bend codes will not perfectly match the geometrical considerations. Section 10.4 examines more in detail the relative sensor orientation and the influence on the stub bend codes.

In summary, even though the validation of the stub finding logic was not the main goal of the beam test, the functionality of the stub finding logic was confirmed. Not only the turn-on curve of the stub efficiency over the particle inclination match the expectation but also the recorded bend codes. However, only one configuration set of the stub finding logic was tested in the beam. Future measurements of multiple stub logic configurations and with the final 2S modules have to confirm the functionality of the stub finding algorithm.

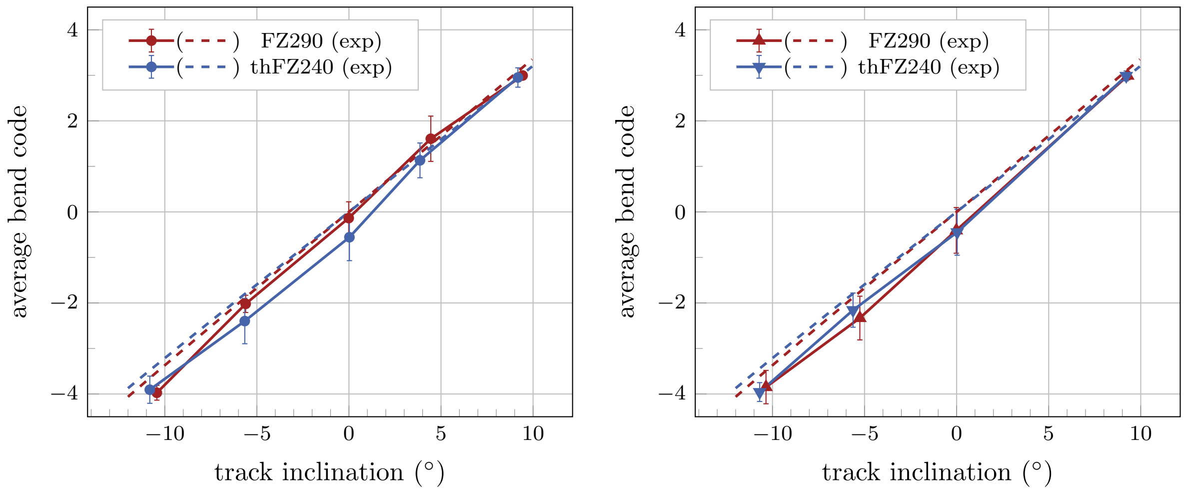

(a) MiMo1, 20 °C, 4800 e⁻ threshold, 400 V bias voltage

(b) MiMo3, −22 °C, 4800 e⁻ to 5500 e⁻ threshold, 600 V bias voltage

Figure 10.13: Recorded average stub bend code over the track inclination for MiMo1 (a) and MiMo3 (b) and geometrical estimation (dashed lines) for perfectly aligned sensors in the module. The recorded average bend codes match the expectation within the uncertainties. A relative rotation and shift between the sensors of one stack change the stub bend code (see section 10.4).

10.4 Sensor Alignment Reconstruction using Stub Bends and Particle Tracks

Precise alignment of the two sensor layers in the 2S modules is crucial for the stub finding logic to work correctly. A relative rotation of the sensors changes the stub bend along the strip length. Thus, the specified limit for the relative sensor rotation is 400 µrad [CMS18]. However, for the construction of the Mini Modules no special measures were taken to ensure a perfect alignment of the sensors. The alignment was done by using alignment pins during the sensor glueing process. Compared to the final 2S modules the precision of the glueing chuck is worse and the sensors were not pushed by springs against the pins during the glue curing process.

The alignment of the DUTs (sensors) with software in the beam test analysis yields the relative orientation of the sensors to each other. However, the stub bend and the particle track position along the strip (y-axis) offers another approach to determine the relative rotation of the sensors. Figure 10.14a illustrates the working principle of the measurements. As mentioned before, a relative rotation of the sensors varies the bend code along the strip axis. In particular, the relative rotation ϑ is

$$\tan(\vartheta) = -\frac{b(y) \cdot p}{y - y_0} \tag{10.4}$$

with the average bend $b(y)$ in strips at position y, the pitch p, the track position in y-direction y and the offset y_0 for which the strips are aligned on top of each other. The minus is necessary for geometrical reasons so that the sign of the rotation matches the rotation from the DUT alignment step. The average bend $b(y)$ can be parameterized by a linear function

$$b(y) = m \cdot y + c. \tag{10.5}$$

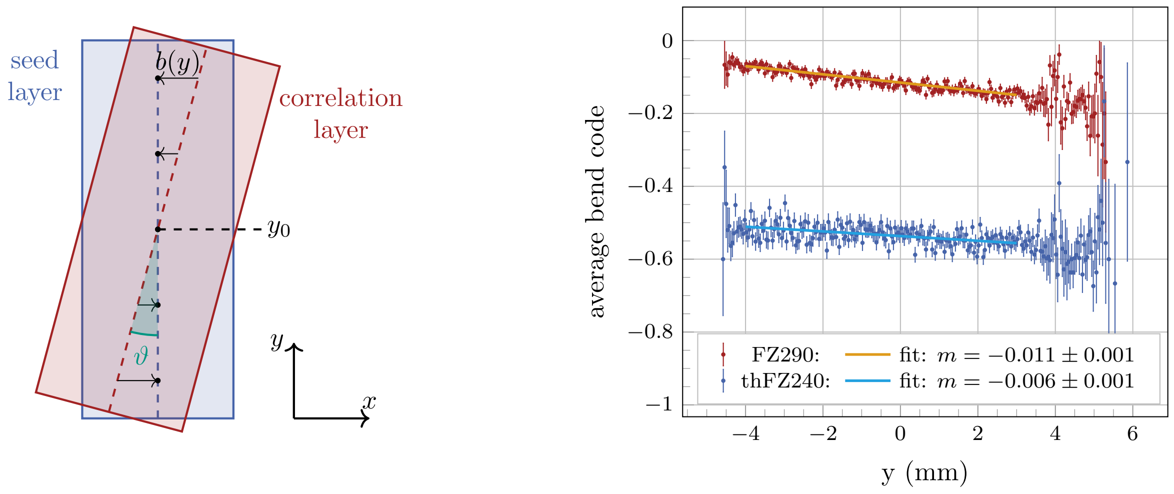

(a) Illustration of bends and alignment

(b) MiMo1, average bend code $b(y)$

Figure 10.14: Illustration of the effect of a relative sensor rotation on the average stub bend code $b(y)$ (a). The rotation results in different bends along the strip axis (y-axis). Measurement and fit of the average bend code b along y (b) for vertically inclined tracks for the two sensors stacks of MiMo1. Compared to the FZ290 sensors, the thFZ240 sensors are less tilted with respect to each other (slope) but show a larger shift perpendicular to the strips $b(y = 0)$.

The coordinate transformation $y' = y - y_0$ shifts the coordinate system in such a way that the sensor rotation is in the origin of the new coordinate system. Thus, equation 10.5 simplifies to

$$b(y') = m \cdot y' \tag{10.6}$$

Combining equations 10.4 and 10.6 with the coordinate transformation and assuming small rotation angles ϑ the calculation of the relative rotation simplifies to

$$\vartheta \approx -m \cdot p. \tag{10.7}$$

Figure 10.14b shows the average bend code along the strip axis for vertically inclined tracks measured with MiMo1. Furthermore, it shows the linear fit and the corresponding slope m. On the one hand, the relative rotation (slope) of the FZ290 sensors is larger compared to the thFZ240 sensors. On the other hand, the average bend codes are not zero, which means that there is a shift of the sensors perpendicular to the strips. Since $y = 0$ corresponds to the strip center the relative shift of the sensors to each other is the offset c from the linear fit multiplied with the strip pitch. The shift of the thFZ240 sensors is approximately half a strip ($-45\,\mu\text{m}$) and larger compared to the FZ290 sensors where the shift is approximetaly a tenth of the strip pitch ($-9\,\mu\text{m}$). However, the shift does not negatively affect the performance of the stub finding logic since it can be corrected by changing the programmable offset of the stub logic. This result also explains the shift in the measurements of the average bend code over the track inclination displayed in figure 10.13a. The sensor shift perpendicular to the strip axis lowers the average bend code, with a larger impact on the thFZ240 sensors.

Figure 10.15 summarizes the relative sensor rotations for the three Mini Modules investigated in the beam test. For all sensor stacks the reconstructed relative rotation from the bend codes confirms the value from the alignment process. Even though during the construction of the modules a perfect alignment was not intended, two sensor stacks fulfill the 2S module requirement.

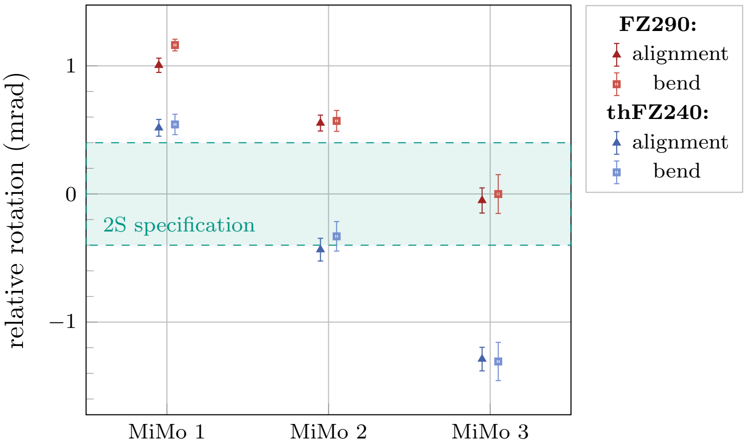

Figure 10.15: Relative rotation of the sensor stacks in the three Mini Modules calculated from the DUT alignment (triangles) and reconstructed from the bend codes (squares). The results of both measurements match for all sensors stacks. Even though a perfect alignment was not intended, two stacks fulfill the 2S module specification.

10.5 Conclusions for the Outer Tracker Material Decision

In September 2019 the Outer Tracker community had to finally decide which sensor material (FZ290 or thFZ240) will be ordered for the application in the future Outer Tracker. The performance of the CMS detector during more than a decade of high-luminosity operation will be affected by this decision. Thus, a wide range of studies had been performed to evaluate and compare the performance of the two materials.

The results shown in this chapter were essential for the material decision, since it was the first and only time the two sensor materials have been compared in 2S module prototypes. Besides the unirradiated sensors also the influence of radiation damage and sensor annealing on the performance has been examined in detail. The fluences and annealings have been chosen to match the expected sensor states after the nominal 3000 fb^{-1} and ultimate 4000 fb^{-1} scenario.

Regarding the cluster detection efficiency, both materials exhibit very good performance. For all sensor states a set of operation parameters (threshold, bias voltage) has been found for which the sensors reach a cluster detection efficiency of more than 99.5 % at an acceptable noise occupancy level. In general, the thicker FZ290 sensor material yields a larger charge signal and thus it is fully efficient for a wider threshold range. The only exception is the ultimate scenario with long annealing time of the sensors. For this scenario, the sensors show a higher sensitivity to annealing and the cluster efficiency for vertically inclined tracks drops below the one of the thFZ240 sensor. However, this sensor state will only occur for a very small fraction of 2S modules and can be compensated by increasing the sensor bias voltage to at least 800 V. Furthermore, the effect vanishes for inclined tracks, since the longer path length of particles in the sensor increase the charge deposition.

Taking into account the results of the beam test, charge collection measurements, thermal simulations, the higher mechanical robustness of the FZ290 material and its lower price, the Outer Tracker community finally decided to order FZ290 sensors for the future Outer Tracker.

Part IV

High Rate Studies of the 2S Module Readout Chain

11

Commissioning and Characterization of the KARATE Setup

It is essential to commission and characterize the KARATE setup before starting with high rate measurements of the 2S module readout chain. The commissioning includes the channel offset trimming and noise measurements with focus on the KARATE injector channels. Since a common clock domain synchronizes the signal injector and readout systems of KARATE the correct timing of the signal sampling ensures efficient data acquisition. Thus, this chapter presents measurements of the injector pulse shape and the method to determine the best sampling time for the high rate measurements. Furthermore, the analog signal injection requires the conversion of charge signals into the corresponding injection pulse length. The calibration procedure to determine the conversion factors for the individual channels is another topic of this chapter. The chapter closes with the proposal and the demonstration of an algorithm to prevent CBC readout buffer overflows for very high trigger rates.

11.1 Noise and Offset Trimming of the Injection Channels

The photodiodes of the receiver part of KARATE have capacitance similar to the final strip sensors. Thus, the noise should behave similarly as for a module with real sensors. The measurements of the noise reveal an average noise of 7.5 Vcth for the KARATE injector channels (see figure 11.1a). Since all other channels of the two front-end hybrids are not connected to a sensor the load capacitance is much lower, resulting in a low noise of about 2.4 Vcth. Comparing the noise measurements with those of the Mini Modules the noise of the injector channels is slightly higher than for the prototype modules.

Even though the load capacitance and noise of the injector channels differ strongly from the other channels the trimming still worked very precisely (see figure 11.1b). All channels have been sharply trimmed to a common pedestal at about 597 Vcth. The injector channels have a slightly lower pedestal. The small deviation from the other channels of about 0.5 Vcth results in a threshold uncertainty of less than $100\,\mathrm{e}^-$. This is low compared to fluctuations from random noise and thus will not affect the measurement results.

11.2 Pulse Shape and Timing

The signal injection of KARATE runs at 40 MHz and synchronously with the sampling of the readout. Thus, optimal timing is essential for sampling the charge signals most efficiently. To identify the best timing, the pulse shape of the injected signals was recorded for different injection pulse lengths and all injector channels. For most efficient operation the pulse has to be sampled in its peak, when the comparator sees the maximum of the signal. Figure 11.2a displays the signal shapes for different injection lengths recorded with one injector channel and 2.0 V LED pre-load. The measurement procedure was the same as for the test pulse measurement described in section 5.1.6. Larger latencies are earlier in time.

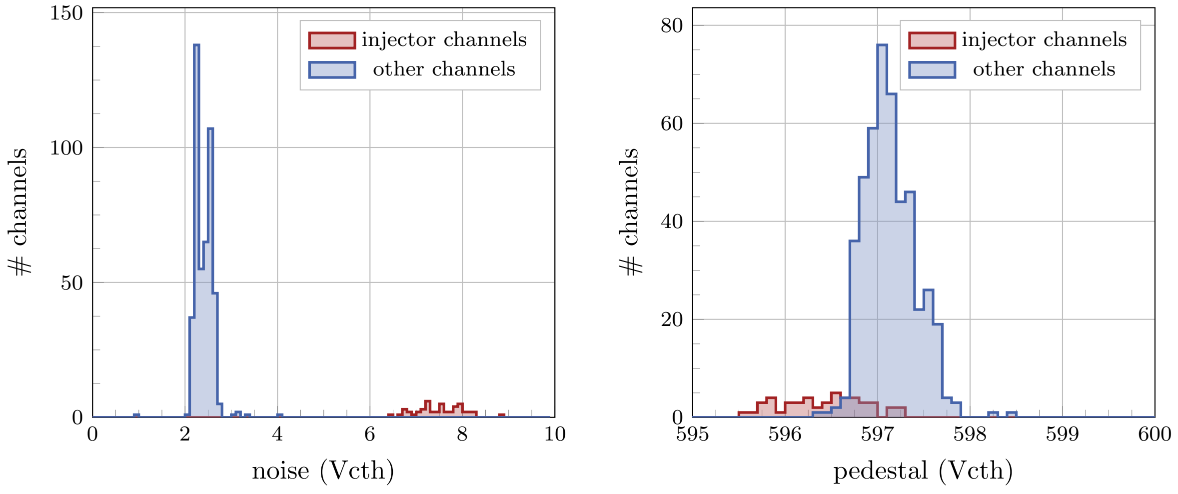

(a) Noise distribution **(b)** Pedestal distribution after trimming

Figure 11.1: Comparison of the noise (a) and pedestal (b) distributions of the injector channels and the other channels of the two CBCs connected to the KARATE receiver. The injector channels have a noise of about 7.5 Vcth, which is slightly above the noise of the prototype modules. The non-bonded channels have a low noise of about 2.4 Vcth. The trimming of all channels is very uniform and sharply around a common pedestal at about 597 Vcth. The average pedestal of the injector channels is about 0.5 Vcth lower.

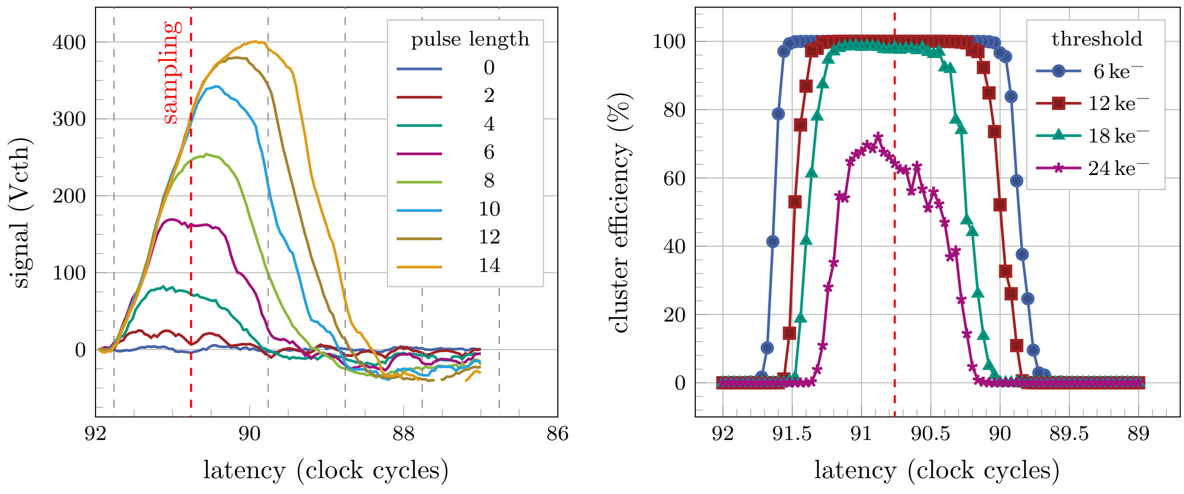

(a) Signal scan for LED pre-load 2.0 V **(b)** Cluster efficiency for pulse length 6, LED pre-load 2.0 V

Figure 11.2: Reconstructed pulse shape for different injection pulse lengths and one exemplary injector channel (a). The pulse length modulation causes a large time-walk. The red dashed line highlights the sampling time for the high rate measurements with analog signals. The gray lines indicate sampling times in the previous/subsequent clock cycles. Cluster efficiency as a function of latency (b) for a fixed signal injection and multiple thresholds. With increasing threshold the latency range for full efficient sampling decreases.

As expected the recorded peak signal increases with longer injection pulse length. However, the pulse length modulation causes a very strong time-walk. That means the peaking time of the signal pulse strongly depends on the injection pulse length.

This is not the same behavior as expected for signals from charged particles in silicon sensors. The injection with KARATE lasts up to 46.875 ns. In contrast, the ionization time of a charged particle is much faster. In particular, it is much faster than the shaping time of the analog front-end. Thus, the pulse shape and peaking timing for ionizing particles is driven by the analog front-end. As a result, the signals of ionizing particles peak at the same time or with very low time-walk for different charge depositions. The same holds for CBC internal test pulses, which discharge a capacitor into the analog front-end. Figure C.1 displays the pulse shape for different test pulse amplitudes. The peaking time does not depend on the injected signal.

For binary-like signal injection KARATE injects signals with fixed pulse length. Thus, the ideal sampling time for the corresponding pulse length can be determined. All bandwidth studies presented in the scope of this thesis use such binary-like signal injections. However, when injecting analog-like signals, with varying injection pulse length, there is no perfect common timing for all pulse lengths. The chosen trade-off is to operate at latency 90 and DLL value of 5, as highlighted with the red dashed line in figure 11.2a. The DLL values adjusts the phase of the pulse sampling in 1 ns with respect to the 40 MHz from the CBC. Furthermore, the maximum injection pulse length is limited to eight (25 ns). The combination of the timing and the pulse length limitation ensures that even the short pulses are still sampled in the signal plateau region. With 2.0 V LED pre-load still signals of up to 250 Vcth (43 000 e^-) can be injected, which is twice the expected most probable value of the FZ290 sensors. Another reason to limit the injection length is the afterglow of the pulses. The longer the injection is, the longer the signal remains at a high value. This will cause latched hits when triggering a bunch crossing after a previous injection. Futhermore, the sampling should not take place at an earlier phase of latency 90 (later in time). This would create fake hits by already detecting the rising edge of the pulses that are injected in the bunch crossing after. The gray dashed lines in figure 11.2a symbolize sampling times in the previous and subsequent clock cycles.

Figure 11.2b displays a timing scan of the cluster efficiency for different thresholds. The injected pulse length was fixed to 6 (18.75 ns) at 2.0 V LED pre-load. The expected peak signal is about 150 Vcth (26 000 e^-). With increasing threshold the latency range for which efficient detection is possible decreases. Again the sampling time for the high rate measurements is highlighted with a red dashed line.

11.3 Injector Channel Signal Calibration

To inject pulses with respect to a given signal spectrum it is mandatory to calibrate the injector channels. However, the signal generation of the individual injector channels must not be the same. For a given pulse length the recorded signal amplitude in the front-end is different for each channel. These variations have various sources. The light emission performance of the injector LEDs can differ. In addition, the coupling of the light into the optical fibers depends on the relative alignment of the LEDs and the fiber endings and the quality of the fiber cuttings. The same holds for the alignment of the photodiodes at the other end of the fibers. Besides possible variations of the transmission coefficient of the fiber the sensitivity of the photodiodes can differ. All these factors result in a non-identical sensitivity of the injector channels and are addressed by the injector channel calibration.

To extract the calibration curves the system has to be operated in exactly the same configuration as foreseen for the measurements. In particular, the timing and the LED pre-load

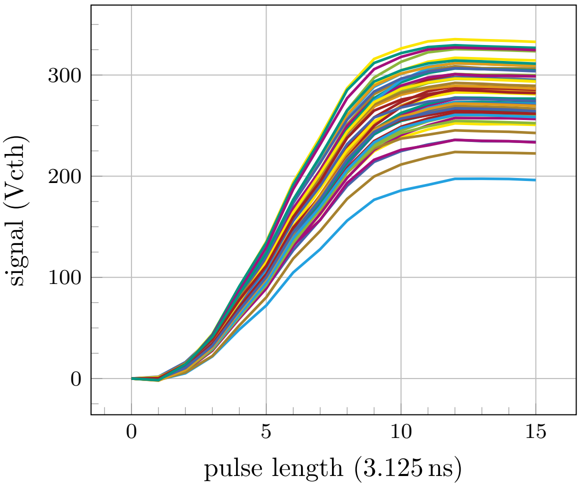

Figure 11.3: Calibration curves for the KARATE injector channels at 2.0 V LED pre-load, latency 90 and DLL 5. The recorded signal for a given pulse lengths varies strongly from channel to channel. For pulse length above 8, the signals saturate for timing reasons.

voltage have to be the same. For this configuration the expected signal for every channel and pulse length was measured. The signal S_l^{ch} of one channel is given by the difference of the s-curve's pedestal p_l for a given pulse length l and the pedestal without pulse injection p_0.

$$S_l^{\mathrm{ch}} = p_l - p_0 \tag{11.1}$$

The result of the calibration measurement is a lookup table which contains the signal amplitudes for every channel and injection pulse length at the given configuration. To inject a given signal S into a channel the pattern generator identifies the pulse length l of the channel which generates the best matching signal S_l^{ch}. To do so, it minimizes the distance $|S - S_l^{\mathrm{ch}}|$. Figure 11.3 shows the signal dependence on the injection pulse length for the 48 injection channels of the KARATE setup. The LEDs had a pre-load of 2.0 V and the timing settings were latency 90 and DLL 5. The sensitivities of the individual channels vary strongly. For pulse lengths above 8 the signals saturate. The reason for this behavior is the time-walk effect. Figure 11.2a demonstrates that for the given sampling time (red dashed line) the signal for pulse lengths 10 or higher are all the same. The signals in the analog front-end are still rising for this timing and pulse lengths ≥ 8.

11.4 CBC Readout Buffer Overflow Protection

The CBCs comprise a 32 events deep readout buffer to temporarily store triggered events awaiting the readout. Since the CBC emits the level-1 data without sparsification the readout time is independent of the number of hits and requires exactly 38 clock cycles. Thus, for a constant trigger rate the minimum separation between two consecutive trigger is 38 clock cycles or approximately 1.05 MHz. However, the triggers in the CMS detector have no fixed separation. The trigger probability of each event is the same. Thus, it could happen that the readout buffer fills or even overflows when having too many triggers in a short time interval. In general, this becomes more probable the higher the trigger probability is.

To investigate the probability of a readout buffer overflow to occur, simulations of the buffer state during HL-LHC runs have been performed. The simulations emulate the CBC's

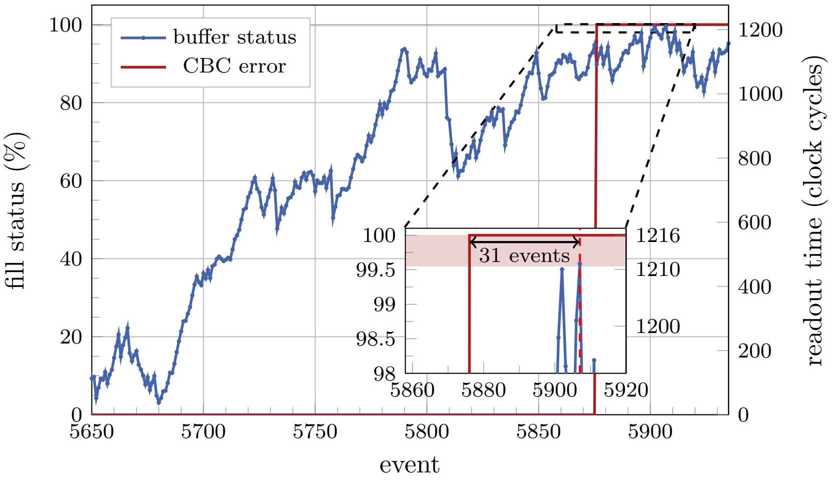

Figure 11.4: The CBC readout buffer state for every triggered event recorded with the KARATE setup and an average trigger separation of 38 clock cycles. The readout buffer overflow occurs when exceeding a remaining readout time of more than 1210 clock cycles. Then all events in the buffer are corrupted (this and the 31 events before) and the CBC raises an error flag.

readout buffer state over time and returns the number of events until a CBC buffer overflow occurs. A detailed description of the simulation and results is given in appendix C. For the nominal trigger rate (750 kHz) the average time until a readout buffer overflow is approximately 5300 s. However, the simulation showed that the occurence of a buffer overflow has a constant probability, hence it can occur even much earlier in a run. Since a run of the HL-LHC can last for several hours [CER21a] a CBC readout buffer overflows will occur during operation. Thus, the consequences of CBC readout buffer overflows have to be considered.

Running into a readout buffer overflow corrupts all data in the readout buffer. Thus, the CBC raises an error flag and suppresses the emission of any further hit information. To return to normal operation the CBC requires a fast reset signal. The fast reset involves down time and clears all module buffers. Since all detector systems of CMS receive the same triggers, not only a single CBC but all 2S modules in the Outer Tracker run at the same time into the buffer overflow and cause large data loss. To reduce the data loss the DAQ system has to identify overflows and emit the fast reset as fast as possible.

A more elegant way is to prevent the CBCs to run into a readout buffer overflow. This is possible by carefully monitoring the readout buffer state and vetoing triggers which would cause a readout buffer overflow. Such a system already exists for the LHC and is called the Trigger Throttling System (TTS) [Rác00]. Regarding the CBC it is not possible to directly request the current buffer state from the chips. Thus, this section proposes a supervising algorithm that can determine the current buffer state by knowing the trigger history. This algorithm can be implemented in the TTS to veto critical triggers. It prevents the CBC from running into a buffer overflow, while exploiting the maximum available capacity of the CBC readout buffer.

The idea of the algorithm is to monitor the buffer state by calculating the remaining readout time in clock cycles t for the data in the buffer and comparing it to the maximum acceptable readout time. To do so the algorithm performs the following steps for every trigger reception:

- Subtract the time in clock cycles since the last trigger from the buffer state t to calculate the current buffer state, without the new trigger. If t becomes negative the buffer is empty and t is set to 0.

- Veto the trigger if $t + 38$ exceeds the buffer limit. The theoretical limit is $32 \cdot 38 = 1216$ clock cycles to read out 32 events in the buffer.
- If there is no veto, increment t by 38 clock cycles to calculate the new buffer state including the newly triggered event.

This algorithm has been implemented for the CBC buffer overflow protection of the KARATE pattern generator. The buffer overflow protection does not veto events on the fly but during the pattern generation. It goes through the pattern list, calculates the trigger state and removes the triggers for events that would cause a CBC buffer overflow. Regarding CMS this algorithm would have to be implemented in the TTS to veto triggers which would cause readout buffer overflows.

However, measurements with the KARATE setup showed that the real readout time limit is 1210 clock cycles and hence slightly below the theoretical limit from the buffersize considerations. Figure 11.4 shows the CBC buffer state for a run without overflow protection. The average trigger separation was set to 38 bunch crossings (trigger probability of 2.63 %) to stress the CBC readout. With increasing number of triggered events the readout buffer starts to fill and as soon as the buffer exceeds a value of 1210 clock cycles the CBCs run into a readout buffer overflow. Since the overflow corrupts all events in the readout buffer, the CBCs start emitting an error flag already 31 events before. Figure C.5 proves the functionality of the algorithm. Running the system with enabled CBC buffer overflow protection it reaches the buffer state $t = 1210$ multiple times without causing a readout buffer overflow. All measurements with non-constant trigger rates were performed with enabled CBC readout buffer overflow protection. The system ran perfectly stable without causing a single readout buffer overflow for the limit of 1210 clock cycles.

12

Level-1 Data Bandwidth Studies

The 2S modules emit two data streams, the stub and the triggered level-1 data stream. This chapter focusses on stress tests of the level-1 data stream. In a first study the 2S module readout chain was stressed for different constant trigger rates and front-end occupancies. This method provides a very clean environment to compare the expected limitations with the measurement. The second part of the chapter presents the results of stress tests with CMSSW-based pattern injection. These patterns provide the best possible approximation of the expected bandwidth rates in the future Outer Tracker. In particular, this part demonstrates that for all module positions within the tracker and the expected pileup and trigger rates no data losses due to bandwidth limitations will occur. In addition, the study investigates also trigger rates and pileups exceeding the nominal conditions to identify critical scenarios which could lead to bandwidth related data losses.

12.1 Constant Trigger Frequency and Occupancy

The description of the 2S module readout chain already highlighted the key parameters limiting the throughput on the level-1 data stream. On the one hand, the CBC emits the data unsparsified and the readout of one event requires exactly 38 clock cycles. Thus, the trigger rate is limited to about 1.05 MHz for constant trigger rates. The CBC buffers up to 32 events in a readout buffer to compensate short time periods of higher trigger rates. On the other hand, the CIC performs a clustering of the hits from the CBCs to reduce the amount of data for transmission. By doing so, the size of an event scales linearly with the number of clusters detected. Thus, the combination of high trigger rates and many clusters per front-end limits the CIC.

This study determines the ultimate limitations of the 2S module readout chain by injecting a fixed number of clusters per front-end and event at constant trigger rates. This very clean environment does not mimic a realistic scenario but it checks the system limitations and compare the observed limitations with the expectations. Figure 12.1 shows the cluster efficiency for a two-dimensional scan over the separation between consecutive triggers S and the number of clusters per front-end and event n_{cl}. For the scan the trigger separation was varied between 36 and 240 clock cycles and n_{cl} between 1 and 130. For every combination 40 000 events were recorded. The threshold was set to $8000\,\mathrm{e}^-$ and the injector operated with a fixed pulse length of 7 (21.875 ns) at 2.0 V LED pre-load. In this configuration the injected signal is approximately $32\,000\,\mathrm{ke}^-$ (see section 11.3).

For this scan events with a CIC error and no CBC error flags were not treated as inefficient. This flag combination indicates the violation of the CIC's cluster limit and occurs for $n_{\mathrm{cl}} > 127$. Furthermore, all runs for which the DAQ crashed and not the correct number of events were recorded are shown as empty bins (white). The plot highlights four regions representing the different limitations of the readout system.

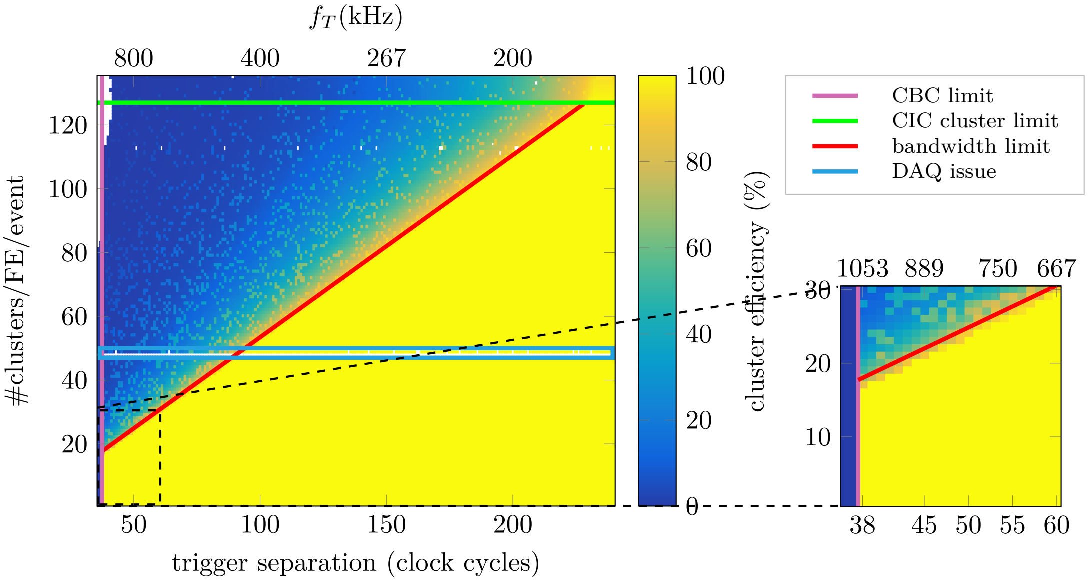

Figure 12.1: Cluster efficiency scan over the trigger separation and the number of clusters per front-end and event. The scan illustrates the ultimate limitations of the system. For trigger separations below 38 clock cycles the CBC runs into a readout buffer overflow (magenta line and detailed view). The maximum number of clusters for one CIC event is 127 (green line). Exceeding this value, the CIC drops the clusters with the lowest address. The red line shows the expected readout bandwidth limit of the CIC, which has a linear behavior. For 48 clusters per front-end and event the DAQ is interrupted. This issue is most likely firmware-related and not solved by the developers up to now.

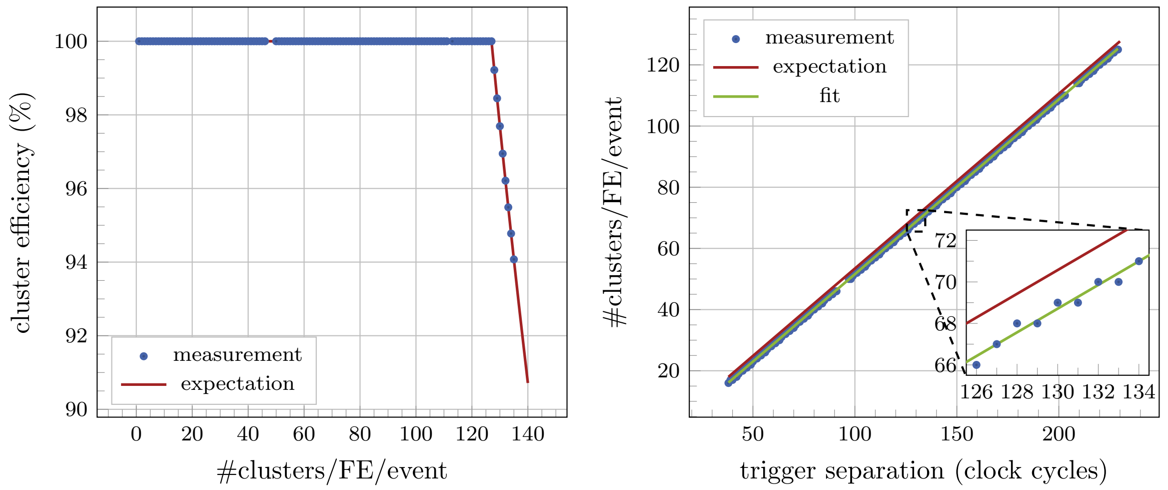

(a) CIC cluster limit. Cluster efficiency over cluster per front-end and event for 240 clock cycles trigger separation. Exceeding 127 clusters, the CIC starts to drop clusters and the cluster efficiency decreases as expected

(b) Maximum number of clusters per front-end and event transmitted by the CIC vs. the trigger separation with linear fit and the expectation. For a given trigger separation the maximum number of clusters per front-end and event is lower than expected.

Figure 12.2: Details on the CIC cluster (a) and bandwidth (b) limit.

The DAQ Issue

The measurements with the KARATE setup discovered an issue with the DAQ that is unsolved up to now. As soon as one event with exactly 48 clusters in one front-end occurs, the data acquisition stops and no further events are recorded. Thus, the scan displays a white vertical line around the injection of 48 clusters as highlighted in blue in figure 12.1.

This issue was reported to the firmware developers and DAQ group. Even though it is strongly expected to be a firmware related issue, the issue was not identified and corrected up to now. Before starting the operation of the modules in the tracker this issue must be solved, since for particle collisions there is a non-vanishing probability to record 48 clusters in an event (see section 7.3.2).

The CBC limit

The CBC requires 38 clock cycles to transmit one event. This hard limit is independent of the occupancy since the CBC event format encodes the channel hit information unsparsified. The measurements with the KARATE setup verify this limit (magenta colored line and detailed view in figure 12.1). For all measurements with a trigger separation of less than 38 clock cycles the CBC ran into a readout buffer overflow. Since the CBC cannot recover from this error state without a fast reset all following events of the run are corrupted. Figure C.6 shows the fraction of events containing at least one CBC error for the same scan. For trigger separations of less than 38 clock cycles almost all events are flagged with an CBC error since it requires only a small number of triggers to run into the readout buffer overflow.

The CIC Cluster Limit

The output event format of the CIC only foresees the encoding of up to 127 clusters per event. If there are more clusters the CIC begins to drop surplus clusters and emits an error flag. To visualize the reduction of the cluster efficiency caused by the CIC's cluster dropping, events only containing a CIC error were not treated as inefficient. The expected cluster efficiency η_{cl} for 127 clusters or more is

$$\eta_{\mathrm{cl}} = 1 - \frac{N^{\mathrm{cl}}_{\mathrm{missed}}}{N^{\mathrm{cl}}_{\mathrm{inj}}} = 1 - \frac{N^{\mathrm{cl}}_{\mathrm{inj}} - 127}{N^{\mathrm{cl}}_{\mathrm{inj}}} = \frac{127}{N^{\mathrm{cl}}_{\mathrm{inj}}}, \quad \forall\, N^{\mathrm{cl}}_{\mathrm{inj}} \geq 127. \tag{12.1}$$

The green line in figure 12.1 highlights the injection of 127 clusters per front-end and event. As expected, the injection of more clusters causes a drop of the cluster efficiency. Figure 12.2a displays a cut through the 2D histogram of the cluster efficiency for the trigger separation of 240 clock cycles. The measurement perfectly matches the expectation, which is shown in red. Exceeding 127 clusters per front-end and event the efficiency begins to drop. Figure C.7 displays the fraction of events with CIC error. The CIC emits an error flag when it drops a cluster. Thus, all events for which more than 127 clusters were injected are flagged with an CIC error.

The CIC Level-1 Bandwidth Limit

The red line in figure 12.1 marks the expected level-1 bandwidth limit of the CIC in the 2S module readout chain. The available bandwidth B is one link with $320\,\mathrm{Mbit/s} = 8\,\mathrm{bits/clock\,cycle}$. Taking into account the event size N defined in equation 5.4, the number of clock cycles S to read out one event with n_{cl} clusters per front-end is

$$S = \frac{N}{B} = \frac{52\,\mathrm{bits} + 14\,\mathrm{bits/cluster} \cdot n_{\mathrm{cl}}}{8\,\mathrm{bits/clock\,cycle}}. \tag{12.2}$$

This is also the theoretical minimum separation between consecutive triggers at constant trigger frequencies. For a lower trigger separation the bandwidth will not last to read out all data. Solving equation 12.2 for n_{cl} yields the maximum number of clusters per front-end and event for a given trigger separation S

$$n_{\mathrm{cl}} = \frac{8\,\mathrm{bits/clock\,cycle} \cdot S - 52\,\mathrm{bits}}{14\,\mathrm{bits/cluster}}. \tag{12.3}$$

In figure 12.1 the violation of the bandwidth limit is shown as a cluster efficiency loss in the upper left hand region. The transition from full efficient data acquisition to the region in which the efficiency drops has the expected linear behavior. In particular, the violation of the bandwidth limit causes an overflow of the readout FIFO of the CIC, which is also called soft overflow. For such an event an already existing event in the FIFO is overwritten. The CIC recognizes the missing event identifier and emits an empty event which is flagged with error bits for all CBCs and the CIC. Figure C.8 displays the fraction of events with soft overflow for the same scan. Fortunately, when running into this undesired state the CIC continues operating properly and emits the remaining events in the FIFO unaffected. The consequence of CIC readout FIFO overflows are single corrupted events in the readout data stream.

However, the observed bandwidth limit is actually slightly below the expected limit as shown in the zoomed region of figure 12.1. Thus, the maximum number of clusters transmitted by the CIC without violating the bandwidth limit was extracted for every trigger separation S in the range between 38 and 230 clock cycles. Figure 12.2b shows the recorded cluster limit in blue and the expected maximum number of clusters in red. A linear fit of the data using equation 12.3 with the header size n_{h} and the cluster encoding size m_{cl} as free parameters is shown in green. The result of the fit is

$$\begin{aligned} n_{\mathrm{h}} &= (78.07 \pm 0.73)\,\mathrm{bits} \\ m_{\mathrm{cl}} &= (14.00 \pm 0.01)\,\mathrm{bits/cluster}. \end{aligned} \tag{12.4}$$

The scaling (m_{cl}) of the event size with the number of clusters perfectly matches the expected value from the event format. However, the average header size is about 26 bits larger. Actually not the event header is larger in the readout but the CIC emits multiple times a 01 bit pattern to synchronize with the GBTx. The measurements showed that this pattern is 26 bits long on average.

Putting this into perspective of the expected operation scenario, no bandwidth related data losses are expected for constant trigger rates and nominal operation parameters. As described in section 7.3, the modules that are exposed to the highest particle flux are the ones of the innermost ring on the outermost endcap disk. For the nominal pileup of 200 the CMSSW simulation yield on average 13 clusters per front-end and event for these modules. The measurements presented in this section demonstrated that the bandwidth is sufficient to operate these modules even with *constant trigger rates* of up to 1.05 MHz before running into the CBC readout limit. This is far more than the expected 750 kHz average trigger rate.

12.2 CMSSW Based Stress Test of the Level-1 Data Path

The measurements of the previous section with fixed trigger rates and constant number of clusters per front-end and event are well suited to determine the ultimate limitations of the components of the 2S module readout chain. However, this scenario does not reflect realistic data rates as expected for the operation of the 2S modules in the Outer Tracker of the CMS experiment. Thus, this section investigates more realistic pattern injection based on CMSSW simulation. In particular, KARATE injects CIC cluster distributions as expected during the operation of the Outer Tracker in the HL-LHC. Section 7.3.3 describes the algorithm of the cluster injection. Besides the BC0 trigger check and the CBC readout buffer overflow protection another check had to be implemented to prevent the injection of 48 clusters. The presence of 48 clusters in one front-end and event causes a DAQ interruption (see DAQ issue in section 12.1). In case of the occurence of 47, 48 or 49 clusters in the pattern the algorithm determines a new random cluster number for the injection. This prevents the injection of 47 to 49 clusters. However, this large number of clusters is a very unlikely case and only occurs for very high pileup scenarios and for the modules exposed to the highest particle flux.

For each run a pattern list with 500 000 entries was generated and injected 20 times. The triggers were distributed randomly with a fixed trigger probability p. E.g. for a targeted average trigger separation of 50 clock cycles (average trigger rate $f_T = 800\,\text{kHz}$) the trigger probability is $p = 2\,\%$. In this example the pattern list contains approximately 10 k triggers which yields 200 k events for the run. For all measurements the injector operated with a fixed pulse length of 9 (28.125 ns) and 1.8 V LED pre-load. This equals an injected charge signal of about $30\,\text{ke}^-$. The threshold was set to $12\,\text{ke}^-$ and sampled at 90 clock cycles latency and a DLL value of 12. These settings differ from the constant trigger separation injection. However, randomly distributed triggers require not only the optimization of the cluster detection efficiency to determine the KARATE settings but also the reduction of the fake hit rate from latched hits. The chosen values are a trade-off between the cluster efficiency and fake hits.

Three parameters have been scanned by the measurements: the average trigger separation (trigger rate), the module position within the tracker and the expected average pileup. Figure 12.3 displays the cluster efficiency scanned over the average trigger separation and pileup for the modules of the innermost ring of the outermost endcap disk (position 20). For this position the CMSSW simulations yield the highest number of clusters per front-end and event. Thus, modules on this position will violate the bandwidth limit first. The average pileup was scanned up to 400, which is of course a very unrealistic scenario and will not appear for the

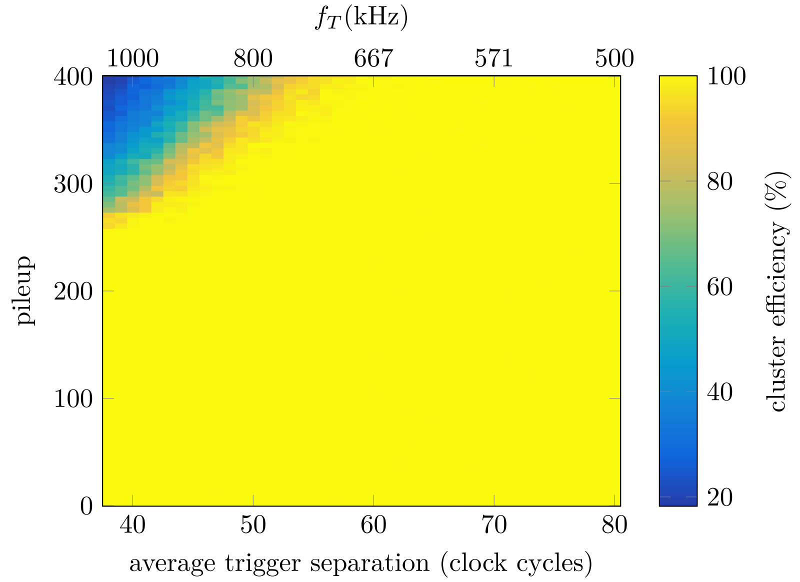

Figure 12.3: Cluster efficiency scanned over the pileup and average trigger separation for the modules of ring 8 on endcap disk 5 (position 20). The injected pattern is extracted from the cluster per front-end and event distribution from CMSSW simulations. The bandwidth limits the data acquisition only for very high pileup and trigger rates (upper left hand corner). For the nominal pileup 200 the level-1 data readout operates efficiently up to an average trigger rate of about 1.05 MHz.

HL-LHC. However, the intention is to identify the pileup limit at the nominal trigger rate for which the module readout begins to fail.

As expected from the CIC bandwidth limitations the cluster efficiency begins to drop only for very high trigger rates in combination with high pileup (upper left hand corner). Figure C.10 demonstrates that soft overflows of the CIC cause the efficiency loss and hence the CIC is the bottleneck of the 2S module readout chain. Furthermore, the scan shows that at nominal operation conditions (pileup 200 and $f_T = 750\,\mathrm{kHz}$), no data losses due to bandwidth limitations are expected. Moreover, the average trigger rate can even be boosted up to 1.05 MHz (38 clock cycles average trigger separation) at pileup 200 without being limited by the bandwidth. Running at the nominal trigger rate, a pileup increase up to approximately 300 is still possible for the level-1 data stream before being limitted by the readout bandwidth.

To demonstrate the stability for all 2S modules in the tracker a scan over the reference module position and the average trigger separation at pileup 400 was performed. Figure 12.4 displays the cluster efficiency for this scan. Even for this extremely high pileup all barrel modules and the majority of the endcap modules can operate efficiently for trigger rates up to 1.05 MHz. Only for four reference module positions the efficiency begins to drop for very high trigger rates due to the bandwidth limitation. In particular, the innermost rings of the three outer endcaps and the second ring of the outermost endcap lose cluster detection efficiency. The analysis of the CMSSW simulations already indicated such a behavior. Exactly those modules see the highest average number of clusters per front-end and event (see figure 7.7b for pileup 200). For the sake of completeness the corresponding scan for the nominal pileup 200 is shown in figure C.11. However, under this operation conditions no efficiency loss due to bandwidth limitations occurs for any of the modules. The very small efficiency losses are caused by missed hits due to the relatively high threshold for the measurement.

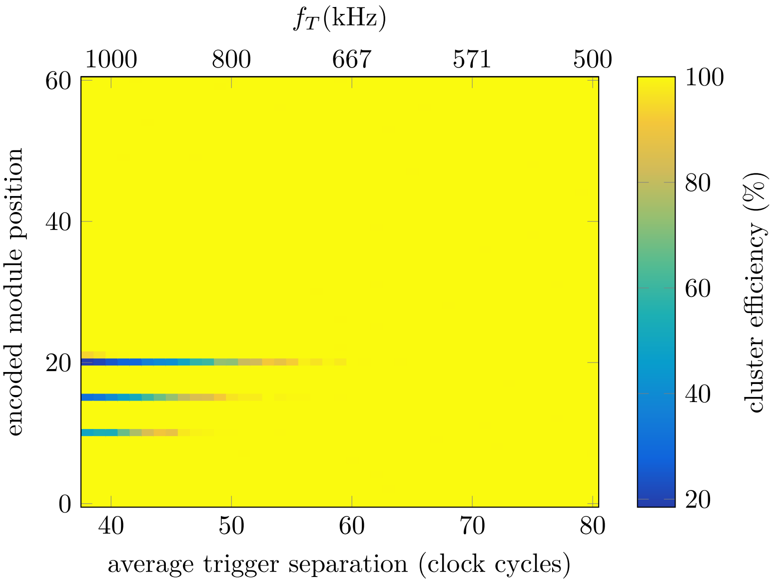

Figure 12.4: Cluster efficiency scanned over the encoded reference module position and average trigger separation for pileup 400. Four modules in the endcaps (positions 1 to 24) start to lose efficiency for high trigger rates due to bandwidth limitations. For the barrel (positions 25 to 60) no limitations are observed. The position encoding is described by tables C.1 and C.2.

The measurements presented in this chapter demonstrate that if under very unlikely conditions a readout buffer overflow of the CIC occurs, the data acquisition will continue without failing. In this unlikely case only the hit information of the affected front-ends and events are lost. The events of all other front-ends and events will not be affected. This is of importance since, in contrast to the CBC, due to the random distribution of the particle tracks there is no possibility to veto or predict a CIC buffer overflow.

Regarding the operation in the Outer Tracker the measurements confirmed that under nominal operation conditions no efficiency losses due to bandwidth limitations in the level-1 data stream will occur. Moreover, from the bandwidth point of view, the level-1 data stream of the 2S modules can also cope with higher pileup or trigger rates.

13

CMSSW Simulation Based Analog Signal Injection

The simulation of particle collisions with CMSSW makes the sensor charge signals entering the analog front-end of the CBCs accessible. These simulation results form the basis for the analog signal injection with KARATE. In order to inject analog-like signals at 40 MHz the KARATE setup makes use of the injection pulse length modulation. This method allows the evaluation of the readout's performance with most realistic signal patterns at high rates. The injection method was described in detail in section 7.3.4. Since the patterns were generated for all reference module positions and pileup scenarios individually, they contain all features like cluster size distribution, charge and seed signal fluctuations, hit and cluster occupancy, as they will occur in the future Outer Tracker. This chapter investigates the influence of different operation parameters like the trigger rate and pileup on the cluster detection efficiency and noise hit occupancy. Furthermore, it presents a scan over the different module positions in the Outer Tracker for the nominal HL-LHC operation parameters.

For all measurements described in this chapter the same injector parameters were chosen. The pulse length was limited to 8 (25 ns) to reduce time-walk effects and latching hits into the next event. The pre-load of the LEDs was 2.0 V and the system was timed to latency 90 and DLL value 5. As described in section 11.2, this timing offers the best trade-off between sampling the pulses in the peak, reducing latching and preventing the detection of subsequent injections. This choice of parameters limits the maximum injected signal per channel to about 50 ke$^-$, which is far above the expected most probable signal for the FZ290 sensors. Figure 13.1 displays an example of the simulated cluster and seed signals from CMSSW simulations and the corresponding injected distributions with the KARATE setup. The digitization of the pulse length into eight values does not allow the exact reproduction of the simulated seed signal spectrum. However, the injected cluster signal comprises multiple hits and hence matches the simulated cluster signal much better.

13.1 Module Position and Discrete Signal Injection

The simulations of the sensor signals with CMSSW reveal slightly different cluster and seed charge distributions for the individual module positions. This is a consequence of the different particle incident angles on the sensors, energy spectra and particle admixtures expected for the different module positions. Furthermore, the particle flux strongly differs for the different module positions. Thus, the cluster efficiency was measured with KARATE for every module position in the tracker with nominal HL-LHC parameters. In particular, the average trigger separation was 53 (754 kHz), the simulated pileup 200 and the threshold was set to 5000 e$^-$.

The slice view through one quarter of the Outer Tracker in figure 13.2 displays the cluster efficiency (color code) for the 2S modules. The cluster efficiency varies between 96.5 % in the barrel (at $|z| = 0$) and more than 99 % for the modules on the innermost rings of the tracker endcaps. Furthermore, the map shows the numbering scheme for the reference module positions

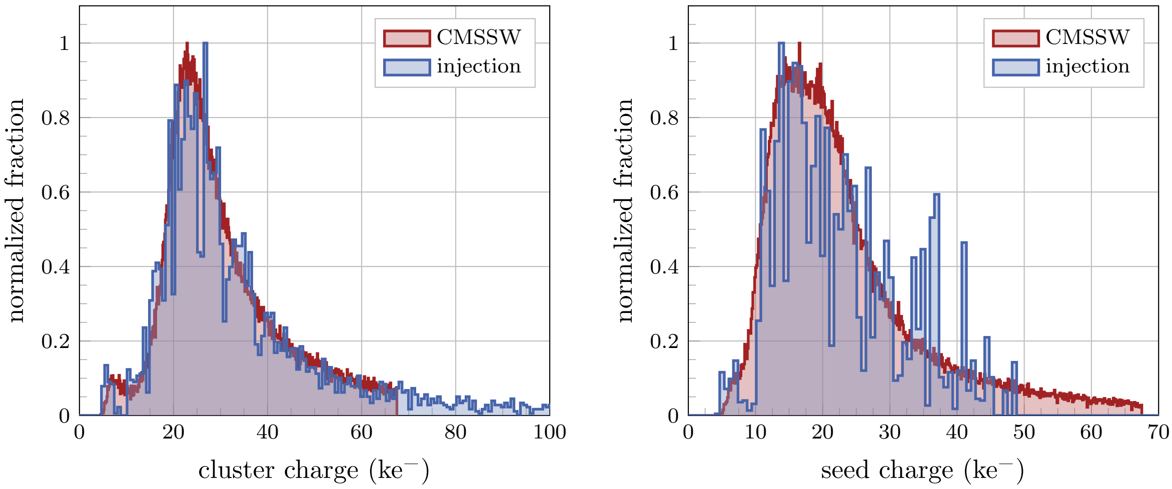

(a) Cluster charge from CMSSW and injection **(b)** Seed charge from CMSSW and injection

Figure 13.1: Cluster charge (a) and seed charge (b) distribution from CMSSW simulations compared with signals injected using KARATE. The example displays the distributions for module position 20. The coarse injection modulation with eight different values limits the resolution for charge injections into one channel. The cluster charge combines multiple injections and matches the simulations much better.

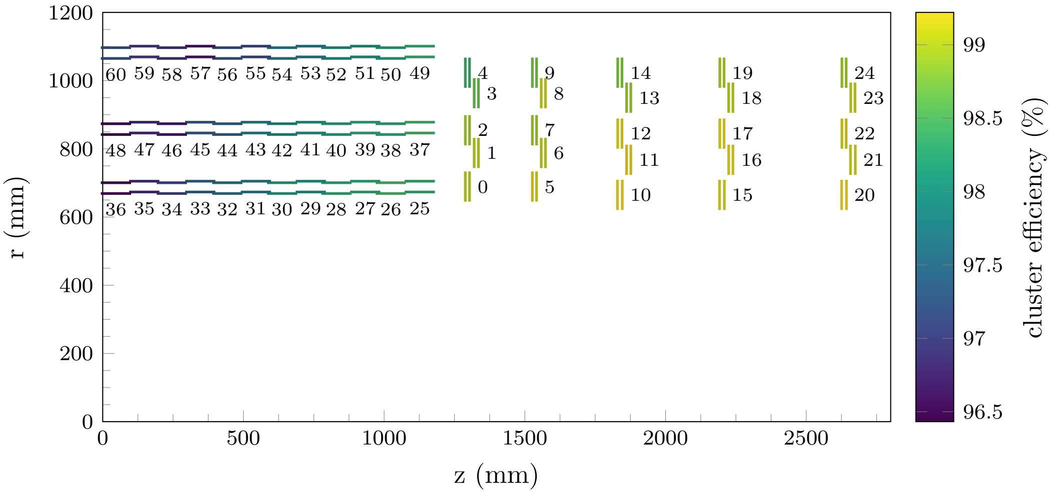

Figure 13.2: Slice view through one quarter of the Outer Tracker displaying the cluster efficiency of 2S modules recorded for analog signal injection with the KARATE setup. The pileup was 200 and the average trigger separation was 53 bunch crossings (754 kHz). The cluster efficiency varies between about 96.5 % in the barrel and more than 99 % in the endcap regions. The finite injection resolution causes the large efficiency loss. The barrel modules are less efficient due to a larger fraction of clusters with small seed signals. The map also shows the numbering scheme of the reference module positions.

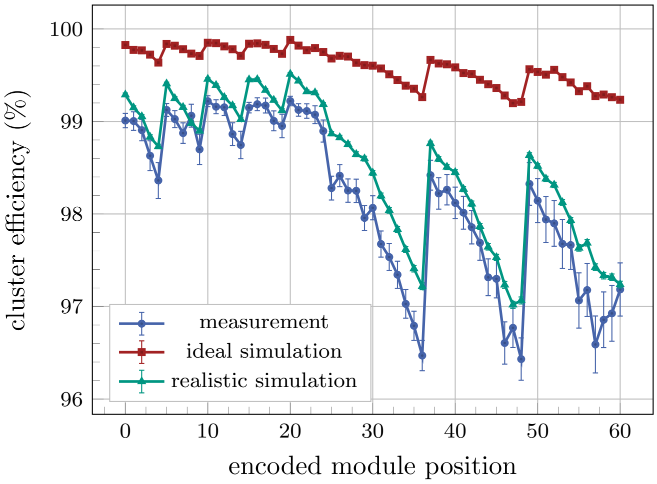

Figure 13.3: Cluster efficiency for the different module positions in the tracker from the measurement (blue), the simulation of an ideal injection system (red) and the realistic simulation (green). The simulation creats 200 000 clusters with a system noise of 7.5 Vcth (1300 e^-) and calculated the cluster efficiency for a threshold of 5000 e^-. The finite signal injection resolution of the KARATE setup strongly reduces the cluster detection efficiency. In addition the cluster efficiency depends on the module position.

in the Outer Tracker. The main reason for the efficiency losses is the finite signal injection resolution of the KARATE setup (see next section). However, there are strong differences between the barrel and endcap region. The modules in the barrel additionally suffer from a larger fraction of clusters with small seed signals. Figure C.12 displays the corresponding cluster and seed charge distribution for the module position 36 in the barrel.

13.1.1 Monte Carlo Simulation of Binned Signal Injection

To investigate the influence of the finite injection resolution on the cluster efficiency a Monte Carlo simulation was implemented. The simulation calculates the expected cluster efficiency for a given module position, threshold and channel noise. The cluster matching of the KARATE run analysis checks whether the seed strip of the cluster was detected. Thus, the starting point for every simulated cluster is the seed signal distribution for a given module position. The steps performed by the simulation are the following:

1. Generate a random seed signal following the seed signal distribution.
2. Choose randomly one of the 48 injection channels and determine the expected injected signal by using the channel calibration lookup tables. It follows the same approach as for the analog pattern injection (section 7.3.4), which chooses the pulse length best matching the targeted signal injection.
3. Add random noise following a gaussian distribution.
4. Apply the same threshold as the CBC. Only if the injected seed signal exceeds the threshold it is efficient.

This step is performed for a large number of clusters. The expected cluster efficiency is then the fraction of simulated seeds exceeding the threshold. Step two mimics the finite signal injection of the KARATE setup. An ideal injector (or the real detector) would inject the simulated signals with infinite precision and this step would not be necessary.

Figure 13.3 compares the cluster efficiency measurement for the different module positions with the realistic simulation of the KARATE injection and the ideal case with infinite injection resolution. The simulation was performed with the same operation parameters as chosen for the measurements: the threshold was set to 5000 e^- and the noise is 7.5 Vcth (1300 e^-), which equals the noise measured for the injector channels. For every module position a sample comprising 200 000 events was generated to determine the expected cluster efficiency. The resulting realistic simulation of the cluster efficiency reproduces the measurement very well.

However, the simulation shows a slightly higher efficiency. On the one hand, the applied threshold has a strong influence on the cluster efficiency. Increasing the threshold by only 150 e^- (approximately one threshold DAC value, 1 Vcth) reduces the cluster efficiency so far that it matches the measurement. Figure C.14a demonstrates the influence of different thresholds on the simulated cluster efficiency. Such small threshold variations can occur during operation by temperature drifts or imperfect offset trimming of the channels. On the other hand, there are efficiency losses in the measurements which are not considered by the simulation, like dipped hits in the undershoot after a signal injection. The hit efficiency loss caused by dipped hits Δ_h is the number of dipped hits N_d^h over the total number of injected hits $N_\mathrm{inj}^\mathrm{h}$:

$$\Delta_\mathrm{h} = \frac{N_\mathrm{d}^\mathrm{h}}{N_\mathrm{inj}^\mathrm{h}}. \tag{13.1}$$

For the nominal operation conditions (pileup 200 and 750 kHz trigger rate) it is in the order of 0.4 %, depending on the module position. Figure C.14b shows the hit efficiency loss by dipped hits for all reference module positions. The combination of the uncertainty on the threshold and dipped losses explains the slightly lower cluster efficiency of the measurement compared to the analysis.

In summary, the efficiency losses due to the finite signal injection does not allow to measure absolute efficiencies expected for the operation in the Outer Tracker. However, with KARATE the investigation of relative effects appearing for a change of the operation conditions (pileup, threshold, trigger rate) on the cluster efficiency and noise is possible.

13.2 Trigger Rate and Pileup

Even though the analog signal injection with the KARATE setup does not allow the correct measurement of the expected cluster efficiency in the future Outer Tracker, the observation of relative changes dependent on other operation parameters is possible. This section examines the influence of the trigger rate and pileup on the cluster efficiency.

Operating only 48 channels as for the analog pattern injection mode will not stress the readout bandwidth. Furthermore, the trigger rate should not influence the cluster detection efficiency. However, resonance or crosstalk effects in the front-end could lead to efficiency losses. To confirm the independence of the cluster efficiency from the trigger frequency and to investigate the influence of the hit occupancy, the average trigger separation and pileup was scanned. For the measurements the module position 20 (outermost endcap disk, innermost ring) was selected, since these modules are exposed to the highest particle flux. Thus, pileup related effects are maximal for this module position.

Figure 13.4a displays the two-dimensional scan of the cluster efficiency as a function of the pileup and average trigger rate. Indeed the cluster efficiency does not depend on the trigger rate. For low pileup only very few particles pass the module and the number of signals is very low. Thus, the observed fluctuations between the different runs are of statistical nature. The

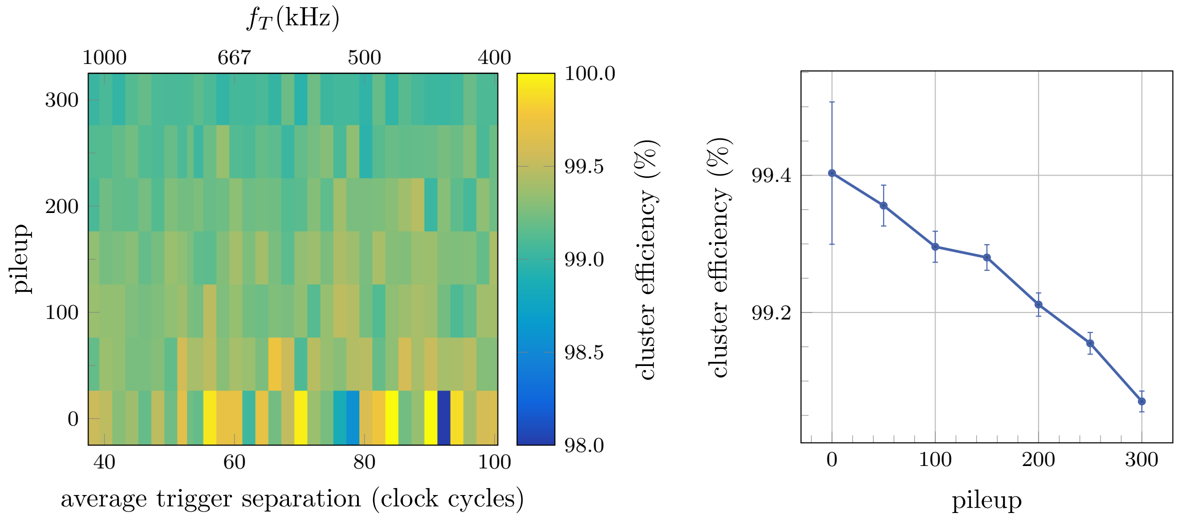

(a) 2D cluster efficiency scan

(b) Cluster efficiency projection

Figure 13.4: Cluster efficiency scanned over the average trigger separation and pileup for analog signal injection (a) recorded with the KARATE setup. The cluster efficiency does not depend on the trigger rate. The projection on the pileup axis (b) reveal a cluster efficiency loss with increasing pileup (particle flux).

independence of the trigger rate allows to project the scan on the pileup axis to increase the statistics. Figure 13.4b shows the projection on the pileup axis for the cluster efficiency scan. Increasing the pileup clearly reduces the cluster efficiency. The reuction is in the order of 0.2 % for the nominal pileup value of 200.

The cause for the efficiency reduction is the larger fraction of dipped hits for higher pileup. Increasing the pileup intensifies the particle flux exposing the module. Thus, the average time difference between two consecutive hits in the same channel reduces. As a consequence, the probability to inject hits in the undershoot of a previous injection increase. Figure 13.5a displays the projection of the hit efficiency loss caused by dipped hits Δ_h for the same scan. With increasing pileup the efficiency loss by dipped hits increase and is about 0.7 % for a pileup value of 200. Figure C.15 shows the full two-dimensional scan of the hit efficiency loss by dipped hits.

Another important aspect of the high rate operation is the noise stability. The measurements showed that the noise hit occupancy does not depend on the trigger rate (see figure C.16). The noise hit occupancy is the probability to detect a noise hit in an injector channel and is given by

$$\eta_\mathrm{n} = \frac{N_\mathrm{n}^\mathrm{h}}{N_\mathrm{inj} \cdot N_\mathrm{ch}}, \tag{13.2}$$

with the number of noise hits N_n^h in the injector channels, the number of injections (events) N_inj and the number of injector channels $N_\mathrm{ch} = 48$. Figure 13.5b displays the projection of the noise hit occupancy on the pileup axis. The noise hit occupancy increases with pileup. The higher activity on the front-end due to the larger number of injections can increase the baseline fluctuations and hence also enhance the noise hit occupancy.

In the future Outer Tracker the actual pileup will influence the efficiency of the tracker. Furthermore, the choice of the applied threshold should not only rely on noise measurements without particle collisions but also consider the changing noise hit occupancy with particle

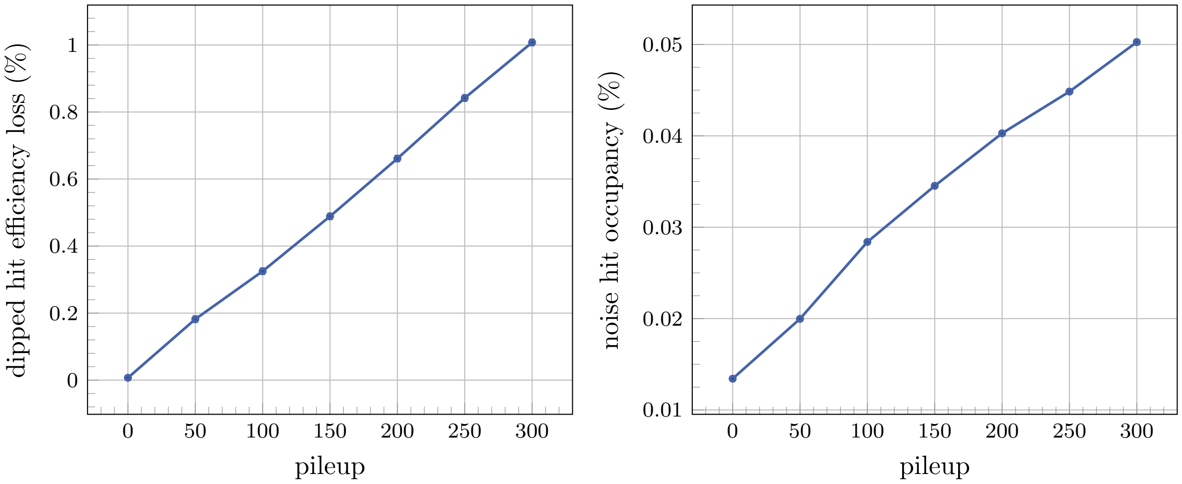

(a) Projection of hit efficiency loss by dipped hits

(b) Projection of noise hit occupancy

Figure 13.5: The hit efficiency loss caused by dipped hits (a) increase with the pileup. At nominal pileup 200 about 0.7 % of the hit efficiency loss is caused by dipped hits. The noise hit occupancy (b) increases with pileup and reaches about 0.4 % at pileup 200.

collisions. The next chapter discusses the influence of the threshold on the noise occupancy more in detail. However, even at high trigger rates and pileup the noise hit occupancy is on an acceptable level (0.04 % at pileup 200) and far below the expected hit occupancy (1 % at pileup 200). Furthermore, the scan of the trigger separation did not uncover resonance effects that reduce the cluster efficiency or increase the noise hit occupancy. Thus, no additional trigger rules that forbid distinct trigger patterns are required.

13.3 Threshold and Pileup

To operate the 2S modules efficiently the choice of the optimal threshold is essential. A too low threshold causes a large noise hit occupancy but a high threshold decreases the cluster detection efficiency of the system. Furthermore, the previous high rate measurements showed that the pileup has a non-negligible influence on the cluster efficiency. Thus, this section evaluates the influence of the threshold and pileup on the cluster efficiency and noise hit occupancy at high rates.

Figure 13.6 displays the cluster efficiency scanned over the threshold and pileup at 750 kHz average trigger frequency. As expected, the cluster efficiency drops with increasing threshold. Again the increased probability for dipped hits reduces the cluster efficiency with increasing pileup. Lowering the threshold can compensate the efficiency loss but has the drawback of a larger fraction of noise hits.

Figure 13.7 shows the recorded noise occupancy for four pileup scenarios[1], the result of a background measurement without any signal injections and the expected noise occupancy from Gaussian-shaped noise with a width of 7.5 Vcth. The measurements confirm the observation that the noise occupancy increases with pileup. Furthermore, the measured noise occupancy differs from the theoretical expectation for Gaussian-distributed noise signals. The higher occupancy for large threshold comes from a tail to high noise signals. A possible reason is

---

[1] results of the same scan as shown in the 2D plots

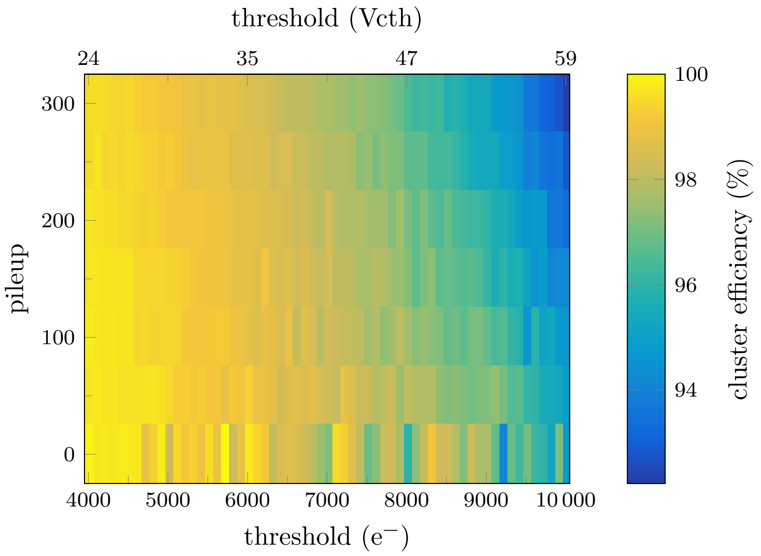

Figure 13.6: The cluster efficiency scanned over the pileup and threshold for analog signal injections. The measurements were performed for module position 20 at 750 kHz average trigger rate. With increasing threshold and pileup the cluster efficiency decreases.

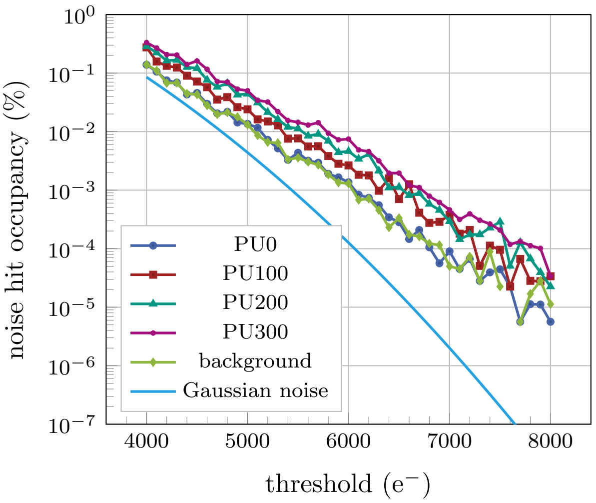

Figure 13.7: Measured noise hit occupancy for four different pileup scenarios, the recorded background noise hit occupancy without signal injection and the expected noise hit occupancy for Gaussian-distributed noise of 7.5 Vcth. Pileup and hence more activity on the channels increases the noise hit occupancy. The measured noise hit occupancy differs from the theoretical expectation.

electro-magnetic interference of external signals which shift the system's global baseline or affect single analog-front ends.

Part V

Summary and Outlook

14

Summary and Outlook

In 2026 the Large Hadron Collider (LHC) will enter high-luminosity operation. In the course of the upgrade the instantaneous luminosity will be increased by a factor of five to seven. To prepare the Compact Muon Solenoid (CMS) experiment for the upcoming high-luminosity operation several subdetector systems have to undergo an upgrade. One part of the upgrade is the complete replacement of the Outer Tracker.

The requirements for the tracking device change to cope with the intensified particle flux from the collisions. For the correct separation of the individual tracks the sensors have to provide finer granularity. Furthermore, improved radiation tolerance of the sensors is required to guarantee efficient tracking for more than ten years of operation. The most fundamental novelty of the future Outer Tracker is its contribution to the first trigger stage (Level-1 trigger) of the CMS experiment at the collision rate of 40 MHz. Silicon detector modules called p_T modules identify particles with large transverse momentum p_T already on module level. Only hit information from such particles is transmitted to the Level-1 trigger. The p_T module concept relies on two closely separated silicon sensors and is realized in two module flavors: the pixel-strip (PS) modules with higher granularity for the inner region and strip-strip (2S) modules for the outer region of the Outer Tracker. The magnetic field of the CMS detector only slightly bends the trajectories of charged particle with large p_T. Thus, hits of high-p_T particles are closely spaced in the two sensors layers. For such a spatially correlated hit pair a so called stub signal is generated, which contains information about the location and bend of the tracks. The stubs are streamed at 40 MHz bunch crossing rate to the track trigger, which then performs a quasi real-time tracking of the high-p_T particles. The tracking information is provided to the Level-1 Trigger to support the trigger decision.

The thesis at hands investigates these aspects using 2S module prototypes to identify the best suitable sensor material. Furthermore, it demonstrates the high rate stability of the 2S module readout chain and determines the limitations for the most critical operation parameters.

2S Module Prototypes

The development of the components of the 2S modules is performed by different working groups. Even though the individual components are extensively tested by the working groups also the combined system with sensors, readout chips and the other electronic components on the module have to be tested within module prototypes. In the scope of this thesis, four 2S module prototypes of reduced size, the Mini Modules, have been designed and built. The Mini Modules comprise two readout chips, the CMS Binary Chips (CBCs), and four silicon strip sensors with the final strip geometry. Like in the 2S modules the sensors are arranged in two sensor layers to also validate the functionality of the stub finding logic.

Sensor Material and Radiation Hardness

The most critical component of the 2S modules regarding radiation tolerance are the silicon sensors. Two sensor materials (thFZ240 and FZ290) from the vendor Hamamatsu Photonics

K.K. (HPK) were the final available materials considered for the application in the Outer Tracker modules. One main objective of this thesis is the comparison of the two sensor materials in combination with the CBC in prototype 2S modules. Thus, each Mini Module comprises two thFZ240 and two FZ290 sensors. The sensors of two Mini Modules have been irradiated with neutrons to two different fluences ($2.5 \times 10^{14}\,\mathrm{n_{eq}/cm^2}$ and $5 \times 10^{14}\,\mathrm{n_{eq}/cm^2}$). Another aspect to consider is annealing of the sensors. For the Outer Tracker annealing takes place during maintenance periods. To study the influence of annealing on the module performance the irradiated sensors have been annealed to two different equivalent annealing times at room temperature (13 d and 204 d).

The sensor efficiency and resolution in the Mini Modules have been determined with a beam test using a 5.6 GeV electron beam at the Deutsches Elektronen-Synchrotron (DESY). By tracking the electrons with a beam telescope the cluster detection efficiency and tracking resolution of the sensors have been quantified. Both sensor materials show excellent performance and reach cluster detection efficiencies of more than 99.9 % at reasonable noise levels. In particular, for all fluences and annealing times investigated both sensor materials outperform the minimum requirements of 99.5 % cluster efficiency at a noise occupancy below 10^{-4}. However, the FZ290 sensors provide a better performance in all configurations except for the highest fluence and long annealing time. This scenario only holds for less than one percent of the 2S modules in an extended High Luminosity LHC (HL-LHC) operation scenario. Furthermore, the measurements demonstrate that for this scenario the performance of the two materials converge by a boost of the sensor bias voltage from nominal 600 V to at least 800 V. Besides that, it is shown that the cluster efficiency profits from inclined particle tracks.

Another important performance parameter is the spatial resolution of the sensors. The measured spatial resolution of all sensors is in the order of the binary resolution for one-strip clusters (26 µm) or better. The resolution reaches a minimum of 22 µm for tracks with an inclination of about 15°. For this inclination the resolution heavily profits from charge sharing between neighboring strips.

Putting all these results into perspective of the future Outer Tracker requirements the FZ290 material provides a better performance for the 2S modules. Following the results of this thesis and other complementary studies on charge collection measurements, the sensor working group decided to order sensors made from FZ290 silicon for the future Outer Tracker.

Performance of the Stub Finding Algorithm

The double layered structure of the Mini Modules allows performance tests of the stub finding logic. Efficient stub detection is crucial for the tracking of high-p_T particles by the track trigger. The beam test measurements yield a stub efficiency of 99 % and more for the prototype modules. The lower efficiency compared to the cluster efficiency is caused by a programmable cut on the maximum cluster size performed by the stub finding logic. For the measurements the stub logic only accepted clusters with three strips or fewer. The average cluster size increases with the sensor thickness. Thus, the FZ290 sensors have a slightly lower stub efficiency compared to the thFZ240 material. However, the maximum accepted cluster size can be increased to a larger value which would improve the stub detection efficiency of the FZ290 material.

The functionality of the bend reconstruction and filtering on the bends was proven by scanning the stub efficiency over the particle inclination angle. On the one hand, the recorded bends for different track inclinations agree with the expectations from the geometry of the module design. On the other hand, the stub detection efficiency goes to zero for inclinations above the programmed bend cut. All the measurements confirmed the correct functionality of the CBC's stub finding logic.

Operation Conditions, Threshold Calibration and Sensor Defects

Operation conditions like the temperature, sensor bias voltage and leakage current impact the behavior of the Outer Tracker modules. Measurements with the Mini Modules showed a linear increase of the module noise with temperature. Furthermore, temperature shifts without retrimming worsen the trimming quality of the channels. The sensor bias voltage does not influence the module noise for voltages above 200 V, which is far below the nominal operation voltage of 600 V. In contrast, leakage current contributes to the noise of the sensors. Since radiation damage increases the leakage current of the sensors during the operation time in the HL-LHC the impact of the sensor leakage current on the noise was quantified. A linear increase of the noise with leakage current was observed. However, this effect is very small. For the extended HL-LHC scenario and the most irradiated 2S modules the current induced noise increase is in the order of 10 % compared to the unirradiated modules. Even for this worst-case scenario the noise of the modules will remain below the specified limit of 1000 e^-.

In the scope of the thesis, the threshold digital-to-analog converter (DAC) value Vcth of the CBC has been calibrated into a charge equivalent signal using CBC-internal test pulses. Besides that a novel calibration method was presented which compares the signal spectrum of a radioactive ^{90}Sr source recorded by the CBC with the measurement of a calibrated reference system. The combination of both methods resulted in a calibration factor of 173 e^-/Vcth. The ability to convert the threshold DAC value into a charge equivalent signal allows the comparison of the results obtained with the CBC with other systems.

Even though all sensors undergo a wide range of tests before constructing the final 2S modules defects of the sensors can occur. The occurence of defects can have several reasons like production failures, inappropriate handling in the course of the module assembly and testing or defects can even occur during the operation. Three classes of sensor defects (AC and DC shorts of adjacent channels, pinholes) have been artificially generated on the Mini Modules to study their impact on the module performance. AC shorts result in a non-predictable noise behavior of the affected strips so that they have to be masked during operation. DC shorts increase the noise of the affected strips by more than 50 % and lower the sensitivity to charge signals. Pinholes are a defect known to be critical in other systems. These defects short-circuit the strip implants and the aluminum strip so that the sensor leakage current can drain into the readout chip. The measurements with the Mini Modules showed that pinholes do not affect the strip sensitivity or noise, even for high sensor leakage currents.

High Rate Bandwidth Tests of the 2S Module Readout Chain

Commonly used particle sources like test beams or tests with radioactive sources do not provide the hit occupancies or trigger rates as expected during the high-luminosity operation in the Outer Tracker. Thus, Maier [Mai19] developed the KArlsruhe High RAte TEst (KARATE) setup to perform high rate test of the CBC. The KARATE setup injects pulse height modulated signals at the LHC's bunch crossing rate (40 MHz) into 48 front-end channels of the CBCs. In the course of this thesis, the setup has been extended to perform stress tests on the full 2S module readout chain. This readout chain includes 16 CBCs version 3.1, two Concentrator Integrated Circuits (CICs) version 2, one Gigabit Transceiver (GBTx) and one Versatile Link Transceiver (VTRx). The first two stages of the readout chain (CBCs and CICs) are the bottlenecks for the data transmission.

Having full knowledge about the injected hit patterns KARATE enables efficiency studies by comparing the injected patterns with the recorded hits. A very clean approach to determine the ultimate limitations of the system is the injection of a constant number of clusters at a fixed trigger rate. By doing so the specified limits for the triggered data stream of the CBC and CIC have been confirmed.

However, this method does not represent realistic conditions as expected in CMS. Thus, injection patterns have been generated based on simulations with the CMS Software (CMSSW) package. The CMSSW package simulates proton-proton collisions, then it uses Geant4 to determine the interaction of the emerging particles with the detector and it emulates the response of the detector electronics. From the CMSSW simulations the analog charge signals in the strips for every 2S module were extracted and served as input for the pattern generation.

Based on these simulations stress tests of the readout bandwidth for all module positions in the tracker, different pileup scenarios and trigger rates have been performed. The measurements demonstrated the stability of the 2S module readout chain at a nominal average pileup value of 200 and 750 kHz average trigger rate. Furthermore, the margins to even higher pileup scenarios and trigger frequencies have been determined. For the modules exposed to the highest particle flux, either the pileup can be increased up to 300 or the trigger rate boosted to about 1 MHz (CBC limit) without running into bandwidth limitations.

The ability of the KARATE setup to inject pulse-height-modulated signals makes it suitable to inject analog charge signal patterns extracted from the CMSSW simulation. By doing so, the influence of pileup and trigger rate on the cluster efficiency and noise hit occupancy have been evaluated. The results confirm the expectation that the trigger rate does not impact the cluster efficiency or noise hit rate. However, this does not hold for different pileup scenarios. On the one hand, the measurements showed that the increased activity on the analog front-end increases the noise hit occupancy. On the other hand, the cluster efficiency decreases with pileup due to more missed hits in the undershoot of previous injections.

The CBC has a 32 events deep readout buffer that stores triggered events awaiting the readout. Simulations demonstrated that for long runs the probability for the occurence of a readout buffer overflow is not vanishing at nominal 750 kHz trigger rate. Such an overflow will occur for all 2S modules at the same time and cause data losses. Thus, an algorithm has been developed to veto triggers which would cause an overflow of the CBC's readout buffer. The algorithm only relies on the knowledge of the trigger history. The functionality of the algorithm has been proven by measurements using the KARATE setup. Regarding the operation in the CMS detector such an algorithm has to be implemented in the Trigger Throttling System to prevent the failure of the 2S modules during operation.

Outlook

The measurements carried out using Mini Modules and presented in this thesis not only identified the best suitable sensor material for the future 2S modules but also confirmed the correct functionality of the CBC's stub finding algorithm. These milestones pave the way to purchase the final sensors for the upcoming production of 2S module. However, beam test studies with full-sized 2S module prototypes are inevitable. Recently the first beam tests with full 2S module prototypes were carried out. The measurements focused on aspects which could not be covered by the Mini Module studies, like the inefficiency in the region between the two strip rows of 2S sensors and proton-irradiated sensors. Furthermore, the functionality of the stub finding algorithm in full 2S modules with all final readout components are investigated more in detail. The analysis of the recorded beam test data is still ongoing.

The high rate measurements with the KARATE setup investigated the full 2S module readout chain under realistic data and trigger rates to identifiy possible bottlenecks or issues already in an early prototype phase. The measurements demonstrated the stability of the readout chain for the expected data rates at nominal pileup and trigger rates and determined the ultimate limitations of the readout electronics. Future studies will focus on high rate measurements on full 2S modules with signals induced by charged particles in a high intense particle beam. Therefore, the CYRCé[1] cyclotron at the Institut Pluridisciplinaire Hubert Curien (IPHC) in Strasbourg is currently under preparation to provide a 25 MeV proton particle beam line with comparable track densities as expected in the CMS experiment [Nib21]. The beam line will allow high rate measurements of the readout chain with particle induced signals in a high radiative environment similar to the operation conditions in the future Outer Tracker.

---

[1] Cyclotron pour la Recherche et l'Enseignement

Part VI

Appendix

A

Additional Laboratory Test Plots

Sensor Characterization

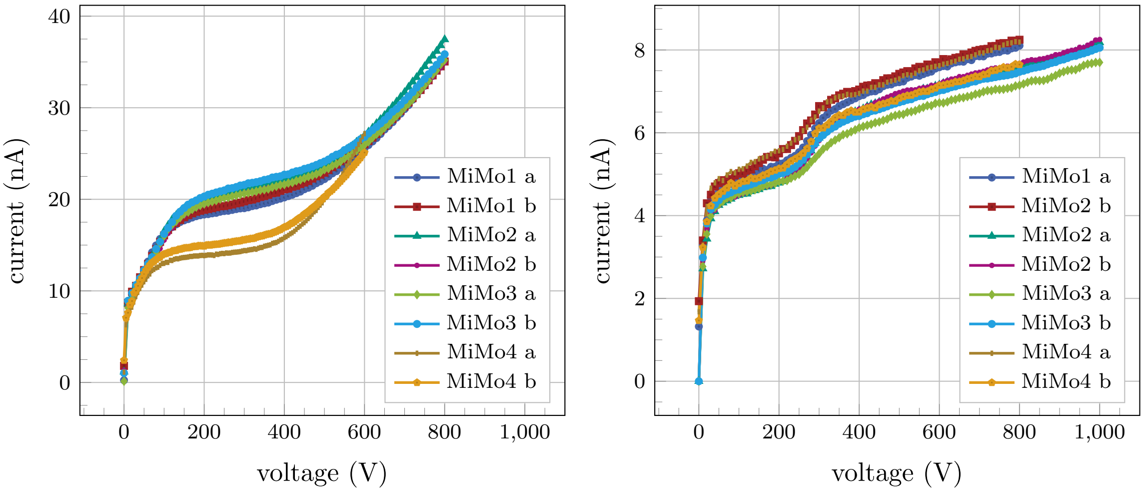

(a) thFZ240 **(b)** FZ290

Figure A.1: I(V) characteristics before irradiation of all baby sensors used for the construction of Mini Modules.

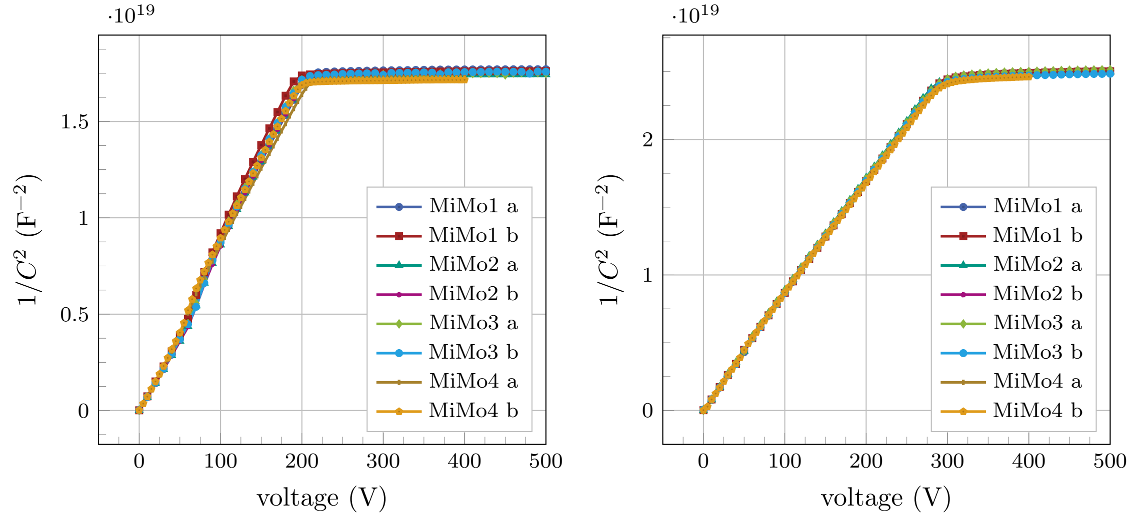

(a) thFZ240 **(b)** FZ290

Figure A.2: C(V) characteristics before irradiation of all baby sensors used for the construction of Mini Modules. The thinner thFZ240 sensors already deplete at about 200 V, the thicker FZ290 sensors at about 300 V. All sensors of the same material show a very similar behavior.

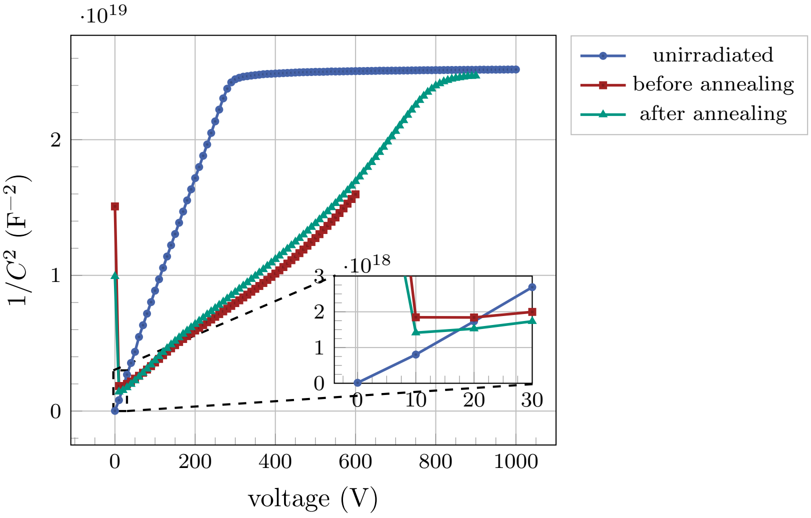

Figure A.3: C(V) characteristics of an FZ290 sensor before and after irradiation to $2.5 \times 10^{14}\,\mathrm{n_{eq}/cm^2}$ and with additional equivalent annealing of 199 d at room temperature. After irradiation the full depletion voltage increases from 300 V to about 800 V (kink in the curves) and the capacitance for very low voltages (< 20 V) is lower compared to the unirradiated sensor. Annealing has only a minor effect on the capacitance of the sensor.

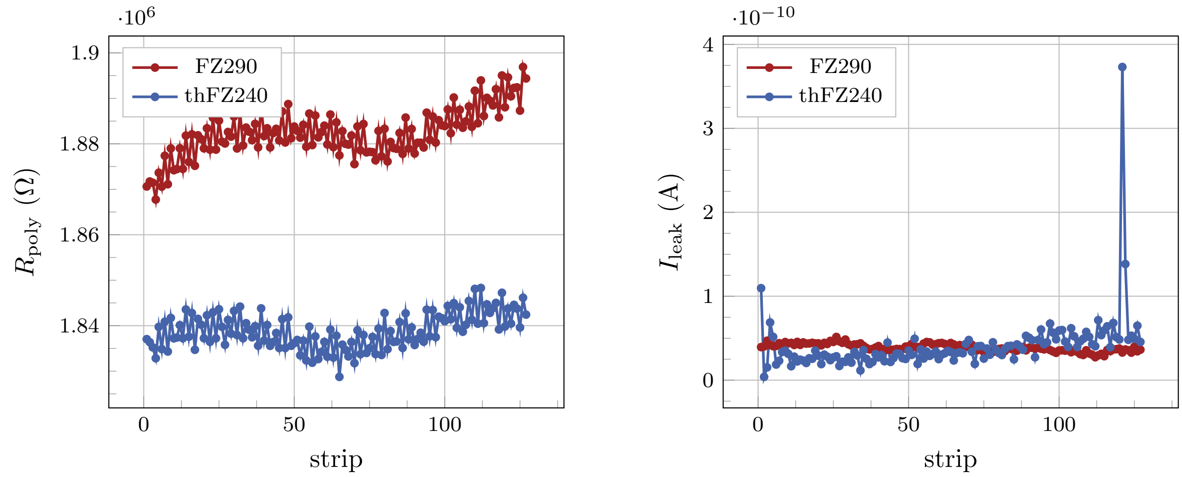

(a) Resistance of the poly resistor R_{poly}

(b) Strip leakage current I_{leak}

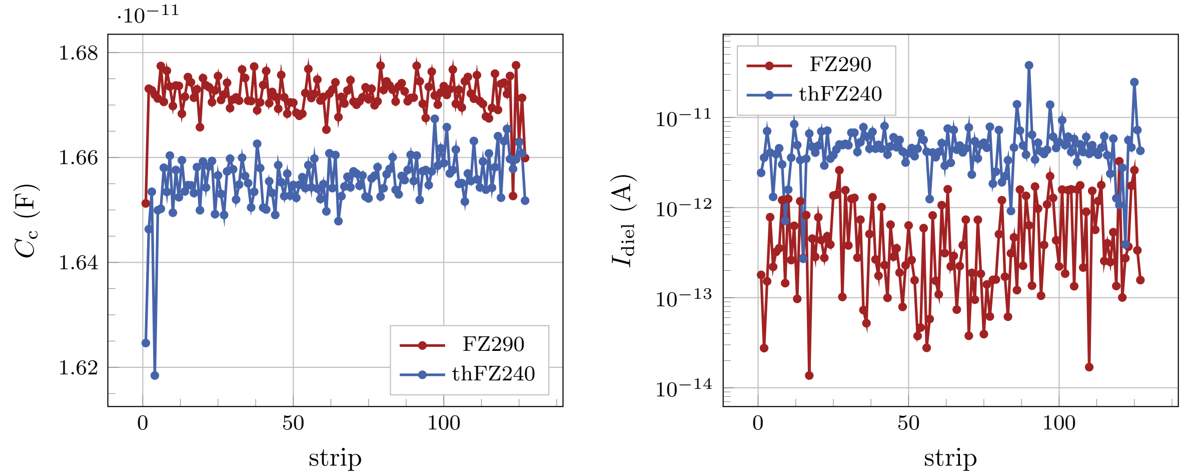

(c) Coupling capacitance C_{c} between implant and Al strip

(d) SiO_2 isolation current I_{diel} identifies pinholes

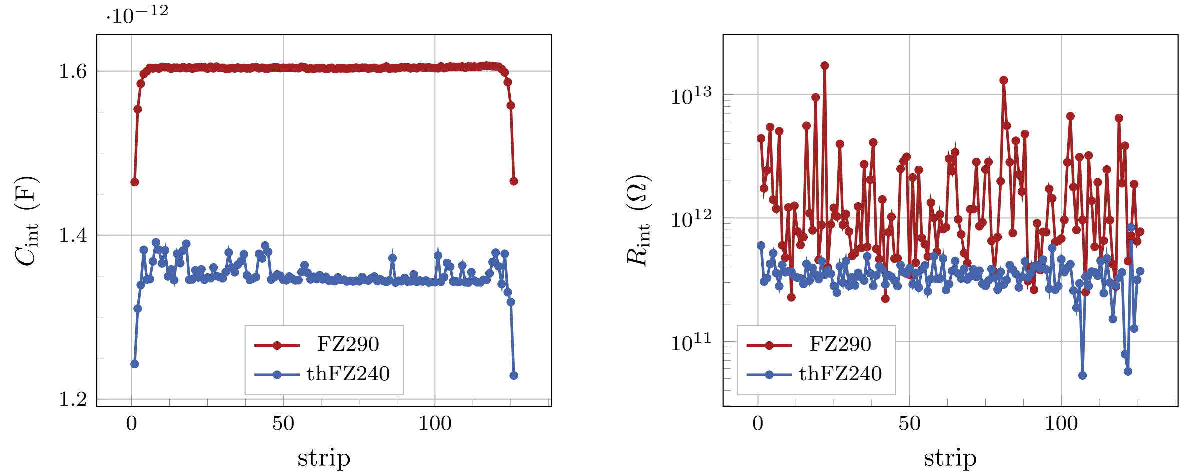

(e) Inter-strip coupling capacitance C_{int}

(f) Inter-strip resistance R_{int}

Figure A.4: Typical results for the strip scans of R_{poly} (a), I_{leak} (b), C_{c} (c), I_{diel} (d), C_{int} (e) and R_{int} (f) recorded with unirradiated baby sensors made of the FZ290 (red) and thFZ240 (blue) silicon. The measurements are a powerful tool to monitor the sensor quality. Furthermore, they discover pinholes (high I_{diel}) or shorts of neighboring implants (low R_{int}).

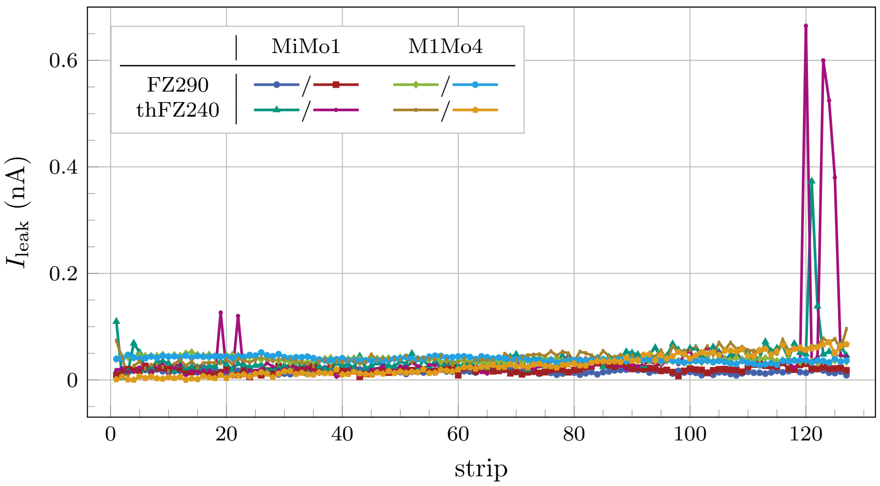

Figure A.5: Strip leakage current I_{leak} of the unirradiated sensors which have been installed in the prototype modules. The measurements were performed at 350 V sensor bias voltage. All sensors have a very uniform and low strip leakage current at about 0.1 nA. The leakage current of some strips of two sensors is increased by a factor of five to six but still very low compared to irradiated sensors.

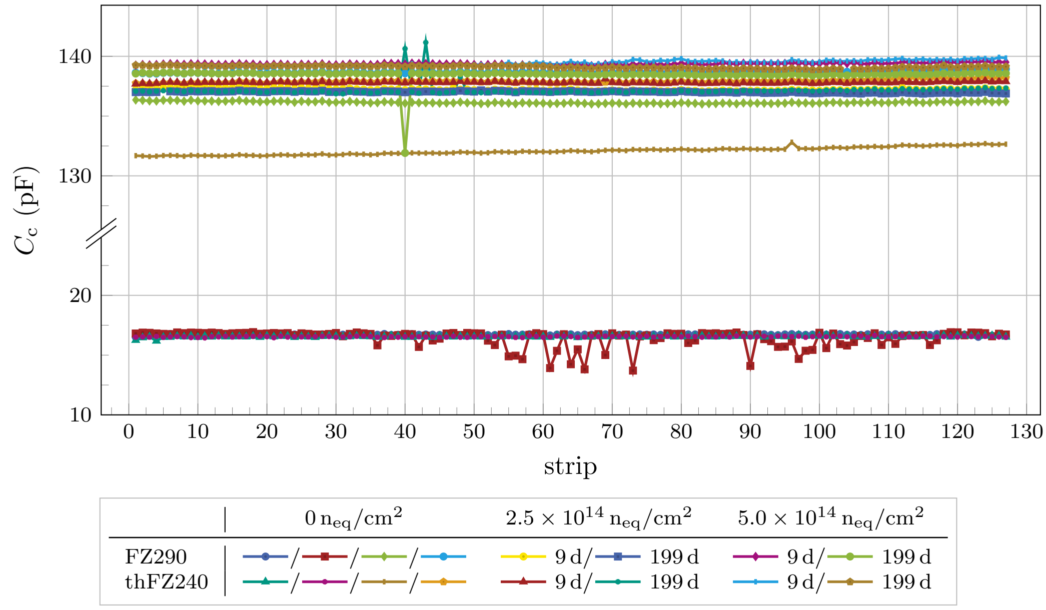

Figure A.6: Strip coupling capacitance C_c of all baby sensors before the installation in the module prototypes. All sensors show a very uniform coupling capacitance. The measurements were performed at 350 V sensor bias (300 V for 5×10^{14} n_{eq}/cm^2 sensors) and at 20 °C (−20 °C for irradiated sensors). For the measurements of one set of sensors the capacitance compensation failed, which is responsible for the large offset of these measurements.

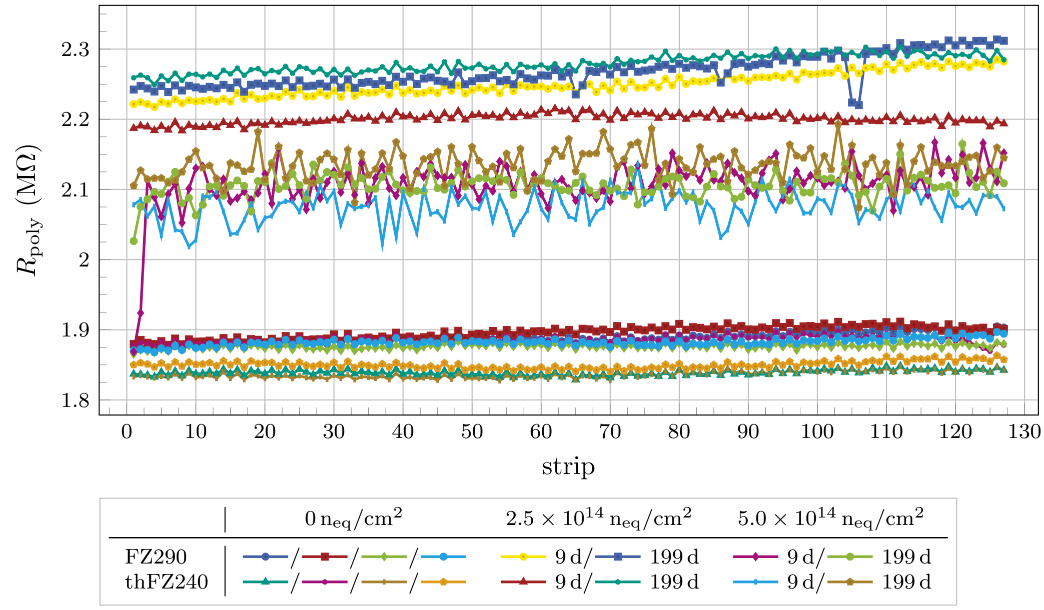

Figure A.7: Measurements of the resistance R_{poly} of the strip poly resistors for all sensors installed in the module prototypes. The measurements were performed at 350 V sensor bias (300 V for 5×10^{14} n_{eq}/cm^2 sensors) and at 20 °C (−20 °C for irradiated sensors). All sensors show a very uniform poly resistance of about 2 MΩ. The offset to higher resistances for the irradiated sensors is caused by the temperature dependent resistance of silicon.

Recorded Seed and Cluster Charge: thFZ240 vs. FZ290

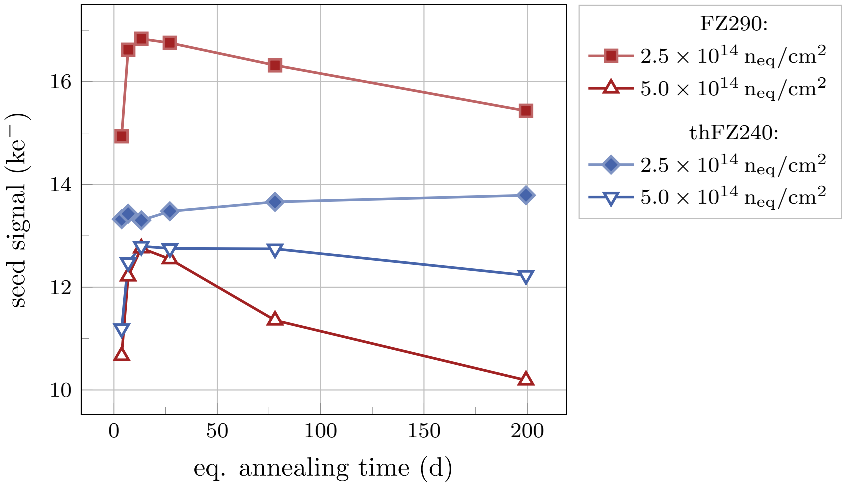

Figure A.8: Seed signal over equivalent annealing time at 21 °C for two different fluences. The FZ290 sensors are more sensitive to annealing. For the FZ290 sensors a short annealing time is beneficial and the seed signal reaches a maximum after 13 d annealing time at 21 °C. For longer annealing times it decreases. The signal of the thFZ240 sensors suffers less of irradiation and annealing. For the higher fluence the thFZ240 sensor shows a beneficial short time annealing and only a very slight long time reverse annealing.

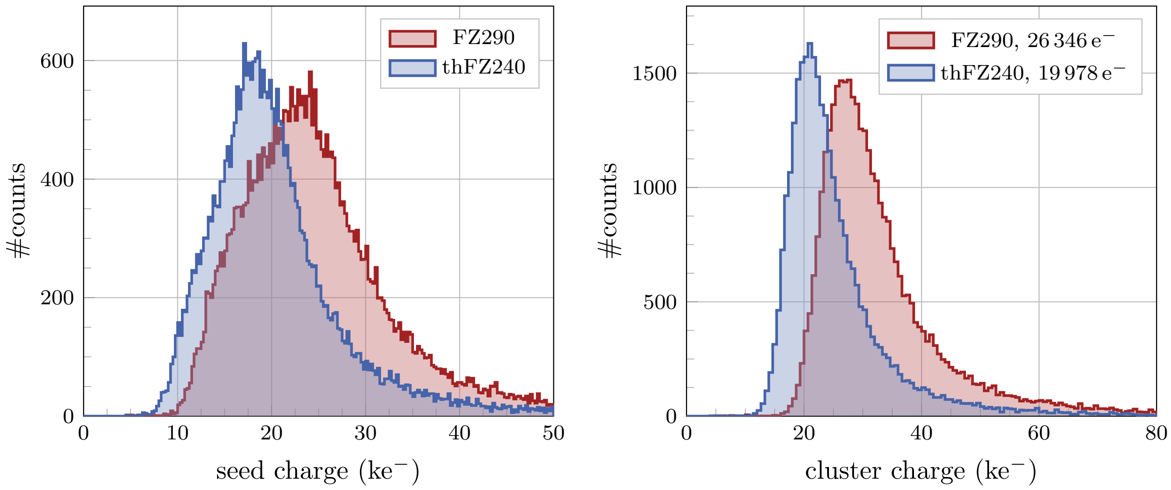

(a) Seed charge

(b) Cluster charge and most probable value (MPV)

Figure A.9: Comparison of the seed charge (a) and cluster charge (b) for energy depositions of electrons emitted by a ^{90}Sr source. The measurements were performed in the ALiBaVa setup for thFZ240 and FZ290 sensors at 20 °C and 400 V bias voltage. Since the FZ290 sensors are thicker the electrons create more charge carriers.

Simulated Energy Deposition in thFZ240

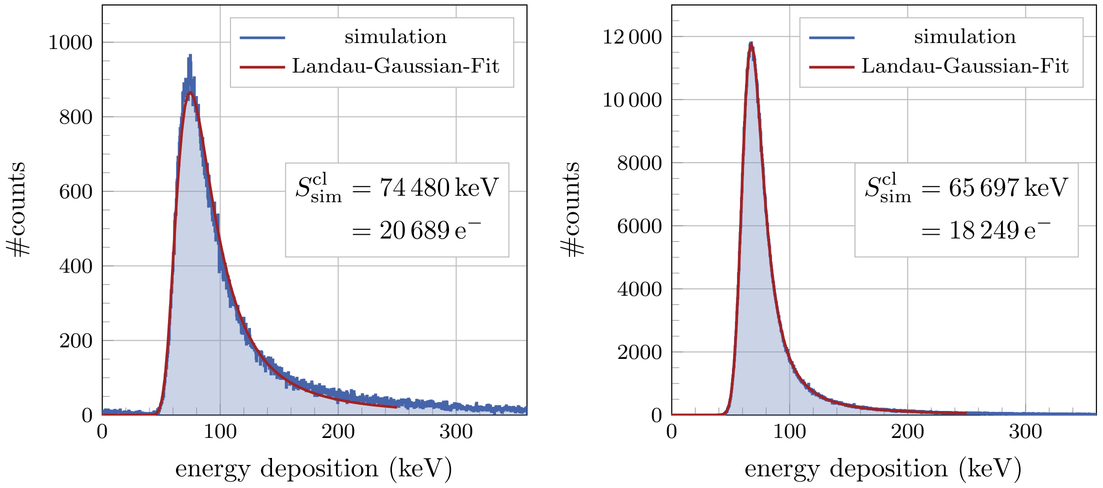

(a) Energy deposition of electrons from ^{90}Sr **(b)** Energy deposition of 100 GeV muons

Figure A.10: Geant4 simulation of the energy deposition of electrons from a ^{90}Sr source in the ALiBaVa setup (a) and 100 GeV muons (MIPs) (b) in a 240 µm thick silicon sensor. Using the mean energy to generate an electron-hole pair 3.6 eV the MPV ($S^{\text{cl}}_{\text{sim}}$) of the energy deposition is converted into a charge signal. The ionisation power from electrons of ^{90}Sr ($86\,\text{e}^-\,\mu\text{m}^{-1}$) is larger compared to that of MIPs ($76\,\text{e}^-\,\mu\text{m}^{-1}$). [Nür21]

Sensor Defects and Bias Voltage

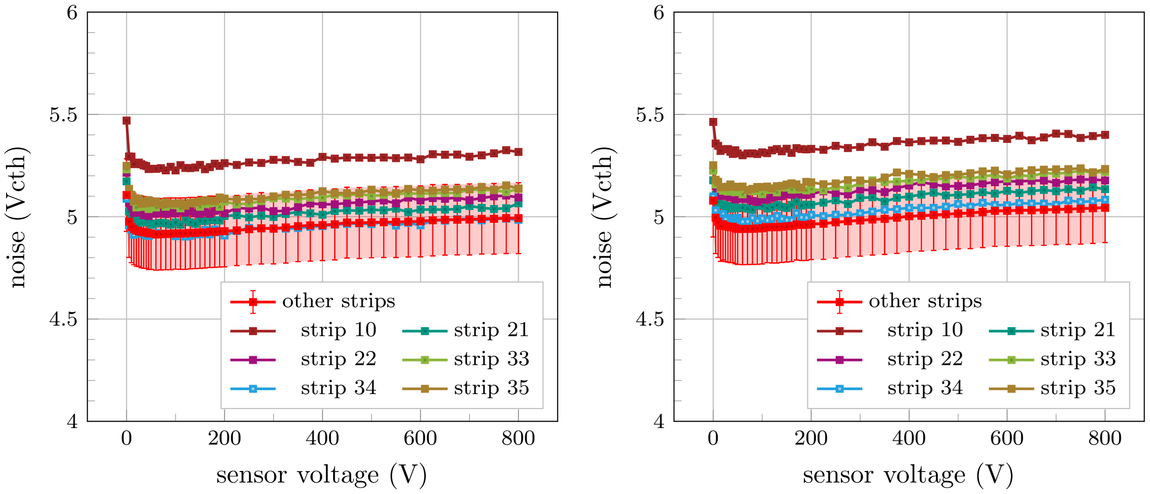

(a) Before adding pinholes **(b)** After adding pinholes

Figure A.11: Noise over the sensor bias voltage for the strips of MiMo2 before (a) and after (b) adding pinholes. Futhermore, the plots show the average noise of the other strips without defects in red. The error bars are the standard deviation. The scans were recorded at −20 °C. Adding pinholes does not change the channel noise. The higher noise of the channels with pinholes is a purely random effect by the choice of the channels.

Simulated DATURA Telescope Resolution for the Mini Module Beam Test Setup

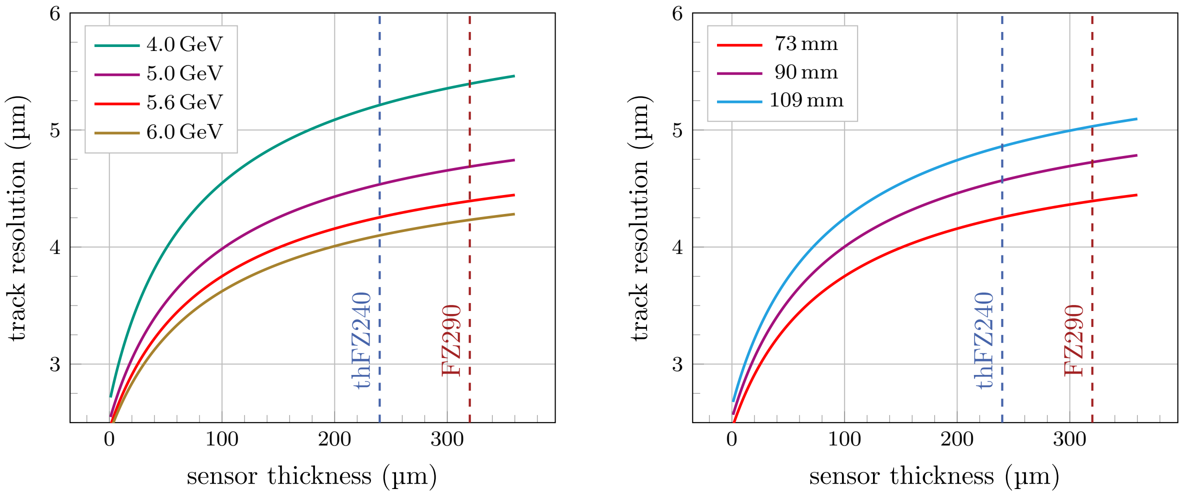

(a) Track resolutions dependence on the beam energy E_b for $x_d = 73\,\mathrm{mm}$

(b) Track resolution dependence on the downstream distance x_d for $E_b = 5.6\,\mathrm{GeV}$

Figure A.12: Simulation of the expected DATURA telescope track resolution with the 2S Mini Module setup geometry for different sensor thicknesses. The track resolution strongly depends on the beam energy E_b as shown in (a). In addition the resolution improves when bringing the telescope closer to the device under test (DUT). For the Module beam test configuration ($E_b = 5.6\,\mathrm{GeV}$ and x_d of 73 mm to 109 mm) the expected track resolution is in the order of 4 µm to 5 µm. This is much better than the binary resolution $p/\sqrt{12} \approx 26\,\mathrm{\mu m}$ of the DUTs [SJ20].

B

Additional Beam Test Plots

Cluster Efficiency and Sensor Voltage

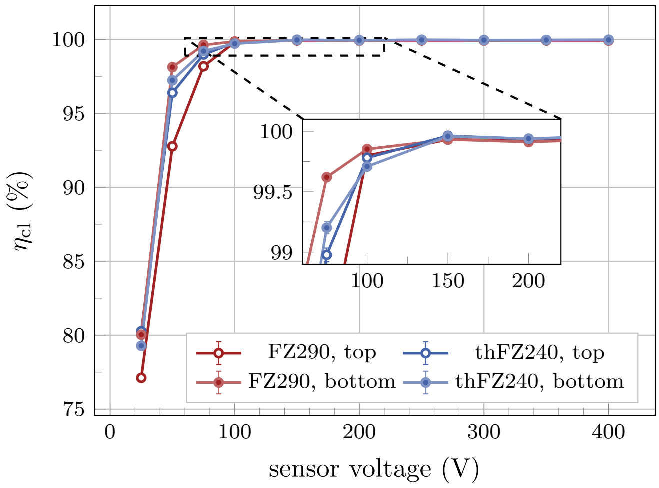

Figure B.1: Cluster efficiency over the sensor bias voltage for the unirradiated MiMo1. The threshold was approximately 4800 e^-. An increase of the sensor voltage improves the cluster detection efficiency. All sensors reach more than 99.8 % cluster detection efficiency at about 150 V. This bias voltage is far below the sensor depletion voltages (200 V for thFZ240, 300 V for FZ290).

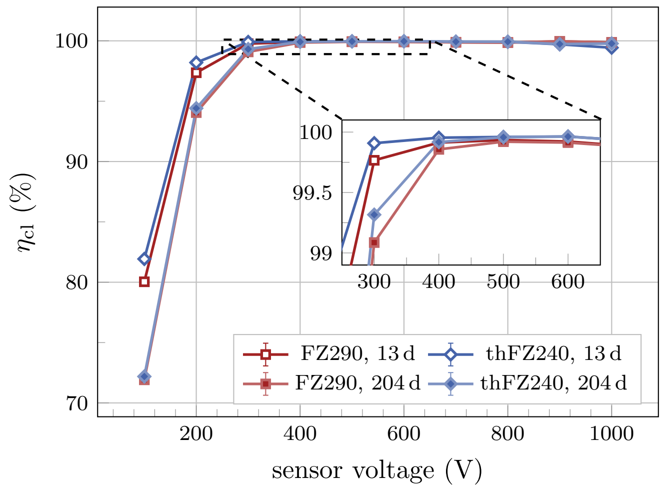

Figure B.2: Cluster efficiency over the sensor bias voltage for MiMo2 ($2.5 \times 10^{14}\,\mathrm{n_{eq}/cm^2}$). The threshold was approximately 3500 e^-. An increase of the sensor voltage improves the cluster detection efficiency. The efficiency of the long annealed sensors (204 d eq. time at 21 °C) saturates at about 400 V. For the short annealed sensors the saturation sets in at already 300 V. All sensors reach more than 99.8 % cluster detection efficiency. The drop of the efficiency at 1000 V comes from a higher threshold (5100 e^-) for this point.

Cluster Efficiency and Track Inclination

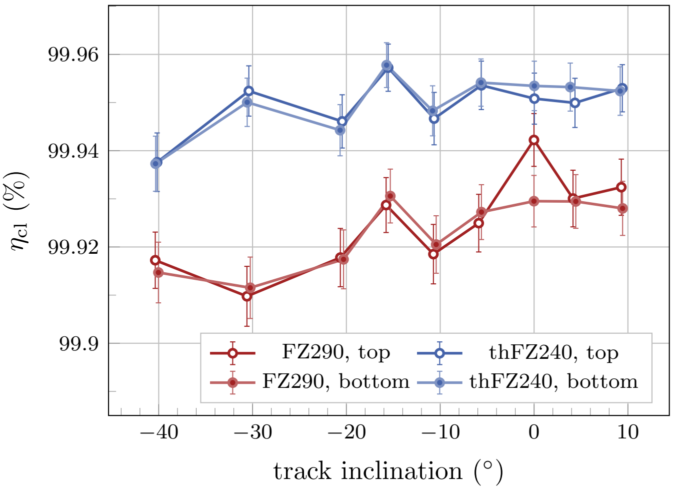

Figure B.3: Cluster efficiency for different track inclinations between −40° to 10° for MiMo1. The bias voltage was 400 V, the threshold approximately 4800 e^- and the module operated at room temperature. At the chosen threshold the cluster efficiency does not depend on the particle incidence angle. All sensors reach an efficiency of more than 99.9 %.

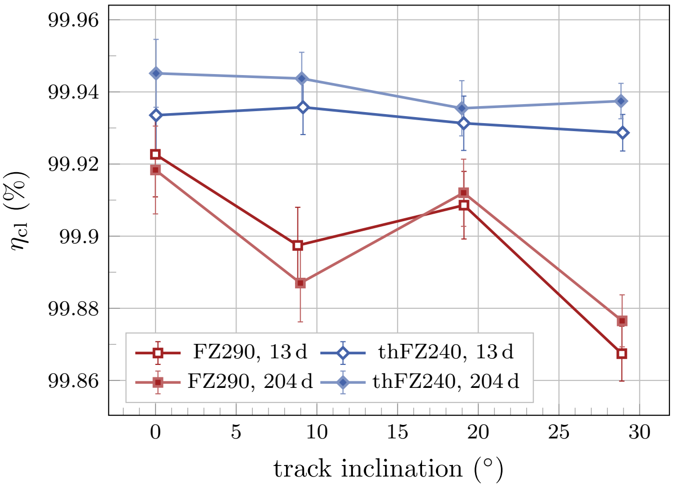

Figure B.4: Cluster efficiency for different track inclinations between 0° to 30° for MiMo2. The bias voltage was 600 V, the threshold approximately 3500 e^- and the module cooled down to −22 °C. Due to the relative low threshold all sensors are fully efficient for all track inclination. Only for the FZ290 sensors the efficiency tend to decrease slightly for large inclinations. But this effect is within the 0.01 % uncertainty coming from the time-to-digital converter (TDC) cut. The sensors reach a cluster detection efficiency of about 99.9 %.

Sub Strip Efficiency and Cluster Size

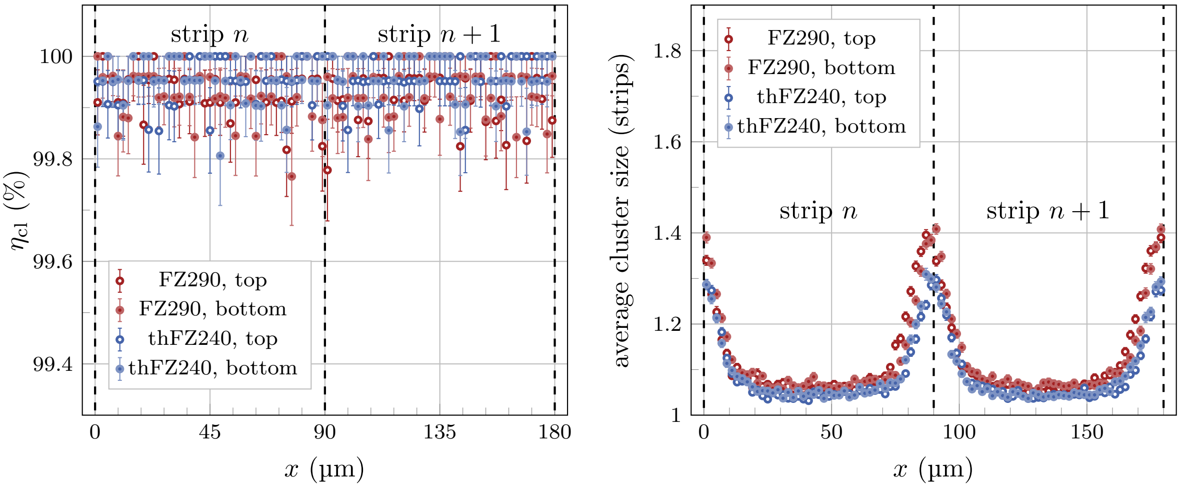

(a) Sub strip cluster efficiency

(b) Average sub strip cluster size

Figure B.5: Sub strip efficiency (a) and average cluster size (b) over the track position in two strip unit cells recorded with MiMo1 (unirradiated). The module temperature was 20 °C, the sensors biased with 400 V and the threshold 4800 e^-. At this nominal threshold the sensors do not exhibit inefficient regions. Charge sharing for tracks hitting the sensor in the region between the strips increase the cluster size. This effect is more pronounced for the thicker FZ290 sensors, since the charges have a larger drift distance through the sensor and the probability for diffusion induced charge sharing increases.

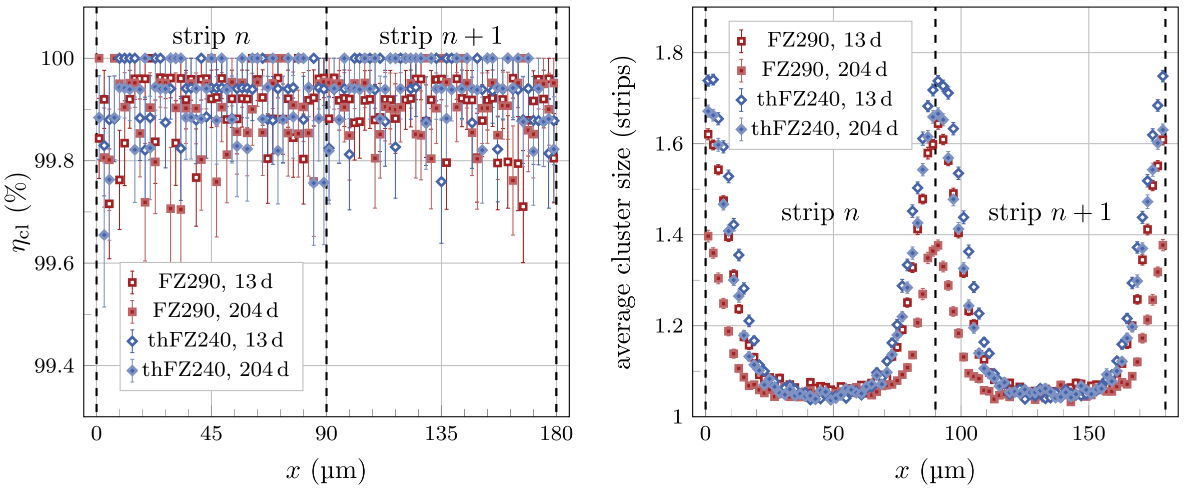

(a) Sub strip cluster efficiency

(b) Average sub strip cluster size

Figure B.6: Sub strip efficiency (a) and average cluster size (b) over the track position in two strip unit cells recorded with MiMo2 ($2.5 \times 10^{14}\,\mathrm{n_{eq}/cm^2}$). The module temperature was −22 °C, the sensors biased with 600 V and the threshold at 4600 e$^-$. At this nominal threshold the sensors do not exhibit inefficient regions. The effect of charge sharing manifests in the larger average cluster size for tracks passing the sensor in the central region between the strip implants. The average cluster size and thus charge sharing increased compared to the unirradiated MiMo1.

Sub Strip Cluster Size and Incidence Angle

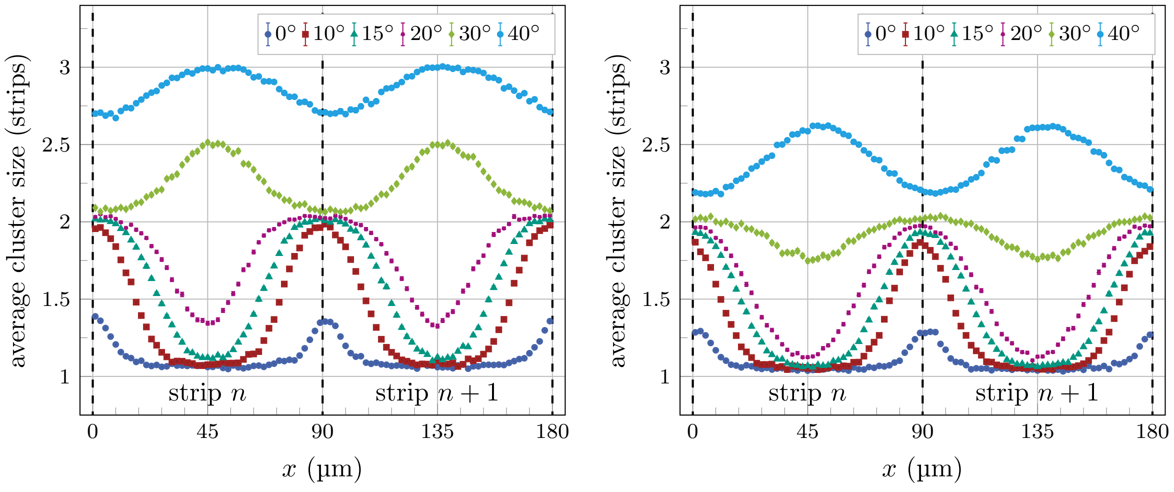

(a) FZ290, bottom

(b) thFZ240, bottom

Figure B.7: The average cluster size over two strip unit cells for multiple track inclinations and for the two materials of the unirradiated MiMo1. The sensors were biased with 400 V and operated at 20 °C. A larger track inclination increases the average cluster size. For the thinner thFZ240 material (b) the track inclination has to be higher to generate the same cluster size as for the FZ290 material (a).

Stub Efficiency Threshold Scan MiMo2

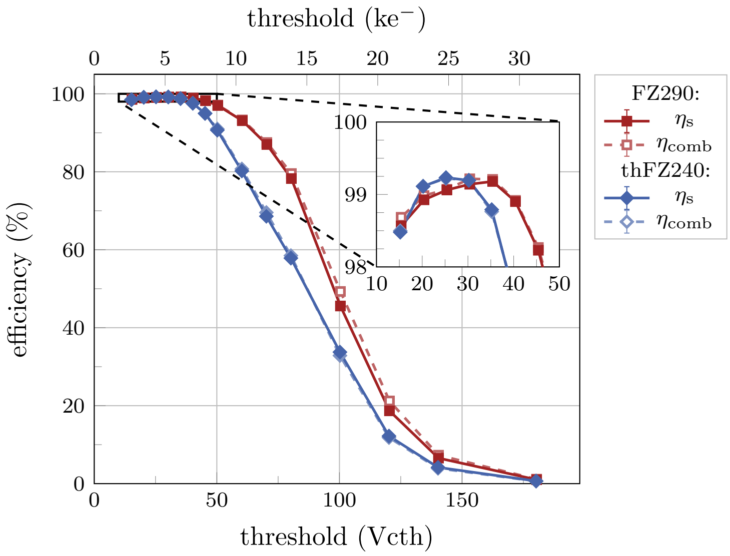

Figure B.8: Stub efficiency and combined cluster efficiency (cluster size < 4) for a threshold scan with MiMo2 and vertically inclined tracks. The sensors were biased with 600 V at a module temperature of $-22\,°\mathrm{C}$. Even after a fluence of $2.5 \times 10^{14}\,\mathrm{n_{eq}/cm^2}$ the sensors reach a stub efficiency of up to 99.2 %. The FZ290 sensors have a wider threshold range for efficient operation compared to the thFZ240 sensors.

Fraction of Different Cluster Sizes and Threshold

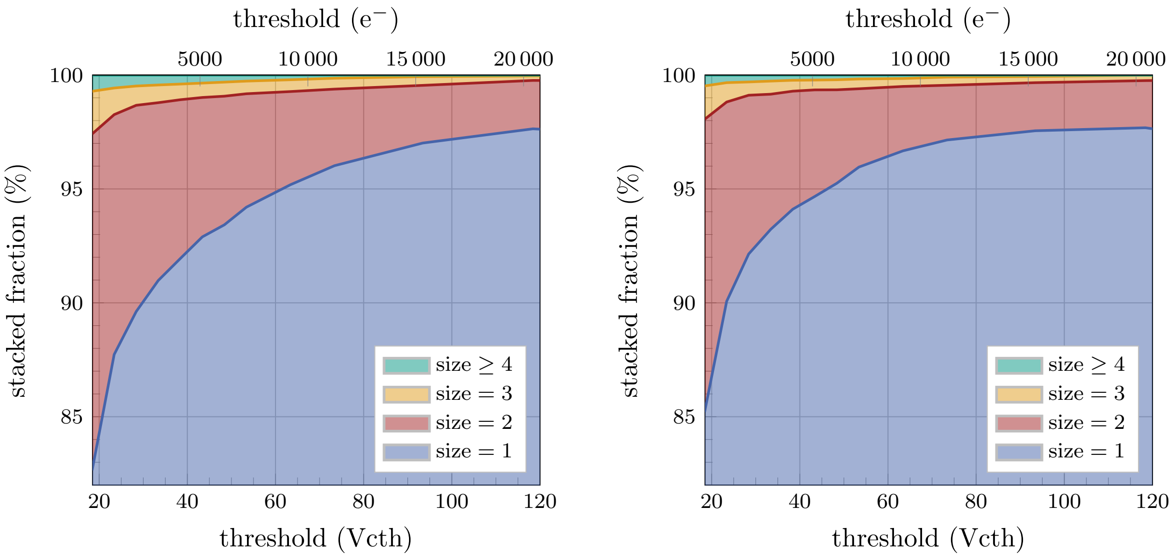

(a) FZ290, bottom

(b) thFZ240, bottom

Figure B.9: Fraction of cluster sizes recorded for a threshold scan with MiMo1 for the bottom FZ290 (a) and thFZ240 (b) sensors. With increasing threshold the probability to detect large clusters reduces. The average cluster size is larger for the thicker FZ290 sensors.

Fraction of Different Cluster Sizes and Sensor Voltage

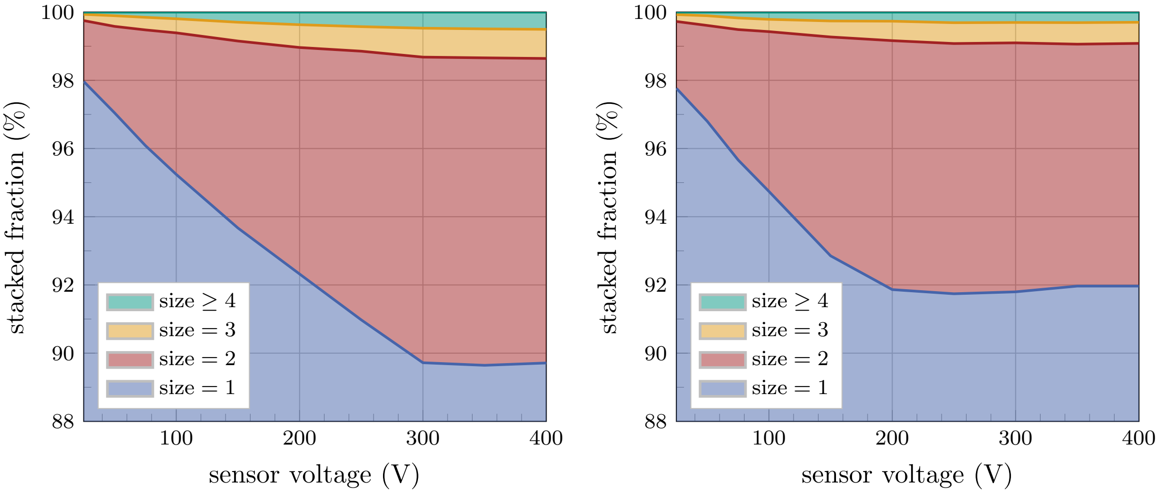

(a) FZ290, bottom

(b) thFZ240, bottom

Figure B.10: Fraction of cluster sizes recorded for a bias voltage scan with MiMo1 for FZ290 (a) and thFZ240 (b) sensors. The full depletion voltage can be read off as a kink in the curves (300 V for FZ290 and 200 V for thFZ240). For bias voltages above the full depletion voltage the fraction do not change any more. The FZ290 shows larger cluster on average. In particular, the fraction of cluster with size ≥ 4 is larger, which reduces the stub detection efficiency of the FZ290 sensors compared to the thFZ240 sensors. The main process for generating clusters with more than two strips is the generation of δ electrons. Due to its larger thickness the probability to generate δ electrons is larger for FZ290 sensors.

C

Additional Information on High Rate Measurements

Test Pulse Signal Shape and Timing

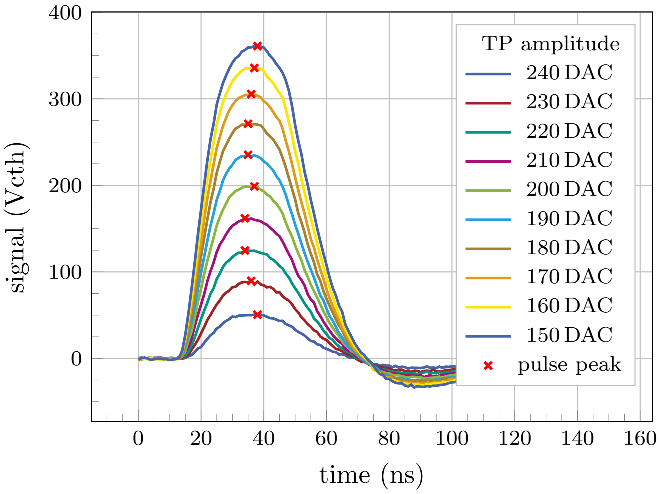

Figure C.1: Test Pulse shape and peaking time for different test pulse amplitudes. The peaking time (red cross) does not depend on the charge signal of the test pulses.

Simulation of the CBC Readout Buffer Overflow

This section introduces a simulation tool to emulate the CBC readout buffer over time and to determine the number of events until an overflow occurs. Furthermore, it presents the simulation results for different trigger frequency scenarios of the HL-LHC.

To emulate the readout buffer status of the CBC the simulation follows an approach similar to the implementation of the CBC readout buffer overflow protection as presented in section 11.4. The basic assumption of the simulation is a constant trigger probability for every collision. For a given average separation $\langle S \rangle$ between two consecutive triggers the trigger probability p is

$$p = \langle S \rangle^{-1} \tag{C.1}$$

E.g. for $\langle S \rangle = 50$ (average trigger frequency of 800 kHz) the trigger probability is 2 %. The simulation evaluates the trigger decision for every collision. For a positive trigger decision the new readout buffer status is calculated. The readout buffer status is represented by the number of remaining 25 ns clock cycles (time between two consecutive collisions) to read out all data in the buffer. For every clock cycle it is lowered by one. For every triggered event the

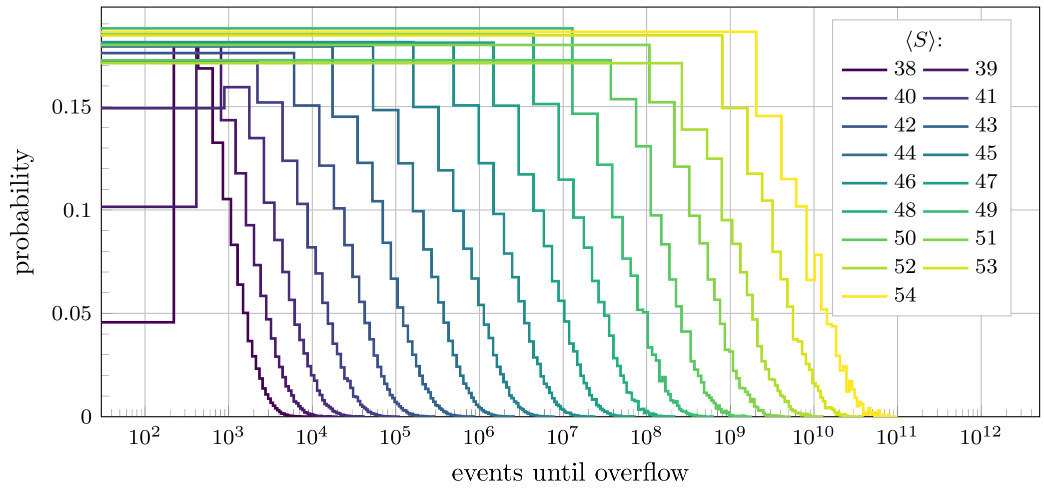

Figure C.2: Probability distribution of the number of events until a CBC readout buffer overflow occurs for different average trigger separations $\langle S \rangle$. With increasing trigger separation it requires on average more events until a buffer overflow occurs.

buffer is incremented by 38, which is the time required by the CBC to emit a full event. If the incremented buffer status exceeds the buffer limit a readout buffer overflow occurs. The theoretical limit for the readout buffer is 1216 which is the buffer depth (32 events) multiplied by the time to read out one event (38 clock cycles). However, the actual real limit measured with the KARATE system is 1210 (see section 11.4). Thus, this value was used for the simulations.

The simulation counts the number of recorded events until a CBC readout buffer overflow occurs. Repeating the simulation multiple times yields a distribution for the number of events until a CBC readout buffer overflow occurs. The normalized histogram is the probability distribution for the occurence of a readout buffer overflow after a certain number of events. Figure C.2 displays the probability distributions for different $\langle S \rangle$. Since the number of events in a run is very high the time until a readout buffer overflow occurs is calculated by:

$$t = \frac{\#\text{events} \cdot \langle S \rangle}{40\,\text{MHz}} \tag{C.2}$$

Figure C.3 displays the result of the buffer simulations for an average trigger separation $\langle S \rangle$ of 53 clock cycles (755 kHz trigger rate). This trigger rate corresponds to the nominal trigger frequency of the HL-LHC. The resulting distribution has an exponential shape which equals a constant probability for the occurence of a CBC readout buffer overflow in any given time interval. The distribution can be described by

$$f(x) = m \cdot \mathrm{e}^{-x/\lambda} + b, \tag{C.3}$$

where m, b and λ are free parameters. The parameter λ is a number of events and can be translated in a time by equation C.2. For the given exponential behavior λ equals the mean number of events until a CBC readout buffer overflow occurs.

Figure C.4 shows the average time until a CBC readout buffer overflow occurs over the average trigger separations. The time was calculated using the average number of events until the buffer overflow $\langle \#\text{events} \rangle$ and the fit parameter λ for the individual probability distributions. For the nominal trigger frequency of 750 kHz the average time for a overflow is approximately 5300 s.

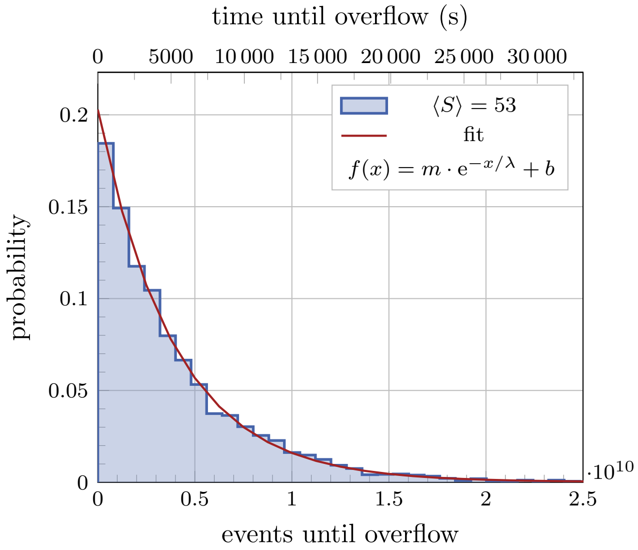

Figure C.3: Probability distribution of the number of events until a CBC readout buffer overflow occurs for an average trigger separation of 53 clock cycles. The distribution follows an exponential behavior, which corresponds to a constant probability that a readout buffer overflow occurs in a given time interval. The fit parameter λ equals the average number of events until a readout buffer overflow occurs.

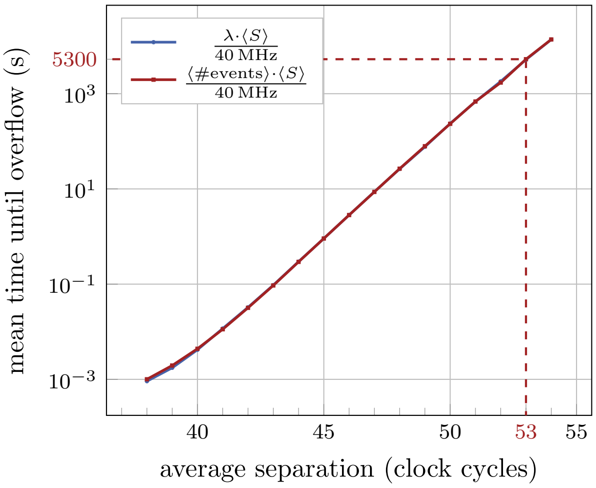

Figure C.4: Simulated mean time until the CBC readout buffer overflow occurs over the average trigger separation $\langle S\rangle$. For the nominal trigger frequency of the HL-LHC the average time until a CBC readout buffer overflow occurs is approximately 5300 s.

CBC Readout Buffer Overflow Protection

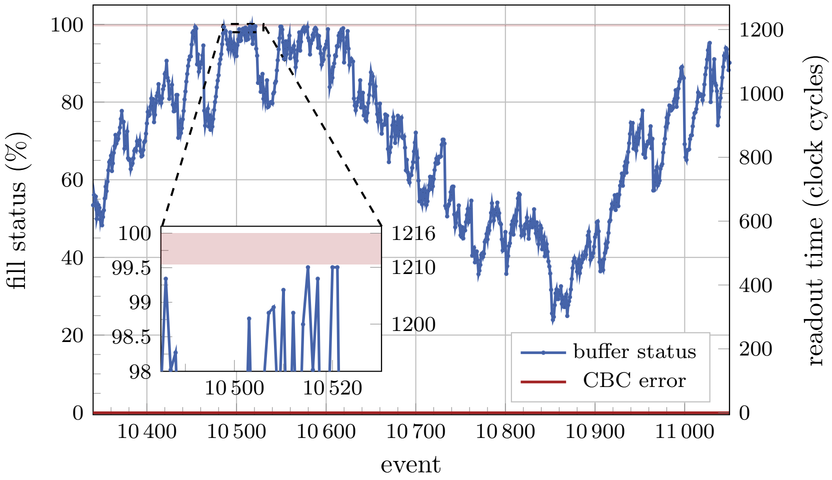

Figure C.5: CBC readout buffer status calculated for every event. The average trigger separation of the run was 38 clock cycles. The readout buffer overflow protection algorithm prevents the CBC readout buffer from an overflow by limiting the remaining readout time to 1210 clock cycles. The buffer becomes filled multiple times up to 1210 without causing a CBC error.

Error Patterns and Bandwidth Violations

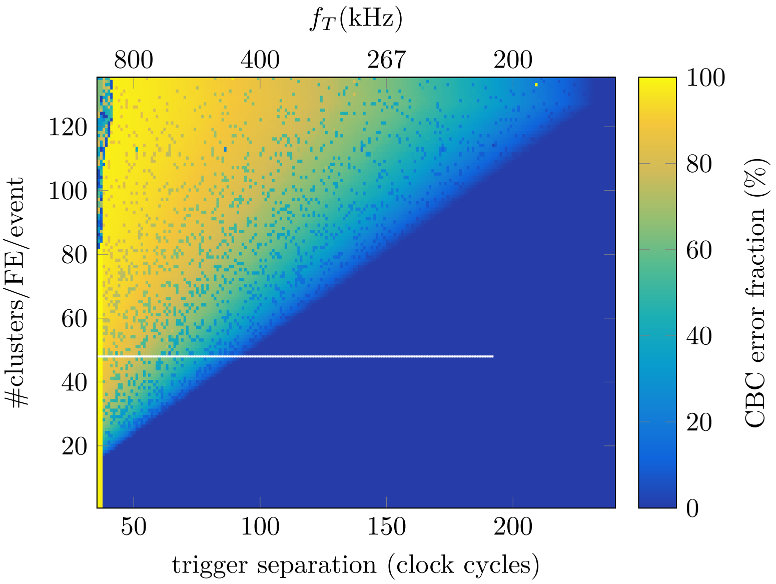

Figure C.6: Fraction of events with at least one CBC error for a scan of the cluster efficiency over the number of clusters per front-end and event and the trigger separation scan. For trigger separations below 38 clock cycles the CBC runs into a readout buffer overflow and all subsequent events have an error flag (yellow band on the left). Violating the bandwidth limit causes a soft overflow of the CIC readout buffer, which is flagged with "high error" for all CBCs and the CIC (triangular region in the upper left-hand corner).

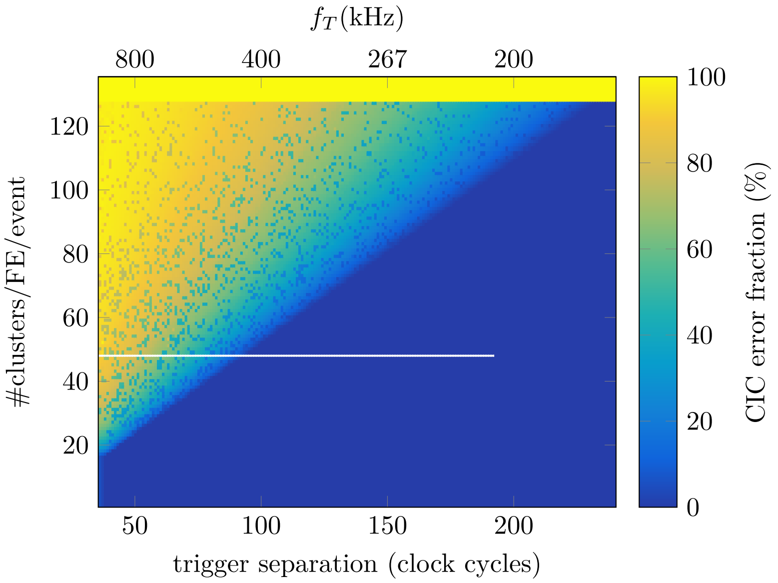

Figure C.7: Fraction of events with CIC error for a scan of the cluster efficiency over the number of clusters per front-end and event and the trigger separation scan. Violating the cluster limit of the CIC triggers a CIC error (yellow band at the top) and the CIC drops surplus clusters. Violating the bandwidth limit causes a soft overflow of the CIC readout buffer, which is flagged with "high error" for all CBCs and the CIC (triangular region in the upper left-hand corner).

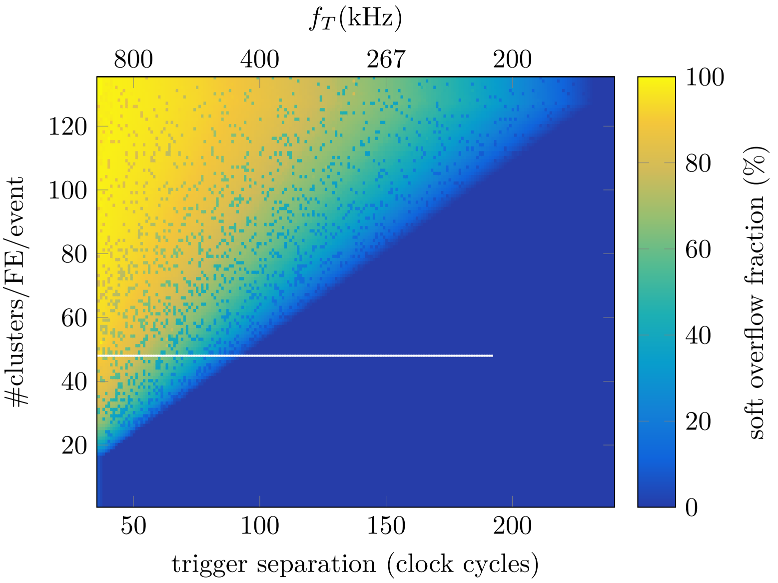

Figure C.8: Fraction of events with soft overflow for a scan of the cluster efficiency over the number of clusters per front-end and event and the trigger separation scan. A soft overflow is the readout buffer overflow of the CIC. Violating the bandwidth limit causes a soft overflow of the CIC readout buffer which is flagged with "high error" for all CBCs and the CIC (triangular region in the upper left-hand corner). Only the events which were overwritten by the overflow are corrupted and the data acquisition can continue even after the occurence of a CIC readout buffer overflow.

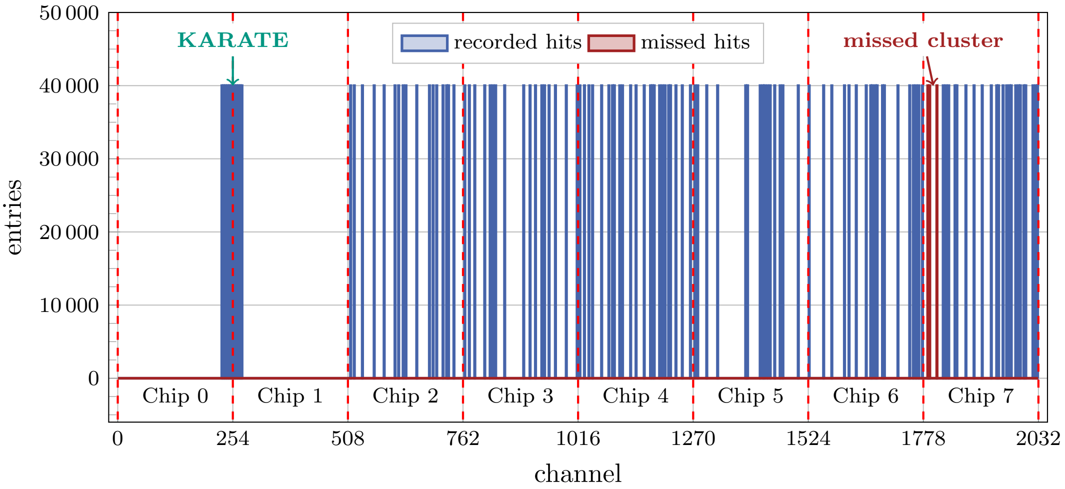

Figure C.9: Hit map in one front-end for an example run with constant trigger separation (53 clock cycles) and fixed number of clusters ($N_{\mathrm{inj}}^{\mathrm{cl}} = 130$). For the run, 40 000 events were recorded. In chips 0 and 1 only the KARATE injector channels inject clusters. The additional clusters are generated by noise and randomly distributed over the remaining six CBCs. The CIC can encode up to 127 clusters per event. The surplus are dropped by the CIC (marked in red).

CMSSW Based Stress Test of the Level-1 Data Path

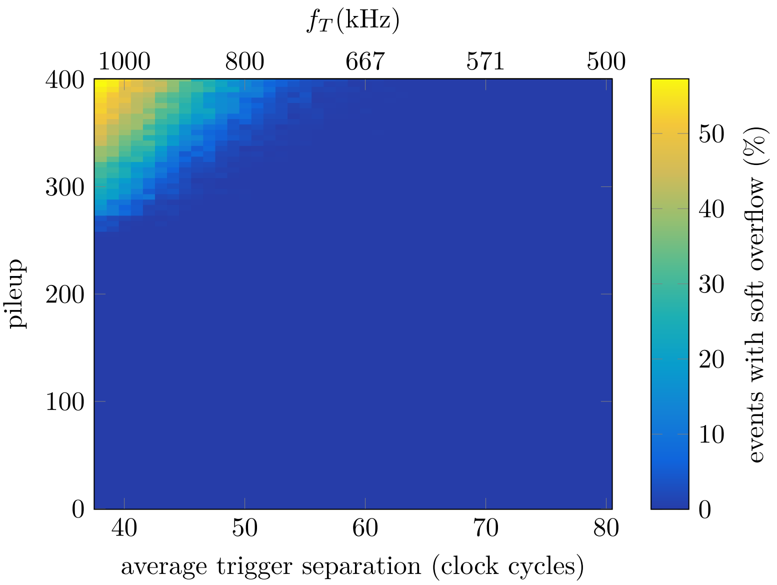

Figure C.10: Fraction of soft overflow events scanned over the average trigger separation and pileup for the modules on reference position 20. Those modules will see the highest particle flux in the future Outer Tracker. Soft overflow events represent the readout buffer overflow of the CIC. In the upper left-hand corner (high pileup and high trigger rate) the bandwidth limits the data throughput.

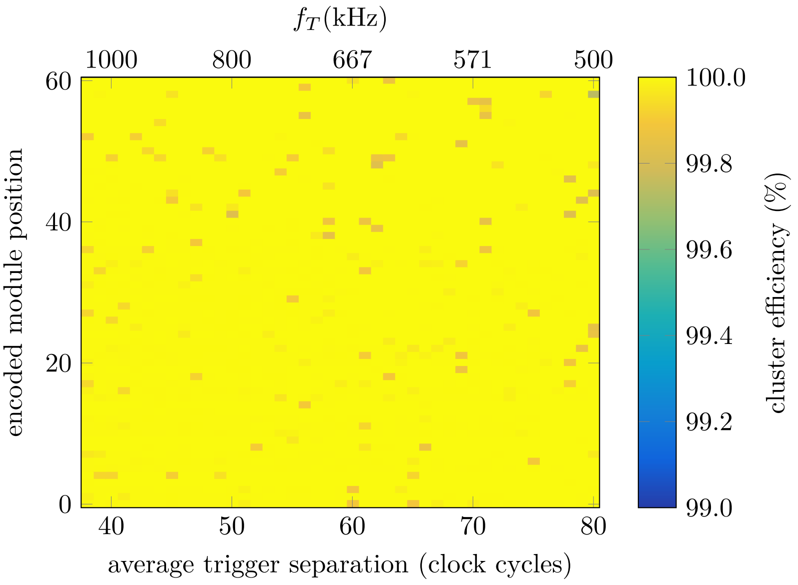

Figure C.11: Cluster efficiency scanned over the encoded module position and average trigger separation for pileup 200. No module position loses efficiency due to bandwidth limitations of the 2S module readout chain. Undetected injections result in small efficiency loses that are randomly distributed. The working point of the injector is a trade-off between maximizing the cluster efficiency and minimizing the fake hit rate.

Lookup Tables for the Encoded 2S Module Positions in the Phase-2 Outer Tracker Layout

Table C.1: 2S module positions with the same z and r in the Outer Tracker endcap. The modules at position 20 see the highest particle flux of all 2S modules, hence this position is the reference for the measurements.

position	**disk**	**ring**	**r (mm)**	**|z| (mm)**
0	1	11	689	1296
1	1	12	788	1328
2	1	13	855	1296
3	1	14	963	1328
4	1	15	1023	1296
5	2	11	689	1534
6	2	12	788	1566
7	2	13	855	1534
8	2	14	963	1566
9	2	15	1023	1534
10	3	8	665	1838
11	3	9	768	1869
12	3	10	845	1838
13	3	11	950	1869
14	3	12	1023	1838
15	4	8	665	2200
16	4	9	768	2232
17	4	10	845	2200
18	4	11	950	2232
19	4	12	1023	2200
20	5	8	665	2634
21	5	9	768	2666
22	5	10	845	2634
23	5	11	950	2666
24	5	12	1023	2634

Table C.2: 2S module positions with the same z and r in the Outer Tracker barrel.

position	layer	ladder pos.	r (mm)	|z| (mm)
25	4	1, 24	689	1127
26	4	2, 23	685	1024
27	4	3, 22	689	933
28	4	4, 21	685	830
29	4	5, 20	689	739
30	4	6, 19	685	637
31	4	7, 18	689	544
32	4	8, 17	685	443
33	4	9, 16	689	347
34	4	10, 15	685	246
35	4	11, 14	689	148
36	4	12, 13	685	47
37	5	1, 24	862	1127
38	5	2, 23	858	1024
39	5	3, 22	862	933
40	5	4, 21	858	830
41	5	5, 20	862	739
42	5	6, 19	858	637
43	5	7, 18	862	544
44	5	8, 17	858	443
45	5	9, 16	862	347
46	5	10, 15	858	246
47	5	11, 14	862	148
48	5	12, 13	858	47
49	6	1, 24	1085	1127
50	6	2, 23	1081	1024
51	6	3, 22	1085	933
52	6	4, 21	1081	830
53	6	5, 20	1085	739
54	6	6, 19	1081	637
55	6	7, 18	1085	544
56	6	8, 17	1081	443
57	6	9, 16	1085	347
58	6	10, 15	1081	246
59	6	11, 14	1085	148
60	6	12, 13	1081	47

Analog Signal Injection with the KARATE Setup

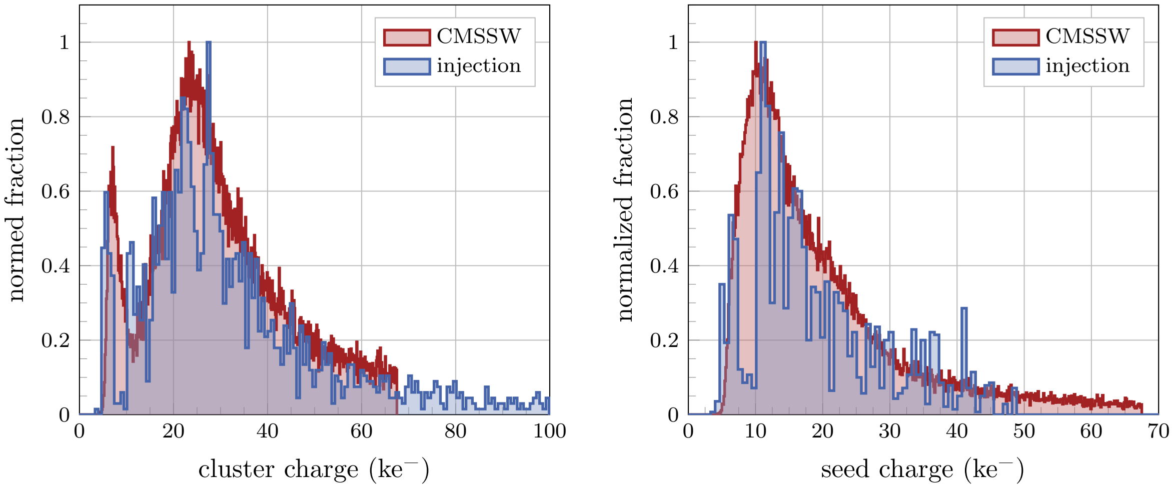

(a) Cluster charge from CMSSW and injection **(b)** Seed charge from CMSSW and injection

Figure C.12: Cluster charge (a) and seed charge (b) distribution from CMSSW simulations compared with the injected signals using KARATE. The example displays the distributions for module position 36. The coarse injection modulation with eight different values limit the resolution for charge injections into one channel. The cluster charge combines multiple injections and by averaging the injected charge matches the simulations much better. KARATE cannot properly resolve low seed signal injections and hence underestimates these. That fact causes an efficiency loss for the analog signal injections.

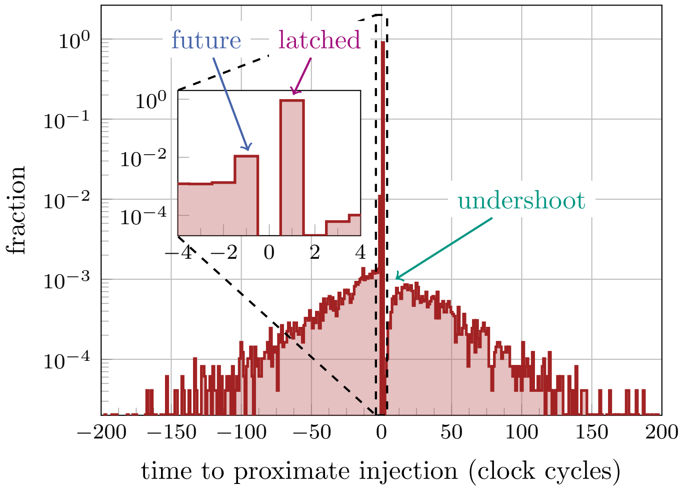

Figure C.13: Normalized fake hits correlation with the time to the proximate injection. Negative times are future injections, positive times are previous injections. Latched hits cause most fake hits at time $t = 1$. Future hits which are from the detected rising edge of the next injection show up at $t = -1$. There is a reduction of fake hits for injections in the undershoot of the previous injection for $t < 5$.

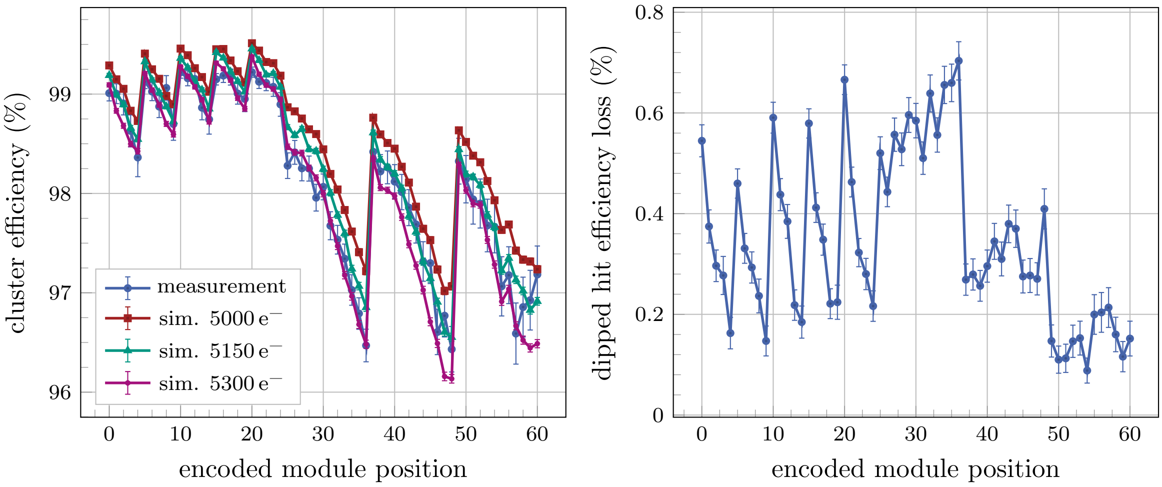

(a) Threshold variations

(b) Hit efficiency loss by dipped hits

Figure C.14: Two effects cause the cluster efficiency discrepancy between the simulation and the measurements. A small increase of the threshold has a strong effect on the simulated cluster efficiency (a). In addition, injections in the undershoot of previous signals are less efficient. The hit efficiency loss due to those dipped hits (b) depend on the module position in the tracker and is in the range between 0.1 % and 0.7 %. This effect also reduces the measured cluster efficiency.

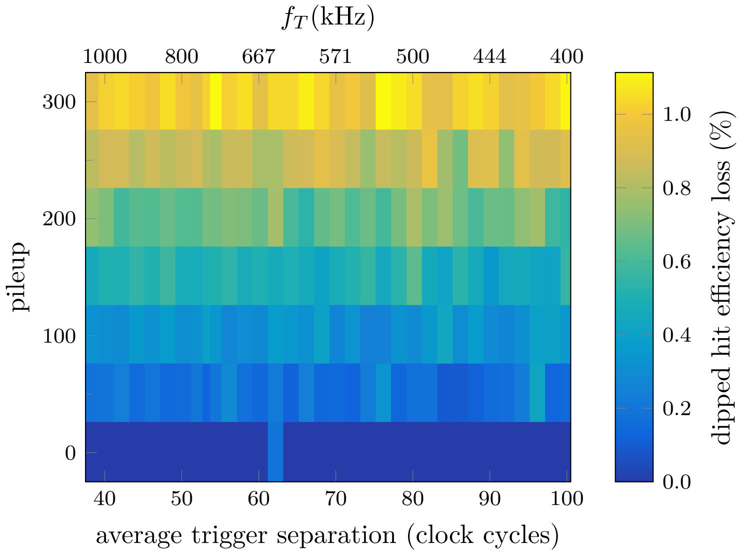

Figure C.15: Scan of the hit efficiency loss caused by dipped hits over the average trigger separation and pileup. The measurements were performed for module position 20 which are the modules on the innermost ring of the outermost endcap. The hit efficiency loss from dipped hits increases with pileup and is independent of the trigger rate.

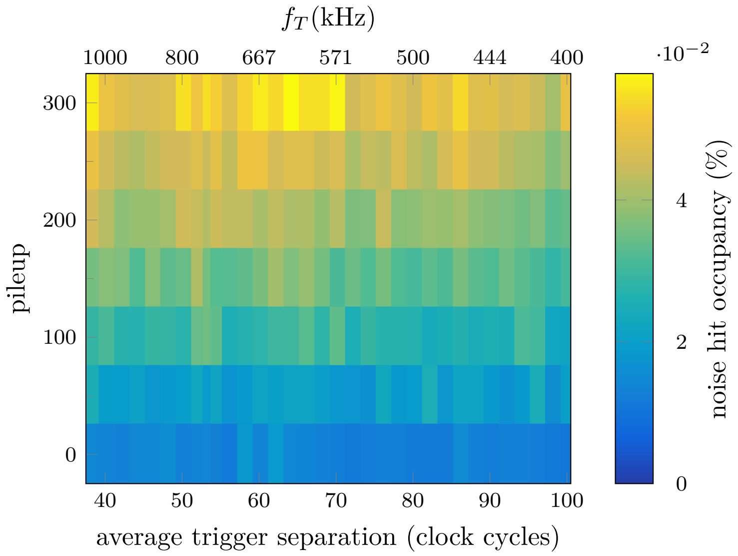

Figure C.16: Scan of the noise hit occupancy over the average trigger separation and pileup. The measurements were performed for module position 20 which are the modules on the innermost ring of the outermost endcap. The noise hit occupancy increases with pileup and is independent of the trigger rate.

List of Figures

2.1 The European Organization for Nuclear Research (CERN) Accelerator Complex 6
2.2 The CMS Detector Layout 8
2.3 Schematic Slice view of the Current CMS Tracker Layout 10

3.1 The High Luminosity LHC Upgrade Schedule 14
3.2 The Phase-2 Tracker Layout 15
3.3 FLUKA Fluences for the Phase-2 Tracker 16
3.4 p_T Module Concept 18
3.5 The p_T Module Flavors 18
3.6 Exploded View of the 2S Module 20

4.1 Schematic Band Structure of Solids 22
4.2 Band Structure of Silicon 23
4.3 Illustration of Silicon Doping 24
4.4 Illustration of the pn-Junction 26
4.5 Stopping Power of Anti-Muons in Copper 29
4.6 Normalized Energy Deposition Distribution of Pions in Silicon 31
4.7 Schematic Drawing of a Silicon Strip Sensor 33
4.8 Bulk Defects in the Crystal Lattice 34
4.9 Radiation Induced Vacancies in Silicon 34
4.10 Radiation Induced Defects in the Band Model 36
4.11 Annealing of the Damage Rate 37
4.12 Annealing of the Effective Doping Change 38

5.1 Analog Front-end of the CBC 41
5.2 S-curve of one CBC Channel 44
5.3 Trimmed CBC Pedestal and Noise Distribution 45
5.4 Reconstructed Test Pulse 46
5.5 Illustration and Example of the ^{90}Sr Threshold Scan 47
5.6 Sketch of the 2S module readout chain 48
5.7 CIC Sparsified Level-1 Data Output Format 49

6.1 Seed Signal Dependence on Sensor Thickness, Fluence and Annealing 54
6.2 The Probe Station 56
6.3 Strip Sensor Contacting 57
6.4 I(V) and C(V) Example 58
6.5 The ALiBaVa Setup 59
6.6 ^{90}Sr Cluster and Seed Charge Distribution 60
6.7 Mini Module CAD Rendering 62
6.8 View into Mini Module Test Station 64
6.9 DESY Test Beam Facility 66
6.10 Sketch of Beam Test Setup Geometry 67
6.11 Picture of the Beam Test Setup 68
6.12 Beam Test Analysis Work Flow 70
6.13 DUT post Alignment 72
6.14 TDC Timing Cut 73
6.15 Illustration of the Cluster and Stub Matching 74

6.16 Residual and Cluster Size 75
6.17 Cluster Matching Cut Scan 75

7.1 Sketch of the KARATE Setup 80
7.2 Picture of the KARATE Setup 80
7.3 Sketch of the KARATE Pattern Injection 82
7.4 Pattern Generation for Cluster Injection 83
7.5 CMSSW Cluster Charge and Size 87
7.6 CIC Clusters per Front-end and Event Distributions 87
7.7 Average Number of CIC Cluster Per Frontend and Event 88
7.8 CMSSW Cluster Charge and Size 89
7.9 Sketch of the Effect of the Cluster Stalling 90

8.1 Outer Tracker Sensor Irradiation 96
8.2 Effect of irradiation and annealing on the I(V) curve of FZ290V sensors 97
8.3 Strip Pinhole Measurement 98
8.4 Strip Leakage Current After Irradiation 98
8.5 Sensor I(V,T) and Module Temperature Measurement 99
8.6 Cluster Signal vs. Annealing 100
8.7 Seed Signal vs. Bias Voltage 101

9.1 Noise Dependence on Sensor Voltage 104
9.2 Noise and Trimming Quality Dependence on Temperature 105
9.3 Pedestal Sensitivity on Temperature 106
9.4 Noise Dependence on Sensor Current 107
9.5 ^{90}Sr Latency Scans and TDC Timing 109
9.6 ^{90}Sr Threshold and Temperature Scan for an FZ290 Sensor 110
9.7 Test Pulse Gain Calibration 111
9.8 CBC Threshold Calibration with ^{90}Sr 111
9.9 Sensor Defect Generation 114
9.10 Strip Noise of Sensor Defects 115
9.11 Pinhole Noise over Temperature for Irradiated Sensors 116
9.12 Pulse Amplitude vs. Injected Charge for Strips with Defects 117
9.13 ^{90}Sr Hit Profiles with Sensor Defects 118

10.1 Cluster Efficiency over Threshold for MiMo1 122
10.2 Cluster Efficiency over Threshold for MiMo2 123
10.3 Cluster Efficiency and Threshold for MiMo3 124
10.4 Cluster Efficiency and Sensor Bias Voltage for MiMo3 125
10.5 Cluster Efficiency and Track Inclination for MiMo3 126
10.6 Sub Strip Efficiency and Average Cluster Size for MiMo3 127
10.7 Resolution and Average Cluster Size over Track Inclination for MiMo1 129
10.8 Resolution and Cluster Size over Track Inclination for MiMo3 130
10.9 Stub Efficiency over Threshold for MiMo1 132
10.10 Stub Efficiency over Threshold for MiMo3 133
10.11 Stub Efficiency and Sensor Bias Voltage 134
10.12 Stub Efficiency and Track Inclination 135
10.13 Stub Bend and Track Inclination 136
10.14 Stub Bend and Sensor Alignment 137
10.15 Relative Rotation of the Sensor Stacks in the Mini Modules 138

11.1 Noise and Pedestal Distribution of the KARATE Receiver 142
11.2 KARATE Pulse Shape and Timing 142
11.3 KARATE Injection Signal Calibration 144
11.4 CBC Readout Buffer Overflow 145

12.1 Cluster Efficiency for Constant Trigger Separation and Clusters per Front-end and Event 148
12.2 Details on CIC Cluster and Bandwidth Limit 149
12.3 Cluster Efficiency over Pileup and Average Trigger Separation 152
12.4 Cluster Efficiency over Module Position and Trigger Separation for PU400 . . 153

13.1 Analog Cluster (Seed) Charge from CMSSW and Injection at Position 20 . . . 156
13.2 Cluster Efficiency Map for Analog Signal Injection at Nominal HL-LHC Parameters 156
13.3 Cluster Efficiency Position Scan Measurement vs. Simulation 157
13.4 Cluster Efficiency scan over Trigger Separation and Pileup for Analog Signal Injection 159
13.5 Dipped Hit Efficiency Loss and Noise Occupancy over Pileup 160
13.6 Cluster Efficiency over Pileup and Threshold for Analog Signal Injection . . . 161
13.7 Noise Hit Occupancy and Threshold for CMSSW Analog Injection 161

A.1 Unirradiated Sensors I(V) 173
A.2 Unirradiated Sensors C(V) 174
A.3 C(V) History FZ290 $2.5 \times 10^{14}\,\mathrm{n_{eq}/cm^2}$ 174
A.4 Strip Characterization Examples 175
A.5 Strip Leakage Current of Unirradiated Sensors 176
A.6 Strip Coupling Capacitance 177
A.7 Strip Poly Resistors 177
A.8 Seed Signal vs. Annealing 178
A.9 ALiBaVa Seed and Cluster Charge for unirradiated thFZ240 vs. FZ290 178
A.10 Geant4 Simulation of Sensor Energy Deposition 179
A.11 Sensor Defects and Bias Voltage for MiMo2 180
A.12 DATURA Track Resolution for the Mini Module Setup 181

B.1 Cluster Efficiency and Sensor Bias Voltage for MiMo1 183
B.2 Cluster Efficiency and Sensor Bias Voltage for MiMo2 184
B.3 Cluster Efficiency and Track Inclination for MiMo1 184
B.4 Cluster Efficiency and Track Inclination for MiMo2 185
B.5 Sub Strip Efficiency and Cluster Size for MiMo1 185
B.6 Sub Strip Efficiency and Cluster Size for MiMo2 186
B.7 Sub Strip Cluster Size and Incidence Angle for MiMo1 186
B.8 Stub Efficiency over Threshold for MiMo2 187
B.9 Cluster Size Distribution and Threshold for MiMo1 188
B.10 Cluster Size Fraction and Sensor Voltage for MiMo1 189

C.1 Test Pulse Shape and Timing 191
C.2 CBC Buffer Simulation Results for Different Trigger Separations 192
C.3 Probability Distribution of the CBC Readout Overflow for Nominal Trigger Frequency 193
C.4 Simulated Mean Time until CBC Readout Buffer Overflow for different Trigger Separations 193
C.5 CBC Readout Buffer Overflow Protection 194

C.6 CBC Error Events Fraction for Constant Trigger Separation and Clusters per Front-end and Event . . . 195
C.7 CIC Error Events Fraction for Constant Trigger Separation and Clusters per Front-end and Event . . . 196
C.8 Soft Overflow Events for Constant Trigger Separation and Clusters per Front-end and Event . . . 197
C.9 Example Hit Map High Rate Cluster Limit . . . 197
C.10 Soft Overflow Event Fraction for Pileup and Trigger Separation Scan . . . 198
C.11 Cluster Efficiency over Module Position and Trigger Separation for PU200 . . 198
C.12 Analog Cluster (Seed) Charge from CMSSW and Injection at Position 36 . . . 202
C.13 Fake Hits Correlation with Proximate Injection . . . 202
C.14 Effects on Cluster Efficiency for Analog Signal Injection . . . 203
C.15 Dipped Hit Efficiency Loss over Trigger Separation and Pileup for Analog Signal Injection . . . 203
C.16 Noise Hit Occupancy scan over Trigger Separation and Pileup for Analog Signal Injection . . . 204

List of Tables

6.1 Overview of the sensor configurations of the four Mini Modules built at Institute of Experimental Particle Physics (ETP). The sensors of two modules were irradiated with neutrons at Jožef Stefan Institute (JSI) and annealed to different equivalent annealing times at 21 °C. 64

8.1 ALiBaVa Annealing Procedure 96

9.1 Noise Temperature Results 106
9.2 Generated Defects and their Strip Position 115

C.1 Endcap Positions 200
C.2 Barrel Positions 201

Acronyms

ADC analog-to-digital converter. 50, 58, 61

Al-CF carbon-fiber reinforced aluminum. 19, 20

ALICE A Large Ion Collider Experiment. 7

ASIC Application Specific Integrated Circuit. 12, 16, 17, 19, 41, 50

ATLAS A Toroidal LHC ApparatuS. 7

CBC CMS Binary Chip. iii, iv, 4, 19, 20, 41–50, 54, 55, 61–64, 67, 71–73, 76, 79–83, 86, 91, 95, 101, 103, 105–110, 112–114, 116, 119, 121, 125, 128, 131, 141–151, 153, 155, 157, 165–168, 191–197, 205, 207

CERN European Organization for Nuclear Research. 5, 6, 13, 53, 205

CIC Concentrator Integrated Circuit. 19, 48–50, 79, 81, 82, 86, 88–91, 147–153, 167, 168, 195–198, 205

CMS Compact Muon Solenoid. 3, 5, 7–12, 16, 17, 19, 21, 32, 33, 41, 42, 44, 46, 48, 50, 53–55, 57, 63, 79, 85, 86, 89, 95, 104, 119, 121, 125–127, 131, 138, 144–146, 151, 165, 168, 169

CMSSW CMS Software. iii, 4, 79, 85–87, 89, 91, 147, 151, 152, 155, 156, 168, 202, 219

DAC digital-to-analog converter. 42, 46–48, 50, 59, 103, 108, 110, 112, 158, 167

DAQ Data Acquisition. 17, 145, 147–149, 151

DESY Deutsches Elektronen-Synchrotron. iii, 53, 65–69, 71, 73, 75, 77, 121, 166

DLL delay locked loop. 41, 42, 46, 47, 143, 144, 151, 155

DUT device under test. 66–72, 74–76, 125, 127–130, 136, 138, 181, 205

ECAL electromagnetic calorimeter. 7, 9, 11

ETP Institute of Experimental Particle Physics. 55–57, 63, 64, 209

FPGA Field Programmable Gate Array. 12, 58, 63, 131

GBL General Broken Lines. 71

GBT-SCA Giga-Bit Transceiver - Slow Control Adapter. 50

GBTx Gigabit Transceiver. 50, 51, 79, 81, 151, 167

GEAR Geometry API for Reconstruction. 71

GRP Glass fiber Reinforced Plastic. 59

GUI graphical user interface. 69

HCAL hadron calorimeter. 7, 9, 11

HL-LHC High Luminosity LHC. 4, 13, 14, 50, 53, 82, 85, 95, 96, 125, 132, 134, 144, 145, 152, 155, 166, 167, 191–193

HLT High Level Trigger. 12

HPK Hamamatsu Photonics K.K.. 53, 55, 165

IPHC Institut Pluridisciplinaire Hubert Curien. 169

JSI Jožef Stefan Institute. 61, 63, 64, 95, 209

KARATE KArlsruhe High RAte TEst. iii, iv, 4, 79–85, 89–91, 141–146, 149, 151, 155–159, 167, 168, 192, 197, 202, 219

KIT Karlsruhe Institute of Technology. 17, 55, 61, 62

L1 Level-1 Trigger. 12, 15–18

LCIO linear collider I/O. 70

LED light emitting diode. 63, 65, 79, 80, 82, 107, 108, 141, 143, 144, 147, 151, 155

LHC Large Hadron Collider. 3–7, 10, 13, 14, 16, 33, 41, 42, 46, 79, 145, 165, 167

LHCb Large Hadron Collider beauty. 7, 58

lpGBT low power Gigabit Transceiver. 19, 48, 50

MIP minimal ionizing particle. 29, 61

MPV most probable value. 30, 60, 61, 86, 87, 178, 179

NIEL non-ionizing energy loss. 35

PCB Printed Circuit Board. 58, 59, 63

Ph2_ACF Phase-2 Acquisition and Control Framework. 44, 63, 82

PKA primary knock-on atom. 33

QCD Quantum Chromodynamics. 5

SLVS scalable low-voltage signalling. 42, 49, 50

SM Standard Model. 5, 7

SRAM static random-access memory. 43, 45

SUSY Supersymmetry. 7

TDC time-to-digital converter. 60, 73, 76, 108, 109, 185

TDR Technical Design Report. 15, 55

TLU Trigger Logic Unit. 67

TTS Trigger Throttling System. 4, 145, 146, 168

UIBv2 Universal Interface Board Version 2. 63–65, 68

VHDCI Very-High-Density Cable Interconnect. 64, 65

VTRx Versatile Link Transceiver. 79, 81, 167

VTRx+ Versatile Link Plus Transceiver. 19, 48, 50

Bibliography

[Ada+17] W. Adam et al. *P-Type Silicon Strip Sensors for the new CMS Tracker at HL-LHC.* In: Journal of Instrumentation 12.06 (2017), P06018–P06018. DOI: `10.1088/1748-0221/12/06/p06018` (cited on p. 53).

[Ada+21] W. Adam et al. *The CMS Phase-1 pixel detector upgrade.* In: Journal of Instrumentation 16.02 (Feb. 2021), P02027–P02027. DOI: `10.1088/1748-0221/16/02/p02027` (cited on p. 10).

[Ago+03] S. Agostinelli et al. *Geant4—a simulation toolkit.* In: Nuclear Instruments and Methods in Physics Research Section A: Accelerators, Spectrometers, Detectors and Associated Equipment 506.3 (2003), pp. 250–303. ISSN: 0168-9002. DOI: `https://doi.org/10.1016/S0168-9002(03)01368-8` (cited on p. 85).

[ALI08] ALICE Collaboration. *The ALICE experiment at the CERN LHC.* In: Journal of Instrumentation 3.08 (Nov. 14, 2008), S08002–S08002. DOI: `10.1088/1748-0221/3/08/S08002` (cited on p. 7).

[Ama+09] L. Amaral et al. *The versatile link, a common project for super-LHC.* In: Journal of Instrumentation 4.12 (Dec. 2009), P12003–P12003. DOI: `10.1088/1748-0221/4/12/p12003` (cited on p. 51).

[Apo+17] G. Apollinari et al. *High Luminosity Large Hadron Collider HL-LHC.* Tech. rep. CERN, May 24, 2017. DOI: `10.5170/CERN-2015-005.1` (cited on p. 13).

[ATL08] ATLAS Collaboration. *The ATLAS Experiment at the CERN Large Hadron Collider.* In: Journal of Instrumentation 3.08 (Aug. 14, 2008), S08003–S08003. DOI: `10.1088/1748-0221/3/08/s08003` (cited on p. 7).

[ATL12] ATLAS Collaboration. *Observation of a new particle in the search for the Standard Model Higgs boson with the ATLAS detector at the LHC.* In: Physics Letters B 716.1 (2012), pp. 1–29. DOI: `10.1016/j.physletb.2012.08.020` (cited on p. 7).

[Bat+15] G. Battistoni et al. *Overview of the FLUKA code.* In: Annals Nucl. Energy 82 (2015), pp. 10–18. DOI: `10.1016/j.anucene.2014.11.007` (cited on p. 16).

[BB48] J. Bardeen and W. H. Brattain. *The Transistor, A Semi-Conductor Triode.* In: Physical Review 74.2 (2 1948), pp. 230–231. DOI: `https://doi.org/10.1103/PhysRev.74.230` (cited on p. 21).

[BBK18] B. Bilin, G. Blanchot, and M. Kovacs. *User guide for the Universal Interface card.* CMS internal document. Dec. 2018. URL: `https://espace.cern.ch/Tracker-Upgrade/Electronics/hybrids/_layouts/15/WopiFrame.aspx?sourcedoc=/Tracker-Upgrade/Electronics/hybrids/Shared%20Documents/Testing/Testing_Hardware/Universal%20Interface%20Board%20V2/Documents/User%20guide/UIB%20V2%20-%20User%20guide%20V2_0.docx&action=default&DefaultItemOpen=1` (visited on 10/14/2021) (cited on p. 63).

[Ber+19] G. Bergamin et al. *CIC2 technical specification.* CMS internal document. Sept. 2019. URL: `https://espace.cern.ch/Tracker-Upgrade/Electronics/CIC/Shared%20Documents/Specifications/CIC2_specs_v1p0.pdf` (visited on 05/17/2021) (cited on pp. 19, 49).

[Bis+20] T. Bisanz et al. *EUTelescope: A modular reconstruction framework for beam telescope data.* In: Journal of Instrumentation 15.09 (Sept. 2020), P09020–P09020. ISSN: 1748-0221. DOI: `10.1088/1748-0221/15/09/p09020` (cited on p. 70).

[Blo07] V. Blobel. *Millepede II - Linear Least Squares Fits with a Large Number of Parameters*. 2007. URL: `https://www.desy.de/~sschmitt/blobel/Mptwo.pdf` (visited on 10/14/2021) (cited on p. 71).

[Boe+02] W. de Boer et al. *Lorentz angle measurements in silicon detectors*. In: Nucl. Instrum. Meth. A 478 (2002). Ed. by M. Jeitler et al., pp. 330–332. DOI: `10.1016/S0168-9002(01)01820-4` (cited on p. 86).

[Bra+16] D. Braga et al. *I/O data formats for the Concentrator Integrated Circuit*. CMS internal document. Mar. 2016. URL: `https://espace.cern.ch/Tracker-Upgrade/Electronics/CIC/Shared%20Documents/Data%20formats%20(OBSOLETE!!)/CIC_IO_Formats_v4.pdf` (visited on 05/17/2021) (cited on p. 49).

[Bra17] J. Braach. *Qualification of 200µm n-in-p Silicon Strip Sensors for the CMS Tracker Upgrade*. Karlsruhe Institute of Technology (KIT), 2017. URL: `https://publish.etp.kit.edu/record/21402` (visited on 10/14/2021) (cited on p. 59).

[Bra20] J. Braach. *Functional Tests of 2S Detector Modules for the CMS Phase 2 Outer Tracker Upgrade including the Development of an IR LED Array*. Karlsruhe Institute of Technology (KIT), 2020. URL: `https://publish.etp.kit.edu/record/22024` (visited on 10/14/2021) (cited on p. 65).

[Brü+04] O. S. Brüning et al. *LHC Design Report*. CERN Yellow Reports: Monographs. Geneva: CERN, 2004. URL: `http://cds.cern.ch/record/782076` (visited on 10/14/2021) (cited on p. 5).

[Car+15] A. Caratelli et al. *The GBT-SCA, a radiation tolerant ASIC for detector control and monitoring applications in HEP experiments*. In: Journal of Instrumentation 10 (2015). DOI: `10.1088/1748-0221/10/03/C03034` (cited on p. 50).

[CER17] CERN. *LHC Guide*. 2017. URL: `https://cds.cern.ch/record/2255762` (visited on 10/14/2021) (cited on p. 5).

[CER20] CERN. *The RD50 collaboration*. 2020. URL: `https://rd50.web.cern.ch/rd50/` (visited on 11/26/2020) (cited on p. 53).

[CER21a] CERN. *Accelerator Performance and Statistics*. 2021. URL: `https://acc-stats.web.cern.ch/acc-stats/#lhc/super-table` (visited on 08/11/2021) (cited on p. 145).

[CER21b] CERN. *The HL-LHC project*. Aug. 12, 2021. URL: `https://hilumilhc.web.cern.ch/content/hl-lhc-project` (visited on 08/12/2021) (cited on pp. 13, 14).

[Chi13] A. Chilingarov. *Generation current temperature scaling*. Tech. rep. Lancaster University, UK, Jan. 30, 2013. URL: `https://cds.cern.ch/record/1511886` (visited on 10/14/2021) (cited on p. 36).

[CMS08] CMS Collaboration. *The CMS experiment at the CERN LHC*. In: Journal of Instrumentation 3.08 (Aug. 14, 2008), S08004–S08004. DOI: `10.1088/1748-0221/3/08/S08004` (cited on pp. 7, 10, 11).

[CMS12] CMS Collaboration. *Observation of a new boson at a mass of 125 GeV with the CMS experiment at the LHC*. In: Physics Letters B 716.1 (2012), pp. 30–61. DOI: `10.1016/j.physletb.2012.08.021` (cited on p. 7).

[CMS14] CMS Collaboration. *Description and performance of track and primary-vertex reconstruction with the CMS tracker*. In: Journal of Instrumentation 9.10 (2014), P10009–P10009. DOI: `10.1088/1748-0221/9/10/P10009` (cited on p. 10).

[CMS17a] CMS Collaboration. *Particle-flow reconstruction and global event description with the CMS detector.* In: Journal of Instrumentation 12.10 (2017), P10003–P10003. DOI: `10.1088/1748-0221/12/10/P10003` (cited on p. 11).

[CMS17b] CMS Collaboration. *The CMS trigger system.* In: Journal of Instrumentation 12.01 (2017), P01020. DOI: `10.1088/1748-0221/12/01/p01020` (cited on p. 12).

[CMS18] CMS Collaboration. *The Phase-2 Upgrade of the CMS Tracker.* Tech. rep. CERN-LHCC-2017-009. CMS-TDR-014. CERN, Apr. 16, 2018. URL: `https://cds.cern.ch/record/2272264` (visited on 10/14/2021) (cited on pp. 10, 15, 16, 18, 20, 32, 42, 54, 55, 104, 136).

[CMS19a] CMS Collaboration. *CMS People statistics.* 2019. URL: `http://cms.cern/collaboration/people-statistics` (visited on 11/27/2019) (cited on p. 7).

[CMS19b] CMS Collaboration. *Public CMS Luminosity Information.* Nov. 26, 2019. URL: `https://twiki.cern.ch/twiki/bin/view/CMSPublic/LumiPublicResults` (visited on 10/14/2021) (cited on pp. 5, 6).

[CMS19c] CMS Collaboration. *The Compact Muon Solenoid Experiment - bending particles.* 2019. URL: `http://cms.cern/detector/bending-particles` (visited on 12/04/2019) (cited on p. 9).

[CMS19d] CMS Collaboration. *The Compact Muon Solenoid Experiment - detector.* 2019. URL: `https://cms.cern/detector` (visited on 12/04/2019) (cited on p. 9).

[CMS21] CMS Collaboration. *CMS Phase 2 Tracker Layout.* 2021. URL: `https://cms-tklayout.web.cern.ch/cms-tklayout/layouts-work/recent-layouts/OT800_IT615/index.html` (visited on 02/12/2021) (cited on pp. 95, 96, 108, 116).

[CMS97a] CMS Collaboration. *The CMS electromagnetic calorimeter project: Technical Design Report.* Geneva, 1997. URL: `http://cds.cern.ch/record/349375` (visited on 10/14/2021) (cited on p. 10).

[CMS97b] CMS Collaboration. *The CMS hadron calorimeter project: Technical Design Report.* Tech. rep. 1997. URL: `http://cds.cern.ch/record/357153` (visited on 10/14/2021) (cited on p. 9).

[CMS97c] CMS Collaboration. *The CMS magnet project: Technical Design Report.* Tech. rep. Geneva, 1997. URL: `https://cds.cern.ch/record/331056` (visited on 10/14/2021) (cited on p. 9).

[CMS97d] CMS Collaboration. *The CMS muon project: Technical Design Report.* Tech. rep. Geneva, 1997. URL: `http://cds.cern.ch/record/343814` (visited on 10/14/2021) (cited on p. 9).

[Cus09] D. Cussans. *Description of the JRA1 Trigger Logic Unit (TLU), v0.2c.* Sept. 11, 2009. URL: `https://www.eudet.org/e26/e28/e42441/e57298/EUDET-MEMO-2009-04.pdf` (visited on 10/14/2021) (cited on p. 67).

[Dav16] S. R. Davis. *Interactive Slice of the CMS detector.* 2016. URL: `https://cds.cern.ch/record/2205172` (visited on 10/14/2021) (cited on p. 8).

[Dem16] W. Demtröder. *Experimentalphysik 3: Atome, Moleküle und Festkörper.* Springer Berlin Heidelberg, 2016. DOI: `10.1007/978-3-662-49094-5` (cited on pp. 21, 22).

[Des19] lpGBT Design Team. *lpGBT Documentation.* Feb. 2019. URL: `https://twiki.nevis.columbia.edu/twiki/pub/ATLAS/SliceTestboard/lpGBT.pdf` (visited on 08/05/2021) (cited on p. 50).

[Deu21a] Deutsches Elektronen-Synchrotron (DESY). *EUTelescope - A Generic Pixel Telescope Data Analysis Framework.* 2021. URL: `https://eutelescope.github.io/` (visited on 03/26/2021) (cited on p. 70).

[Deu21b] Deutsches Elektronen-Synchrotron (DESY). *Test Beams at DESY.* 2021. URL: `http://testbeam.desy.de` (visited on 03/24/2021) (cited on p. 66).

[Dom07] A. Dominguez. *The CMS pixel detector.* In: Nuclear Instruments and Methods in Physics Research Section A: Accelerators, Spectrometers, Detectors and Associated Equipment 581.1 (2007). VCI 2007, pp. 343–346. ISSN: 0168-9002. DOI: `https://doi.org/10.1016/j.nima.2007.07.156` (cited on p. 10).

[EUD16a] EUDAQ Development Team. *EUDAQ User Manual.* Oct. 1, 2016. URL: `http://eudaq.github.io/manual/EUDAQUserManual_v1.pdf` (visited on 10/14/2021) (cited on p. 69).

[EUD16b] EUDET collaboration. *EUDET: Detector R&D towards the International Linear Collider.* 2016. URL: `https://www.eudet.org/index_eng.html` (visited on 09/09/2021) (cited on p. 68).

[EUD21] EUDAQ Development Team. *EUDAQ Data Acquisition Framework.* 2021. URL: `https://github.com/eudaq/eudaq` (visited on 03/26/2021) (cited on p. 68).

[Fel+18] L. Feld et al. *Service Hybrids for the Silicon Strip Modules of the CMS Phase-2 Outer Tracker Upgrade.* Tech. rep. CMS-CR-2018-271. Geneva: CERN, Oct. 2018. DOI: `10.22323/1.343.0127` (cited on p. 19).

[Gad+18] T. Gadek et al. *Front-end hybrids for the strip-strip modules of the CMS Outer Tracker Upgrade.* Tech. rep. CMS-CR-2018-295. Geneva: CERN, Oct. 2018. DOI: `10.22323/1.343.0019` (cited on p. 19).

[Gar+11] M. Garcia-Sciveres et al. *The FE-I4 pixel readout integrated circuit.* In: Nuclear Instruments and Methods in Physics Research Section A: Accelerators, Spectrometers, Detectors and Associated Equipment 636.1, Supplement (2011). 7th International ”Hiroshima” Symposium on the Development and Application of Semiconductor Tracking Detectors, S155–S159. ISSN: 0168-9002. DOI: `https://doi.org/10.1016/j.nima.2010.04.101` (cited on p. 67).

[GM14] R. Gross and A. Marx. *Festkörperphysik.* Berlin, Boston: De Gruyter Oldenbourg, Aug. 2014. ISBN: 978-3-11-035870-4. DOI: `https://doi.org/10.1524/9783110358704` (cited on pp. 22, 23).

[Hal11] G. Hall. *Conceptual study of a trigger module for the CMS Tracker at SLHC.* In: Nuclear Instruments and Methods in Physics Research Section A: Accelerators, Spectrometers, Detectors and Associated Equipment 636.1, Supplement (2011). 7th International ”Hiroshima” Symposium on the Development and Application of Semiconductor Tracking Detectors, S201–S207. ISSN: 0168-9002. DOI: `https://doi.org/10.1016/j.nima.2010.04.110` (cited on p. 15).

[Ham] Hamamatsu Photonics. URL: `https://www.hamamatsu.com` (visited on 11/17/2020) (cited on pp. 53, 55).

[Har17] F. Hartmann. *Evolution of Silicon Sensor Technology in Particle Physics.* 2nd ed. Springer, Nov. 3, 2017. ISBN: 978-3-319-64434-9. DOI: `10.1007/978-3-319-64436-3` (cited on pp. 23, 25, 30, 31, 35, 53, 57).

[Hen21] N. Henze. "Die Binomialverteilung und die Multinomialverteilung". In: *Stochastik für Einsteiger: Eine Einführung in die faszinierende Welt des Zufalls*. Berlin, Heidelberg: Springer Berlin Heidelberg, 2021, pp. 140–151. ISBN: 978-3-662-63840-8. DOI: `10.1007/978-3-662-63840-8_18` (cited on p. 69).

[HJ08] L.-A. Hamel and M. Julien. *Generalized demonstration of Ramo's theorem with space charge and polarization effects*. In: Nuclear Instruments and Methods in Physics Research Section A: Accelerators, Spectrometers, Detectors and Associated Equipment 597.2 (2008), pp. 207–211. ISSN: 0168-9002. DOI: `https://doi.org/10.1016/j.nima.2008.09.008` (cited on p. 31).

[HM18] W. Herr and B. Muratori. *Concept of luminosity*. Aug. 20, 2018. URL: `https://cds.cern.ch/record/941318/files/p361.pdf` (visited on 10/14/2021) (cited on p. 5).

[Huh02] M. Huhtinen. *Simulation of non-ionising energy loss and defect formation in silicon*. In: Nuclear Instruments and Methods in Physics Research Section A: Accelerators, Spectrometers, Detectors and Associated Equipment 491.1 (2002), pp. 194–215. ISSN: 0168-9002. DOI: `https://doi.org/10.1016/S0168-9002(02)01227-5` (cited on p. 34).

[Hun17] S. Hunklinger. *Festkörperphysik*. De Gruyter Oldenbourg, 2017. ISBN: 9783110567755. DOI: `doi:10.1515/9783110567755` (cited on pp. 21, 23, 24).

[Jan+16] H. Jansen et al. *Performance of the EUDET-type beam telescopes*. In: EPJ Techniques and Instrumentation 3.1 (Oct. 2016). DOI: `https://doi.org/10.1140/epjti/s40485-016-0033-2` (cited on p. 66).

[Jun11] A. Junkes. *Influence of radiation induced defect clusters on silicon particle detectors*. PhD thesis. Universität Hamburg, 2011. URL: `https://inspirehep.net/literature/940715` (visited on 10/14/2021) (cited on p. 36).

[Kle12] C. Kleinwort. *General broken lines as advanced track fitting method*. In: Nuclear Instruments and Methods in Physics Research Section A: Accelerators, Spectrometers, Detectors and Associated Equipment 673 (2012), pp. 107–110. DOI: `10.1016/j.nima.2012.01.024` (cited on p. 71).

[Lar19] A. Larkoski. *Elementary Particle Physics: An Intuitive Introduction*. Cambridge University Press, 2019. ISBN: 9781108579285. DOI: `10.1017/9781108633758` (cited on p. 11).

[Leo94] W. R. Leo. *Techniques for nuclear and particle physics experiments: a how-to approach; 2nd ed.* Berlin: Springer, 1994. ISBN: 978-3-642-57920-2. DOI: `10.1007/978-3-642-57920-2` (cited on p. 113).

[LHC08] LHCb Collaboration. *The LHCb Detector at the LHC*. In: Journal of Instrumentation 3.08 (Aug. 14, 2008), S08005. DOI: `10.1088/1748-0221/3/08/S08005` (cited on p. 7).

[Lin+80] V. A. J. V. Lint et al. *Mechanisms of radiation effects in electronic materials*. 1st ed. Vol. 1. Wiley, 1980. ISBN: 978-0471041061 (cited on p. 33).

[Löc02] S. Löchner. *Performance of the Beetle Readout Chip for LHCb*. Sept. 2002. URL: `https://cds.cern.ch/record/1744659` (visited on 10/14/2021) (cited on p. 58).

[Lut07] G. Lutz. *Semiconductor Radiation Detectors*. ISBN: 978-3-540-71678-5 (Print) 978-3-540-71679-2 (Online). Springer, 2007. DOI: `10.1007/978-3-540-71679-2` (cited on pp. 33, 34).

[Mai19] S. Maier. *Assembly and qualification procedures of 2S modules and high rate tests of the CMS Binary Chip for the Phase 2 Upgrade of the CMS Outer Tracker.* PhD thesis. Karlsruhe Institute of Technology (KIT), 2019. URL: `https://publish.etp.kit.edu/record/21941` (visited on 10/14/2021) (cited on pp. 79–81, 167).

[Mar+07] R. Marco-Hernández et al. *Alibava : A portable readout system for silicon microstrip sensors.* In: Proceedings of the Twelfth Workshop on Electronics for LHC and Future Experiments (2007), pp. 412–416. DOI: `10.5170/CERN-2007-001.412` (cited on p. 58).

[MCW21] P. Moreira, J. Christiansen, and K. Wyllie. *GBTx Manual.* Mar. 2021. URL: `https://espace.cern.ch/GBT-Project/GBTX/Manuals/gbtxManual.pdf` (visited on 05/17/2021) (cited on p. 50).

[Met16] M. Metzler. *Radiation Hardness of n-in-p Strip Sensors for the Phase II Upgrade of CMS.* Master's thesis. Karlsruher Institut für Technologie (KIT), 2016. URL: `https://publish.etp.kit.edu/record/21322` (visited on 10/14/2021) (cited on pp. 59–61).

[Met20] M. Metzler. *Irradiation studies on n-in-p silicon strip sensors in the course of the CMS Phase-2 Outer Tracker Upgrade.* PhD thesis. Karlsruhe Institute of Technology (KIT), 2020. URL: `https://publish.etp.kit.edu/record/21943` (cited on pp. 54, 100).

[Mob19] E. Mobs. *The CERN accelerator complex - 2019. Complexe des accélérateurs du CERN - 2019.* General Photo. July 2019. URL: `https://cds.cern.ch/record/2684277` (visited on 10/14/2021) (cited on p. 6).

[Mol99] M. Moll. *Radiation Damage in Silicon Particle Detectors.* PhD thesis. University of Hamburg, 1999. URL: `https://mmoll.web.cern.ch/mmoll/thesis/` (visited on 10/14/2021) (cited on pp. 17, 35–38).

[Mor18] P. Moreira. *LpGBT Specifications.* 2018. URL: `https://espace.cern.ch/GBT-Project/LpGBT/Specifications/LpGbtxSpecifications.pdf` (visited on 04/14/2020) (cited on pp. 19, 50).

[MP14] B. Muratori and T. Pieloni. *Luminosity levelling techniques for the LHC.* Oct. 2014. DOI: `10.5170/CERN-2014-004.177`. arXiv: `1410.5646`. URL: `https://cds.cern.ch/record/1957033` (cited on p. 13).

[Nib21] E. Nibigira. *Test-beam and irradiation facility at the 25 MeV proton cyclotron CYRCé at Strasbourg.* Feb. 2021. URL: `https://indico.cern.ch/event/945675/contributions/4160466/attachments/2186007/3693558/BTTB_2021.pdf` (visited on 09/16/2021) (cited on p. 169).

[Nod+19] B. Nodari et al. *A 65 nm Data Concentration ASIC for the CMS Outer Tracker Detector Upgrade at HL-LHC.* In: PoS TWEPP2018 (2019), p. 099. DOI: `10.22323/1.343.0099` (cited on p. 49).

[Nür14] A. Nürnberg. *Studien an bestrahlten Siliziumsensoren für den CMS Spurdetektor am HL-LHC.* PhD thesis. Karlsruher Institut für Technologie (KIT), July 30, 2014. URL: `https://publish.etp.kit.edu/record/21028` (visited on 10/14/2021) (cited on pp. 26, 61).

[Nür21] A. Nürnberg. personal communication. Feb. 2021 (cited on pp. 61, 179).

[Par18] Particle Data Group. *Review of Particle Physics.* In: Physical Review D 98.3 (Aug. 2018). DOI: `10.1103/physrevd.98.030001` (cited on pp. 28–31).

[Pes+15] M. Pesaresi et al. *The FC7 AMC for generic DAQ & control applications in CMS.* In: Journal of Instrumentation 10.03 (Mar. 2015), pp. C03036–C03036. DOI: `10.1088/1748-0221/10/03/c03036` (cited on p. 63).

[Pfa58] W. G. Pfann. *Zone melting.* Wiley series on the science and technology of materials. New York: Wiley, 1958. DOI: `https://doi.org/10.1007/BF03398137` (cited on p. 55).

[PH10] M. Pesaresi and G. Hall. *Simulating the performance of a p_T tracking trigger for CMS.* In: Journal of Instrumentation 5.08 (2010), pp. C08003–C08003. DOI: `10.1088/1748-0221/5/08/c08003` (cited on p. 17).

[Pry19] M. Prydderch. *CBC3.1 User Manual.* July 18, 2019. URL: `http://www.hep.ph.ic.ac.uk/ASIC/cbc3.1/CBC3p1_User_Manual_V1p4.pdf` (visited on 11/03/2020) (cited on pp. 41, 43, 46, 110, 114).

[Rác00] A. Rácz. *Trigger throttling system for CMS DAQ.* 2000. DOI: `10.5170/CERN-2000-010.405`. URL: `https://cds.cern.ch/record/479701` (cited on p. 145).

[Ram39] S. Ramo. *Currents Induced by Electron Motion.* In: Proceedings of the IRE 27.9 (1939), pp. 584–585. DOI: `10.1109/jrproc.1939.228757` (cited on p. 31).

[Rau20] M. P. Rauch. *Thermal measurements and characterizations for the CMS phase-1 barrel pixel detector and the CMS phase-2 upgrade tracker 2S module with evaporative CO2 cooling systems.* Dissertation. Aachen: RWTH Aachen University, 2020. DOI: `10.18154/RWTH-2020-05630` (cited on pp. 105, 107).

[Sau09] R. Sauer. *Halbleiterphysik: Lehrbuch für Physiker und Ingenieure.* München: Oldenbourg, 2009. ISBN: 9783486588637 (cited on p. 25).

[Sho38] W. Shockley. *Currents to Conductors Induced by a Moving Point Charge.* In: Journal of Applied Physics 9.10 (1938), pp. 635–636. DOI: `10.1063/1.1710367` (cited on p. 31).

[SJ20] S. Spannagel and H. Jansen. *GBL Track Resolution Calculator.* May 2020. URL: `https://github.com/simonspa/resolution-simulator` (visited on 04/02/2021) (cited on p. 181).

[Spi05] H. Spieler. *Semiconductor Detector Systems.* OXFORD UNIV PR, Oct. 11, 2005. 489 pp. ISBN: 9780198527848. URL: `http://www.ebook.de/de/product/4443566/helmuth_spieler_semiconductor_detector_systems.html` (cited on pp. 28, 31).

[SŽT12] L. Snoj, G. Žerovnik, and A. Trkov. *Computational analysis of irradiation facilities at the JSI TRIGA reactor.* In: Applied Radiation and Isotopes 70.3 (2012), pp. 483–488. ISSN: 0969-8043. DOI: `https://doi.org/10.1016/j.apradiso.2011.11.042` (cited on p. 61).

[Tay02] B. G. Taylor. *Timing distribution at the LHC.* In: 8th Workshop on Electronics for LHC Experiments (2002). DOI: `10.5170/CERN-2002-003.63` (cited on p. 82).

[Tay11] L. Taylor. *CMS detector design.* Nov. 23, 2011. URL: `http://cms.web.cern.ch/news/cms-detector-design` (cited on p. 8).

[The20] The Tracker Group of the CMS Collaboration. *Selection of the silicon sensor thickness for the Phase-2 upgrade of the CMS Outer Tracker.* Tech. rep. Geneva: CERN, Dec. 2020. URL: `http://cds.cern.ch/record/2788495` (visited on 10/14/2021) (cited on p. 121).

[Tro+17] J. Troska et al. *The VTRx+, an optical link module for data transmission at HL-LHC.* In: PoS TWEPP-17 (2017), 048. 5 p. DOI: `10.22323/1.313.0048` (cited on pp. 19, 50).

[Uch+18] K. Uchida et al. *The CBC3 readout ASIC for CMS 2S-modules.* Tech. rep. CMS-CR-2018-017. Geneva: CERN, 2018. URL: `https://cds.cern.ch/record/2312215` (visited on 10/14/2021) (cited on p. 19).

[Wun92] R. Wunstorf. *Systematische Untersuchungen zur Strahlenresistenz von Silizium-Detektoren für die Verwendung in Hochenergiephysik-Experimenten.* PhD thesis. Hamburg: University of Hamburg, 1992. URL: `https://bib-pubdb1.desy.de/record/153817` (visited on 10/14/2021) (cited on p. 35).

Acknowledgments — Danksagung

The thesis in hands would not have been possible without the support of many people. To all of you I want to express my sincere thanks!

Die vorliegende Arbeit wäre nicht ohne die Unterstützung zahlreicher Kolleginnen und Kollegen und Mitmenschen möglich gewesen. Euch allen möchte ich meinen aufrichtigen Dank aussprechen!

An erster Stelle gilt mein Dank Herrn Prof. Dr. Thomas Müller für die Möglichkeit meine Promotion am Institut für Experimentelle Teilchenphysik durchzuführen. Insbesondere bedanke ich mich für das Vertrauen in meine Fähigkeiten, die zahlreichen Anekdoten und die verlässliche Unterstützung, die mir entgegengebracht wurde.

Prof. Dr. Ulrich Husemann danke ich für die Übernahme des Korreferats und die vielen Anregungen.

Bei Dr. Alexander Dierlamm und Dr. Andreas Nürnberg möchte ich mich für die fachliche Unterstützung, die hilfreichen Hinweise und die Dikussion der Messergebnisse bedanken.

Darüber hinaus gilt mein Dank

- Tobias Barvich und Marius Neufeld für die Unterstützung beim Design und Bau der Mini-Module und Test-Stationen;
- Felix Bögelspacher, Anita Weddigen, Pia Steck und Julian Stanulla für alle gefräßte Platinen, gelötete Kabeln und gesetzte Bond-Verbindungen;
- Dr. Stefan Maier für die Entwicklung von KARATE und die Unterstützung bei der Erweiterung des Aufbaus;
- meinen Mitdoktoranden Roland Koppenhöfer, Jan-Ole Müller-Gosewisch und Florian Wittig für die Unterstützung beim Strahltest und die fruchtvollen Diskussionen;
- Diana Fellner für ihre Unterstütung bei organisatorischen und bürokratischen Fragen;
- Dr. Hans Jürgen Simonis für die IT-Administration und die musikalische Untermalung auf unseren Fluren;
- Dr. Sarah Seif El Nasr-Storey for providing many firmware images to make the KARATE measurements work;
- Prof. Dr. Suchandra Dutta for the introduction into the CMSSW software;
- meiner Familie für die Unterstützung und trotz aller Herausforderungen glückliche Zeit.

The measurements leading to these results have been performed at the Test Beam Facility at DESY Hamburg (Germany), a member of the Helmholtz Association (HGF).

I acknowledge the support by the Doctoral School “Karlsruhe School of Elementary and Astroparticle Physics: Science and Technology”.

This project has received funding from the European Union’s Horizon 2020 Research and Innovation programme under Grant Agreement no 654168.

Declaration

I declare that the work in this dissertation was carried out in accordance with the requirements of the University's Regulations and that it has not been submitted for any other academic award. Except where indicated by specific reference in the text, the work is the candidate's own work. Work done in collaboration with, or with the assistance of, others is indicated as such.

Karlsruhe, October 2021

Alexander Droll